Oxygen transport membranes for biomass gasification and cement industry

Cheng, Shiyang; Hendriksen, Peter Vang; Kaiser, Andreas; Søgaard, Martin

Publication date:
2015

Document Version
Publisher's PDF, also known as Version of record

Citation (APA):
Cheng, S., Hendriksen, P. V., Kaiser, A., & Søgaard, M. (2015). Oxygen transport membranes for biomass gasification and cement industry. Roskilde: Department of Energy Conversion and Storage, Technical University of Denmark.

Oxygen transport membranes for biomass gasification and cement industry

Shiyang Cheng

DEPARTMENT OF ENERGY CONVERSION AND STORAGE

Technical University of Denmark

Roskilde, November 2015

Academic advisors

Main supervisor：Peter Vang Hendriksen, Professor

Department of Energy, Technical University of Denmark, DK-4000, Roskilde, Denmark

Co-Supervisor：Andreas Kaiser, Senior Scientist

Department of Energy, Technical University of Denmark, DK-4000, Roskilde, Denmark

Co-Supervisor：Martin Søgaard, Senior Research Engineer

Meneta Advanced Shims Technology A/S

Preface

The thesis is the review of my PhD research and experiments. I delivery it to fulfil my PhD degree at the Department of Energy Conversion and Storage, Technical University of Denmark. The experimental work was conducted at Technical University of Denmark (DTU) and University of Science and Technology of China (USTC) during the time from September 2012 to August 2015. Thank DSF (Danish Research Council for Strategic Research) for the financial support on project “ENEFOX- Energy Efficient Oxygen Production for a Sustainable Energy System” (11-116387). First of all, I would like to greatly appreciate my principal supervisor,

Prof. *Peter Vang Hendriksen*, for valuable suggestions, discussions and inspirations. I am grateful deeply for his sustained efforts and support on my research. His enthusiasm and professional dedication on science and technology set a good example for me. My co-supervisor Dr. *Martin Søgaard* is greatly appreciated for his patient help on experiments, theoretical knowledge and solving problems in the lab. My co-supervisor Dr. *Andreas Kaiser* is greatly appreciated for his patiently, friendly guide and advice on my research. I benefited a lot from his abundant knowledge and experience on ceramic science and engineering.

I would like to extend my sincere appreciations to my colleagues in DTU Energy. I would express my sincere thanks to Dr. *Christoluolous Chatzichristodoulou* for his patient help and valuable suggestions on defect chemistry, Hebb-Wagner polarization and *in-situ* XRD. I am also thankful to Dr. *Ming Chen* for providing thermodynamic calculation. Dr. *Jonas Gurauskis*, Dr. *Dhavanesan Ramachandran*, Dr. *Astri Haugen*, Dr. *Alfred Samson* and Dr. *Simona Ovtar* are greatly appreciated for their helps on processing and test of the membrane. Dr. *Søren Simonsen* and Prof. *Wei Zhang* are appreciated for their professional advices on TEM analysis. Thanks *Henrik Henriksen* for his great assistance on 5×5 cm^2 cell test. I would like also thank all my Chinese colleagues for their help on my research and life in Denmark.

I would like to greatly thank the colleagues in membrane research group of USTC, China. I would express my sincere thanks to the group leader Prof. *Chusheng Chen* for his considerate support on my five-month external research in his lab. It is a great pleasure to give my sincere thanks to Prof. *Henny Bowumeester* for his advices and encouragements. I would thank Dr. *Hua Huang*, my research partner in China for his patient assistance on phase-inversion tape casting.

Last but not the least, I am greatly grateful to my parents Mr. *Xuegeng Cheng* and Mrs. *Xiaomei Wang* for their understanding and support in my five-year study in Europe.

Roskilde, August 2015

Shiyang Cheng

Abstract

Oxygen transport membranes (OTMs) are of particular interest for their potential applications in high purity oxygen separation, biomass gasification and carbon capture and storage in cement production. $Gd_{0.1}Ce_{0.9}O_{1.95-\delta}$ (GCO) is one of the interesting materials of OTMs because of its high ionic conductivity and excellent chemical stability under strong reducing conditions. However, for special applications in mildly reducing conditions (e.g. pure oxygen production and oxy-coal combustion) the oxygen flux of GCO is not sufficient because the performance is limited by the low electronic conductivity.

In this study various routes for enhancing the electronic conductivity were investigated; either via elemental substitution or via mixing doped-ceria with another material when forming the membrane layers. The increase of electronic conductivity by substitution co-doped Gd and Pr in ceria was investigated by a microelectrode assisted Hebb-Wagner polarization. The electronic conductivity of $Pr_xGd_{0.1}Ce_{0.9-x}O_{1.95-\delta}$ (x=0-0.4) was found to be significantly enhanced relative to that of GCO at high pO_2 (1×10^{-8}- 0.21 bar), by as much as three orders of magnitude in $Pr_{0.4}Gd_{0.1}Ce_{0.5}O_{1.95-\delta}$. The electronic conductivity of $Pr_xGd_{0.1}Ce_{0.9-x}O_{1.95-\delta}$ increases with increasing concentration of Pr. The drastic decline of activation energy of electron hole migration (10-15 at.%) indicates a drastic decrease of hopping energy as continuous percolating “Pr-path” forms in the Face-Centred Cubic (FCC) Unit Cell. This provides a new understanding of small polaron mechanism on basis of crystal structure along with the band structure. In addition, the ionic conductivity of Pr-doped GCO is greater than that of Pr-doped ceria upon the same dopant concentration because of the higher concentration of oxygen vacancy in Pr-doped GCO. The heavily Pr-doped samples showed lower ionic conductivity relative to that of slightly Pr-doped samples. This is due to the more pronounced defect association in heavily doped ceria. The thermal expansion coefficients (TEC) of Pr-doped GCO exhibited a nonlinear feature at 500 ºC and increased with increasing dopant concentration. The sudden increase of TEC is a consequence of the increase of chemical expansion coefficient (CEC), which is induced by the chemical strain due to the increase of oxygen nonstoichiometry as the partial reduction of Pr occurs at elevated temperature. The chemical expansion coefficients were between 0.065-0.08 mol^{-1}, in line with that of Pr-doped ceria. The oxygen flux of $Pr_{0.05}Gd_{0.1}Ce_{0.85}O_{1.95-\delta}$ was enhanced relative to GCO by one order of magnitude. For a 10 μm thick $Pr_{0.4}Gd_{0.1}Ce_{0.5}O_{1.95-\delta}$-based membrane,

the estimated oxygen flux of 10 Nml cm^{-2} min^{-1} (the target for commercialization of OTMs) might be achieved at 900°C under a small oxygen potential gradient.

Substitution of Ce with Zn was also considered. ZnO-containing GCO could be sintered at a relatively lower temperature (1300°C vs. 1600°C). The solubility limit of ZnO in GCO is in the range of 2-3 at.%. As compared to GCO, the *p*-type electronic conductivity of Zn-doped GCO under oxidizing condition was not influenced by the dopant whilst the *n*-type electronic conductivity under reducing conditions was suppressed. The ionic conductivity was slightly suppressed by doping ZnO. This indicates that the zinc ion may be an interstitial defect in GCO.

Also dual phase membranes were studied. A 1-mm thick dual phase composite oxygen membrane (50vol.% $Al_{0.02}Ga_{0.02}Zn_{0.96}O_{1.02}$-50 vol.% $Gd_{0.1}Ce_{0.9}O_{1.95-\delta}$) with catalyst on both sides was observed to sustain an oxygen flux of 0.3 Nml cm^{-2} min^{-1} under air/N_2 at 900 °C. The material was observed to be chemically stable in CO_2 and SO_2 at high temperature. However, the oxygen surface exchange of the material was slow so that a high performance catalyst is required to ensure fast oxygen surface exchange.

Some of the promising material combinations were also prepared as thin films on top of structural supports. An asymmetric (thin dense layer on a porous support) dual phase composite membrane of 70 vol.% $Gd_{0.1}Ce_{0.9}O_{1.95-\delta}$-30 vol.% $La_{0.6}Sr_{0.4}FeO_{3-\delta}$ (GCO-LSF) was fabricated by a “one step” phase-inversion tape casting. Oxygen flux measurement as well as electrical conductivity relaxation indicates that the oxygen permeation flux of the membrane without catalyst is rate limited by oxygen surface exchange. Mass polarization through the porous support is insignificant over a wide range of oxygen partial pressure gradients. A stable high flux of ca. 7.00 (STP) ml cm^{-2} min^{-1} was observed for 200 hours at 850 °C with the membrane placed between air and CO. Partial surface decomposition was observed on the permeate side exposed to CO.

Besides above described investigations on ceria based systems also perovskite type membrane materials were investigated. Asymmetric $Ba_{0.5}Sr_{0.5}(Co_{0.8}Fe_{0.2})_{0.97}Zr_{0.03}O_{3-\delta}$ (BSCFZ)-based oxygen membranes were prepared by phase-inversion tape casting. The oxygen permeation fluxes of 1-mm thick disc and asymmetric membranes were limited by bulk diffusion and oxygen surface exchange in air/N_2. The membranes were not chemically stable under the large chemical potential gradients (oxygen vs. H_2/H_2O) because of fast degradation induced by thermodynamic decomposition. The asymmetric membrane (without catalyst) exhibited a stable flux when tested under more mild conditions (O_2/N_2). A flux of 11.2 Nml cm^{-2} min^{-1} at 950°C was observed over 150 hours and 7 Nml cm^{-2} min^{-1} at 850°C was measured over 300 hours in O_2/N_2. Segregation of barium sulphate and cobalt oxide was found on the surface of the dense membranes, which is ascribed to the reaction between sulphur-containing binder (PESF) and BSCFZ powder. Significant loss of Co, Sr and Fe and enrichment of $BaSO_4$ was observed on the permeate side after the long term test. This is likely due to kinetic demixing driven by the oxygen partial pressure gradient across the membrane.

Abstrakt

I dette projekt er udviklet keramiske ilt-membraner til anvendelse ved fremstilling af ren ilt. Membranerne egner sig endvidere til at levere ilt til en række høj-temperatur processer så som ilt-blæst termisk forgasning af biomasse, cement fremstilling og diverse ”oxyfuel” processer til omsætning af kul med CO_2-indfagning. De udviklede membraner er alle baseret på $Gd_{0.1}Ce_{0.9}O_{1.95-\delta}$ (GCO). Betydningen af diverse substituenter (f.eks. Pr og Co), der kan øge materialets elektronledningsevne, og dermed membranernes ydelse (ilt-produktionskapacitet) er studeret, ligesom muligheden for at kombinere CGO med et andet materiale, med højere elektronledningsevne, så membranerne bliver to-fase kompositter, er studeret i detaljer.

Tilslag (substitution) af varierende mængder af Pr op til 40% Pr i CGO er afprøvet ($Pr_xGd_{0.1}Ce_{0.9-x}O_{1.95-\delta}$ (x=0-0.4)). 40% Pr-substitution fører til en kraftig forøgelse af elektronledningsevnen af materialet (med op til tre størrelsesordener) ved høje ilt-partialtryk (1×10^{-8}- 0.21 bar). Den forøgede elektronledningsevne betyder at membraner baseret på dette materiale vil have en større produktionskapacitet; oxygen-fluxen gennem en membran af $Pr_{0.05}Gd_{0.1}Ce_{0.85}O_{1.95-\delta}$ vil være ti gange større end gennem GCO og en 10-μm tyk $Pr_{0.4}Gd_{0.1}Ce_{0.5}O_{1.95-\delta}$-membran forventes ved 900 °C mellem pO2=0,2 atm. og 0.001 atm. at kunne understøtte en flux på 10 Nml cm^{-2} min^{-1}, hvilket betragtes som en kritisk grænse for kommerciel interesse. Med hensyn til produktionskapacitet er disse materialer således meget lovende. Anvendelse i praksis er dog vanskelig pga. materialernes termo-mekaniske egenskaber – en høj og stærk u-lineær termisk ekspansionskoefficient samt betydelig kemisk ekspansion.

I projektet er endvidere udviklet en række kompositte membraner. Med en ~1 mm tyk 50vol.% $Al_{0.02}Ga_{0.02}Zn_{0.96}O_{1.02}$-50 vol.% $Gd_{0.1}Ce_{0.9}O_{1.95-\delta}$ membran måles en flux på 0.3 Nm cm^{-2} min^{-1} mellem luft og ren N_2 ved 900 °C. Denne komposit er demonstreret at være stabil i CO_2 and SO_2 ved høj temperatur. Det betyder at membraner af denne type potentielt kan integreres direkte i de anlæg, hvor ilten skal leveres. Ilt-produktionskapaciteten kan øges ved i en videreudvikling af konceptet at reducere membranens tykkelse.

I projektet er også sådanne tynd-film-membraner udviklet og studeret, dog baseret på andre sammensætninger. Det er lykkedes at fremstille en komposit bestående af 70 vol.% $Gd_{0.1}Ce_{0.9}O_{1.95-\delta}$-30 vol.% $La_{0.6}Sr_{0.4}FeO_{3-\delta}$ (GCO-LSF) i en et-trins “phase inversion” process. Fremstillingsprocessen resulterer i et høj-porøst bære-lag med orienteret porøsitet. Det er

demonstreret, at med den opnåede mikro-struktur er gasdiffusionen i laget så hurtig, at den er helt uden betydning for ilt-fluxen gennem komponenten. En stabil flux på 7.00 ml cm^{-2} min^{-1} er demonstreret over 200 timer ved 850 °C (mellem luft og CO). Post-test observationer viser en delvis dekomponering af materialet på CO-siden, men termodynamiske betragtninger viser at dette kan undgås ved anvendelse af en fugtig sweep-gas. ”Phase-inversion” båndstøbningsteknikken er også anvendt til fremstilling af asymmetriske $Ba_{0.5}Sr_{0.5}(Co_{0.8}Fe_{0.2})_{0.97}Zr_{0.03}O_{3-\delta}$ (BSCFZ) iltmembraner og disses transportegenskaber er blevet undersøgt. Ved 950 ^{o}C måles en konstant flux på 11.2 Nml cm^{-2} min^{-1} over 150 timer og 7 Nml cm^{-2} min^{-1} ved 850°C over 300 timer (O_2/N_2), hvilket må betragtes som meget lovende ydelser for anvendelse ved høje ilt-partialtryk.

Contents

Chapter 1：Introduction

This chapter gives an introduction about oxygen transport membrane (OTM) technology with special emphasize on its applications in biomass gasification and cement industry.

1.1. Inorganic ceramic oxygen transport membrane (OTM) technology

Oxygen is one of the most widely used chemical commodities in the world. The demand of oxygen is believed to be expanding in the coming years. A large demand of oxygen comes from a variety of industries, i.e. medical industry, steel and glass industry. In future also demand from biomass gasification and in conversion of fossil fuels (e.g. coal and natural gas) is to facilitate the chemical energy conversion into intermediate synthetic gases or into electricity. The synthetic gases generated from oxy-fuel combustion can be further used as the fuel for SOFCs or for synthesis of liquid fuels and other chemical products.

The separation of oxygen from air is achieved by two main technologies: cryogenic distillation and pressure swing adsorption (PSA). The cryogenic distillation is typically reserved for applications that require high purity oxygen (>99%) and large scale productions (tonnage quantities of oxygen) at low temperatures. PSA is a technology that allows to separate oxygen from static ambient air by first absorbing oxygen inside the adsorptive materials under high pressure and then swinging to low pressure to desorb the absorbed oxygen.

Recently, a new technology based on inorganic ceramic oxygen transport membranes (OTMs) has emerged and has been extensively investigated in a number of academic institutions and companies. For instance, Air Products and Chemicals collaborate in a large project with the U.S. Department of Energy (US. DOE), Ceramatec and other partners to develop, scale-up and commercialize OTM technology [1].

OTMs are constructed from inorganic mixed ionic and electronic conducting (MIEC) materials where the transport of the oxygen occurs *via* simultaneous transport of oxide ions and electrons in parallel across the membrane. Compared to cryogenic distillation, especially for small to medium scale plants, MIEC membranes can be used for separation of oxygen from air at lower energy consumption [2]. In general, MIEC membranes work at high temperatures (>700 °C) because of the demand of energy for the movement of charge carriers (oxygen ion and electron/electron hole). OTMs must be operated under a gradient of oxygen partial pressure where air is normally used as the feed gas on the feed side (high pO_2 side) and a variety of mildly or harsh reducing gases are used as the sweep gases on the permeate side (low pO_2 side). The differential oxygen potential gradient across the membrane serves as the driving force for the transport of oxygen across the membrane.

1.2. Applications of oxygen transport membrane in biomass gasification

Biomass is an environmentally friendly energy resource that attracts worldwide attentions to decrease the dependence on fossil fuel. The energy produced from biomass is currently estimated to be approximately 10-14% of the world's energy supply [3]. According to the U.S. Department of Energy (DOE) (Fig. 1-1), biomass has been the largest domestic source of renewable energy for U.S. It is expected that biomass consumption in electric utilities will be double every 10 years until 2030. In the U.K., the government's target is to generate 10% of the national electricity need of 60 GWh/yr from renewable resources, of which biomass will play a vital role [3]. By 2020, the capacity of installed biomass power will be around 30 GW, with the annual use of 50 million tons of biomass pellets, 44 billion cubic meters of biogas, 10 million tons of bio-ethanol, and 2 million tons of bio-diesel [4].

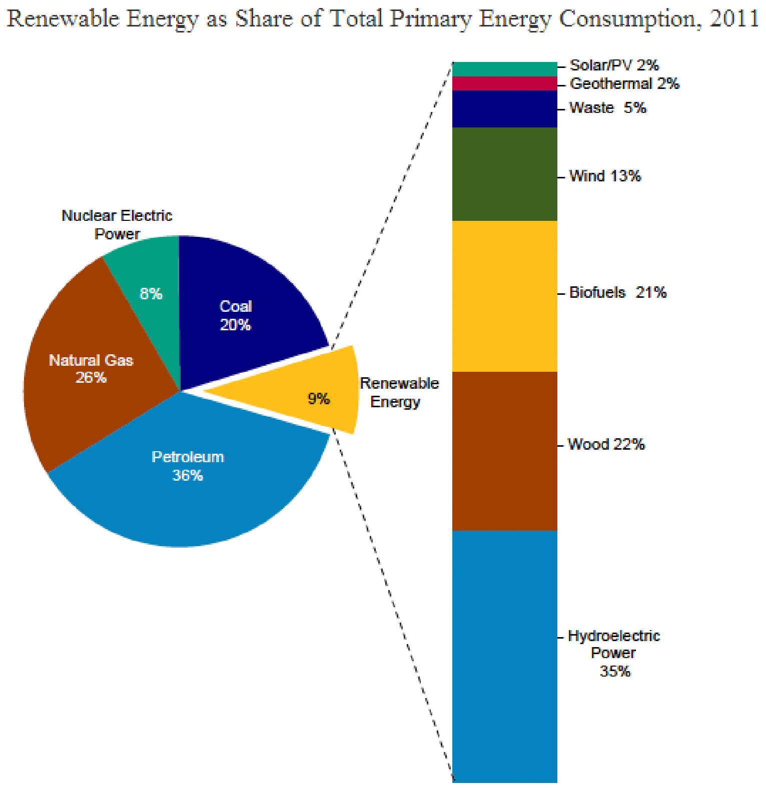

Fig. 1-1 Proportion of energy resources in US. DOE's Energy Information Agency, 2011[5].

Biomass includes agriculture residues, forest residues, energy crops, animal and human being's wastes. It is generally recognized that the reservation of biomass resources are limited worldwide, and falls short of demand in a global fossil fuel energy system, so efforts need to be made to use biomass as efficiently as possible.

Biomass can be incompletely combusted to a mixture of gases consisting of H_2, CO and CH_4 through simultaneous occurrence of exothermic pyrolysis and partial oxidation under limited oxygen supply. These combustible gases produced by biomass gasification can be used in a variety of ways. For example, the gas mixture can be used as the fuel to generate electricity by internal combustion engines and generators. The syngas (CO and H_2) produced by gasification can also be further processed to synthesize a variety of chemicals.

In the biomass combustion and gasification, air is normally used as the oxidant because of the free availability and no cost. However, air-blown biomass gasification contains 70 vol.% N_2, leading to a relatively low heating value of the gas. Use of pure oxygen increases the heating value of the producer gas and using H_2O/O_2 mixtures the ratio between H_2/CO [6] can be increased. A high H_2/CO ratio is beneficial for a downstream Fischer–Tropsch reaction or other chemical upgrades. It is economically impracticable to integrate cryogenic distillation with biomass gasification in the small scale. Oxygen transport membranes (OTMs) are considered as a superior source for oxygen supply for biomass gasification because integration of OTMs into the biomass plant in small and medium scale is feasible. This will boost energy efficiency, reduce the capital cost of CO_2 capture during the gasification and benefit the environment [6].

1.3. Application of oxygen transport membrane in cement industry

Cement industry is a traditional industry that is important and globally consolidated. The product of the cement industry is cement, which is a key ingredient in concrete. Concrete is an important construction material for foundations, buildings, roads, etc. in conjunction with steel reinforcement systems. The production of cement increases annually, and is expected to exceed 3.7 billion tons by 2050 [7]. For a number of developing countries, the growth rate of cement production is rapid, i.e. China, India and Iran. However, the environmental issues associated with the rapid growth are noteworthy, and attract attentions globally.

Environmental issues originating from cement industry is attributed to the large emission of CO_2 arising from heating of limestone and the burning of fossil fuels. The cement industry is the main contributor to the emissions of greenhouse gases from the industry sector, accounting for 5% of global carbon dioxide (CO_2) emissions [8]. Cement industry is energy intensive as it involves the heating and calcination of blended and ground materials to form clinker, as described in the following flow chart (Fig. 1-2).

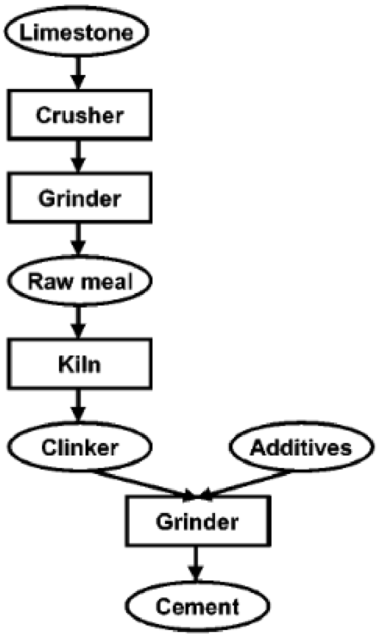

Fig. 1-2 Simplified process schematic of cement making [8].

The clinker production is the most energy-intensive production step, responsible for about 70-80% of total energy consumption. Efforts need to be made to decrease energy consumption in clinkerization at high temperature. In the cement/concrete industry improvement of energy efficiency and reduction of CO_2 emissions can be achieved by oxygen-enriched combustion because a more efficient combustion can be achieved using oxygen instead of air moreover access to oxygen facilities use of waste as fuel in the firing [9].

To mitigate CO_2 emission from the process various carbon capture schemes can be envisaged. In post combustion carbon capture one needs to do a CO_2 sequestration from the $CO_2/N_2/O_2$ flue gas from the plant as illustrated in Fig. 1-3. In oxy-fuel combustion schemes one needs access to pure oxygen for the combustion. The advantage is that no CO_2/N_2 separation is needed and thus that CO_2 capture is easier. Using pure oxygen generated by the thermally integrated OTMs to feed the process can improve the overall energy efficiency of the process. Access to high performance stable OTMs would allow continuous supply of pure oxygen to combust the fuel, yielding a CO_2-enriched exhaust gas. The exhaust gas can be recycled back to the membrane as the sweep gas to drive continuous flow of oxygen and bring this to the kiln. The major final product of the combustion after condensing out the water will be pure CO_2 which will be reused or sequestrated. The advantage of using pure O_2 in the process are: *i*) avoiding a costly post-combustion separation of CO_2 from a CO_2/N_2 steam, *ii*) the overall efficiency and production capacity of the plant can be improved, *iii*) formation of pollutants like NO_x is avoided. Therefore, it is generally expected that using OTMs in cement production can significantly decrease the expected capital cost for CO_2 capture and sequestration. A study of the plant efficiency and economy of cement plants with OTMs can be found elsewhere [10].

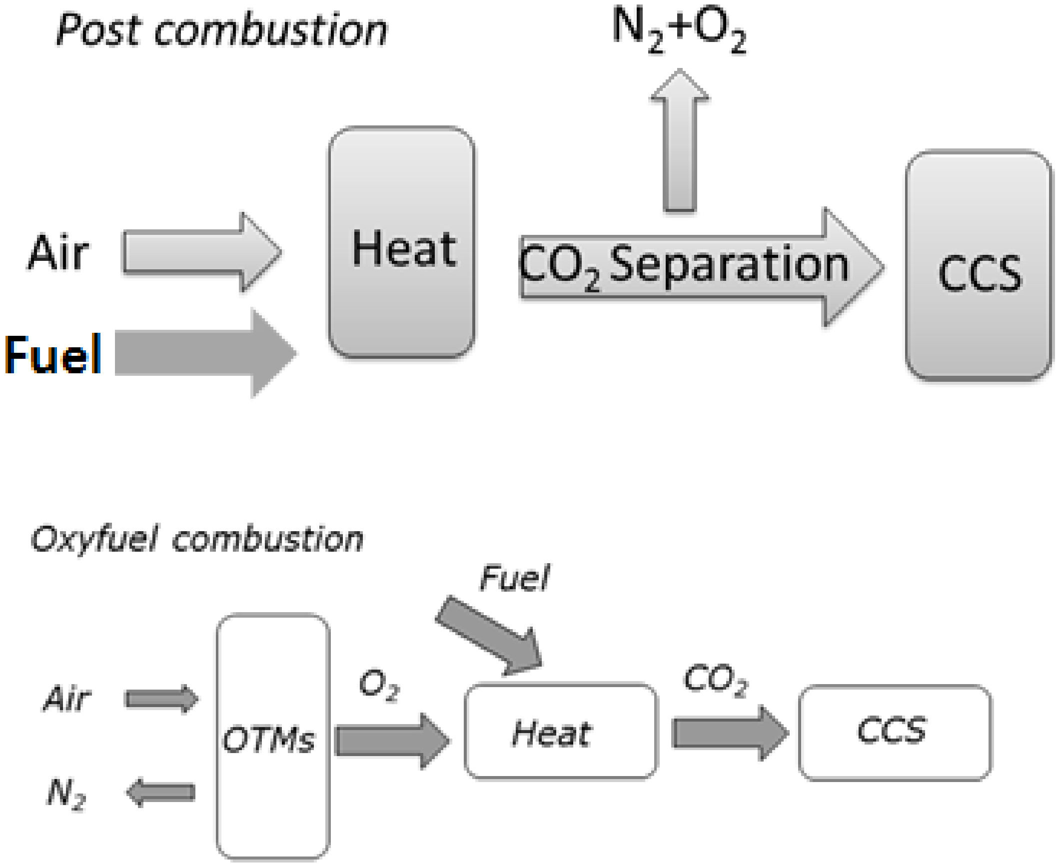

Fig.1-3 Overview of post combustion and oxy-fuel combustion for cement process.

References

[1] P.N. Dyer, R.E. Richards, S.L. Russek, D.M. Taylor, Solid State Ionics, 134 (2000) 21-33.

[2] S. Hashim, A. Mohamed, S. Bhatia, Renewable and Sustainable Energy Reviews, 15 (2011) 1284-1293.

[3] P. McKendry, Bioresource Technology, 83 (2002) 37-46.

[4] J. Huang, RENEWALE ENERGYWORLD.COM, 2014.

[5] U. EIA, Energy Information Administration, US Department of Energy: Washington, DC www. eia. doe. gov/emeu/aer, (2011).

[6] M. Puig-Arnavat, S. Soprani, M. Sogaard, K. Engelbrecht, J. Ahrenfeldt, U.B. Henriksen, P.V. Hendriksen, RSC Advances, 3 (2013) 20843-20854.

[7] M. Rubenstein, The Earth Institute of Columbia University, (2012).

[8] E. Worrell, L. Price, N. Martin, C. Hendriks, L.O. Meida, Annual Review of Energy and the Environment, 26 (2001) 303-329.

[9] D.J. Barker, S.A. Turner, P.A. Napier-Moore, M. Clark, J.E. Davison, Energy Procedia, 1 (2009) 87-94.

[10] M.P. Arnavat, M. Søgaard, K. Hjuler, J. Ahrenfeldt, U.B. Henriksen, P.V. Hendriksen, Energy 2015.

Chapter 2： Background

In this chapter, a short introduction is given on oxygen transport membranes in asymmetric structure and the factors/processes that limit the achievable flux.

2.1. Transport of oxygen through asymmetric membranes

Oxygen transport membranes (OTMs) must be operated under an oxygen partial pressure gradient to ensure a separation. The oxygen partial pressure gradient serves as a driving force that generates the transport of oxygen from the high oxygen partial pressure side (feed side) to the low oxygen partial pressure (permeate side). In order to establish the oxygen potential gradient, pressurized air (21% O_2 and 79% N_2) is usually used as the feed gas on the feed side of the membrane. On the other side (permeate side), mildly or strongly reducing gases such as a mild vacuum, CO_2, CO, CH_4, H_2 are imposed depending on the application. The oxygen potential difference from the feed to the permeate side decreases gradually due to the finite rate of the various transport processes taking place in the porous support, at the two interfaces and in the bulk of the membrane. This is schematically illustrated in Fig. 2-1 where resistance analogue is depicted. To reduce the losses in the bulk of the membrane OTMs are often manufactured in the form of thin films (1-30 μm) on top a porous structured support layer, a so-called “asymmetric membrane”.

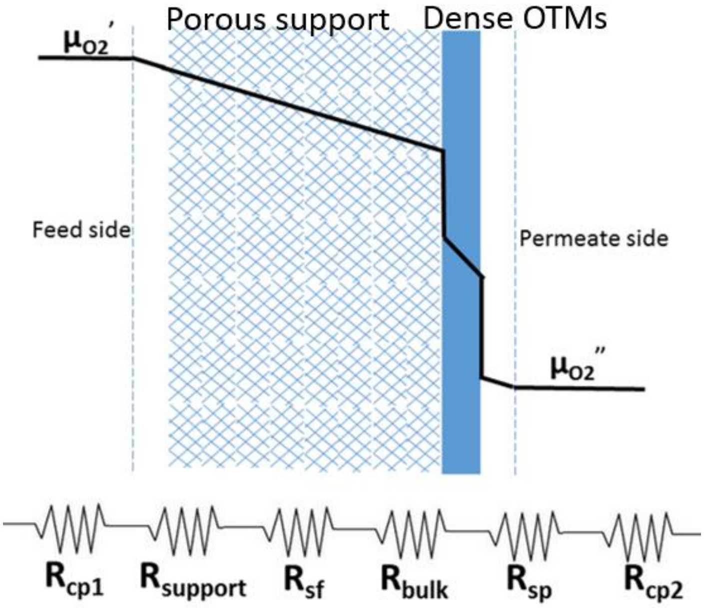

Fig. 2-1 Schematic of loss of chemical potential across the asymmetric oxygen transport membrane.

The different rate limiting processes will all correspond to a loss of driving force ($\Delta\mu_{O2}$) and may be associated with a certain resistance which is expressed in Ωcm^2. R_{cp1}, $R_{support}$ and R_{cp2} are gas diffusion resistances across the stagnant gas layer on the feed side, in the porous support and in the gas stagnant layer on the permeate side, respectively. R_{sf} and R_{sp} are the surface exchange resistances for the feed- and permeate-side, respectively. R_{bulk} is the resistance from diffusion in the bulk of the materials. The dominating rate limiting process (largest resistance) governs the overall performance. The gas diffusion occurs when the gaseous oxygen physically diffuses to the surface of the membrane across a stagnant gas layer and in the porous support media. The oxygen surface exchange occurs on the two surfaces, where oxidization and reduction reactions ($O_2+4e^-=2O^{2-}$) occur. The rate of the bulk diffusion process occurring in the dense membrane layer is often found to constitute a major part of the losses. In the following sections 2.1.1. to 2.1.3., the various rate limiting processes will be briefly discussed.

2.1.1. Gas diffusion resistance

If the driving force and flux are sufficiently large, an oxygen gradient occurs adjacent to the porous support because of the existence of stagnant gas layer. For example, the oxygen permeation flux of a 1-mm thick $La_{0.6}Sr_{0.4}CoO_3$ (LSC) membrane may become partially limited by gas diffusion when the pO_2 of the permeate side is sufficiently low [1]. This corresponds to a decline of the chemical potential starting from inlet gas to the surface of the porous support (Fig. 2-1). The flux through a stagnant gas layer will be proportional to the concentration gradient through the layer;

$$J_{O_2} = -D_{O_2-N_2}\frac{\Delta C_{O_2}}{\Delta x} \quad (2\text{-}1)$$

where Δx is the thickness of the stagnant gas layer, $D_{O_2-N_2}$ is the binary diffusion coefficient of oxygen in nitrogen, ΔC_{O_2} is the concentration difference across the layer. The fast diffusion of oxygen in air (large values of $D_{O2/N2}$) will in general lead to a negligible loss of oxygen activity except for cases with low absolute oxygen concentration.

A more significant loss of driving force is normally observed over the porous support layer. $R_{support}$ is associated with diffusion of oxygen and nitrogen across the porous substrate (S1). Concentration polarization is related to the resistance to the transport of gaseous oxygen over the support. Gas transport through the porous media occurs *via* Knudsen diffusion, binary diffusion in the phase and a viscous flow. The effective binary diffusivity of mixed gases through the porous media can be evaluated in experimental and mathematical models. Zhao and Virkar [2] used a customized electrochemical cell to evaluate the gas diffusion resistance across a porous $La_{0.6}Sr_{0.4}MnO_3$ (LSM) layer. They used the dusty gas model to evaluate the theoretical gas diffusion resistance across the porous support. According to their model, the limiting current density due to mass transport polarization can be written:

$$i_{cs} = \frac{4FD_{O_2-N_2}^{eff}}{RTl} p_0 \left(\frac{p}{p-p_0} \right) \quad (2\text{-}2)$$

where p_0 is the oxygen partial pressure outside the support. p is the total pressure (bar), $D_{O_2-N_2}^{eff}$ is the effective oxygen diffusion coefficient of O_2 in N_2 (cm^2s^{-1}), which is the oxygen diffusion coefficient $D_{O_2-N_2}$ corrected by porosity and tortuosity factor of the porous substrate. In terms of the limiting current the concentration polarization through the support can be calculated as

$$\eta_{con} = -\frac{RT}{4F} \ln\left(1 - \frac{i}{i_{cs}} \right) \quad (2\text{-}3)$$

$$i = 4FJ_{O_2} \quad (2\text{-}4)$$

$$R_{con} = \frac{\eta_{con}}{i} \quad (2\text{-}5)$$

where η_{con} is the overpotential associated with mass transport through the support, R_{con} is the equivalent resistance due to finite diffusion rate. Based on the calculation, the mass transport polarization through the porous substrate or stagnant gas layer is only weakly dependent on temperature. Compared to other rate limiting steps (oxygen surface exchange and bulk diffusion), gas diffusion is usually insignificant when the flux is not high.

2.1.2. Bulk diffusion

The bulk diffusion is strongly thermally activated illustrating that the nature of the underlying transport of the defects in the lattice scales with the concentration of point defects, for example oxygen vacancies and interstitial oxygen ions. The transport of charge carriers in the typically applied mixed conducting materials relies on the presence of an electrochemical potential gradient across the layer. The flux of a certain charged species is jointly governed by electric field and chemical potential gradient.

As oxygen membrane works in “open circuit mode” the flux through the material is related to the chemical potential difference over the membrane *via* the equation:

$$j_{O^{2-}} = -\frac{kT}{8e^2 L}\int_{I}^{II}\frac{\sigma_{O^{2-}}\sigma_{e^-}}{\sigma_{O^{2-}}+\sigma_{e^-}}d\mu_{O_2} \quad (2\text{-}6)$$

Because the fact that $1/2\, j_{O^{2-}} = j_{O_2}$ and the definition of the oxygen chemical potential $\mu_{O_2} = \mu_{O_2}^0 + RT\ln p_{O_2}$ (where $\mu_{O_2}^0$ is the reference chemical potential at absolute temperature T, R is the gas constant), the net oxygen permeation flux across a mixed conducting membrane can be written:

$$j_{O_2} = -\frac{kT}{16e^2 L}\int_{\mathrm{lnp}_{O_2^I}}^{\mathrm{lnp}_{O_2^{II}}}\frac{\sigma_{O^{2-}}\sigma_{e^-}}{\sigma_{O^{2-}}+\sigma_{e^-}}d\ln p_{O_2} \quad (2\text{-}7)$$

where pO_2^{II} and pO_2^{I} are the oxygen partial pressures on the permeate and feed side right in the solid/gas interface, respectively. This is the so-called Wagner’s equation that is generally used to analyse the bulk diffusion flux of OTMs. The term $\frac{\sigma_{O^{2-}}\sigma_{e^-}}{\sigma_{O^{2-}}+\sigma_{e^-}}$ in the Wagner’s equation is sometimes referred to as the ambipolar conductivity. The maximum ambipolar conductivity occurs when the ionic and electronic conductivities are identical. In most of the perovskite-based single or dual phase materials, the electronic conductivity is at least ten times higher than the oxide ion conductivity ($\sigma_{e^-} >> \sigma_{O^{2-}}$) and the Wagner’s equation thus simplifies to

$$j_{O_2} = -\frac{kT}{16e^2 L}\int_{\mathrm{lnp}_{O_2^I}}^{\mathrm{lnp}_{O_2^{II}}}\sigma_{O^{2-}}d\ln p_{O_2} \quad (2\text{-}8)$$

2.1.3. Oxygen surface exchange

Evidently from equation 2-8 the flux scales with 1/L. In the case of very thin membranes the losses associated with oxygen incorporation from the gas into the bulk material may become limiting for the transport over the membrane. The oxygen surface exchange process occurs through a series of reaction steps. For instance, reaction steps relevant for oxygen reduction may include adsorption, dissociation, charge transfer, and diffusion of intermediate species (O_{ads}). Anyone of these reaction steps can be the prevailing rate determining step for the overall surface exchange reaction. In the steady state, the oxygen flux across the surface is assumed to be proportional to the chemical potential drop over the interface (linear kinetics);

$$j_{O_2} = -\frac{k_s c_O}{4RT} \Delta\mu_{O_2}^{\text{int}} \quad \text{(2-9)}$$

where $\Delta\mu_{O_2}^{\text{int}}$ is the chemical potential drop across the interface and k_s is the surface exchange coefficient, and c_O denotes the oxide ion concentration at the surface. k_s can be measured by a variety of techniques, i.e. electrical conductivity relaxation (ECR), ^{18}O-^{16}O exchange and depth profiling *via* secondary ion mass spectroscopy (SIMS).

To evaluate the competition between surface exchange and bulk diffusion, Bowumeester [3] defined the characteristic thickness (L_c) for oxygen transport membranes. With respect to MIECs, L_c is defined by the ratio between self-diffusion coefficient of oxygen (D_O^*) and surface exchange coefficient (k_s). When the thickness of a membrane is close to L_c, the flux will be governed both by bulk diffusion and surface exchange. When the thickness of the membrane is far lower than L_c, the limitation by oxygen surface exchange prevails. L_c is not an intrinsic property of a MIEC because L_c is not only influenced by the intrinsic electrical properties of the material, but also dependent of a variety of extrinsic conditions, i.e. temperature [4], oxygen partial pressure [5, 6], roughness and the porosity at the surface [7]. When surface exchange is partially limiting the flux one has to use a pO_2 in equation 2-8 that is corrected for the loss over the surface, i.e. a value different from the one prevailing in the gas phase. A simple but approximate way to take into account surface loss is by using a modified Wagner's equation where the integral is multiplied with a correction factor $1/(1+2L_c/L)$ [3], which is written:

$$j_{O_2} = -\frac{1}{\left(1+\frac{2L_c}{L}\right)} \frac{kT}{16e^2L} \int_{\ln p_{O_2^{I}}}^{\ln p_{O_2^{II}}} \frac{\sigma_{O^{2-}}\sigma_{e^-}}{\sigma_{O^{2-}}+\sigma_{e^-}} d\ln p_{O_2} \quad \text{(2-10)}$$

A more elaborate but accurate approach can be found in Hendriksen *et al.* [8], Dalslet *et al.* [9] and Chatzichristodoulou *et al.* [10].

2.2. Materials for OTMs

2.2.1. Single phase membranes based on doped ceria

Gd-doped ceria ($Gd_xCe_{1-x}O_{1-0.5x}$, abbreviated as GCO) is a high performance oxide ion conductor that has been used as the electrolyte in intermediate temperature SOFCs (IT-SOFCs) [11]. Compared with another well-known material yttrium stabilized zirconia (YSZ), GCO shows one order of magnitude higher ionic conductivity below 600 °C [12]. At high temperature and low oxygen partial pressure, Ce^{4+} in GCO will be partially reduced to Ce^{3+}, leading to a significant *n*-type electronic conductivity in the material [12]. Therefore, GCO is not the optimal electrolyte for high temperature SOFCs because the high electronic conductivity leads to partial internal electronic short circuit, resulting in reducing the SOFCs efficiency with increasing temperature above 550 °C [9]. However, the electronic conductivity (or leak current) of GCO is advantageous for other applications such as OTMs and SOFC anodes.

The oxygen permeability of GCO has been studied under various oxygen potential gradients [13, 14]. GCO exhibits high oxygen flux under strongly reducing conditions because of the sufficient electronic conductivity [15]. However, the oxygen flux under mildly reducing conditions (1×10^{-5}- 0.21 bar) and at temperatures below 800 °C is relatively low because the *p*-type electronic conductivity originating from electron hole hopping is ~100 times lower than the ionic conductivity [16, 17].

Doping redox active elements can effectively enhance electronic conductivity of ceria. Pr-doped GCO has been found to show enhanced electronic conductivity relative to GCO under high oxygen partial pressure [18-22]. Apart from doping with Pr, addition of cobalt oxide in ceria has been reported to give significant enhancement of electronic conductivity under high pO_2 [23-28]. It is proposed that the enhancement of electronic conductivity is due to the formation of a CoO_y-enriched percolating pathway along the grain boundary. However, the enhancement of the electronic conductivity of GCO by addition of cobalt oxide seems to be dependent on the fabrication conditions (e.g. sintering temperature) and final microstructure. Published results on the electronic conductivity of Pr, Gd and Co doped ceria under high pO_2 (pO_2=0.21 bar) are summarized in Fig. 2-2. It seems like co-doping Pr and Co in GCO may lead to high electronic conductivity, which is expected to give rise to a pronounced enhancement of oxygen flux in ceria based membranes applied under high pO_2 conditions.

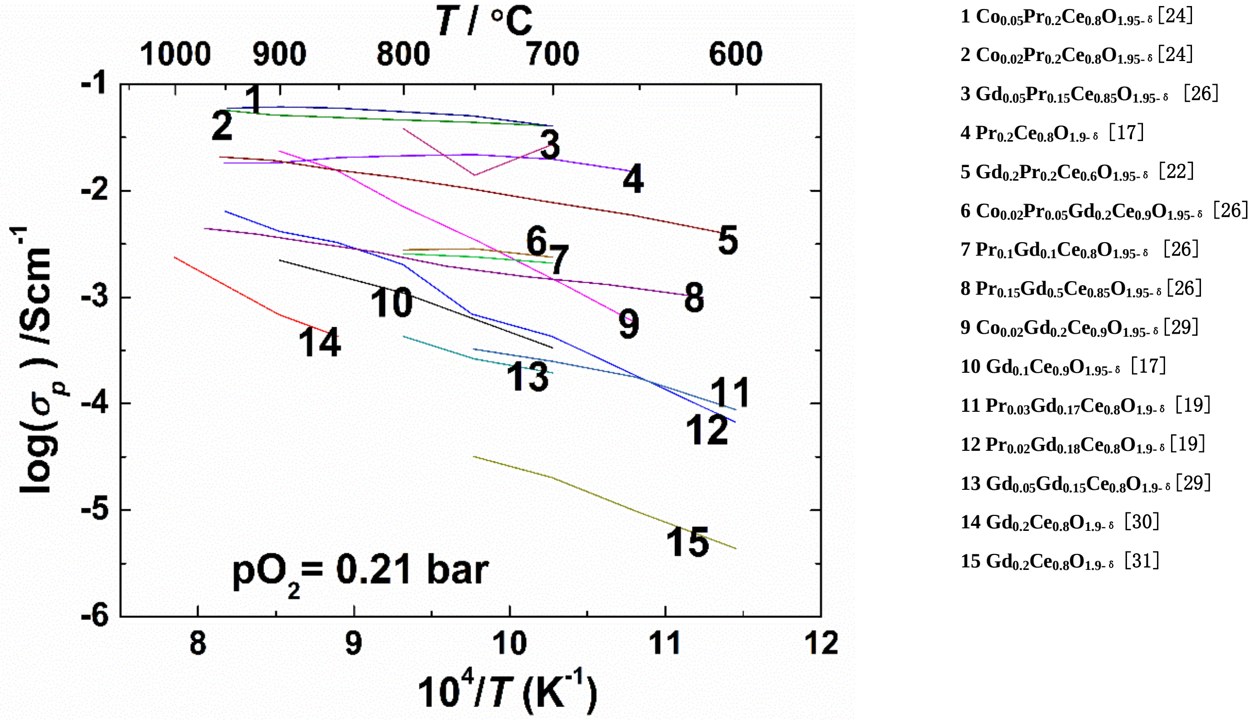

Fig. 2-2 Review of electronic conductivity of co-doping Pr, Co in Gd-doped ceria in air.

A single phase ceria doped with high concentration of redox active elements thus have high concentrations of oxygen vacancy and electron/electron hole. This will result in a thermomechanical instability when the membrane is subjected to thermal cycling [32]. For example, doping Pr in GCO or ceria may lead to an abrupt apparent jump of TEC above 600 °C [33]. This is due to the chemical expansion resulting from the increase of oxygen nonstoichiometry as reduction of Pr emerges at elevated temperature [33]. Very large strains are associated with this chemical expansion which may lead to mechanical failure of the component under practical use. Therefore, the increase of the apparent TEC induced by doping with Pr needs to be evaluated to ensure a reliable thermomechanical properties. Average apparent TEC values, evaluated between RT to 1000 °C, are plotted in Fig. 2-3 for different degrees of Pr, Co, Tb substitutions. It is evident that the integrated TEC of Pr containing ceria increases linearly with increasing dopant concentration. Doping GCO with 5 at.% Pr enhances the TEC to ca. 14×10^{-6} K^{-1} which is close to that of MgO and would allow the use of this cheap material as a mechanical support for the membrane. In comparison, addition of cobalt oxide (<15 at.%) in GCO gives only a small increase of the TEC, suggesting the feasibility of adding cobalt oxide to boost the electronic conductivity of GCO, without risking mechanical instability.

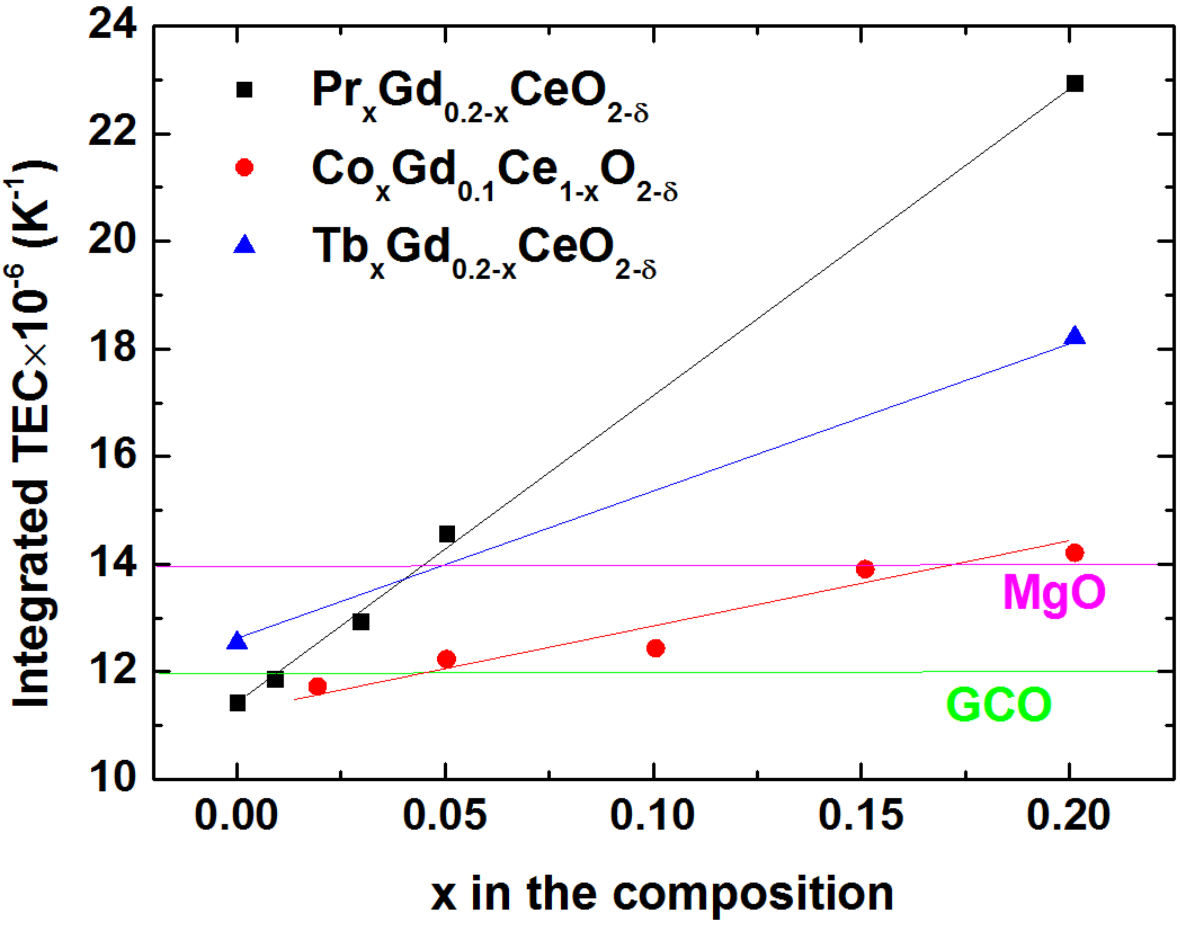

Fig. 2-3 Review of integrated TEC (from RT to 1000 °C) of Co, Pr and Tb doped GCO as a function of dopant concentration. The plots are all based on data from literature $Pr_xGd_{0.2-x}Ce_{0.8}O_{1.9}$ [18, 20], $Tb_xGd_{0.2-x}Ce_{0.8}O_{1.9}$ [20], MgO [34] $Co_xGd_{0.1}Ce_{1-x}O_2$ [21] $Gd_{0.1}Ce_{0.9}O_{1.95}$ [35].

2.2.2. GCO-based dual phase composite membranes

Alternatively to enhancing electronic conductivity by substitutions the effective electronic transport can be enhanced by mixing GCO with a good electronic conductor. The prerequisite is that the amount of the two components must be sufficient to form continuous percolating pathways for the transport of oxide ions and electrons/electron holes. In addition, the electronic conductor should be chemically compatible with GCO (no reactions between the two phases during fabrication and operation). The two phases must have close TEC to ensure good thermomechanical stability upon the thermal cycling.

According to Samson's [36] work on GCO-based dual phase composite membranes, the flux of a GCO-based composite membrane can be described by a modified Wagner's equation;

$$j_{O_2} = -\frac{kT\kappa}{16e^2 L\tau} \int_{\ln p_{O_2^I}}^{\ln p_{O_2^{II}}} \sigma_i d \ln p_{O_2} \quad (2\text{-}11)$$

where κ is the volume percent of GCO, τ denotes the tortuosity factor of GCO. In order to achieve high oxide ion conductivity, two strategies have been considered. First, using an electronic conductor with considerable oxide ion conductivity is preferred rather than using pure electronic conductor without oxide ion conduction. The high oxide ion conductivity in the electronic conductor leads to a less tortuous path for the transport of oxide ions because they can be transported in both phases [36]. Second, one can use a pure electronic conductor in GCO composite membranes, but for this case the volume percent of the electronically conducting phase and the tortuosity factor should be as low as possible to mitigate blocking of oxide ions.

2.2.3. BSCF-based membranes

The perovskite material, $Ba_{0.5}Sr_{0.5}Co_{0.8}Fe_{0.2}O_3$ (BSCF) is a commonly studied material of OTMs that so far shows the top oxygen permeability [37]. BSCF is a derivative of commonly studied material $SrCo_{0.8}Fe_{0.2}O_3$ (SCF). Perovskite-structured SCF exhibits high oxygen flux of ca. 5×10^{-6} mol cm^{-2} s^{-1} at 800 ^{o}C (air/He) [38] . The high flux of SCF is due to the high concentration of oxygen vacancies in the crystalline structure. However, SCF is subjected to a phase transformation from perovskite to brownmillerite at ca. 700 ^{o}C [39]. Shao *et al.*[37] found that substitution of Sr with Ba (so-called BSCF) not only stabilizes the cubic structure of the perovskite SCF but also enhances the oxygen flux. Nevertheless, the stability of BSCF is still insufficient for many practical applications. Pitfalls associated with high chemical and thermal expansion [40], high creep rate [41], poor mechanical properties and low chemical stability [42] limit the use of this material. Especially, the lattice expansion arising from the phase transition (cubic to hexagonal) results in chemical instability and mechanical failure. The phase transition between cubic and hexagonal occurs in the temperature range from 850 °C to 900 °C [43] where OTMs are generally operated. B-site doping with Zr can stabilize the high-temperature cubic phase of BSCF and in turn preserve relatively stable oxygen transport and surface exchange properties [44]. Ravkina *et al.* found that the maximum solubility of Zr in BSCF is up to 3 at.% and Zr-doped BSCF shows better stability and comparable oxygen flux as that of pure BSCF [42]. It is thus technologically favourable to use Zr-doped BSCF instead of BSCF.

2.3. Aim and contents of this thesis

The purpose of this thesis is:

To identify chemically stable materials for high temperature oxygen transport membranes for direct use in biomass gasification and cement industry. The materials investigated for the purpose fall in three classes; (a) co-doped ceria (b) composite of doped ceria and a good electronic conductor (c) BSCF for high pO_2 applications.

The fundamental properties of the materials were characterized and for the most suitable compositions tubular and planar asymmetric membranes were developed and evaluated in terms of the performance.

The main part of this thesis consists of five manuscripts. A brief introduction of the content in the thesis is provided below;

The Chapter 3 and 4 are introductory chapters showing applied characterization and manufacturing techniques.

Chapter 5: Manuscript I, "A novel CO_2- and SO_2- dual phase composite membrane for oxygen separation." The oxygen permeation flux and long term stability of a novel composition $Al_{0.02}Ga_{0.02}Zn_{0.96}O_{1.02}$- $Gd_{0.1}Ce_{0.9}O_{1.95-\delta}$ was characterized.

Chapter 6: Manuscript II, "High performance microchanneled asymmetric composite $Gd_{0.1}Ce_{0.9}O_{1.95-\delta}$-$La_{0.6}Sr_{0.4}FeO_{3-\delta}$ membranes for oxygen separation" investigates the oxygen permeation flux and chemical stability of a LSF-GCO dual phase composite membrane prepared by phase-inversion tape casting under oxygen partial pressure gradients of Air/He and Air/CO. The oxygen surface exchange rate and bulk diffusion were studied by oxygen flux measurement and electrical conductivity relaxation (ECR). The chemical stability of the membrane under reducing conditions was investigated by XRD, SEM, TEM and thermodynamic calculations.

Chapter 7: Manuscript III, "Enhanced mixed ionic and electronic conductivity of Pr-doped $Gd_{0.1}Ce_{0.9}O_{1.95-\delta}$" focuses on the defect chemistry, thermodynamic behaviour, thermomechanical properties, mixed ionic and electronic conductivity and oxygen permeation flux of Pr/Gd co-doped ceria, aiming to investigate the possible use of the compositions in OTMs or the cathode of SOFCs.

Chapter 8: Manuscript IV, “Performance of $Ba_{0.5}Sr_{0.5}(Co_{0.8}Fe_{0.2})_{0.97}Zr_{0.03}O_{3-\delta}$ oxygen transport membranes fabricated by phase-inversion tape casting”. In this work the oxygen permeability of asymmetric BSCFZ-based membranes was studied over a wide range of oxygen partial pressures. The degradation mechanism was discussed.

Chapter 9: Manuscript V, “Effects of addition of ZnO to $Gd_{0.1}Ce_{0.9}O_{1.95-\delta}$ on electrical conductivity” This manuscript dedicates the influence of adding ZnO dopant in GCO on the transport properties.

Chapter 10: “Fabrication of ceria based tubular oxygen transport membrane.” focuses on preparation of asymmetric ceria-based membranes by dip coating.

References

[1] M. Søgaard, PhD thesis, Technical University of Denmark, 2006.

[2] F. Zhao, T.J. Armstrong, A.V. Virkar, Journal of The Electrochemical Society, 150 (2003) A249-A256.

[3] H.J.M. Bouwmeester, H. Kruidhof, A.J. Burggraaf, Solid State Ionics, 72, Part 2 (1994) 185-194.

[4] J.A. Lane, S.J. Benson, D. Waller, J.A. Kilner, Solid State Ionics, 121 (1999) 201-208.

[5] J.A. Lane, J.A. Kilner, Solid State Ionics, 136–137 (2000) 997-1001.

[6] C.B. Gopal, S.M. Haile, Journal of Materials Chemistry A, 2 (2014) 2405-2417.

[7] J.H. Joo, G.S. Park, C.-Y. Yoo, J.H. Yu, Solid State Ionics, 253 (2013) 64-69.

[8] P.V. Hendriksen, P.H. Larsen, M. Mogensen, F.W. Poulsen, K. Wiik, Catalysis Today, 56 (2000) 283-295.

[9] B. Dalslet, P. Blennow, P. Hendriksen, N. Bonanos, D. Lybye, M. Mogensen, J Solid State Electrochem, 10 (2006) 547-561.

[10] C. Chatzichristodoulou, M. Søgaard, P.V. Hendriksen, J. Electrochem. Soc., 158 (2011) F61-F72.

[11] B.C.H. Steele, Solid State Ionics, 129 (2000) 95-110.

[12] S. Wang, T. Kobayashi, M. Dokiya, T. Hashimoto, J. Electrochem. Soc., 147 (2000) 3606-3609.

[13] C. Chatzichristodoulou, T.P. Blennow, M. Søgaard, P.V. Hendriksen, M.B. Mogensen, Ceria and its use in solid oxide cells and oxygen membranes, Catalysis by Ceria and Related Materials, World Scientific Publising Co., 2013, pp. 623-782.

[14] C. Chatzichristodoulou, M. Søgaard, J. Glasscock, A. Kaiser, S. P. V. Foghmoes, and P. V. Hendriksen, J Electrochem Soc, 158 (2011) F73.

[15] H.L. Tuller, A.S. Nowick, Journal of The Electrochemical Society, 122 (1975) 255-259.

[16] C. Chatzichristodoulou, M. Søgaard, P.V. Hendriksen, Journal of The Electrochemical Society, 158 (2011) F61-F72.

[17] C. Chatzichristodoulou, P.V. Hendriksen, Physical Chemistry Chemical Physics, 13 (2011) 21558-21572.

[18] V.V. Kharton, A.P. Viskup, F.M. Figueiredo, E.N. Naumovich, A.A. Yaremchenko, F.M.B. Marques, Electrochimica Acta, 46 (2001) 2879-2889.

[19] S. Lübke, H.D. Wiemhöfer, Solid State Ionics, 117 (1999) 229-243.

[20] C. Chatzichristodoulou, P.V. Hendriksen, A. Hagen, Journal of The Electrochemical Society, 157 (2010) B299-B307.

[21] V.V. Kharton, F.M. Figueiredo, L. Navarro, E.N. Naumovich, A.V. Kovalevsky, A.A. Yaremchenko, A.P. Viskup, A. Carneiro, F.M.B. Marques, J.R. Frade, Journal of Materials Science, 36 (2001) 1105-1117.

[22] D.P. Fagg, I.P. Marozau, A.L. Shaula, V.V. Kharton, J.R. Frade, Journal of Solid State Chemistry, 179 (2006) 3347-3356.

[23] A. Kaiser, A.S. Prasad, S.P. Foghmoes, S. Ramousse, N. Bonanos, V. Esposito, Journal of the European Ceramic Society, 33 (2013) 549-556.

[24] D.P. Fagg, S. García-Martin, V.V. Kharton, J.R. Frade, Chemistry of Materials, 21 (2008) 381-391.

[25] M. Balaguer, C. Solís, J.M. Serra, Chemistry of Materials, 23 (2011) 2333-2343.

[26] K. Schmale, M. Grünebaum, M. Janssen, S. Baumann, F. Schulze-Küppers, H.-D. Wiemhöfer, physica status solidi (b), 248 (2011) 314-322.

[27] C.M. Kleinlogel, L.J. Gauckler, Journal of Electroceramics, 5 (2000) 231-243.

[28] Y. Ji, J.A. Kilner, M.F. Carolan, Journal of the European Ceramic Society, 24 (2004) 3613-3616.

[29] D. Fagg, V. Kharton, J. Frade, Journal of Electroceramics, 9 (2002) 199-207.

[30] V.V. Kharton, A.P. Viskup, F.M. Figueiredo, E.N. Naumovich, A.L. Shaulo, F.M.B. Marques, Materials Letters, 53 (2002) 160-164.

[31] S. Lübke, H.D. Wiemhöfer, Berichte der Bunsengesellschaft für physikalische Chemie, 102 (1998) 642-649.

[32] A. Kaiser, S. Foghmoes, C. Chatzichristodoulou, M. Søgaard, J.A. Glasscock, H.L. Frandsen, P.V. Hendriksen, Journal of Membrane Science, 378 (2011) 51-60.

[33] S.R. Bishop, D. Marrocchelli, C. Chatzichristodoulou, N.H. Perry, M.B. Mogensen, H.L. Tuller, E.D. Wachsman, Annual Review of Materials Research, 44 (2014) 205-239.

[34] Y. Shiratori, F. Tietz, H.P. Buchkremer, D. Stöver, Solid State Ionics, 164 (2003) 27-33.

[35] S. Wang, M. Katsuki, T. Hashimoto, M. Dokiya, J. Electrochem. Soc., 150 (2003) A952-A958.

[36] A.J. Samson, M. Søgaard, P.V. Hendriksen, J. Membr. Sci., 470 (2014) 178-188.

[37] Z. Shao, W. Yang, Y. Cong, H. Dong, J. Tong, G. Xiong, Journal of Membrane Science, 172 (2000) 177-188.

[38] Y. Teraoka, H.-M. Zhang, S. Furukawa, N. Yamazoe, Chemistry Letters, 14 (1985) 1743-1746.

[39] L. Qiu, T.H. Lee, L.M. Liu, Y.L. Yang, A.J. Jacobson, Solid State Ionics, 76 (1995) 321-329.

[40] R. Kriegel, R. Kircheisen, J. Töpfer, Solid State Ionics, 181 (2010) 64-70.

[41] J.X. Yi, H.L. Lein, T. Grande, S. Yakovlev, H.J.M. Bouwmeester, Solid State Ionics, 180 (2009) 1564-1568.

[42] O. Ravkina, T. Klande, A. Feldhoff, Journal of Solid State Chemistry, 201 (2013) 101-106.

[43] S. Švarcová, K. Wiik, J. Tolchard, H.J.M. Bouwmeester, T. Grande, Solid State Ionics, 178 (2008) 1787-1791.

[44] S. Yakovlev, C.-Y. Yoo, S. Fang, H.J.M. Bouwmeester, Applied Physics Letters, 96 (2010) -.

Chapter 3: Electrochemical characterization and oxygen flux measurement

In this chapter, the experimental methods for electrochemical characterization and oxygen permeation flux measurements of MIECs in conjunction with the fundamental theory, uncertainties and limitations of the methods are summarized,

3.1. Electrical conductivity relaxation (ECR)

ECR is a commonly used technique to measure the oxygen diffusion and surface exchange coefficients of mixed ionic and electronic conductors (MIECs). It is based on measuring the total conductivity change of a dense sample upon an instantaneous change of the surrounding oxygen partial pressures. Before the test, the rectangular shaped sample must be finely polished by the sand paper to ensure a well-defined surface. The sample (Fig. 3-1) was then wrapped with four Pt wires with painted Pt ink at four terminals: two on the ends and two in the central part (see Figure 3-1). The voltage is measured *via* the two terminals in the central part. The current is applied *via* the terminals on the two ends. The sample is placed in a sealed compartment where the atmosphere can be controlled. Upon a change in the oxygen partial pressure a change of electrical conductivity will be measured. This is due to the change of concentration of electrons and electron holes, which is directly linked to a change of oxygen nonstoichiometry (δ) *via* the electroneutrality requirement.

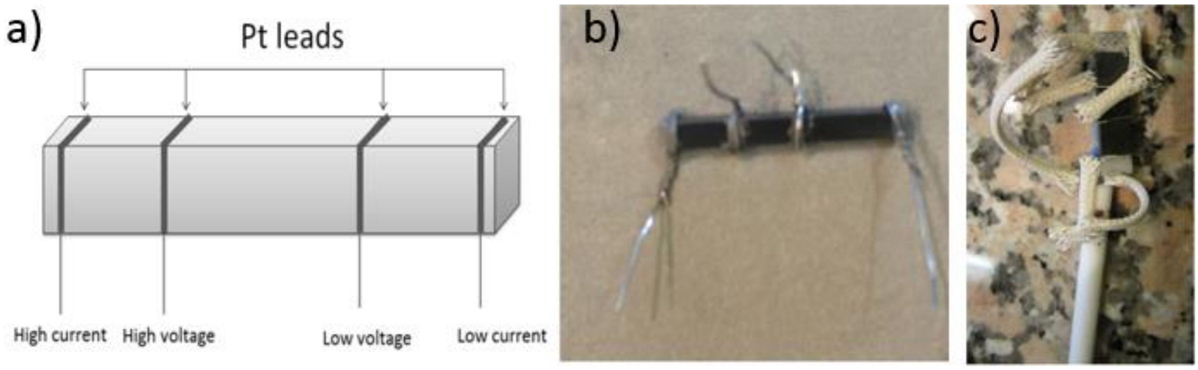

Fig. 3-1 The sample used in the ECR measurement: (a) schematic of the sample (b) a photo of the sample (c) a photo of the sample with Pt leads.

When using ECR the following assumptions are made as prerequisites for the analysis: *(i)* local electroneutrality, *(ii)* the conductivity is proportional to the charge carrier concentration, *(iii)* the surface exchange reaction is a first order reaction with respect to the oxygen vacancy concentration, which can be written:

$$J = D_{chem} \frac{\partial C\left(\pm l_x, t\right)}{\partial x} = k_{ex}\left(C\left(\pm l_x, t\right) - C\left(\pm l_x, \infty\right)\right) \quad \text{(3-1)}$$

where J is the flux of oxide ions from the surface to the bulk. k_{ex} is the first order rate constant, $C\left(\pm l_x, t\right)$ denotes the concentration of oxygen ions at the surface to time t, $C\left(\pm l_x, \infty\right)$ represents the concentration of oxygen ions at the surface at equilibrium $\left(t = \infty\right)$, *(iv)* the change of the oxygen partial pressure should be much faster compared to the conductivity change of the sample, *(v)* D_{chem} can be considered constant within the pO_2-step range, *(iv)* Lx should be significantly larger than Ly and Lz where Lx and Ly are the width and height of the specimen, defining a cross sectional area perpendicular to the direction of current.

Based on Fick's laws of diffusion with the appropriate boundary conditions the normalized conductivity as a function of time can be written [1]:

$$\frac{\sigma_\infty - \sigma(\mathrm{t})}{\sigma_\infty - \sigma(\mathrm{t}=0)} = \sum_{n=1}^{\infty} \frac{2L_x^2 \exp(\frac{-\beta_{n,x}^2 D_{chem} t}{l_x^2})}{\beta_{n,x}^2(\beta_{n,x}^2 + L_x^2 + \mathrm{L}_x)} \sum_{n=1}^{\infty} \frac{2L_y^2 \exp(\frac{-\beta_{n,\mathrm{y}}^2 D_{chem} t}{l_y^2})}{\beta_{n,\mathrm{y}}^2(\beta_{n,\mathrm{y}}^2 + L_y^2 + \mathrm{L}_y)} \quad \text{(3-2)}$$

where σ_∞ denotes the conductivity after the relaxation has reached the new equilibrium, $\sigma(\mathrm{t})$ is the conductivity $\sigma(\mathrm{t}=0)$ represents the initial conductivity before instantaneous gas change. It is in the above equation assumed that the gas change takes place at time t=0. $\beta_{n,x,y}^2$ is the n'th positive root given by equation

$$\beta_{n,x,y}^2 \tan \beta_{n,x,y}^2 = L_{x,y} \quad \text{(3-3)}$$

where $L_{x,y}$ is the dimensionless number.

$$L_{x,y} = \frac{l_{x,y}}{L_c} \quad \text{(3-4)}$$

where L_c is called the characteristic thickness [2], which can be written

$$L_c = f\,\frac{D_{chem}}{k_{ex}} \quad (3\text{-}5)$$

where f is the correction factor (0.5<f<1, f=0.78 for vacancy mechanism). Eventually, the two variables k_{ex} and D_{chem} can be extracted by fitting the experimental data for the electrical conductivity as a function of time by Eq. 3-2 (with 3-3, 3-4 and 3-5).

3.2. Electrochemical Impedance Spectroscopy (EIS)

Electrochemical Impedance Spectroscopy (EIS) is a commonly applied technique to characterize the electrochemical and electrical properties of materials. This particular technique makes it possible to specifically study the electrical characteristics of grain interior, as well as grain boundaries in polycrystalline materials. Also, EIS is a very useful tool for studying a variety of electrochemical devices, for instance SOFCs [3], solid oxide electrolysis cells (SOECs) [4] and batteries [5].

By direct current (DC) characterization methods, the voltage response of an imposed constant current is measured. For alternating current (AC) impedance spectroscopy time varying perturbations are applied. Once a sinusoidal voltage is applied, a sinusoidal current response will be observed. The sinusoidal voltage can be described by the frequency f, (or angular frequency $\omega = 2\pi f$), and the amplitude U_0. The corresponding current will have the same angular frequency of the perturbation signal, but different amplitudes and phase angles are observed with varying frequency due to the existence of capacitive or inductive circuit elements, the current will exhibit a phase shift θ. The sinusoidal voltage and current are $U = U_0 \sin \omega t$ and $I = I_0 \sin(\omega t + \theta)$, respectively. The impedance is defined as $Z = \frac{U_0 \sin \omega t}{I_0 \sin(\omega t + \theta)}$.

There are two components in the current. One component in the current is in phase with the voltage and the other one is 90° degrees out of the phase. Therefore, the impedance is divided into two parts. The one in phase part (real part R) corresponds to the voltage divided by the in-phase component, and reflects the resistance of charge carriers passing through the elements; the other part is 90° out of phase (imaginary part X), reflecting the charge carriers not really transport through the impedance. The total impedance is described by a two-dimensional vector with real and imaginary parts. The impedance is the sum of real and imaginary impedance [6]:

$$Z = Z' + jZ'' = Z(\mathrm{Re}) + jZ(\mathrm{Im}) = R + jX\left(j = \sqrt{-1}\right) \quad (3\text{-}6)$$

Doing impedance measurements one records amplitude and phase of the current introduced by the voltage perturbation as a function of frequency. Typical results are presented by plotting the real part of the impedance and the negative imaginary part from the maximum to minimum frequency. This is called a Nyquist plot (negative imaginary part –X versus resistance R).

There are several interfaces in a polycrystalline electrolyte/MIEC materials coated with electrodes, e.g. grain boundaries, and interfaces between the sample and the electrodes. These interfaces can be charged so that they can impede the transport of charge carriers, showing effects of resistance, capacitance and inductance. Three passive electrical circuit elements, resistance, inductance and capacitance, are introduced to describe the electrochemical process occurring in each segment of the sample under investigation. The response from the sample can be described by an equivalent circuit model which consists of several passive electrical circuit elements. A typical way to simulate a process in the sample (at an interface) is to use resistor and capacitor in parallel, labelled (RC). In a Nyquist plot, the (RC) circuit element corresponds to a perfect semicircle with a peak frequency given by

$$\omega = \frac{1}{RC} = \frac{A}{L\rho}\frac{L}{\varepsilon_0\varepsilon_r A} = \frac{\sigma}{\varepsilon_0\varepsilon_r} \quad (3\text{-}7)$$

where R is the resistance; C is the capacitance, ε_r is the relative permittivity of the material; $\varepsilon_0=8.85\times10^{-12}$ Fm^{-1} is the vacuum permittivity; L is the thickness; A is the area; ρ is the resistivity; σ is the conductivity. Nevertheless, the microstructure is fairly complicated in real crystalline materials. The size and orientation of grains are different and some of grain boundaries are distorted. Therefore, the response from these practical elements in the impedance could be different from those of the ideal passive elements. Actually, the impedance spectra measured on real samples exhibit depressed semicircles in the Nyquist plot (n<1). A compatible constant phase element (CPE or Q) is thus introduced to describe this non-ideal case by defining two parameters n and Y whose admittance is written as

$$Y = Y_0\left(j\omega\right)^n = Y_0\left[\omega^n\cos\left(\frac{n\pi}{2}\right) + i\omega\sin\left(\frac{n\pi}{2}\right)\right] \quad (3\text{-}8)$$

The corresponding impedance is;

$$Z = Y\left[\left(j\omega\right)^{n}\right]^{-1} \quad (3\text{-}9)$$

The Pseudo-capacitance of each (RQ) equivalent circuit is calculated henceforth from

$$C = Y^{\frac{1}{n}} R^{\frac{n-1}{n}} \quad (3\text{-}10)$$

The electrical/electrochemical process at the interfaces and in the bulk can be distinguished by the values of pseudo-capacitance of the process. In general the relation $C_{grain} \ll C_{grain\ boundary} \ll C_{electrode}$ holds. Hence, the impedance of the electrode manifests itself at low frequencies, the grain boundary at intermediate and the grain interior at high frequency.

3.3. Hebb-Wagner polarization

MIECs may simultaneously conduct electrons and ions. It is important and challenging to separately determine the values of both electronic and the ionic conductivity. A variety of methods exist to characterize the ionic and electronic conductivity exclusively. For instance, electromotive force (EMF) has been successfully applied to indirectly measure the transport number of ionic and electronic conductors by means of measuring the open circuit voltage of a cell under different chemical potential gradients [7]. However, the EMF method is sensitive to the charge surface exchange rates and not only dependent on bulk material properties. A sample with fast surface exchange or a good electrode is needed for a precise measurement; otherwise the potentially large EMF drop across the surface will erroneously be ascribed to bulk properties. Similarly, many studies deduce the ionic conductivity of MIECs from measured oxygen flux results. This is also a viable method but possible flux losses at the surfaces must be taken into account in the analyses to give accurate determinations.

Alternatively, the electronic and ionic conductivity of mixed ionic and electronic conductors can be measured directly by use of blocking electrodes in Hebb-Wagner polarization experiments. The method is based on conductivity measurements with one reversible electrode acting as reference and the other electrode that is used to feed a given charge carrier (ions or electrons). One can either use ion-blocking electrodes to measure electronic conductivity of MIEC or use electron-blocking electrodes to measure ionic conductivity.

In Hebb-Wagner polarization measurements, a variety of types of cells have been explored. In Hebb's early study [8], a cell in the configuration of (-)Ag/AgBr/Pt (+) was used to measure the electronic conductivity of AgBr using Pt as the blocking electrode and Ag as the reversible electrode. The theoretical equation that describes the I-V relation for the cell is written [8]:

$$I = I_{elelctron} = -\frac{kTS}{qL}[\sigma_e(0)(1-\mathrm{e}^{-qV\beta}) + \sigma_p(0)(\mathrm{e}^{qV\beta}-1)] \quad (3\text{-}11)$$

I denotes the current, *V* represents the applied voltage, *T* is the absolute temperature, *k* is Boltzmann constant, ß=1/*kT*, *q* is the elementary charge, *S* is the cross section area, *L* is the thickness of the sample. The sum of electron and electron hole conductivity can be derived by taking derivation of I relative to *V*:

$$\frac{\partial I}{\partial V} = \frac{S}{L}\left[\sigma_e(0) + \sigma_p(0)\right] \quad (3\text{-}12)$$

The analysis of the Hebb-Wagner experiments carried out to determine the electronic conductivity relies on the following assumptions [9, 10].

1. Charge transfer only occurs at the contact area between the sample and the electrodes. Transport of charge carriers through free area that is not covered by the working or reference electrode should be insignificant.
2. The oxygen activity of the reference electrode must be constant.
3. The chemical potential gradient of the targeted blocked charge carrier must be zero.
4. The minority charge carriers are diluted and follow Boltzmann statistics.
5. The targeted blocked ion should have a single absolute value of charge.
6. Decomposition of the sample does not occur.
7. Insignificant ionic leak through the "working electrode".

Many researchers successfully measured the ionic and electronic conductivity of MIECs using such blocking setups [11-13]. It takes relatively long time (several hours) to achieve the steady state because the surface area for the oxygen exchange is relatively large, and a good sealing of the blocking electrode with a large area is relatively difficult. To ease these difficulties, a microelectrode two-point Hebb-Wagner cell was developed by Lübker *et al.* [14] (c.f. Fig. 3-2a). Such a modified Hebb-Wagner cell is very suitable to measure the electronic conductivities of acceptor doped-ceria [14, 15]. Use of the blocking microelectrode has the following benefits: *i)* the small contact area is readily sealed, and *ii*) the steady state is reached quickly. The relaxation time (τ) for a plane surface can be calculated by $\tau = L^2/D_O$, where *L* is the diameter of the circular sample, D_O denotes the chemical diffusion coefficient of oxide ion. The smaller contact area, the shorter time is needed to achieve the steady state. Taking GCO as an example, the oxygen diffusion coefficient of GCO is 9×10^{-6} cm^{2}s^{-1} [16]. Assuming the radius of the microelectrode is 150 μm, the relaxation time is solely 2.5s. In the present work, the electronic conductivities of the ceria based samples have been measured by the microelectrode Hebb-Wagner polarization. This will be discussed in detail in chapter 7.

In order to fulfil the second assumption, a glass seal is used to cover the surface where oxygen surface exchange is not desired. The oxide ion and electron current density in the material can be written:

$$j_{O^{2-}} = \frac{\sigma_{O^{2-}}}{2q} \nabla \eta_{O^{2-}} \tag{3-13}$$

$$j_{e^-} = \frac{\sigma_{e^-}}{q} \nabla \eta_{e^-} \tag{3-14}$$

Ideally, the blocking electrode enforces the condition $j_{O^{2-}} = 0$.

Several studies have proposed the possible existence of a single charged oxygen vacancy $V_O^{\bullet}$. If the $V_O^{\bullet}$ exists during the Hebb-Wagner polarization measurement, the assumptions behind the method are not valid. Here, we shall assume that such single charged vacancies are not a dominant defect.

Based on the aforementioned assumptions, it is viable and feasible to measure the electronic conductivity of doped-ceria by Hebb-Wagner polarization. In the steady state of the Hebb-Wager polarization, the transport of the oxide ions vanishes ($\nabla \eta_{O^{2-}} = 0$) in the ideal case where the ionic transport is totally blocked and if the interference between electronic and ionic is assumed insignificant. The oxygen partial pressure in the vicinity of the microelectrode is eventually calculated by:

$$a_{o_{2,\text{micro}}} = a_{o_{2,\text{ref}}} \exp \frac{4FV}{RT} \tag{3-15}$$

where V is the polarization voltage applied on microelectrode relative to the reference electrode. In addition, the standard Hebb-Wagner equation is used for analysing the response [8, 17]

$$I = 2\pi r_c \frac{RT}{F} \left\{ \sigma_e \left[\exp\left(\frac{FV}{RT}\right) - 1 \right] + \sigma_h \left[1 - \exp\left(-\frac{FV}{RT}\right) \right] \right\} \quad (3\text{-}16)$$

where r_c is the radius of the circular microelectrode. From Hebb-Wagner theory, the sum of electron and electron hole conductivity in the vicinity of the ion-blocking microelectrode can be calculated in terms of the derivative of the steady state I-V curve as follows

$$\frac{\partial I}{\partial V} = 2\pi r_c (\sigma_e + \sigma_h) \quad (3\text{-}17)$$

If the microcontact is circular rather than spherical, $2\pi r_c$ is replaced by 4r [11]. The uncertainty of the electronic conductivity mainly originates from the uncertainty on determination of the contact radius r_c. The radius for a microelectrode or cone electrode can be precisely determined by Newman's formula. $r_c = 1/4R_s\sigma$ where R_s is the series resistance found from the intercept on the real axis at high frequency by impedance spectroscopy and σ is the specific conductivity of the material.

For the electron-blocking cell, a simple two point cell can be adopted. As illustrated in Fig. 3-2(b), pure ionic conductors (GCO/YSZ) were used to block the flux of electrons. LSM-YSZ and GCO-LSC were introduced in the interfaces between the blocking electrode and material in order to reduce the contact resistance. Ideally, the total resistance of the cell is the ratio between applied voltage and responsive current $R_t = V/I$. The resistance of electronic conduction in the MIECs is $R_e = R_t - R_{block}$, where R_{block} is the resistance of the oxide ion conduction of the blocking electrode. Glass sealant was used to block the electron leakage along the edge of the sample.

a) Oxide ion blocking cell

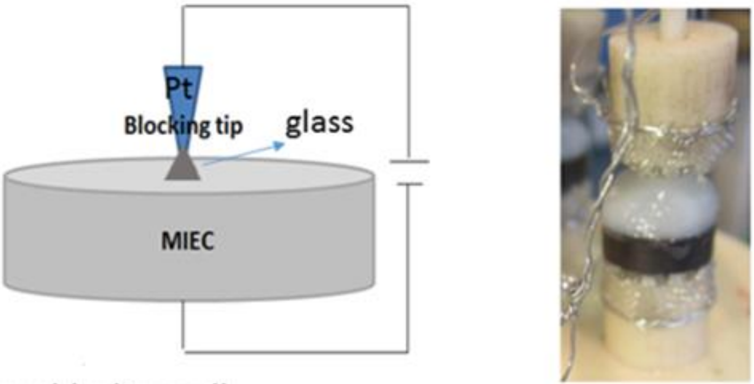

b) Electron blocking cell

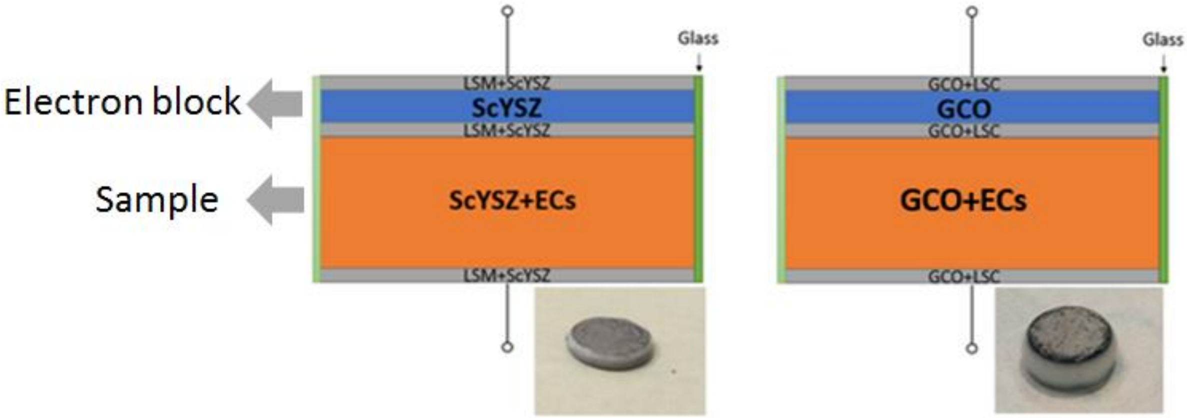

Fig. 3-2 (a) Microelectrode two-point ion-blocking Hebb-Wagner cell (b) Simple two-point electron-blocking cell. (ECs：electronic conductors)

3.4. Flux measurements

Oxygen permeation flux measurements in this work were conducted in three membrane rigs as illustrated in Fig. 3-3. Fig. 3-3 (a) shows the membrane rig established at DTU Energy. The gases are controlled by mass flow controllers (MFCs). The oxygen partial pressure of the inlet and outlet was analysed by two ex-situ zirconia oxygen sensors. Nitrogen was used as the protective gas inside the chamber so that the leakage of oxygen from ambient toward the permeate side of the membrane is reduced.

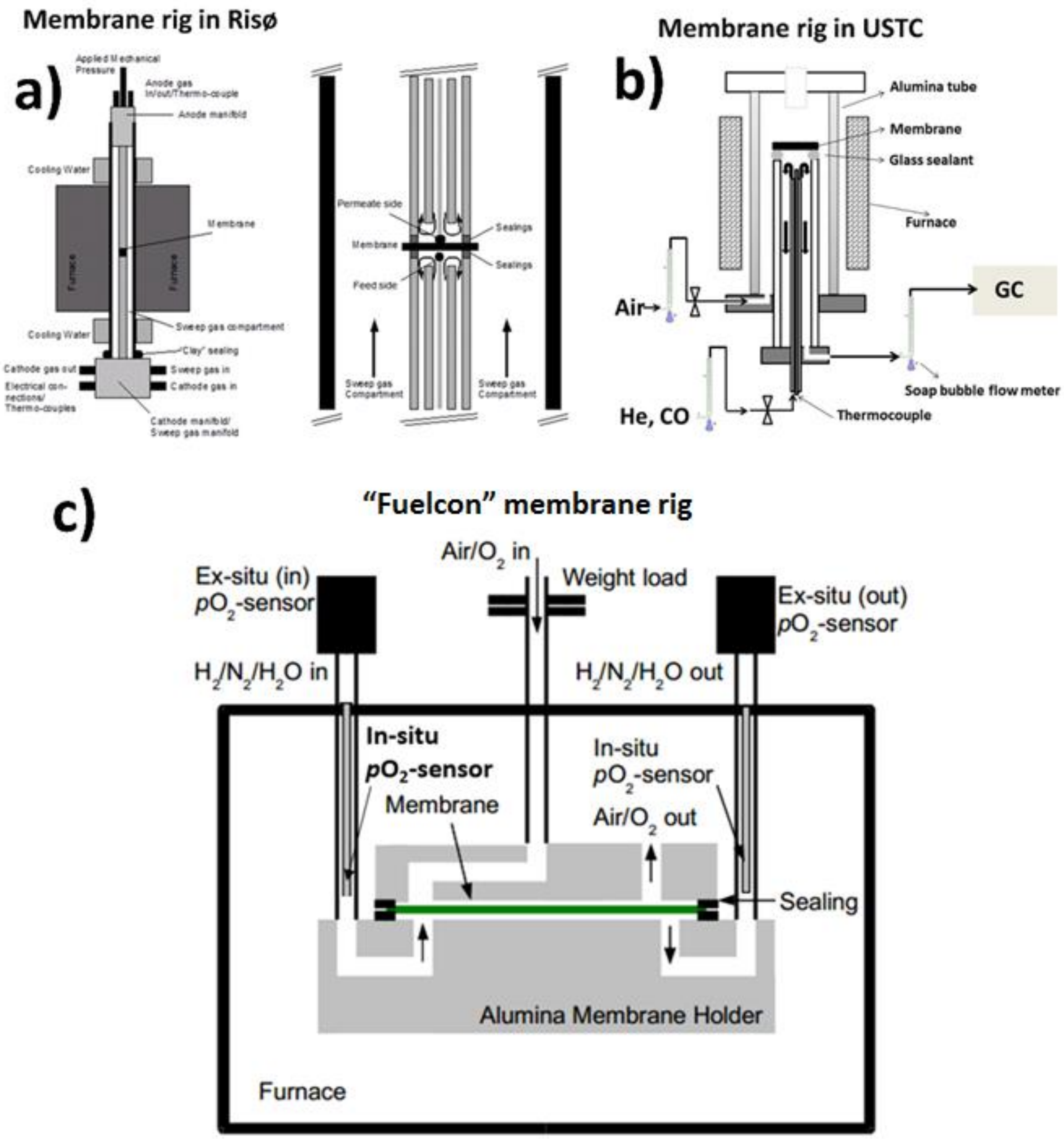

Fig. 3-3 Schematic representation of the three membrane rigs used in this work for oxygen permeation measurement (a) setup for circular membrane with 0.7 cm^2 at DTU (b) setup for circular membrane with 0.7 cm^2 at USTC (b) setup for square membrane with 25 cm^2 at DTU Energy.

For the membrane rig developed by USTC (Fig. 3-3b), the flow rate of gases was controlled by soap bubble flow meters. The concentration of gases was analysed by an online GC station. Prior to the measurement, the GC station has been calibrated using standard calibration gases.

For the test of 25 cm^2 membranes, a "Fuelcon" rig was used (Fig 3-3c). The membrane was tested in a modified test house previously used for SOFC tests. The membrane was sealed by

YS2B glass together with two Fe/Cr alloy frames on the test house made of alumina. A weight load was applied to ensure a good sealing. The oxygen partial pressure of the sweep gases was analysed by two ex-situ zirconia oxygen sensors. The flow rate of the gases was monitored by mass flow controllers. The quality of glass sealing was estimated by comparing the flow of the inlet and outlet.

References

[1] H.S. Carslaw, J.C. Jaeger, Oxford: Clarendon Press, 1959, 2nd ed., 1 (1959).

[2] H.J.M. Bouwmeester, H. Kruidhof, A.J. Burggraaf, Solid State Ionics, 72, Part 2 (1994) 185-194.

[3] R. Barfod, M. Mogensen, T. Klemensø, A. Hagen, Y.-L. Liu, P. Vang Hendriksen, Journal of The Electrochemical Society, 154 (2007) B371-B378.

[4] C. Graves, S.D. Ebbesen, M. Mogensen, Solid State Ionics, 192 (2011) 398-403.

[5] P. Zhang, H. Wang, Q. Si, M. Matsui, Y. Takeda, O. Yamamoto, N. Imanishi, Solid State Ionics, 272 (2015) 101-106.

[6] H. Fjeld, PhD thesis, University of Oslo, 2008.

[7] T. Norby, Solid State Ionics, 28–30, Part 2 (1988) 1586-1591.

[8] M.H. Hebb, The Journal of Chemical Physics, 20 (1952) 185-190.

[9] I. Riess, Solid State Ionics, 91 (1996) 221-232.

[10] I. Riess, R. Safadi, H.L. Tuller, Solid State Ionics, 72, Part 2 (1994) 3-6.

[11] C. Chatzichristodoulou, P.V. Hendriksen, Physical Chemistry Chemical Physics, 13 (2011) 21558-21572.

[12] X. Li, H. Zhao, F. Gao, Z. Zhu, N. Chen, W. Shen, Solid State Ionics, 179 (2008) 1588-1592.

[13] W. Zipprich, H.D. Wiemhöfer, Solid State Ionics, 135 (2000) 699-707.

[14] S. Lübke, H.D. Wiemhöfer, Solid State Ionics, 117 (1999) 229-243.

[15] S. Lübke, H.D. Wiemhöfer, Berichte der Bunsengesellschaft für physikalische Chemie, 102 (1998) 642-649.

[16] J.A. Lane, J.A. Kilner, Solid State Ionics, 136–137 (2000) 997-1001.

[17] C. Wagner, Zeitschrift fuer Elektrochemie und Angewandte Physikalische Chemie, 60 (1956) 4.

Chapter 4: Fabrication of asymmetric Oxygen Transport Membranes (OTMs)

4.1. Dip coating

Dip-coating is a commonly used technique to fabricate very thin layers by withdrawal of a substrate from a chemical solution. Depending on the chemical solution (sol-gel or slurry), layers with a thickness in the range of 1 to 100 µm can be fabricated. Layer thickness of less than 1 µm are usually achieved by using Sol-Gel method whereas thicker coating of more than 1 µm are prepared by multiple Sol-Gel coatings or by slurry coating. Dip coating is a relative simple and cost-efficient coating technique which is applied in laboratory scale and in industrial production. For application of porous catalytic layers, or mixed conducting membrane layers in OTM, dip coating offers good control of the thickness, porosity and microstructure which depend on several factors including size and structure of the precursors, relative rates of condensation and evaporation, capillary pressure, and substrate withdrawal speed [1]. In dip coating, the substrate is withdrawn vertically from a suspension and the especially the coating thickness can be well controlled by the withdrawal speed under well-controlled temperature and atmospheric conditions, as shown in Fig. 4-1.

The deposited thickness is related to the position of the streamline dividing the upward and downward moving layers [2]. When the viscosity of the slurry η and the withdrawal speed U_o are sufficiently high to lower the curvature of the gravitational meniscus, the deposited thickness of the layer is a result of viscous drag and gravity force.

$$h = c_1 \left(\frac{\eta U_o}{\rho g} \right)^{\frac{1}{2}} \quad (4\text{-}1)$$

where g is 9.8 m s^{-2} and ρ is the density of the slurry. The constant c_1 is approximately 0.8 for Newtonian liquids. For relatively low withdrawal speeds and low viscosity of the slurry, the thickness of the green layer (wet thin film) can be semi-experimentally predicted by the Landau and Levich (LL) model [3]

$$h = \frac{0.94(\eta U_0)^{\frac{2}{3}}}{\gamma_{LV}(\rho g)^{\frac{1}{2}}} \quad (4\text{-}2)$$

where γ_{LV} is the liquid-vapour surface tension.

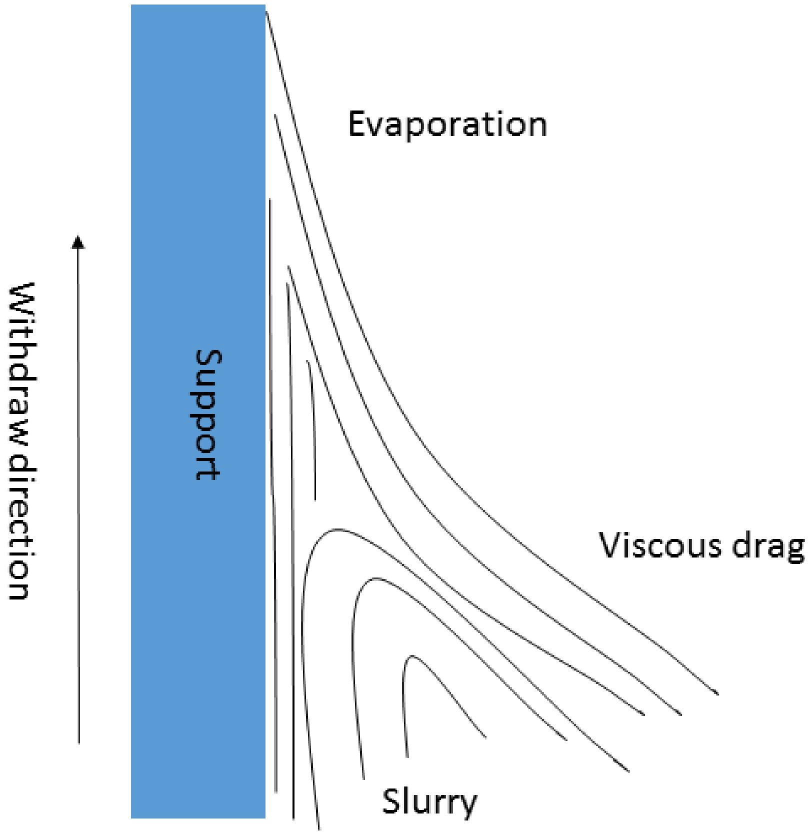

Fig. 4-1 Schematic of withdrawal of a support from a suspension.

The LL model predicts that the thickness of the layer increases with increasing withdrawal speed. Nevertheless, Grosso [4] found that the LL model is not always valid. A reverse tendency can be observed when the withdrawal speed is extremely low where evaporation and capillary convective effects jointly govern the deposition rate [4]. Based on his conclusions, the thickness of the layer will be controlled by two depositions: capillary regime of deposition and viscous drag regime of deposition. The equation [4] that considers the viscous drag and capillary convection effects is written;

$$h = k_i\left(\frac{E}{LU_0} + DU_0^{\frac{2}{3}}\right) \quad (4\text{-}3)$$

where the first term E/LU_0 represents the capillary regime of deposition where E denotes the evaporate rate. The second term $DU_0^{\frac{2}{3}}$ describes the viscous drag regime of deposition which is consistent with LL model. It is also reported by Grosso [4] that the thickness is commonly within the viscous drag regime when the withdrawal speed is above 1 mm s^{-1}, whilst the deposition is governed by capillarity and evaporation effects when the speed is below 0.1 mm s^{-1}.

In this work, oxygen transport membranes were dip-coated on MgO and 3YSZ tubular supports using a customized dip-coater, as shown in Fig. 4-2. The tubes were initially inserted into a slurry basin through an opening (a hole with a rubber limb) and were mounted (fixed) between two aligned rods on both ends of the tube. The slurry was filled into the movable slurry basin (white basin in Fig. 4-2) before starting of the coating process. The height and the speed of the slurry basin which moves along the tube, is digitally controlled by an engine through a computer program. As the slurry basin moves along the tube, the slurry is coating the outside of the tube.

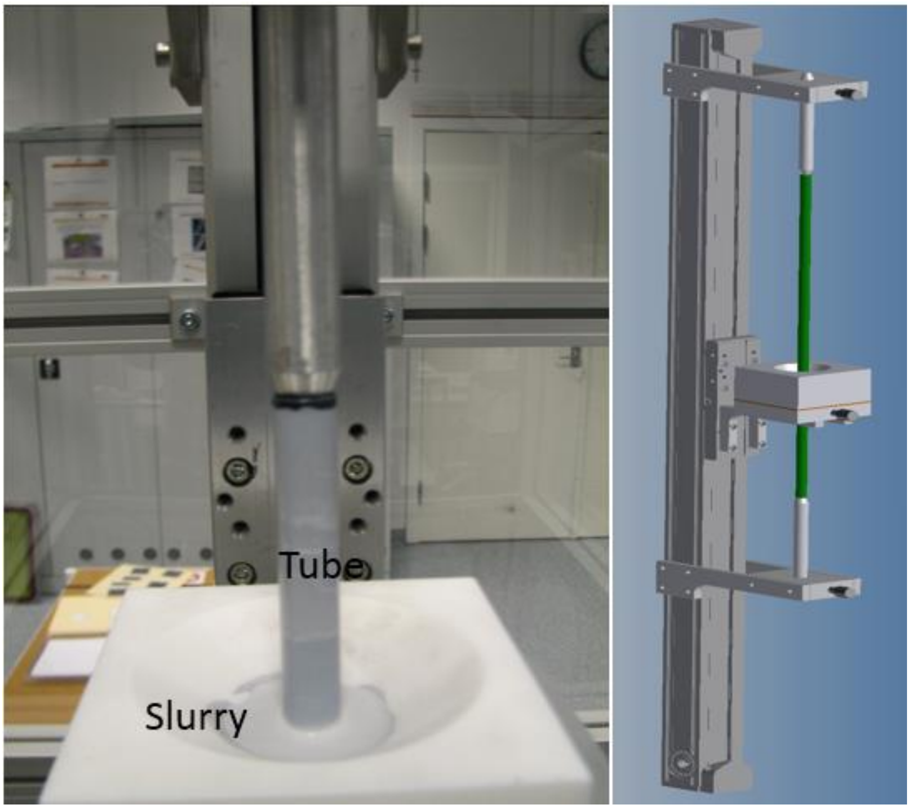

Fig. 4-2 A photo and schematic of the dip-coater for application of thin film catalytic and membrane layers on MgO and YSZ tubes for oxygen transport membranes (OTM).

4.2. Phase-inversion tape casting

4.2.1. General description of phase-inversion process

Phase-inversion is a controlled process in which a polymer is transformed from a liquid phase to a solid phase. The earliest use of the phase inversion technique dates back to the 1960s when Loeb *et al.* [5] developed this novel one-step shaping technique to process high polymer asymmetric membranes. Phase inversion *via* immersion precipitation is a widely-used process to prepare asymmetric membranes with highly orientated pore structure. In phase-inversion, a polymer binder plus solvent (a "polymer solution"; or a "suspension" if ceramic particles are added) is cast on a supporting layer and then submerged in a coagulation bath containing nonsolvent. The polymer binder (e.g. PESF) is miscible to the solvent (e.g. NMP), but immiscible to the non-solvent (e.g. H_2O). The phase-inversion process is initiated when the suspension (polymer solution) interacts with the nonsolvent. The miscibility between the solvent and nonsolvent leads to an interfacial exchange, resulting in a convective flow and subsequent formation of finger-like pores.

4.2.2. Application of phase-inversion process in tape casting

The phase-inversion technique has been initially developed for producing hollow fibre, polymer based water or gas separation membranes. In the case of ceramic hollow fibre membranes, challenges arise with the mechanical strength and sealing (handling) of the membrane fibres, especially if integration into a high temperature module is required. Therefore, asymmetric planar or tubular membranes are generally considered as an alternative for mixed conducting oxygen transport membranes. More recently, phase-inversion technique coupled with tape casting, so called "phase-inversion tape casting", was developed to produce planar asymmetric membranes. In general, the resulting membranes show a hierarchical structure, as illustrated in Fig. 4-3. A thin top layer (skin layer) with a thickness of 1 to 5 µm [6] under which finger-like pores with relatively large diameters (of several microns) are orientated perpendicular to the tape casting plane. The finger-like pores will end with a dense layer on the bottom (sponge layer). In many studies, the bottom layer serves as the functional layer for the separation of liquids and gases [7-9].

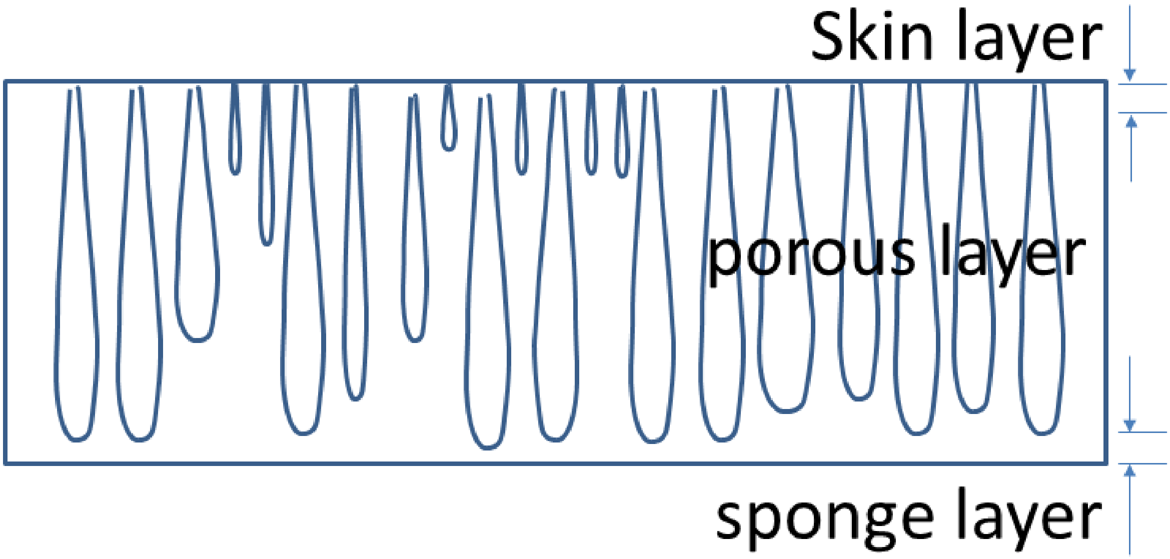

Fig. 4-3 Schematic drawing of the hierarchical structure of a membrane prepared by phase-inversion tape casting.

4.2.3. Theoretical description of phase-inversion process

Phase-inversion is a complicated process associated with mass transfer and phase separation. The existing mechanisms cannot always completely explain the phase-inversion process and void formation detected during experiments. However, the phase-inversion process can be satisfactorily explained by the thermodynamics and kinetics of solvent/nonsolvent system. A thermodynamic phase diagram can be established based on the Flory-Huggins theory. Flory-Huggins theory is a mathematical model to describe the thermodynamics of a polymer solution which takes into account the great dissimilarity in molecule sizes when adapting the usual expression for the entropy mixing. It is an equation for the Gibbs free energy change for a mixture of a polymer and a solvent (equation. 4-5). Upon the mixing of a polymer with a solvent, both entropy and enthalpy increases [10].

$$\Delta G_m = \Delta H_m - T\Delta S_m \quad (4\text{-}4)$$

The result obtained by Flory and Huggins is

$$\Delta G_m = RT\left(n_1 \ln \phi_1 + n_2 \ln \phi_2 + n_1\phi_2\chi_{12}\right) \quad (4\text{-}5)$$

where n_1 and ϕ_1 are number of moles and volume fraction of solvent, while n_2 and ϕ_2 are number of moles and volume fraction of polymer. χ_{12} is a parameter to take account of the energy of inter-dispersing polymer and solvent. R is the gas constant, T is the absolute temperature. Using the Gibbs free energy deduced by FH theory, the thermodynamics equilibrium curve for the polymer-solvent system can be obtained.

Figure 4-4a displays an example of thermodynamic equilibrium curve of a mixture of two phases A and B. One of the phases is the solvent and the other one is the polymer. In the binary phase diagram, the two phases are mutually and spontaneously miscible when the condition $\Delta G < 0$ is fulfilled. Binodal and spinodal are two important transition points in the system. From thermodynamic point of view, binodal is the minimum points in the curve (e.g. "m_1" in Fig. 4-4a) and spinodal corresponds to the inflection points (e.g. "m_2" in Fig. 4-4a). Mathematically, the expressions of binodal and spinodal are $\Delta G / \Delta\phi = 0$ and $\Delta^2 G / \Delta\phi^2 = 0$, respectively.

Binodal: Within the region (m_1-m_2), the sum of the free energy is M which is higher than the corresponding energy on the equilibrium curve ("m" in Fig. 4-4a). In that case, the system will not decompose spontaneously to the neighbouring two phases ϕ'_b and ϕ'_s. In other words, small fluctuation in composition will not lead to phase decomposition. The system thus maintains a metastable state. With respect to the T vs. composition diagram, the region between binodal and spinodal corresponds to a metastable state in which the phase separation follows a nucleation and growth mechanism because the energy barrier needs to overcome ("n_2" in Fig. 4-4a).

Spinodal: Within the spinodal region, the system will undergo a phase separation. In the free energy vs. composition diagram (Fig. 4-4a), the composition within the region encompassed by n_1 and n_2 vertical lines has a total free energy of N which is lower than the corresponding free energy n on the thermodynamic equilibrium curve. Therefore, phase separation will occur spontaneously with respect to little fluctuation of composition and without the need of any driving force to overcome the energy barrier. As for the temperature vs. composition diagram, the composition within the spinodal region cannot be stable and will separate to ϕ'_s and ϕ''_s.

In the triple-phase diagram as shown in Fig. 4-4b, the definition of spinodal and binodal is the same. The triple-phase diagram is established in the isothermal condition. It is already known from Fig. 4-4a that the region surrounded by the spinodal curve is not stable and the two phases will separate. The region encompassed by the binodal will be metastable where the two phases are miscible. The separation of the two phases will undergo nucleation and subsequent growth.

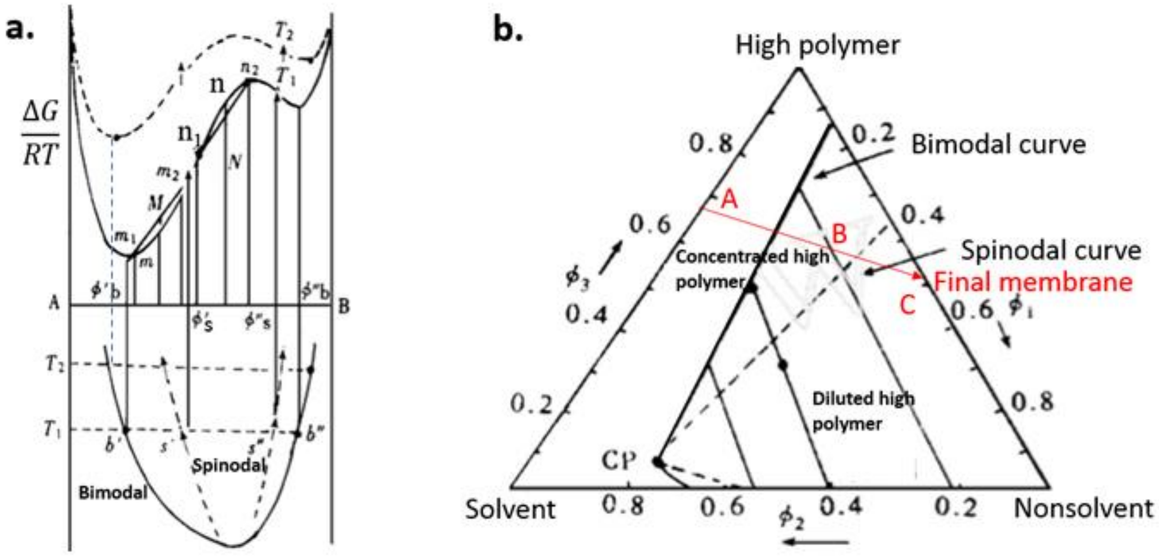

Fig. 4-4 a. Free energy vs. composition and temperature vs. composition b. Polymer-solvent-nonsolvent triple phase diagram.

The formation of the finger-like pores in the asymmetric membrane as shown in Fig. 4-3 is a dynamic process [6]. In the process of mass transfer between solvent and nonsolvent, the separation along the cross-section of membrane will follow the mechanisms as follow:

Formation of skin layer: at the beginning of the phase-inversion process, the nonsolvent initially contacts the surface of the fresh membrane, which is rich in polymer and solvent (point A in Fig. 4-4b). The onset of formation of macrovoids occurs at the interfacial boundary between the immersed membrane and the nonsolvent bath. This process corresponds to the shift from A towards B in Fig. 4-4b.

Reuver [11] defined two distinct mechanisms for macrovoids formation: instantaneous and delayed demixing. The mechanisms proposed that the demixing is not just thermodynamically controlled but also a kinetically controlled process. Instantaneous demixing describes the instantaneous polymer demixing after inter-diffusion between solvent and nonsolvent. Delayed demixing describes the occurrence of demixing after an extended period of time after the inter-diffusion.

The concentration gradient serves as the driving force for the inter-diffusion of solvent and nonsolvent. During the inter-diffusion, polymer chains are stationary because of their large molecule weight. It is a kinetically limited process for the shift of composition following the red arrow marked in Fig. 4-4b. During the delayed time the membrane losses more solvent to the nonsolvent bath than it takes up nonsolvent. Therefore, the amount of loss of solvent in the membrane drastically decreases and the concentration of the high polymer on the surface increases [6]. The composition on the surface will pass the region encompassed by binodal and spinodal curve and jump directly to the composition inside the region surrounded by spinodal curves (Fig. 4-4b). It will eventually end up with a point on the axis of polymer-nonsolvent. The polymer is immiscible to nonsolvent so that the polymer will agglomerate, followed by precipitation/solidification. It may be a reasonable explanation for a thin dense layer normally formed on the top surface. The thin dense layer is also called skin layer as marked in Fig 4-3. The thickness of the skin layer is associated with the delayed time.

Growth of the macrovoids: as skin layer forms, the resistance for the inter-diffusion of solvent and nonsolvent becomes large because the inter-diffusion is partially blocked by the skin layer. The growth of the macrovoids is caused by convective flow: nonsolvent penetrates inside the casted membrane and solvent enters into the nonsolvent across the skin layer. The driving force for the formation of the finger-like pore is related to the miscibility of nonsolvent and solvent. A higher miscibility gives rise to a higher convection rate [6]. Once a finger-like pore is initiated, shrinkage of the polymer causes it to grow by draining the freshly surrounding precipitated polymer [6].

Smolders *et al.* [6] suggests that the growth of finger-like pores is caused by the gradient of solvent across the membrane. They proposed a new explanation for the growth of pores based on the nucleation of polymer clean solution. With the flow of nonsolvent across the skin layer, the composition usually resides in the region encompassed by binodal curve where the nucleation and growth occurs. As the nucleation of polymer leans solution and solidification of the surrounding polymer proceeds, the large pore forms. With the increasing depth of the pore, the driving force decays. That may be the reason for the termination of the pores.

Eventually, a dense layer forms adjacent to the plate. The mechanism for the formation of the bottom layer is so far not fully understood. It may be caused by the adhesion of the casting solution to the plate, preventing the last polymer fluid at the bottom of the finger-like pores from moving to the sides of the finger. This fluid polymer thus solidifies in place and seals off the finger-like pores [12].

4.2.4. Empirical factors influencing the formation of finger-type pores in phase-inversion tape casting

Although the mechanism for the formation of the finger-like structure is not completely clarified, factors that may influence on the formation of the finger-like pores have been observed experimentally, and are summarized as follows:

Concentration of polymer: a higher concentration of polymer in the casted membrane will suppress the formation the pores [13].

Miscibility: the miscibility between the solvent and the nonsolvent influences the distance between the pores. Shao *et al.* [14] reported that the length of the pore is shorter when the solubility between the solvent and the nonsolvent is poor.

Viscosity: a higher viscosity of the slurry will result in shorter and less intensive pores because the high viscosity increases the resistance to the diffusion of solvent [15]. The viscosity of the slurry generally increases with increasing amount of ceramic solid load and polymer (binder).

Immersion time: the immersion time can influence the pore structure [14]. Usually, the immersion should be stopped before the diffusion rates of nonsolvent and solvent have been equalized. When this threshold is passed, the amount of nonsolvent entering into the slurry is larger than the amount of solvent entering into the pores. In that case the diffusion rate of the solvent will be slow, leading to an expansion of slurry. The pores will therefore be shortened.

4.2.5. Special treatments to achieve ideal asymmetric membranes by phase-inversion tape casting

To achieve a perfect asymmetric structure by phase-inversion tape casting, the dense top skin layer or the sponge layer on the bottom of the membrane structure should ideally be removed. There are three available ways reported to remove the dense layers. The simplest way is to polish off the dense layers mechanically after sintering. This method is particularly suitable for the flat membranes. Another two methods are based on removing the dense layer away from the green body before sintering. Huang *et al.*[16] successfully removed the bottom sponge layer of NiO-YSZ based membranes using graphite as a sacrificial pre-forming agents. The fuel cell prepared based on the structure as illustrated in Fig. 4-5 exhibited a negligible concentration polarization because the gas diffusion is facilitated by the open straight pores. In addition, either the sponge layer or skin layer can be easily removed by a mesh template covering on the corresponding side before submerging the casted layer into the water (Fig. 4-6) [9]. It is also reported that this method may not only remove the dense layer, but also yield more intensive straight pores as compared to that prepared by mesh-free scenario.

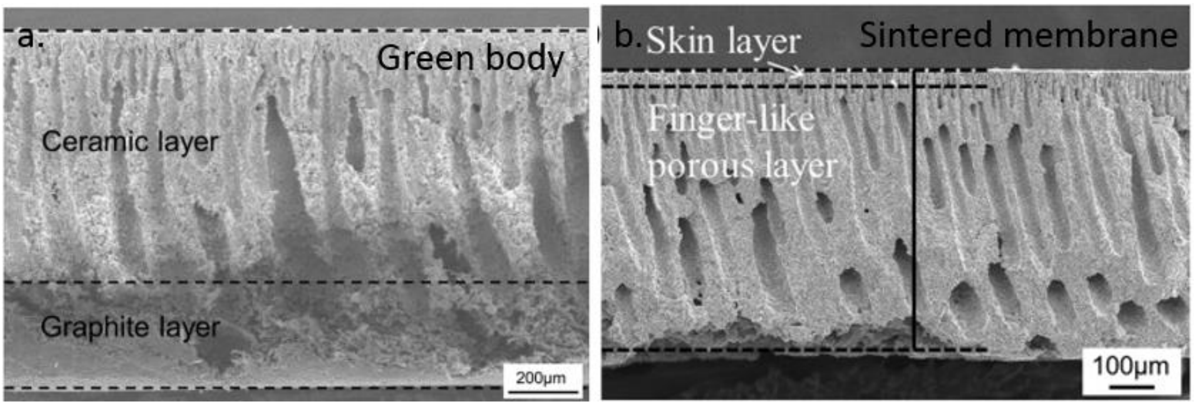

Fig. 4-5. a. Cross sectional SEM micrograph of a green tape. b. SEM micrograph of the sintered tape [16].

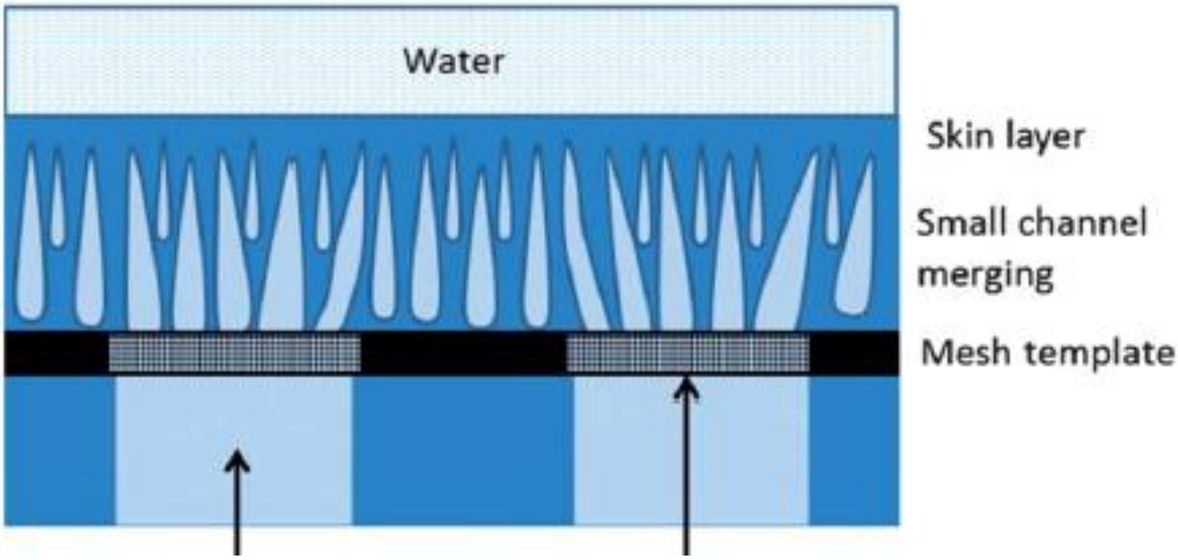

Fig. 4-6. Schematic representation of templated microchannel by mesh apertures during the phase-inversion process [9].

References

[1] C.J. Brinker, G.C. Frye, A.J. Hurd, C.S. Ashley, Thin Solid Films, 201 (1991) 97-108.

[2] C.J. Brinker, A.J. Hurd, P.R. Schunk, G.C. Frye, C.S. Ashley, Journal of Non-Crystalline Solids, 147–148 (1992) 424-436.

[3] L.D.Landau, B.G. Levich, Acta Physiochim, 17 (1942).

[4] D. Grosso, Journal of Materials Chemistry, 21 (2011) 17033-17038.

[5] L. Sidney, S. Srinivasa, Google Patents, 1964.

[6] C.A. Smolders, A.J. Reuvers, R.M. Boom, I.M. Wienk, Journal of Membrane Science, 73 (1992) 259-275.

[7] W. He, H. Huang, J.-f. Gao, L. Winnubst, C.-s. Chen, Journal of Membrane Science, 452 (2014) 294-299.

[8] H. Huang, S. Cheng, J. Gao, C. Chen, J. Yi, Materials Letters, 137 (2014) 245-248.

[9] X. Shao, D. Dong, G. Parkinson, C.-Z. Li, Journal of Materials Chemistry A, 1 (2013) 9641-9644.

[10] P.J. Flory, The Journal of chemical physics, 10 (1942) 51-61.

[11] A.J. Reuvers, J.W.A. van den Berg, C.A. Smolders, Journal of Membrane Science, 34 (1987) 45-65.

[12] H. Strathmann, K. Kock, Desalination, 21 (1977) 241-255.

[13] C. Jin, C. Yang, F. Chen, Journal of Membrane Science, 363 (2010) 250-255.

[14] X. Shao, D. Dong, G. Parkinson, C.-Z. Li, Journal of Membrane Science, 454 (2014) 444-450.

[15] B.F.K. Kingsbury, K. Li, Journal of Membrane Science, 328 (2009) 134-140.

[16] H. Huang, J. Lin, Y. Wang, S. Wang, C. Xia, C. Chen, Journal of Power Sources, 274 (2015) 1114-1117.

Chapter 5： A novel CO_2- and SO_2-tolerant dual phase composite membrane for oxygen separation

S. Cheng[a*], M. Søgaard[a], L. Han[a], W. Zhang[b], M. Chen[a], A. Kaiser[a] and P.V. Hendriksen[a]

Article published in **Chemical Communications**

A novel dual phase composite oxygen membrane ($Al_{0.02}Ga_{0.02}Zn_{0.96}O_{1.02}$ – $Gd_{0.1}Ce_{0.9}O_{1.95-\delta}$) was successfully prepared and tested. The membrane shows chemical stability against CO_2 and SO_2, and a stable oxygen permeation over 300 hours in CO_2 was demonstrated. ZnO is cheap and non-toxic and is therefore highly advantageous compared to other common materials used for the purpose.

Dense ceramic oxygen transport membranes (OTMs) can selectively separate oxygen from air at temperatures above 600 °C. The energy consumption of oxygen produced by OTMs can be significantly lower compared to conventional technologies such as cryogenic distillation or vacuum pressure swing adsorption, especially if the OTMs are thermally and/or chemically integrated with a high temperature process[1]. Main applications considered for OTMs include small scale oxygen production, oxygen for biomass gasification or oxy-fired cement plants, oxy-fuel combustion in power plants and partial oxidation of methane to synthesis gas[2]. In recent years, a significant number of papers have been dedicated to dual phase membranes, which consist of an ionic conductor and an electronic conductor[3-8]. Doped ceria or zirconia is normally used as the ionic conductor. Several different electronic conducting materials have been investigated for the purpose, including perovskite structured oxides[3, 5], spinel structured oxides[7, 9] and metals[8, 10](see Table S1 ESI†). Preferably the dual phase membranes should be tolerant against CO_2, which is particularly advantageous for a chemical integration of the membrane with a flue gas on the permeate side. Besides CO_2, one of the inevitable impurities arising from the combustion of sulfur-containing coals or biomass is SO_2. This corrosive gas can react quickly with most alkaline-earth doped perovskite based materials leading to reduced permeability due to the formation of alkaline earth sulphates.[11, 12] Alkaline-earth elements should be avoided and stable performance in CO_2 or SO_2 containing atmospheres can be achieved. For example $NiFe_2O_4$–$Ce_{0.8}Tb_{0.2}O_{1.9}$ membrane shows good stability in CO_2- and SO_2- atmospheres[7]. The use of Ni, as well as Co and Cr, which are preferred elements for both single phase and composite membranes, is problematic both in terms of the cost and due to their toxicity. It is therefore highly desirable to avoid these elements in an industrial manufacturing process. The development of a CO_2- and SO_2-stable membrane without expensive and toxic transition metals is therefore necessary for commercialization of OTMs.

Here we report on the use of doped ZnO with $Gd_{0.1}Ce_{0.9}O_{1.95-\delta}$ (GCO10) for high temperature oxygen transport membranes. ZnO offers the following advantages for the use in OTM: *i*) The electronic conductivity of ZnO is susceptible to tailoring *via* extrinsic doping. Doping of a slight amount of trivalent elements e.g. Al, Ga and In can drastically enhance the electronic conductivity of ZnO[13], rendering it a good electronic conductor. *ii*) ZnO is chemically stable in both CO_2 and SO_2 containing atmospheres. According to thermal dynamic calculation, decomposition of $ZnCO_3$ into ZnO and CO_2 occurs above 200 °C in air. A phase diagram (Fig. S3 ESI†) shows that the reaction between ZnO and SO_2 will only occur under high oxygen and sulfur dioxide partial pressures at low temperature. Typical conditions in an oxy-fuel power plant or cement plant would include SO_2 levels up to 100 ppm on the permeate side of the membrane. The chemical stability of ZnO should thereby meet the requirements for the membranes under the aforementioned conditions. *iii*) Furthermore, a ZnO dopant can enhance the electronic conductivity of the ceria itself over a wide range of temperature and oxygen partial pressure. It is found that this enhancement may occur without a sacrifice of ionic conductivity[14]. The grain boundary conductivity of GCO10 can even be enhanced by doping 1 mol % ZnO at low temperatures (< 500 °C)[15]. Schmale *et al*. reported that the electronic conductivity of Zn-doped ceria exhibits a striking jump when the concentration of ZnO is above 30 mol%, due to the formation of a ZnO-rich percolation network along the grain boundary[16]. *iv*) The thermal expansion coefficient (TEC) difference between ZnO (8×10^{-6} K^{-1} at 300 K[17]) and GCO10 (12×10^{-6} at 300 K-1273 K[18]) is moderate and therefore cracks between the micro grains of the two different phases can be avoided for suitable composite microstructures. *v*) Finally, zinc oxide is non-toxic, abundant and inexpensive. ZnO based dual phase OTMs thus has numerous merits for the use in the commercialization of the technology.

The composite membrane investigated in the present study consists of 50 vol.% Al,Ga co-doped ZnO ($Al_{0.02}Ga_{0.02}Zn_{0.96}O_{1.02}$) and 50 vol.% $Gd_{0.1}Ce_{0.9}O_{1.95-\delta}$ (GCO10) (the composite is abbreviated AGZO-GCO55). $Al_{0.02}Ga_{0.02}Zn_{0.96}O_{1.02}$ and $Gd_{0.1}Ce_{0.9}O_{1.95-\delta}$ serve as electronic and oxide ion conducting phase, respectively. Fig. 1 displays the XRD patterns of GCO10, AGZO powder and crushed powder of a membrane sintered at 1200 °C. The reference XRD patterns of GCO10 and ZnO are also shown for comparison. According to Han *et al.*[19], doping small amount of Al and Ga into ZnO will not change the crystal structure. From the XRD patterns, it can be seen that the dual phase system merely consists of cubic fluorite structured GCO10 (space group 225: *Fm3m*) and hexagonal wurtzite structured AGZO (space group 186: *P63mc*). No secondary phases resulting from reactions could be detected within the resolution limit of the XRD, indicating sufficient mutual stability between GCO10 and AGZO. The crystal structure of the composite remains unaltered in the temperature range from 25 to 900 °C in air (Fig. S9 ESI†). XRD patterns of AGZO-GCO55 powders annealed in 100% CO_2 (flow=50 Nml min^{-1}) for 120 hours at 850 °C, shows that AGZO-GCO55 is chemically stable in CO_2 at high temperature. Also, identical XRD patterns for the powder before and after annealing in a SO_2 rich atmosphere indicate no formation of sulphate, whereas formation of $SrSO_4$ (Fig. S8 ESI†) is observed from a reference sample ($La_{0.6}Sr_{0.4}FeO_{3-\delta}$-$Gd_{0.1}Ce_{0.9}O_{1.95-\delta}$). This implies that AGZO-GCO55 with respect to SO_2 tolerability is superior to the Sr-containing perovskite.

The results are also in good agreement with thermodynamic predictions (Fig. S3 ESI†).

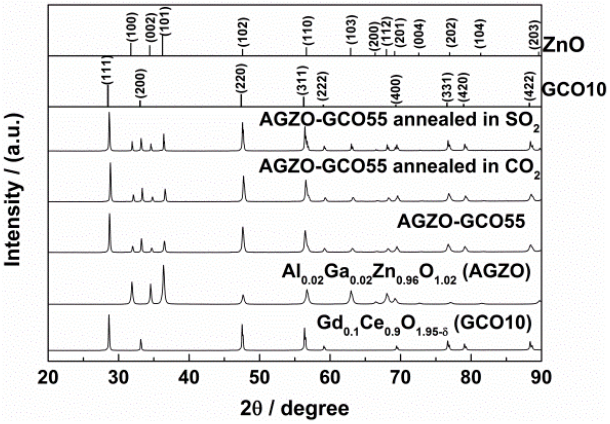

Fig.1 Normalized XRD patterns of dual phase AGZO-GCO55 membrane sintered at 1200 °C for 5 hours, sintered membrane annealed in 100% CO_2 for 120 hours and membrane annealed in SO_2 for 2 hours at 850°C. Diffraction patterns for single phase $Al_{0.02}Ga_{0.02}Zn_{0.96}O_{1.02}$ and $Gd_{0.1}Ce_{0.9}O_{1.95-\delta}$ are also shown.

Fig. 2 displays the scanning transmission electron microscopy (STEM) (See Fig.2a), EDX elemental mapping (Figs. 2b and 2c), EDX spectrum (Fig. 2d) and high resolution TEM (HR-TEM) image (Fig. 2e) of the crushed powder of the AGZO-GCO55 membrane. According to the Ce and Zn maps, GCO10 and AGZO grains are homogeneously distributed without any agglomeration of one phase and no obvious correlation of the Ce and Zn distribution could be observed, indicating no significant reaction between the grains or the formation of grain boundary layers. By HRTEM imaging of the grain boundary between a GCO10 and a AGZO grain (Fig. 2e), the characteristic (111) GCO10 and (100) ZnO planes were identified on each side of the grain boundary. The presence of new phases could not be detected along the grain boundary.

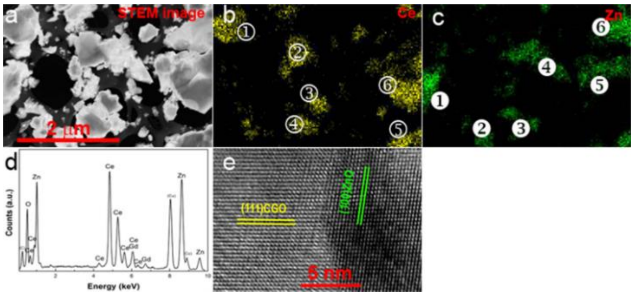

Fig. 2 a Bright-field STEM images of crushed powder of the membrane. EDX elemental maps of b. Cerium and c. Zinc. d. EDX spectrum. Cu/C comes from the carbon film/copper grid supporting for the powder. The symbols ①-⑥and ❶-❻ represent different GCO10 and AGZO grains, respectively e. HRTEM image of a grain boundary contact in a dual phase membrane (GCO10 on the left and AGZO on the right).

Fig. 3 shows Arrhenius type plots of the oxygen permeation fluxes of a 1.1 mm thick GCO10 pellet coated with $La_{0.6}Sr_{0.4}CoO_{3-\delta}$(LSC) layer and AGZO-GCO55 membranes with and without LSC coating measured with pure N_2 and CO_2 as sweep gas under a fixed oxygen partial pressure gradient ($\ln(pO2'/pO2'')$=5 and 8) in the temperature range between 600 °C and 1000 °C. LSC catalytic layers were used to ensure that the surface exchange reaction does not limit the flux. The flux data is also plotted for a fixed outlet flow (flow fixed over the temperature variation rather than fixing the driving force). Also, a calculated maximum flux for an ideal short circuited GCO10 and a pure GCO10 membrane (calculated based on the ionic conductivity and electronic conductivity from Ref. [20, 21]) under the same driving force is plotted for comparison. The uncertainty of the measured flux mainly originates from the uncertainty on the area of the membrane being tested and small leaks at the sealing (ESI† Table S1). Based on two nominally identical tests, the obtained results are clearly reproducible (Fig. S5 ESI†). Oxygen permeation fluxes for both sweep gases (N_2 and CO_2) show thermally activated feature with apparent activation energies (*E*a) of 74.5±2 $kJmol^{-1}$ and 75.4±2 $kJmol^{-1}$, respectively. The almost equivalent oxygen flux observed under the same driving force conditions suggests that the prevailing rate limiting process is identical when using N_2 or CO_2 as sweep gas. In addition, the oxygen permeation flux measured using CO_2 as the sweep gas is slightly lower than that measured in N_2. "A slight suppression of the oxygen permeation flux in CO_2" when compared to N_2/He has also been found in other studies of OTMs.[22-26] The phenomenon is suggested to be a consequence of suppressed oxygen surface exchange rate due to the chemisorption of CO_2 on the surface of the activation layer with the occupation of oxygen vacancies by the oxide ions of CO_2[24]. On the other hand, the existence of a stagnant gas layer in the vicinity of the permeate side of OTMs has also been reported[27]. Such a stagnant gas layer can give rise to diffusion limitations at low oxygen partial pressures. The binary diffusion coefficient of oxygen in nitrogen ($D_{O_2\text{-}N_2}$= 0.75 cm^2s^{-1}) is slightly higher than that in carbon dioxide ($D_{O_2\text{-}CO_2}$=0.70 cm^2s^{-1}) at 900 °C. The different binary diffusion coefficients can therefore lead to different local oxygen partial pressures on the surface of the permeate side and as consequence lead to slightly different oxygen fluxes even though the pO_2 of the effluent gas is identical.

The oxygen permeation flux of AGZO-GCO55 is ca. half of the calculated flux of short circuited GCO10 and two orders of magnitude higher than that measured for single phase GCO10. The enhanced oxygen flux of AGZO-GCO55 relative to GCO10 is due to the contribution of the *n*-type electronic conductivity originating from the percolating doped ZnO, as evidenced by the flux increase and the larger electrical conductivity (ESI† Fig.S6). The depressed flux of AGZO-GCO55 relative to short circuited GCO10 is ascribed to the partial blocking of the oxide ion paths by the AGZO and the more tortuous path for oxide ions, which is a general phenomenon observed in dual phase OTMs[3]. The membrane behaves as expected from the reported absence of chemical inter-reaction between the two phases simply as an ideal composite where naturally the addition of the electronic conductor takes up a volume otherwise available to ionic transport thus reducing the flux relative to ideally achievable in a pure ceria membrane. It is noted that the apparent activation energy of AGZO-GCO55 (74.5±2 kJ mol^{-1}) is slightly higher than that expected from the conductivity of GCO10 (66.1 kJ mol^{-1}). The larger apparent activation energy may originate from: *i)* a not insignificant contribution from the surface activation since the typical activation energy for a LSC electrode is 106 $kJmol^{-1}$.[28] *ii)* For the bulk diffusion, oxide ions will jump in the crystal structure of GCO10. The presence of ZnO surrounding GCO10 may result in strain effects or grain boundary effects that can possibly increase the energy barrier for oxide ion movement. Noticeably, the flux of a bare membrane is found to be more than one order of magnitude lower than that of the membrane with LSC activation layers. The lower flux and larger activation energy must be attributed to poor catalytic activity towards oxygen exchange of the composite AGZO-GCO55, which is consistent with the work on the use of ZnO as a SOFC electrode material[29]. It should be pointed out that the activation energy of the flux for a fixed flow of the effluent is 62 kJmol^{-1}, and thus lower than that measured under a fixed driving force. The lower activation energy is due to a continuous change of the driving force, as the oxygen permeating through the membrane reduces this with increasing temperature.

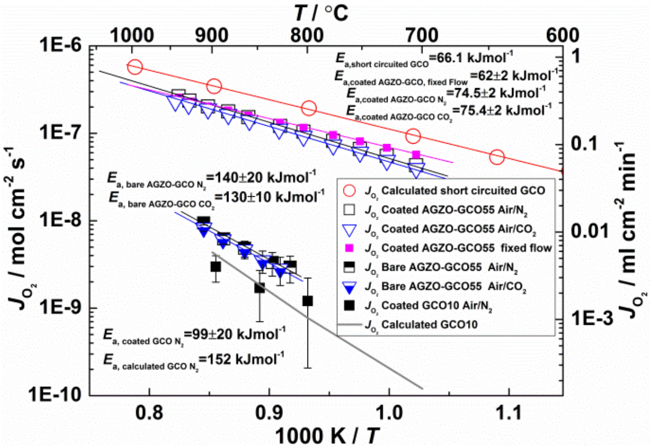

Fig.3 Arrhenius plot of the oxygen permeation flux (J_{O2}) of a GCO10 membrane with LSC coating and AGZO-GCO55 membranes with and without LSC activation layer measured in N_2 and CO_2 on the permeate side under a fixed driving force as a function of inverse temperature. The flux measured at fixed outlet flow is also plotted. For comparison the calculated flux of a short circuited membrane GCO10 is given (open circles).

The tested AGZO-GCO55 shows an oxygen permeation flux comparable to numerous ceria based dual phase membranes (ESI† Table S2). However, compared to most other systems studied in literature, the use of ZnO as the electronic conductor is advantageous due to its low cost and non-toxicity as previously stated. It is clear that future commercial membrane applications require significantly higher oxygen fluxes than reported here for 1.1 mm thick disks. A higher flux can be achieved by using a thin film membrane on a porous support structure. An additional advantage of the use of composites of GCO and ZnO is the possibility to tailor a thermal expansion coefficient of the composite to match that of cheap high toughness ceramics such as $Y_{0.03}Zr_{0.97}O_{1.985}$ (3YSZ) or mixtures of magnesia and alumina.

As shown in Fig. 4, the membrane flux was tracked for close to one month with N_2/CO_2 as the sweep gas at 860 °C followed by a measurement at 940 °C. The measurement was voluntarily terminated. A stable flux of 0.22 (STP) mlcm^{-2} min^{-1} with N_2 as the sweep gas in the first 30 hours was observed. After switching the sweep gas to 100% CO_2, the flux decreases to 0.19 (STP) ml cm^{-2} min^{-1} and levels off at 0.18 (STP) ml cm^{-2} min^{-1} after 100 hours. After the sweep gas was switched back to 100% N_2, the flux effectively recovered to the initial level. The XRD patterns (Fig. S10 ESI†) of the feed and permeate side with the LSC activation layers before and after the measurement show no formation of new phases. No changes in the microstructure of the membrane layer itself compared to a fresh membrane could be observed after the 500 hour test (ESI† Fig.S11b). Also no microstructural changes of the feed side activation layer of LSC could be detected after test. The permeate side activation layer, however, showed a densified region (extending approximately 10 µm adjacent to the membrane) after test. EDS analysis (Fig.S12b ESI†) revealed the formation of a strontium rich layer along the interface between the activation layer and the membrane, which is ascribed to a reaction between $La_{0.6}Sr_{0.4}CoO_{3-\delta}$ and CO_2[25].

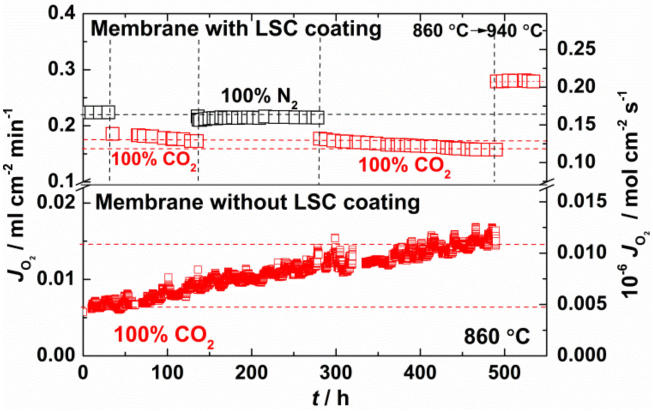

Fig.4 Oxygen permeation flux of AGZO-GCO55 dual phase membrane with and without LSC activation layer as a function of time at 860 °C and 940 °C. Feed gas: 100 ml min^{-1} air. Sweep gas: N_2 or CO_2 (total sweep gas flow: 150 N ml min^{-1}).

Over the 350 hours of test in CO_2 the flux through the coated membrane reduced by 7% with a tendency of a decreasing rate (Fig.S13 ESI†). Over a similar period (500 hours), the flux through an uncoated membrane (though much smaller) showed a clear increase (100%). This, together with the post-test microstructural findings, clearly shows that the dense membrane layer itself is chemically stable in CO_2, and that the decreasing flux observed for the coated membrane must be ascribed to the catalyst layer on the permeate side. For most common membrane materials based on perovskite or similar structures, such as $Ba_{0.5}Sr_{0.5}Co_{0.8}Fe_{0.2}O_{3-\delta}$ (BSCF), the oxygen flux usually dramatically drops once CO_2 is introduced[23] . The dual phase AGZO-GCO55 membrane material studied here shows in contrast a relatively stable flux in CO_2. Further improved CO_2 stability can be expected if a more CO_2 stable electrocatalysts is used instead of LSC.

Conclusions

A novel CO_2 and SO_2 tolerant dual phase composite membrane material, consisting of 50 vol.% $Al_{0.02}$ $Ga_{0.02}Zn_{0.96}O_{1.02}$ - 50 vol.% $Gd_{0.1}Ce_{0.9}O_{1.95-\delta}$ (AGZO-GCO55) was synthesized and tested as oxygen transport membrane. The total conductivity of the composite is mainly *n*-type electronic and originates from the percolating $Al_{0.02}Ga_{0.02}Zn_{0.96}O_{1.02}$ network. Fairly stable oxygen permeation in CO_2 could be proven in a 1.1 mm thick membrane for more than 500 hours at 860 °C and 940 °C. The AGZO-GCO55 composite material showed also sufficient stability in SO_2, making it a very good candidate for integration schemes of oxygen transport membrane into industrial applications that require direct contact with CO_2 and SO_2 containing environments.

Acknowledgments

The authors are thankful for the finical support by the Ministry of Energy Efficient Oxygen Production for a Sustainable Energy System (ENEFOX) Project (Project no. 48091 x-1), Graded membranes for energy efficient new generation carbon capture process (GREEN-CC, EU-FP7, no. 608524) and ForskEL through the project: Ceramic Membranes for Oxy-Fired Biomass Gasification (12202). The help of Henrik Paulsen, Simona Ovtar, Christodoulos Chatzichristodoulou, Mehdi Salehi, Alfred Samson and Jonas Gurauskis is greatly appreciated.

Notes and references

a Department of Energy Conversion and Storage, Technical University of Denmark, Risø campus, Frederiksborgvej 399, DK-4000 Roskilde, Denmark

b Department of Materials Science and Key Laboratory of Mobile Materials MOE, Jilin University, 130012 Changchun, China.

†Electronic Supplementary Information (ESI) available: See DOI: 10.1039/c000000x/

1. M. Puig-Arnavat, S. Soprani, M. Sogaard, K. Engelbrecht, J. Ahrenfeldt, U. B. Henriksen and P. V. Hendriksen, *RSC Advances*, 2013, **3**, 20843-20854.
2. R. Bredesen, K. Jordal and O. Bolland, *Chem. Eng. Process. Process Intensif.*, 2004, **43**, 1129-1158.
3. A. J. Samson, M. Søgaard and P. V. Hendriksen, *J. Membr. Sci.*, 2014, **470**, 178-188.
4. B. Wang, J. Yi, L. Winnubst and C. Chen, *Journal of Membrane Science*, 2006, **286**, 22-25.
5. V. V. Kharton, A. V. Kovalevsky, A. P. Viskup, A. L. Shaula, F. M. Figueiredo, E. N. Naumovich and F. M. B. Marques, *Solid State Ionics*, 2003, **160**, 247-258.
6. X. Zhu and W. Yang, *AIChE Journal*, 2008, **54**, 665-672.
7. M. Balaguer, J. García-Fayos, C. Solís and J. M. Serra, *Chem. Mater.*, 2013, **25**, 4986-4993.
8. C. S. Chen, H. Kruidhof, H. J. M. Bouwmeester, H. Verweij and A. J. Burggraaf, *Solid State Ionics*, 1996, **86-88**, 569-572.
9. H. Luo, K. Efimov, H. Jiang, A. Feldhoff, H. Wang and J. Caro, *Angew. Chem. Int. Ed.*, 2011, **50**, 759-763.
10. E. Ruiz-Trejo, P. Boldrin, A. Lubin, F. Tariq, S. Fearn, R. Chater, S. N. Cook, A. Atkinson, R. I. Gruar, C. J. Tighe, J. Darr and N. P. Brandon, *Chem. Mater.*, 2014, **26**, 3887-3895.
11. J. Gao, L. Li, Z. Yin, J. Zhang, S. Lu and X. Tan, *Journal of Membrane Science*, 2014, **455**, 341-348.
12. S. Engels, T. Markus, M. Modigell and L. Singheiser, *Journal of Membrane Science*, 2011, **370**, 58-69.
13. T. Minami, *MRS Bulletin*, 2000, **25**, 38-44.
14. C. Chatzichristodoulou, P. V. Hendriksen, S. P. V. Foghmoes, S. Ricote, A. Kaiser, J. Classcock and S. Cheng.
15. L. Ge, S. Li, Y. Zheng, M. Zhou, H. Chen and L. Guo, *J. Power Sources*, 2011, **196**, 6131-6137.
16. K. Schmale, M. Daniels, A. Buchheit, M. Grünebaum, L. Haase, S. Koops and H.-D. Wiemhöfer, *J. Electrochem. Soc.*, 2013, **160**, F1081-F1087.
17. H. Ibach, *Phys. Status Solidi (b)*, 1969, **33**, 257-265.
18. S. Wang, M. Katsuki, T. Hashimoto and M. Dokiya, *J. Electrochem. Soc.*, 2003, **150**, A952-A958.
19. L. Han, L. Hung, N. Nong, N. Pryds and S. Linderoth, *J. Electron. Mater.*, 2013, **42**, 1573-1581.
20. S. Wang, T. Kobayashi, M. Dokiya and T. Hashimoto, *J. Electrochem. Soc.*, 2000, **147**, 3606-3609.
21. C. Chatzichristodoulou and P. V. Hendriksen, *Physical Chemistry Chemical Physics*, 2011, **13**, 21558-21572.
22. W. Li, T.-F. Tian, F.-Y. Shi, Y.-S. Wang and C.-S. Chen, *Ind Eng Chem Res.* , 2009, **48**, 5789-5793.
23. K. Zhang, L. Liu, Z. Shao, R. Xu, J. C. Diniz da Costa, S. Wang and S. Liu, *J. Mater. Chem. A*, 2013, **1**, 9150-9156.
24. X. Tan, N. Liu, B. Meng, J. Sunarso, K. Zhang and S. Liu, *J. Membr. Sci.*, 2012, **389**, 216-222.
25. V. Esposito, M. Søgaard and P. V. Hendriksen, *Solid State Ionics*, 2012, **227**, 46-56.
26. H. Luo, H. Jiang, K. Efimov, F. Liang, H. Wang and J. Caro, *Ind. Eng. Chem. Res.*, 2011, **50**, 13508-13517.
27. M. Søgaard, Technical University of Denmark, 2006.
28. P. Hjalmarsson, M. B. Mogensen and M. Søgaard, *Solid State Ionics*, 2008, **179**, 1422-1426.
29. H. J. Park and S. Kim, *Electrochemical and Solid-State Letters*, 2007, **10**, B187-B190.

Electronic Supplementary Information (ESI)

In the Experimental section, details of the synthesis and the characterization of the materials are presented, followed by further details about the electrical and oxygen permeation flux measurements. Illustrations of the experimental setups are included.

Experimental details

Preparation of powders and membranes

The starting materials used in the investigation were ZnO (99.9%, 200 mesh powder; Alfa-Aesar), - γ-Al_2O_3 (99.5%, 40 nm to 80 nm APS powder; Alfa-Aesar), Ga_2O_3 (99.99%, 50 mesh powder; Alfa-Aesar), and GCO10 powder (ultra-low surface area (ULSA) powder from Rhodia S.A., France).

For synthesis of the AGZO powder ($Al_{0.02}Ga_{0.02}Zn_{0.96}O_{1.02}$), γ-$Al_2O_3$ and Ga_2O_3 were mixed with ZnO at a molar ratio of 1:1:96 (atomic ratio Al:Ga:Zn = 2:2:96) by roll milling for 24 h in ethanol using zirconia balls. The resulting mixtures were then dried at room temperature for 24 hours followed by further drying at 130 °C for 3 h. The dried powders were calcined in an alumina crucible at 900 °C in N_2 for 5 hours. After calcination, the powders were sieved using a mesh (U.S. Mesh 325), corresponding to mean particle agglomerate-size of 48 μm. GCO10 powder was later mixed with as-prepared AGZO powder by ethanol aided roll milling for 48 hours. The powder mixture consisted of 50 vol.% AGZO ($Al_{0.02}Ga_{0.02}Zn_{0.96}O_{1.02}$) and 50 vol.% GCO ($Gd_{0.1}Ce_{0.9}O_{1.95-\delta}$), abbreviated as AGZO-GCO55. The final mixture was dried at 120 °C overnight, followed by sieving using a mesh (U.S. Mesh 100). The 18 mm diameter membrane was prepared by pressing the powder with a uniaxial pressure of 50 MPa followed by conducting an isostatic pressuring at 60 MPa. The membrane was subsequently sintered at 1200 °C for 5 hours in air. The membrane was polished by SiC sand paper and diamond paper to achieve a smooth and clean surface. The relative density (geometrical) of the dual phase composite is close to 99% of the theoretical density (XRD). In order to promote surface oxygen exchange, $La_{0.6}Sr_{0.4}CoO_{3-\delta}$ (LSC) porous activation layers were introduced by screen printing an in-house developed pure LSC ink on both sides of the polished, dense membrane since LSC is a good electrocatalyst for oxygen exchange reactions[1]. The printed membrane was sintered at 900 °C to ensure a good adhesion between the membrane and the catalytic layers.

Characterization of powders and membranes

The powder XRD in this work was conducted on a Bruker Robot in Bragg-Brenano geometry with Cu Kα in a 2ϑ range of 20 °-90 °. *In-situ* XRD was carried out in a high temperature chamber from room temperature to 900 °C. The powder of the crushed membrane is uniformly dispersed on a flat Pt foil that serves a sample holder. The heating rate utilized in this work is 2 °C min^{-1} and the XRD at each temperature was measured before and after holding for 1 hour to ensure the chemical and thermal equilibrium. The XRD patterns were indexed and compared by the data database of ICCD (International Centre for Diffraction Data) by the software DIFFRAC plus. The morphology and chemical composition of the specimens in this work was further investigated by a field emission gun scanning electron microscope (FEG-SEM) using a voltage of 20 kv. The high-resolution transmission electron microscopy (HRTEM) and scanning transmission electron microscopy (STEM) images were performed using a JEM 3000F transmission electron microscope, operated at 300 kV.

Electrical conductivity measurement

The electrical conductivity measurement was conducted using a standard 4-terminal technique on a bar with dimension 12×0.8 cm×0.8 mm^3. Prior to the measurement, the bar was polished with a SiC paper #1500. Four Pt wires were ramped on separate spots of the bar. The electrical conductivity of the sample was measured under a constant voltage (1 volt). The bar was mounted in a quartz tube in which the gas was controlled by varying the gas flow around the sample. The oxygen partial pressure was monitored by a zirconia sensor.

Investigation of powders annealed in CO_2 and SO_2 containing atmospheres

The material stability was investigated both by membrane test in flowing gas and in material exposure tests of the crushed powder materials as further outlined below.

Annealing the powder in CO_2 and SO_2 at high temperature was carried out using a tube furnace allowing control of the gas atmosphere. The flow of CO_2 was monitored by a ball flowmeter. For the pretreatment of the powders in SO_2, $Al_2(SO_4)_3$ powder was placed in a crucible and covered by a thin layer of super wool. Fresh powders of AGZO-GCO55 and $La_{0.6}Sr_{0.4}FeO_{3-\delta}$-$Gd_{0.1}Ce_{0.9}O_{1.95-\delta}$ (internal standard) were dispersed on the super wool and the crucible was heated inside the tube furnace. Air is flowed for circulation. Upon heating, the $Al_2(SO_4)_3$ decomposes exposing the candidate materials to a high SO_2 activity. The generation of SO_2 by the thermal decomposition of $Al_2(SO_4)_3$ was confirmed by an external mass spectrometer.

Oxygen permeation measurement

Oxygen permeation measurements were performed in an in-house built rig displayed in Fig. S 1. The membrane with a thickness of approximately 1.1 mm and a diameter of 15 mm was initially sealed between two alumina tubes with a 30/70 vol.% MgO/sodium aluminosilicate glass composite. The membrane was placed in the middle zone of a height adjustable tube furnace. The feed side tube below the membrane was supplied with gas from the feed side manifold which has a feed gas inlet and outlet. Similarly, the permeate side of the membrane was purged with gas from an "anode" manifold. The feed side was flushed with air/O_2 with a constant flow rate of 100 Nml min^{-1} and the permeate side was flushed with various flows of N_2/CO_2. The flow of gases was monitored by mass flow controllers (See Fig. S 2). The net oxygen permeation flux can be deduced from the pO_2 difference between inlet and outlet gases flowing through the permeate side. The pO_2 is precisely monitored by two in-house built YSZ-based oxygen sensors. The oxygen permeation flux of the membrane may be written

$$J_{O_2} = \frac{\dot{N}\left(pO_2^{out} - pO_2^{in}\right)}{A} \quad (1)$$

Where A is the net area of the permeate side of the membrane, pO_2^{in} and pO_2^{out} denote oxygen partial pressure of inlet and outlet, respectively. $\dot{N}$ represents the mass flow rate of outlet gases. The oxygen partial pressures are calculated *via* the Nernst equation from the Emf's measured with the zirconia sensors.

$$E = \frac{RT}{4F} \ln \frac{pO_2}{pO_{2,ref}} \quad (2)$$

Where *E* is the open circuit voltage of the oxygen sensor. R is the gas constant. $pO_{2,ref}$ is the oxygen partial pressure at reference electrode which retains at 0.21 bar, T is the temperature of the senor.

The leak in the system was assessed by means of a mass flow meter on the permeate stream. When a perfect sealing is achieved, the outlet gas flow rate should be equivalent to the inlet flow. If there are leaks in the membrane or pinholes or cracks in the glass encapsulation, the flow rate of the outlet gas will be lower than that of the inlet gas. Typically, in the cases where a significant leak is observed during the permeation measurement, a thermally activated increase in oxygen flux is not observed. In the data reported here the inlet and outlet flows are within the uncertainty (1%) identical and a thermal activated oxygen permeation flux was observed, indicating a perfect sealing. The maximum leak originating from pinholes in the sealant and due to other sources of oxygen in the permeate flow through the membrane is estimated to be lower than 5% at low temperature (600 °C) based on the gas sensor. Below 600 °C a large leak arises due to thermal expansion mismatch driven failure at the sealant. We check a worst case estimate of leakage flux in each membrane based on the lowest flux during cooling (<600 °C), before an obvious compromise of the seal is detected. This was indicated by a sudden drop of measured voltage of pO_2 outlet sensor which typically occurs at temperatures between 400 °C and 600 °C. The worst leakage was subtracted from the measured flux to ensure an underestimated resulting flux. The worst leakage fluxes for each measurement were listed in Table S1.

Table S1. Estimated worst leakage for each membrane

Membrane	JO2,leak/ mol cm^{-2} s^{-1}	% difference of JO2,leak at 900 ° C
GCO-AGZO55 with coating	2.08×10^{-9}	1%
GCO-AGZO5 without coating	1.99×10^{-9}	17%

Furthermore, the peak for N_2 arising from the leak from ambient air through the membrane or the sealing cannot be observed by an Agilent 490 micro gas chromatograph during the test, further demonstrating the gas tight during the permeation measurements.

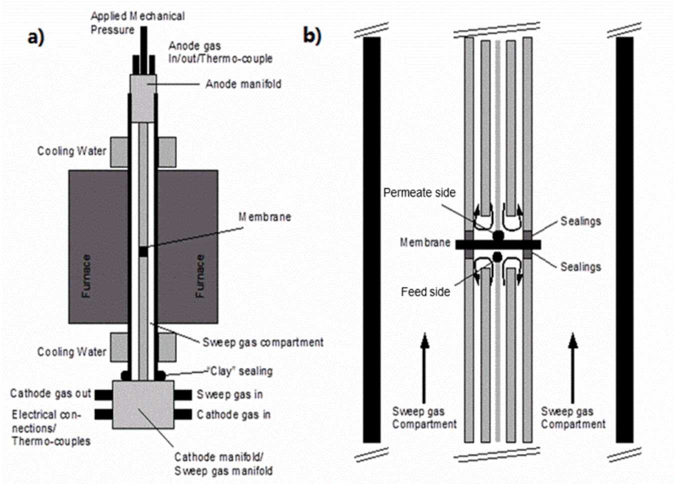

Fig. S 1 a) Schematic illustration of the membrane test rig. b) Zoom into the heated part of the membrane test rig.

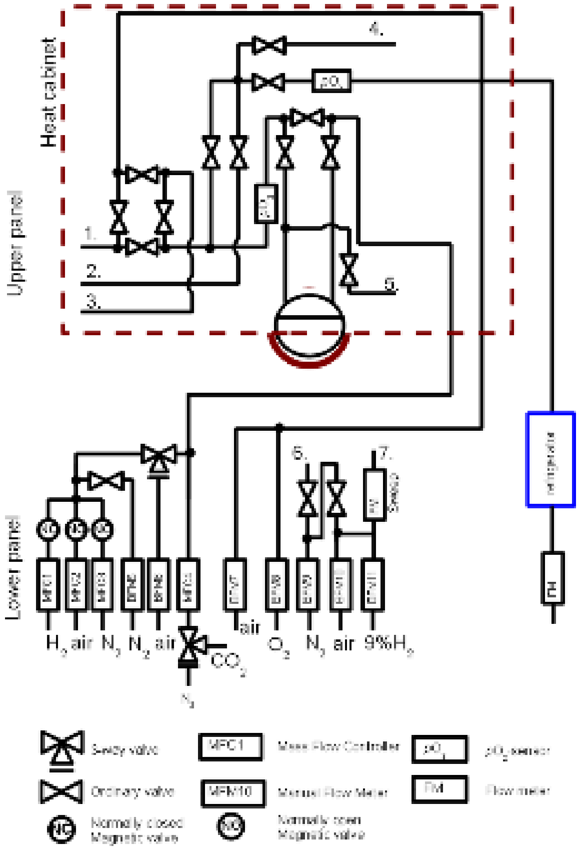

Fig. S 2 Flow diagram of the upper and lower panel and outlet through refrigerator and flow meter . The numbers in the diagram represents the following 1. Gas to the permeate side of the membrane (typically the reducing side) 2. Gas from the permeate side of the membrane. 3. Gas to the feed side of the membrane. 4. Gas to refrigerator and flow meter 5. N/A 6. Gas outlet for further extensions of the rig, 7. Gas to the sweep gas compartment.

Additional results

Fig. S 3 shows the calculated phase diagram of Zn-S-O at 700-900 °C as functions of pO_2 and pSO_2. The calculations were carried out using the FACTSAGE Thermochemical Software and Databases[2]. $ZnCO_3$ will completely decompose to ZnO and CO_2 above 200 °C. The lines mark the phase boundary, illustrating the combination of pO_2 and pSO_2 where $ZnSO_4$ may form at 700 °C, 800 °C and 900 °C. The upper part of the phase boundary demonstrates the atmosphere for $ZnSO_4$ and the lower part corresponds to the condition for a stable ZnO.

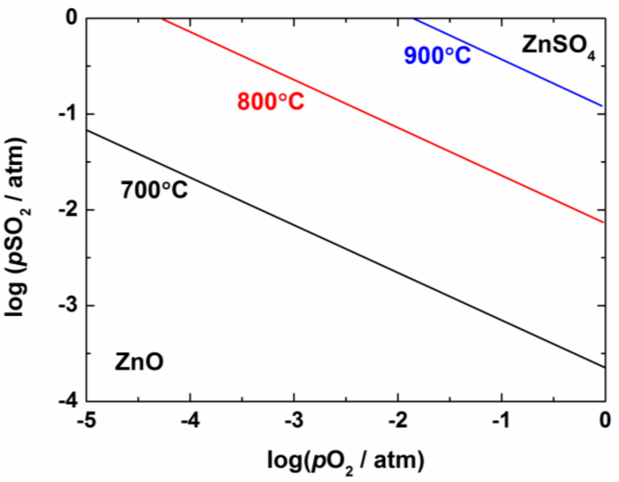

Fig. S 3 Calculated phase diagram as functions of logarithm oxygen partial pressure and sulfur dioxide partial pressure at 700 °C, 800 °C and 900 °C.

Fig. S 4 shows the oxygen flux of AGZO-GCO5 membrane with and without LSC coating as a function of ln (pO_2'/pO_2'') when using either N_2 or CO_2 as the sweep gas in the temperature range 705-940 °C. The red lines in Fig. S4 a) are a linear fit to the results. The solid lines in Fig. S4 b) are plotted as a guide to the eye. The vertical dashed line is the fluxes at a fixed driving force from which the Arrhenius curves (Fig. 3 in the main article) are obtained. The linear fit follows the Wagner equation for calculating bulk diffusion controlled flux:

$$J_{O_2} = \frac{RT\sigma_{amb}}{16F^2L} \ln \frac{pO_2^{/}}{pO_2^{//}} \tag{3}$$

As shown in Fig. S 5, permeation flux measurements for two nominally identical membranes were also carried out. The difference between the fluxes is less than 5% illustrating very good reproducibility. The largest uncertainty on the flux values originates from the estimation of the surface area.

Several studies report on the oxygen permeability of various composites based on doped ceria as the ionic conducting phase. Selected results are summarized in Table S. 1 together with the oxygen flux results of the AGZO-GCO55 membrane reported in this work. The AGZO-GCO55 membranes virtually display oxygen permeation fluxes comparable to literature . It should be noted that the electronic conductors used in the studies in the literature either contain relatively expensive metals (Ag), toxic elements (Cr, Ni and Co) or alkaline earth elements (Sr). For the economical comprehensiveness of the technology expensive and toxic elements should be avoided. For alkaline earth elements containing electronic conductors, the stability of these materials in CO2 and SO2 is problematic. AGZO-GCO55 avoids the use of toxic, expensive and alkaline earth elements.

Fig. S 6 shows the total conductivity of AGZO-GCO55 and GCO10 as a function of oxygen partial pressure at 700 °C, 800 °C and 900 °C, respectively. The total conductivity of AGZO-GCO55 is more than one order of magnitude larger than that of GCO, indicating that the total conductivity of the composite is dominated by the percolating AGZO phase. In addition, it can be observed that as the oxygen partial pressure decreases the electronic conductivity increases, illustrating a behavior of *n*-type electronic conductivity, which is consistent with literature[3, 4].

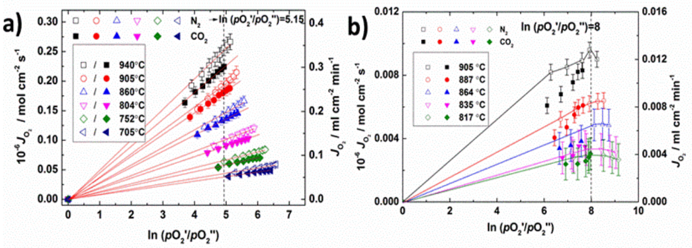

Fig. S 4 Oxygen permeation flux JO2 through a 1.1 mm thick AZGO-GCO55 composite membrane a) with and b) without LSC coating as a function of the natural logarithm of the ratio between the oxygen partial pressure on feed and the permeate side. N2 (hollow) and CO2 (fill) were used as sweep gas, respectively.

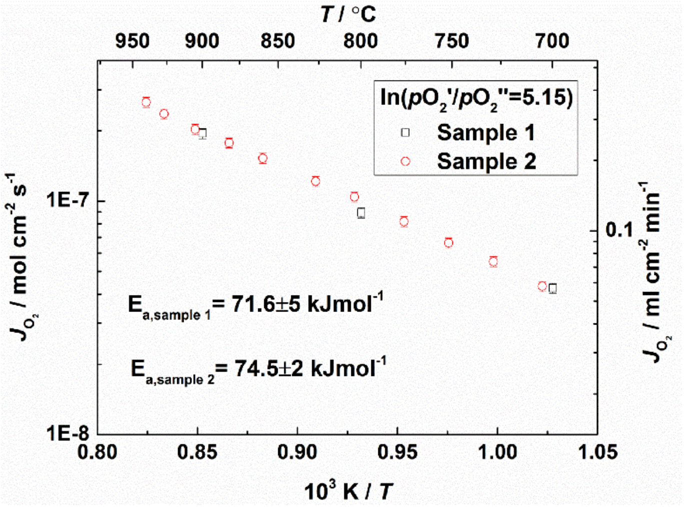

Fig. S 5 Arrhenius plot of the oxygen permeation flux (JO2) of two nominally identical AGZO-GCO55 membranes (Sample 1 and 2) measured in N2 on the permeate side under a fixed driving force (ln (pO2//pO2//=5.15) as a function of inverse absolute temperature.

Table S.2 Oxygen permeation fluxes of dual phase composites involving doped ceria. The values represent volume percent of each phase.

Membrane	T (°C)	J_{O2} (mol cm^2 s^{-1})	Thickness (mm)	$pO_2^{/}/pO_2^{//}$	Ref.
$^*Gd_{0.1}Ce_{0.9}O_{2-\delta}(60)/NiFe_2O_4(40)$	900-1000	7.93×10^{-8}-2.28×10^{-7}	0.5	Air/He,Ne	5
$^*Gd_{0.1}Ce_{0.9}O_{2-\delta}(60)/NiFe_2O_4(40)$	900-1000	6.79×10^{-8}-2.05×10^{-7}	0.5	Air/He,Ne	5
$Sm_{0.15}Ce_{0.85}O_{1.925}(75)/ Sm_{0.6}Sr_{0.4}FeO_{3-\delta}(25)$	750-940	1.7×10^{-7}-5.92×10^{-7}	0.5	Air/He	6
$Sm_{0.15}Ce_{0.85}O_{1.925}(75)/ Sm_{0.6}Sr_{0.4}CrO_{3-\delta}(25)$	750-940	5.87×10^{-8}-2.00×10^{-7}	0.5	Air/He	6
$Tb_{0.2}Ce_{0.9}O_{2-\delta}(60)/NiFe_2O_4(40)$	800-1000	2.84×10^{-8}-1.51×10^{-7}	0.68	Air/CO_2	7
$Gd_{0.1}Ce_{0.9}O_{2-\delta}(84)$/Ag-CuO (16)	600-890	1.12×10^{-8}-2.20×10^{-7}	1.1	Air/N_2	8
$Gd_{0.2}Ce_{0.9}O_{2-\delta}$ (48)/$La_{0.8}Sr_{0.2}Fe_{0.8}Co_{0.2}O_{3-\delta}(52)$	950	6.3×10^{-8}	1.0	Air/He	9
$Gd_{0.2}Ce_{0.9}O_{2-\delta}$	950	9.94×10^{-10}	1.35	Air/Ar	9
$Gd_{0.1}Ce_{0.9}O_{2-\delta}(50)/Al_{0.02}Ga_{0.02}Zn_{0.96}O_{1.02}$ (50)	700-940	4.36×10^{-8}-2.67×10^{-7}	1.1	Air/N_2	This work
$Gd_{0.1}Ce_{0.9}O_{2-\delta}(50)/Al_{0.02}Ga_{0.02}Zn_{0.96}O_{1.02}$ (50)	700-940	3.94×10^{-8}-2.33×10^{-7}	1.1	Air/CO_2	This work

***weight percent**

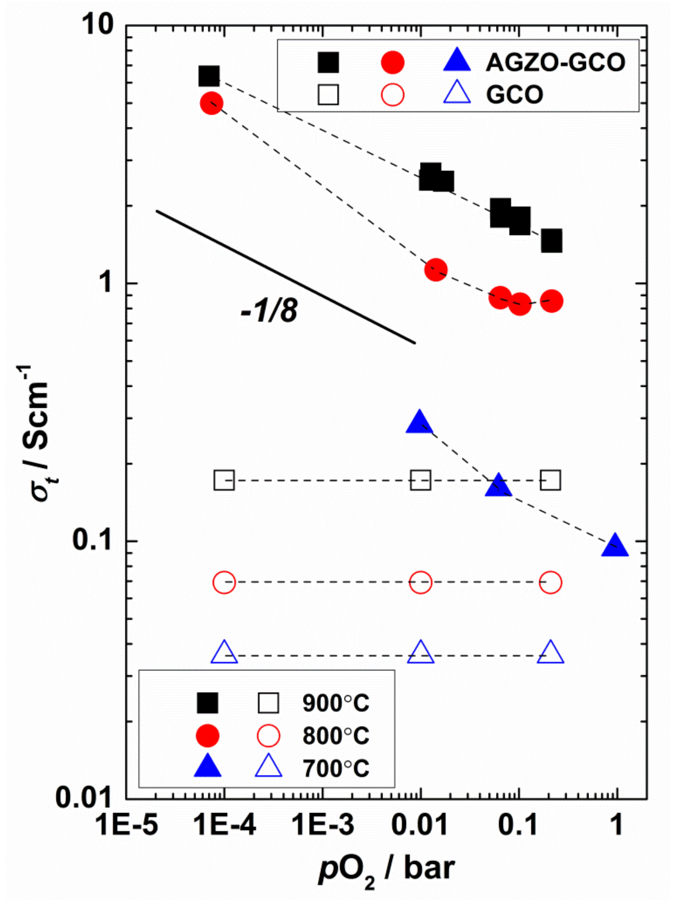

Fig. S 6 Logarithm total conductivity of AGZO-GCO (solid symbols) and GCO[10] (open symbols) as a function of logarithm oxygen partial pressure. Dotted lines are plotted as a guide to the eye.

Fig. S 7 shows a SEM micrograph of a polished and thermally etched (1200°C for 0.5 hour) polished membrane disk. A distinct separation of the two phases can be clearly observed. The average grain size for both phases is less than 4 µm. The homogenous distribution of the two phases yields a good percolation for both phases.

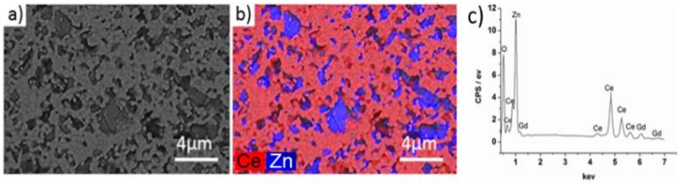

Fig. S 7 a) BSEM micrograph of a polished and thermally etched membrane b) EDX mapping micrograph Ce (red), Zn (blue) c) EDX spectrum

Fig. 1 (main manuscript) shows the XRD patterns of powders of GCO-AGZO55 annealed in a SO_2 containing atmosphere. A powder of 50 vol. % $Gd_{0.1}Ce_{0.9}O_{1.95-\delta}$ -50 vol. % $La_{0.6}Sr_{0.4}FeO_{3-\delta}$(GCO-LSF55), which serves as an internal standard, was annealed together with AGZO-GCO55 for the same experimental condition.

Fig. S 8 shows the XRD patterns of LSF-GCO55 annealed in the SO_2 containing atmosphere at 850 °C for 2 hours. For the LSF-GCO composition $SrSO_4$ could be detected while for ZnO no formation of sulfates could be observed (see Fig. 1). The reaction between Sr and SO_2 is also reported for $La_{0.6}Sr_{0.4}Co_{0.8}Fe_{0.2}O_{3-\delta}$ samples annealed in SO_2 above 800 °C[11].

Fig. S 9 shows *in-situ* XRD patterns of a powder of crushed AGZO-GCO55 dual phase membrane in the temperature range of 30-900 °C obtained in air. The peaks corresponding to AGZO, GCO and Pt are present up to 900 °C. No other peaks could be detected, illustrating the phase stability of AGZO and GCO at high temperature.

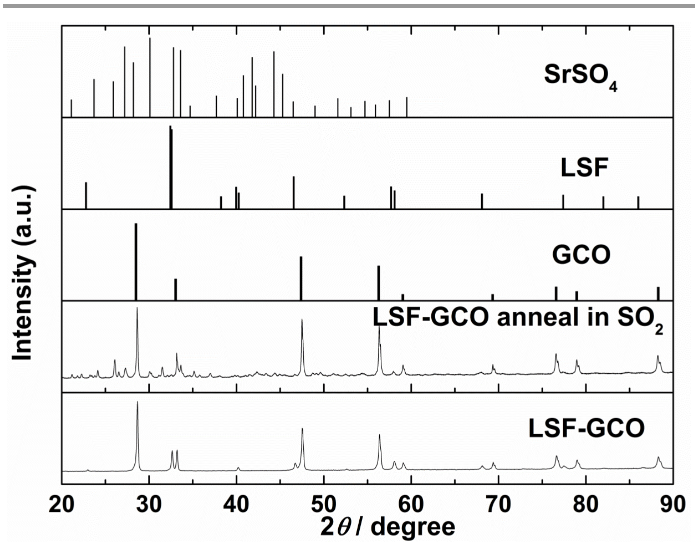

Fig. S 8 XRD patterns of CGO-LSF55 dual-phase composite membrane annealed in SO_2 at 850 °C for 2 hours.

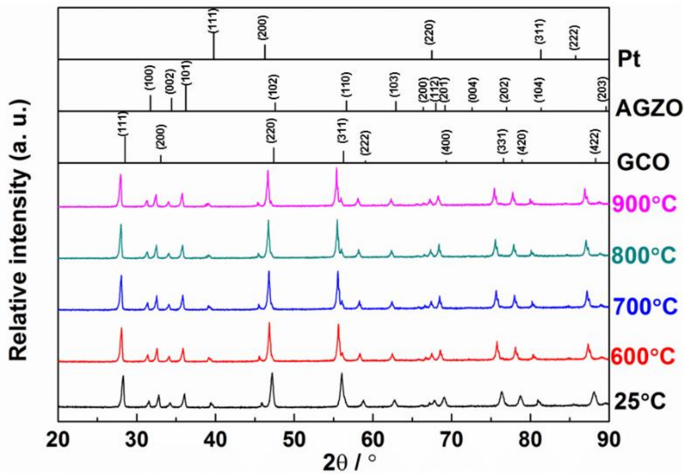

Fig. S 9 *In-situ* XRD patterns of CGO-AZGO55 composites at elevated temperature. Dwell time at each temperature was 1 hour to reach steady state. The XRD data collection last for 1 hour at each temperature. The sample holder is a Pt foil.

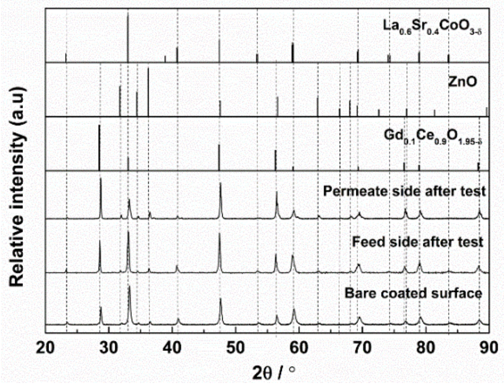

Fig. S 10 Normalized XRD patterns of an AGZO-GCO dual phase membrane with LSC64 catalytic layers on both side before and after test. Zero shifts of 0.23°, 0.10° and 0.30° (arising from the XRD system) of permeate side "after test", feed side "after test" and bare coated surface respectively, are corrected for.

Fig. S 10 shows XRD patterns of the surfaces of pre-test AGZO-GCO55 with a LSC catalytic layer and feed side as well as permeate side of AGZO-GCO55 with LSC layer after permeation measurement. For the feed side, no obvious change of the peaks can be observed after test. Compared to the pre-test XRD patterns and the feed side pattern, the intensity of LSC peaks of the permeate side is lower and the width of the peaks is broadening. The reason for the change of the peaks will be further discussed in conjunction with the results of SEM-EDX.

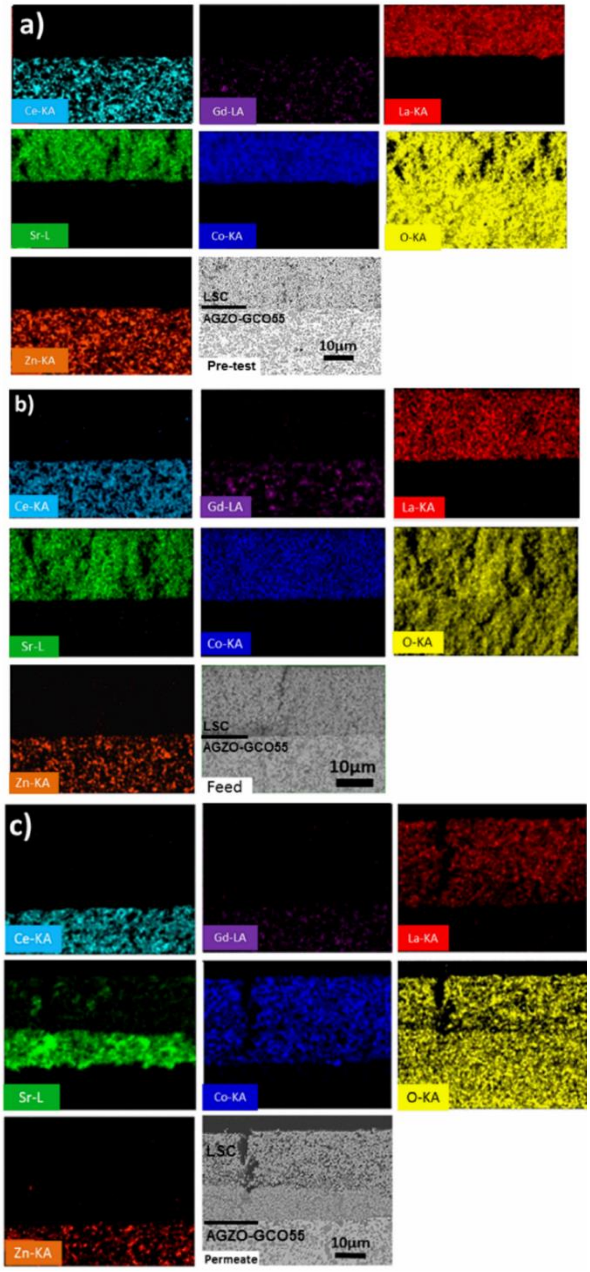

Fig. S 11 BSEM and EDX elemental mapping micrographs of the interfaces between the AGZO-GCO55 membrane and the LSC catalytic layer: a) pre-test interface b) Feed side interface after measurement c) permeate side interface after measurement (involving aging test in CO_2).

Fig. S 11 a) shows SEM elemental mapping of the cross section of a pre-test AGZO-GCO55/LSC interface. For the pre-test AGZO-GCO55/LSC interface, no trace of cation diffusion or reaction can be detected. Fig. S 11 b) and c) shows elemental mapping of the same interface after test for the feed and permeate side, respectively. Fig. S 12 a) and b) show line scans of the AGZO-GCO55/LSC interface of the feed and permeate side after measurement, respectively. It can be seen that the concentration of Sr is pronouncedly increased in a 10 μm thick layer adjacent to the membrane on the permeate side. Segregation of Sr can occur in Sr-doped perovskite based cathodes at high temperatures and is found to significantly inhibit the oxygen reduction reaction.[12-15] According to thermodynamic calculation, LSC is more likely to react with CO_2 in high pO_2. Therefore, $SrCO_3$ arising from the reaction between SrO and CO_2 has formed closest to the interface where the pO_2 is higher than in the gas stream. Sr from the rest of the electrode has in turn diffused towards the interface. Upon re-oxidation/cooling in N_2 the pervoskite forms again with a high Sr content perovskite adjacent to the membrane. The variation of the Sr content can also be seen from the peak broadening in the XRD pattern (See Fig. S 10).

Fig. S 13 displays the degradation rate of the membrane as a function of time, which is obtained by taking the derivative of oxygen permeation flux versus time. In general, the degradation rate when using N_2 as the sweep gas is scattering in the range of ± 5×10^{-6} ml cm^{-2} min^{-1}/ h, which is negligible. It indicates that the flux is extremely stable when using 100% N_2 as the sweep gas. Notice that the degradation rate when using 100% CO_2 as the sweep gas is about -2×10^{-4} ml cm^{-2} min^{-1}/ h at the beginning, followed by a decreased rate subsequently leveling off. This shows that the flux degrades in CO_2, but with a continuously decreased rate (860 °C). With respect to the membrane without LSC coating measured using 100% CO_2 as the sweep gas, the flux increases as a function of time following the rate of 3×10^{-5} ml cm^{-2} min^{-1}/ h.

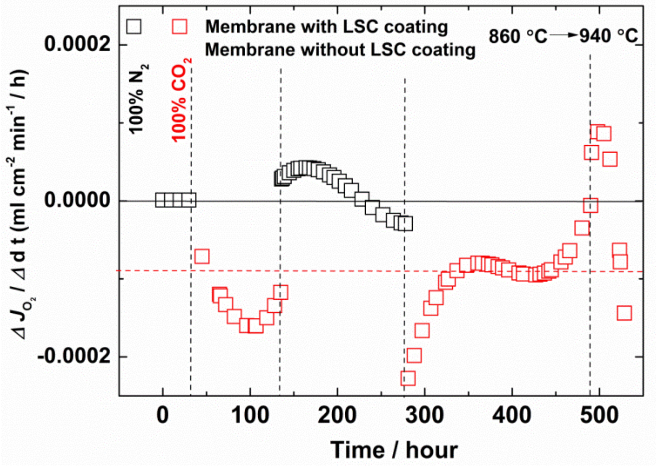

Fig. S 13 The degradation rate of the oxygen permeation fluxes of the membrane with and without LSC coating as a function of time. The results are calculated by taking the derivative of flux vs. time (See Fig. 4 in the main article)

References

1. M. Søgaard, P. V. Hendriksen, M. Mogensen, F. W. Poulsen and E. Skou, *Solid State Ionics*, 2006, 177, 3285-3296.
2. C. W. Bale, P. Chartrand, S. A. Degterov, G. Eriksson, K. Hack, R. Ben Mahfoud, J. Melançon, A. D. Pelton and S. Petersen, *Calphad*, 2002, 26, 189-228.
3. S. Erdal, C. Kjølseth and T. Norby, *The Journal of Physical Chemistry C*, 2010, 114, 16785-16792.
4. T. S. Bjørheim, S. Erdal, K. M. Johansen, K. E. Knutsen and T. Norby, *The Journal of Physical Chemistry C*, 2012, 116, 23764-23772.
5. H. Luo, K. Efimov, H. Jiang, A. Feldhoff, H. Wang and J. Caro, *Angew. Chem. Int. Ed.*, 2011, 50, 759-763.
6. X. Zhu, M. Li, H. Liu, T. Zhang, Y. Cong and W. Yang, *Journal of Membrane Science*, 2012, 394–395, 120-130.
7. M. Balaguer, J. García-Fayos, C. Solís and J. M. Serra, *Chem. Mater.*, 2013, 25, 4986-4993.
8. A. J. Samson, M. Søgaard and P. V. Hendriksen, *J. Membr. Sci.*, 2014, 470, 178-188.
9. V. V. Kharton, F. M. Figueiredo, L. Navarro, E. N. Naumovich, A. V. Kovalevsky, A. A. Yaremchenko, A. P. Viskup, A. Carneiro, F. M. B. Marques and J. R. Frade, *Journal of Materials Science*, 2001, 36, 1105-1117.
10. S. Wang, T. Kobayashi, M. Dokiya and T. Hashimoto, *J. Electrochem. Soc.*, 2000, 147, 3606-3609.
11. J. Gao, L. Li, Z. Yin, J. Zhang, S. Lu and X. Tan, *Journal of Membrane Science*, 2014, 455, 341-348.
12. M. Kubicek, A. Limbeck, T. Frömling, H. Hutter and J. Fleig, *Journal of The Electrochemical Society*, 2011, 158, B727-B734.
13. V. I. Sharma and B. Yildiz, *Journal of The Electrochemical Society*, 2010, 157, B441-B448.
14. P. Hjalmarsson, M. B. Mogensen and M. Søgaard, *Solid State Ionics*, 2008, 179, 1422-1426.
15. E. Bucher, W. Sitte, F. Klauser and E. Bertel, *Solid State Ionics*, 2012, 208, 43-51.

High Performance Microchanneled Asymmetric $Gd_{0.1}Ce_{0.9}O_{1.95-\delta}$-$La_{0.6}Sr_{0.4}FeO_{3-\delta}$-based Membranes for Oxygen Separation

Shiyang Cheng[*,†,‖], *Hua Huang*[‡], *Simona Ovtar*[†], *Søren B. Simonsen*[†], *Ming Chen*[†], *Wei Zhang*[§], *Martin Søgaard*[†], *Andreas Kaiser*[†], *Peter Vang Hendriksen*[†], *Chusheng Chen*[‡]

[†]Department of Energy Conversion and Storage, Technical University of Denmark, Risø campus, Frederiksborgvej 399, DK-4000 Roskilde, Denmark

[‡]CAS Key Laboratory of Materials for Energy Conversion, Department of Materials Science and Engineering, University of Science and Technology of China, Hefei 230026, China

[§]Department of Materials Science and Key Laboratory of Mobile Materials MOE, Jilin University, 130012 Changchun, China

ABSTRACT: A microchanneled asymmetric dual phase composite membrane of 70 vol.% $Gd_{0.1}Ce_{0.9}O_{1.95-\delta}$-30 vol.% $La_{0.6}Sr_{0.4}FeO_{3-\delta}$ (CGO-LSF) was fabricated by a “one step” phase- inversion tape casting. The sample consists of a thin dense membrane (100 μm) and a porous substrate including “finger-like” microchannels. The oxygen permeation flux through the membrane with and without catalytic surface layers was investigated under a variety of oxygen partial pressure gradients. At 900 °C, the oxygen permeation flux of the bare membrane was 0.06 (STP) ml cm^{-2} min^{-1} for the air/He-case and 10.10 (STP) ml cm^{-2} min^{-1} for the air/CO-case. Oxygen flux measurements as well as electrical conductivity relaxation show that the oxygen flux through the bare membrane without catalyst is limited by the oxygen surface exchange. The surface exchange can be enhanced by introduction of catalyst on the membrane surface. An increase of the oxygen flux of ca. 1.49 (STP) ml cm^{-2} min^{-1} at 900 ºC was observed when catalyst is added for the air/He-case. Mass transfer polarization through the finger-like support was confirmed to be negligible, which benefits the overall performance. A stable flux of 7.00 (STP) ml cm^{-2} min^{-1} was observed between air/CO/CO_2 over 200 hours at 850 °C. Partial surface decomposition was observed on the permeate side exposed to CO, in line with predictions from thermodynamic calculations. In a mixture of CO, CO_2, H_2 and H_2O at similar oxygen activity the material will according to the calculation not decompose. The microchanneled asymmetric CGO-LSF membranes show high oxygen permeability and chemical stability under a range of technologically relevant oxygen potential gradients.

KEYWORDS: phase inversion; dual phase composite membranes; electrical conductivity relaxation; surface exchange; mass transfer polarization; thermodynamic calculation

1. Introduction

Recently, oxygen transport membranes (OTMs) have been investigated for their potential use in supplying pure oxygen in different high temperature applications, such as high purity oxygen production [1], partial oxidation of methane for syngas production [2], oxy-fuel combustion [3] and biomass gasification [4]. OTMs need to fulfil the following requirements for industrial applications, *i*) provide a high oxygen flux, *ii*) have sufficient chemical stability under the relevant oxygen activities and temperatures, *iii*) be low cost, and *iv*) have high thermo-mechanical stability. Often these requirements are mutually contradicting; it is especially difficult to find a material that is both thermodynamically stable and provides high oxygen flux. Several materials belonging to the perovskite class; $(A,B)MO_3$ (A=Rare earth, B=Ca, Sr, Ba, M=Fe, Co, Cu, Zn) have been shown to provide fast oxygen transport [5-11]. In particular with respect to flux and oxygen surface exchange, $Ba_xSr_{1-x}Co_yFe_{1-y}O_{3-\delta}$ (BSCF) is one of the best performing materials [11-12]. However, the chemical stability of such cobalt containing perovskites is insufficient for the low oxygen partial pressure applications (biomass gasification and syngas production) [13-14] and the material is further unstable in CO_2 [15]. Apart from decomposition under reducing conditions, kinetic demixing arising from cation diffusion has also been reported to lead to the slow degradation of the oxygen flux [16]. Most of the alkaline earth doped perovskites react quickly with corrosive acidic gases, such as SO_2 and H_2S, which are the main gaseous impurities in flue gases [13]. This is a serious material challenge for a membrane to be integrated with flue gases.

In addition to perovskite materials, fluorite-structured lanthanide doped ceria (Ln-doped ceria) has been studied for use in OTMs [17]. These materials have excellent chemical stability, high degree of mixed ionic and electronic conductivity under strongly reducing conditions and unique catalytic activity [18]. These materials are particularly suitable for utilization in partial oxidation of methane [19] and for oxy-fuel combustion [20]. It is noteworthy that the oxygen permeation flux of a 27-μm thick 10 at.% Gd-doped ceria (CGO) membrane exceeds 10 Nml cm^{-2} min^{-1} using air as the feed gas and wet hydrogen as the sweep gas at 850 °C [19], indicating an application potential in the chemical industry. However, the oxygen permeation flux of CGO-based membranes under a small oxygen potential gradient is low because of the low electronic conductivity under oxidizing conditions ($<1\times10^{-3}$ Scm^{-1} at 900 ºC in air) [21]. To provide technologically relevant fluxes, the electronic conductivity must be substantially enhanced. One strategy is to produce so-called dual phase membranes by adding a second percolating electronic conducting phase. For example, ceria doped with rare earth elements have been combined with a variety of electronic conductors and have shown oxygen fluxes under a wide range of oxygen potential gradients [22-25]. Some of the dual phase membranes seem to tolerate acidic gases relevant for the oxy-fuel applications, for example, CO_2 [10, 26] and SO_2 [27-28]. An additional merit of the composite membrane is the alterable thermal expansion that enables a good TEC match with various suitable high toughness support materials, such as 3YSZ, or low cost support materials, such as MgO [29]. However, there are not many reports of large area dual phase membranes prepared with low membrane thickness as the processing of these dual phase membranes is more complicated than the single phase membranes.

Due to the chemical compatibility with ceria and high electrical conductivity, lanthanide strontium ferrites ($Ln_{1-x}Sr_xFeO_{3-\delta}$ Ln=La, Pr, Nd, Sm, Gd) were recently investigated as the electronic conductor in ceria based composite membranes [23, 30]. $La_{1-x}Sr_xFeO_{3-\delta}$ (LSF) is particularly interesting because it has high chemical stability [31]. According to tenElshof's [8, 32] and Søgaard's [33] early studies, LSF displays appreciable oxygen permeation fluxes at high temperature under both mildly (He, N_2) and strongly reducing (CO, H_2) atmospheres. Additionally, Sr-doped $LaFeO_3$ particles even catalyze CH_4 conversion [34], so LSF is a potential catalyst for the partial oxidation of methane. A CGO-LSF dual phase membrane consisting of percolating LSF and CGO is therefore expected to show a high oxygen flux because of its high mixed ionic and electronic conductivity, and be applicable for both wide pO_2 applications (syngas) and small pO_2 span applications (oxy-fuel combustion and oxygen production).

According to the Wagner's equation describing the transport of oxide ions and electrons, the oxygen permeation flux of a membrane is inversely proportional to its thickness, unless a surface exchange reaction fully or partially limits the oxygen evolution rate [35]. In light of that, membranes are often made as thin as possible (i.e., a few micrometers thick). To ensure their mechanical strength, thin membranes are commonly fabricated on porous substrates in a planar or tubular configuration *via* dip coating [36] and/or tape casting [37] techniques. The fairly novel technique, so-called "phase-inversion tape casting" [38], is able to fabricate membranes in an asymmetric configuration. By using phase-inversion tape casting, a planar structure with orientated finger-like pores in the substrate penetrating through the support, but not through the dense layer, can be produced in one-step casting without pore former [39]. The aligned finger-like pores produced by the technique are particularly favorable for gas diffusion, and can effectively mitigate gas diffusion resistance in OTMs, as well as in solid oxide fuel cells (SOFCs) [39-42]. Besides ensuring high gas permeability in the support, the manufacturing technique allows preparation of thin membranes; 20-100 µm layers on top a structural support.

This study reports the preparation of planar asymmetric CGO-LSF-based membranes by phase- inversion tape casting. The membranes of different effective surface areas (0.8 cm^2 and 16 cm^2) were tested under various oxygen partial pressure gradients (Air,O_2/He,CO_2 and Air/CO) to evaluate their possible applications for oxygen separation, oxy-fuel combustion and biomass gasification.

2. Experimental

2.1. Preparation of the membranes

The asymmetric membranes were prepared by phase-inversion tape casting. First, a polymer solution was prepared by mixing Polyethersulfone (PESF, 0.75 wt.%, Radel A-100, Solvay Advanced Polymers), polyvinylpyrolidone (PVP, 0.9 wt.%, K30, Sinopharm Chemical Reagent Co.) and N-methyl-2-pyrrolidone (NMP, 22.5 wt.%, CP, Sinopharm Chemical Reagent Co.). A mixture of $Gd_{0.1}Ce_{0.9}O_{1.95-\delta}$ (CGO) ultra-low surface area (ulsa) powder from Rhodia S.A. (53 wt.% corresponding to 70 vol.%) and $La_{0.6}Sr_{0.4}FeO_{3-\delta}$ powder (LSF Sigma Aldrich 20 wt%, corresponding to 30 vol.%) were then dispersed in the polymer solution. The polymer solution and the powder were mixed using high energy planetary ball milling for 48 h. Prior to tape casting, the as-obtained slurry was degassed under a vacuum for 10 mins to eliminate gas bubbles. The slurry was cast on a Mylar sheet by a doctor blade using a blade gap of 1.6 mm, followed by immersion in a water bath for ca. 12 hours to allow simultaneous phase-inversion and solidification to occur. The wet green tapes were dried in an oven at 80 ˚C under a small load (~20 g cm^{-2}) to ensure the flatness of the tape during the drying process. Dried tapes were heated to 800 °C at a rate of 2 °C min^{-1} for debindering and were subsequently sintered at 1300 ˚C for 10 hours in air.

2.2. Preparation of the catalytic layers

A porous catalytic layer of 70 vol.% $Gd_{0.1}Ce_{0.9}O_{1.95-\delta}$- 30 vol.% $La_{0.6}Sr_{0.4}FeO_{3-\delta}$ (CGO-LSF) or $La_{0.6}Sr_{0.4}CoO_{3-\delta}$ (LSC) was applied by screen printing on the permeate side of the membrane. The CGO-LSF ink was prepared by mixing CGO ultra-low surface area (ulsa) powder from Rhodia S.A. (53 wt.%) and $La_{0.6}Sr_{0.4}FeO_{3-\delta}$ (LSF40 Sigma Aldrich 20 wt%) with Alpha-Terpineol (AR. Sinopharm Chemical Reagent, Co.) A detailed description of the preparation of LSC powders is given elsewhere [38]. The LSC-ink was prepared by mixing the LSC powder with Alpha-Terpineol (AR. Sinopharm Chemical Reagent, Co.). The feed side was modified by infiltrating a precursor solution composed of stoichiometric amounts of nitrate for the nominal composition $La_{0.6}Sr_{0.4}CoO_{3-\delta}$ (LSC). Infiltrations were repeated five times, followed by calcination at 900 °C for 1 hour.

2.3. Scanning electron microscopy (SEM) and Transmission electron microscopy (TEM)

The microstructure and chemical composition were examined using a Hitachi TM3000 and a FE-SEM Zeiss Supera 35 electron microscope at a voltage of 15 kV. Furthermore, the membrane surface was checked for defects and pinholes by light microscopy and an ethanol leak-through test. After a stability test of the membrane described in detail below, scanning transmission electron microscopy (STEM) was performed with a JEOL 3000F equipped with a 300 kV FEG and high angle annular dark field detector by using a spot size of 0.7 nm and a camera length of 4 cm. Energy-dispersive X-ray spectroscopy (EDS) was carried out for compositional analysis using an Oxford Instruments detector with an ultra-thin window. The analysis was performed using the Inca software. The tested sample was prepared for the STEM analysis by scratching of material from the dense membrane side with a tweezer and grinding it to a fine powder in a mortar with ethanol. A droplet of the suspension powder was placed on a TEM copper grid with a holey carbon film.

2.4. X-ray computed tomography (CT) scans

X-ray computed tomography (CT) scans were conducted on the CGO-LSF membrane with a lab-based Xradia Versa XRM-410 instrument using a W reflection target at a power of 10 W. The scan was performed at a voltage of 150 kV, with an HE03 filter (Xradia), 10× optical magnification, binning 4, an exposure time of 4 s and a total of 1601 projections over a 360° rotation, resulting in a pixel resolution of 3.8 μm. The thickness of the scanned samples was 1.0 mm. The sample width was approximately 0.7 mm, but varied with the sample height. The recorded data were reconstructed using a Feldkamp-Davis-Kress reconstruction with a smooth filter (0.5 kernel size) and beam hardening constant of 0.3. After reconstruction, segmentation was performed, separating membrane solids and pores by using global thresholds with the software Avizo fire 8.0 (for the total 3D pore volume) and ImageJ (for 2D pore diameters and pore density). The 2D image stack was filtered in ImageJ with a mean filter (radius = 3 pixels) prior to the segmentation. Additional segmentations were performed to estimate errors in the quantitative analysis. Here the segmented volumes were grown to make the volumes of the solid and pores as small or as large as possible without introducing obvious errors. The additional segmentations therefore represent the lower and upper limits of the quantitative X-ray CT analysis.

2.5. X-ray powder diffraction (XRD)

The membrane crystal structure was characterized by X-ray powder diffraction (XRD). The sample was ground in a mortar, and the XRD was carried out using a Bruker Robot advanced running in Bragg-Brentano geometry with Cu Kα1 in a 2θ range from 20° to 90°. The obtained XRD patterns were indexed and compared with an ICCD database (International Centre for Diffraction Data) using the software DIFFRAC plus. The lattice parameters and theoretical density of each specimen was calculated by Rietveld refinement of the XRD patterns using the software WINPOW.

2.6. Electrical conductivity relaxation (ECR)

Electrical conductivity relaxation (ECR) was conducted using a standard 4-point technique on a sample with dimension of 1.210×0.182×0.180 cm^3. Prior to measurements, the bar-like sample was polished with diamond 9-μm paste. The relative density of the sample was measured by Archimedes method (ρ=6.57 g cm^{-3}), exceeding a relative density of 95%. Four Pt wires were placed on four separate spots on the bar-like sample. The electrical conductivity of the sample was measured under a constant voltage (1 V). The sample was mounted in a quartz tube with small volume in which the gas flow rate was controlled using mass flow controllers (Brooks). The oxygen partial pressure in the vicinity of the sample was monitored by an *in-situ* zirconia based oxygen sensor. The tube volume and follow controllers allowed change of the gas volume within 10 s.

2.7. Oxygen flux measurements

A schematic illustration of the applied oxygen permeation test setup for circular membranes is shown in Figure 1a. The circular asymmetric membranes were initially mounted on an alumina tube and sealed with a glass sealant at 1050 °C. The finger-like pores in the supporting layer were exposed to ambient air (feed side) and either pure He or CO were used as the sweep gas on the dense side (permeate side). Accurate determination of the flow rates for the inlet and outlet gases were achieved by calibrating the flow controllers versus a soap film flowmeters prior to the membrane test. The gas composition of the effluent stream on the permeate side was measured by an online gas chromatography (GC 9750, FuLi, China). The GC was equipped with a thermal conductivity detector and two chromatographic columns - one was filled with 60-80 mesh GDX-502 for detecting CO and CO_2 and the other was filled with 60-80 mesh 5A molecular sieves for detection of N_2 and O_2. The oxygen permeation fluxes under the gradient of air/He and air/CO were calculated by Eq. 1 and 2, respectively:

$$J_{O_2} = \dot{N}\left(C_{O_2} - 21/79\,C_{N_2}\right)/A \quad (1)$$

$$J_{O_2} = \dot{N}\left(0.5C_{CO_2} + 0.5C_{O_2} - 21/79\,C_{N_2}\right)/A \quad (2)$$

where $\dot{N}$ represents the flow rate of the effluent gas, C_{O2} is the concentration of the oxygen in the effluent gas, C_{N2} is the concentration of leaked N_2 from air, 21/79 C_{N2} is the corresponding concentration of leaked oxygen, and A is the effective surface area exposed to the sweep gas. (Eq. 2 applies to the case of pure CO inlet stream only) Any leakage of oxygen through the glass sealant or the membrane was evaluated by measuring the concentration of nitrogen. The leaked oxygen flux implied by the leaked nitrogen was subtracted from the measured oxygen flux (see the Supporting Information, Figure S4). The leaked oxygen flux was less than 1% of the resultant flux. For an air/He gradient, the oxygen partial pressure (pO_2) of the effluent gas is equivalent to the oxygen concentration. Under an oxygen partial pressure difference of air/CO across the membrane, the partial pressure of CO_2 (pCO_2) and CO (pCO) were calculated as $P_{CO}=P_{tot}x_{CO}/(x_{CO}+x_{CO2}+x_{O2})$ and $P_{CO2}=P_{tot}x_{CO2}/(x_{CO}+x_{CO2}+x_{O2})$, respectively, where x_{CO}, x_{CO2} and x_{O2} are the measured concentrations of CO, CO_2 and O_2, respectively. p_{tot} is the total gas pressure. pO_2 is the calculated oxygen partial pressure using the commercial software HSC Chemistry 5 assuming equilibrium of the chemical reaction: $CO(g)+1/2\,O_2(g)=CO_2(g)$.

A modified test house previously used for planar solid oxide cell tests was used for the test of 5×5 cm^2 planar membranes. The schematic of the setup is shown in Figure 1b. The membranes were sealed using 30/70 vol.% MgO/sodium aluminosilicate glass tapes together with two Fe/Cr alloy frames on the alumina test house. A weight load (2 kg) was applied to ensure a good sealing. The feed side was flushed with air/O_2 with a constant flow rate of 600 Nml min^{-1} and the permeate side was flushed with various flows of N_2/CO_2. The flow of gases was monitored by mass flow controllers. The net oxygen permeation flux can be deduced from the pO_2 difference between inlet and outlet gases flowing through the permeate side. The pO_2 of inlet and outlet gases is precisely monitored by two YSZ-based oxygen sensors. The oxygen permeation flux of the membrane may be written

$$J_{O_2} = \dot{N}\left(x_{O_2}^{out} - x_{O_2}^{in}\right) \Big/ A \tag{3}$$

where $x_{O_2}^{in}$ and $x_{O_2}^{out}$ denote molar fraction of inlet and outlet oxygen, respectively. $\dot{N}$ represents the molar flow rate of outlet gases. The oxygen partial pressures are calculated *via* the Nernst equation from the e.mf measured with the zirconia sensors placed up-stream and down-stream the membrane.

$$E = RT \Big/ 4F \ln\left(pO_2 \Big/ pO_{2,ref} \right) \tag{4}$$

where E is the open circuit voltage of the oxygen sensor. R is the gas constant. $pO_{2,ref}$ is the oxygen partial pressure at reference electrode which retains at 0.21 bar, T is the temperature of the senor. The leak in the system was assessed by means of a mass flow meter on the permeate stream. When a perfect sealing is achieved, the outlet gas flow rate should be equivalent to the inlet flow. If there are leaks in the membrane or pinholes or cracks in the glass encapsulation, the flow rate of the outlet gas (N_2) will be lower than that of the inlet gas. In this work, the inlet and outlet sweep gas flow is identical when N_2 was used as the feed gas, indicating a good sealing.

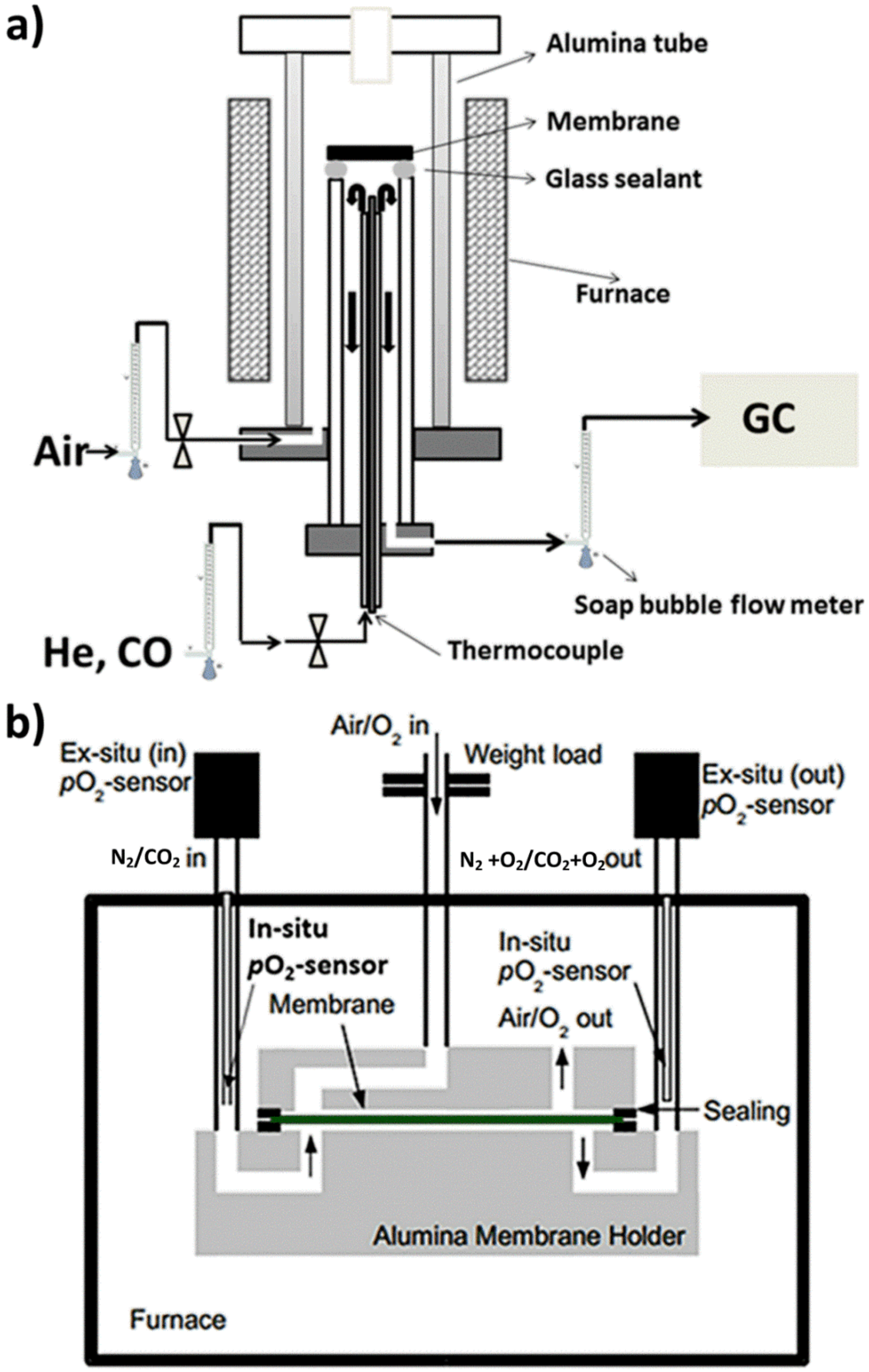

Figure 1. Schematic illustration of the experimental setup used for oxygen permeation measurement of (a) circular CGO-LSF asymmetric membranes and (b) square 5×5 cm^2 membranes.

3. Results and discussions

3.1. Microstructure of the asymmetric CGO-LSF membranes

Figure 2a-d presents (a) a volume rendering and (b) orthogonal slices in the 3D reconstruction of the membrane based on the X-ray CT scan. A thin dense part (left side) and thicker porous part with elongated pores (right side) was observed. Slices in the 3D reconstruction show that the individual pores are cylindrical, with roughly circular cross sections of varying diameter (Figure 2b). Deviations from circular geometry are observed where pores are in contact with each other and in a few instances where cracks have formed between pores. Figure 2c shows a segmentation of the pores and here the finger-like structure is more clearly seen. Note that the finger-like pores are relatively straight all of the way through the support (as shown also in Video S1 in Supporting Information), yielding a low tortuosity for the gas diffusion ($\tau \approx 1$). The pore volume calculated from the segmentation (Figure 2c) is 22 ± 5 %. From 2D slices in the 3D data, the mean pore diameter was measured as a function of the distance from the dense surface (Figure 2d black). The mean pore diameter is ca. 90 µm in the center of the component and drops to ca. 40 µm at the porous surface of the support. Similarly, the density of the 2D pore area was measured and found to be approximately constant (ca. 20 - 30 %) from the porous surface and ca. 600 µm into the membrane, after which it dropped to zero in the dense region. The unique structure is expected to be highly favorable to the gas transport, which is quantitatively elucidated by flux measurements reported in section 3.7. Figure 2e-h shows the SEM micrographs of the membrane infiltrated with LSC solution on the porous feed side and the CGO-LSF catalytic layer applied on the dense permeate side. In Figure 2f, the catalyst layer is the dark layer in the lower part of the image (ca. 20 µm thick). The dense region is not fully dense but contains closed voids at the nanoscale. The voids remain from the sintering and reflect the challenge in simultaneously sintering two phases with slightly different sintering curves to full density. Figure 2g shows the inner surface of a pore and the nano-porous structure of the infiltrated catalyst. An EDS spectrum recorded at a point inside the pore (as indicated in Figure 2h) shows signals originating from La, Sr, Co, Fe and Gd. The Co signal is consistent with presence of the LSC infiltration; the Fe and Gd signal originates from the membrane, and the La and Sr signal can originate from either the membrane or the infiltrate. Based on Figure 2g-h, the feed side of the membrane is considered to be finely decorated by the infiltrated LSC catalyst. Figure 2i-j illustrate a sintered 5.8×5.8 cm^2 square membrane and a circular membrane (area≈1.5 cm^2), respectively. The shining flat surface of the membranes suggests that the membranes are relatively dense.

3.2. Crystal structure and bulk composition

Figure 3 shows XRD patterns of the CGO and LSF powders and a powder obtained by crushing a piece of a CGO-LSF membrane (sintered at 1300 °C). The XRD patterns indicate that the dual phase system merely consists of cubic fluorite structured CGO (space group No. 225: *Fm3m*) and perovskite structured LSF (space group No. 167: *R-3c*). The presence of secondary phases that might arise from the reaction between LSF and CGO cannot be detected within the resolution limit. It also indicates that the co-existence of CGO and LSF is chemically stable in air, as also reported for a similar system of $Ce_{0.8}Sm_{0.2}O_{2-\delta}$–$La_{0.9}Sr_{0.1}FeO_{3-\delta}$ (SDC-LSF) composites [24]. The unit cell parameters and unit cell volume obtained by the Rietveld refinement are given in Table S1 of the Supporting Information. The lattice parameter of CGO (a: 5.42710 Å) in the composite is larger than that of pure CGO (a=5.41841 Å), whereas the lattice parameter of LSF in the composite (a=b=5.51759 Å, c=13.4985 Å) is slightly lower than that of single phase LSF (a=b=5.52496, c=13.4968 Å). Similar studies on a $Gd_{0.1}Ce_{0.9}O_{2-\delta}$-$La_{0.6}Sr_{0.4}Co_{0.2}Fe_{0.8}O_{3-\delta}$ (CGO-LSCF) composite reported that the expansion of the CGO lattice is associated with the diffusion of large La and Sr cations from the $La_{0.6}Sr_{0.4}Co_{0.2}Fe_{0.8}O_{3-\delta}$ grains into the fluorite [43] , which may also be the reason for the slight lattice expansion of the CGO lattice (0.16%) observed here.

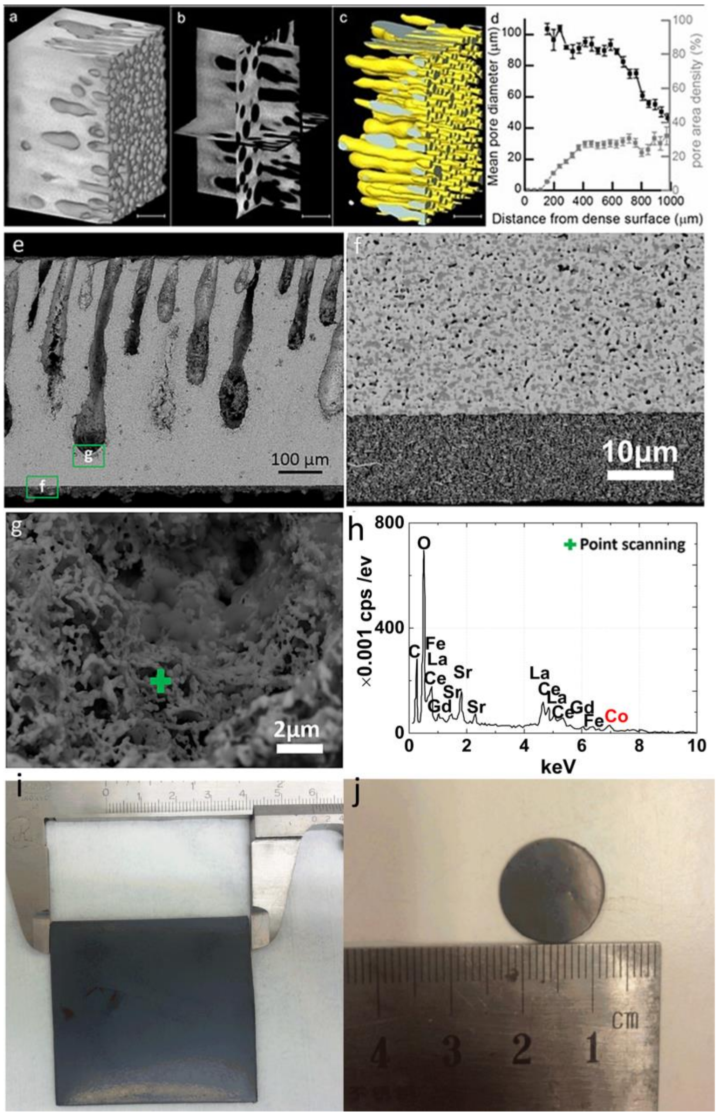

Figure 2. (a) A volume rendering and (b) ortho slices of the 3D reconstruction of the X-ray CT data from a scan of the asymmetric CGO-LSF membrane without the catalytic layer. (c) The segmented pore volume. (d) The mean pore diameter and the pore area density for several 2D slices in the 3D dataset presented as a function of the distance from the dense membrane surface. The error bars indicate the estimated error in the segmentation. Scale bars in (a-c) equal 200 μm. (e) A back-scattered SEM micrograph of a cross-section of the CGO-LSF asymmetric membrane with the catalyst on the porous feed side (LSC infiltration) and the dense permeate side (CGO-LSF coating). (f) A close up of the region “f” in (e). (g) A close up of the region “g” in (e). (h) EDS spectrum from the point in (g) is marked with a green cross. Image of the dense side of (i) a 5.8×5.8 cm^2 square and (j) a circular membrane.

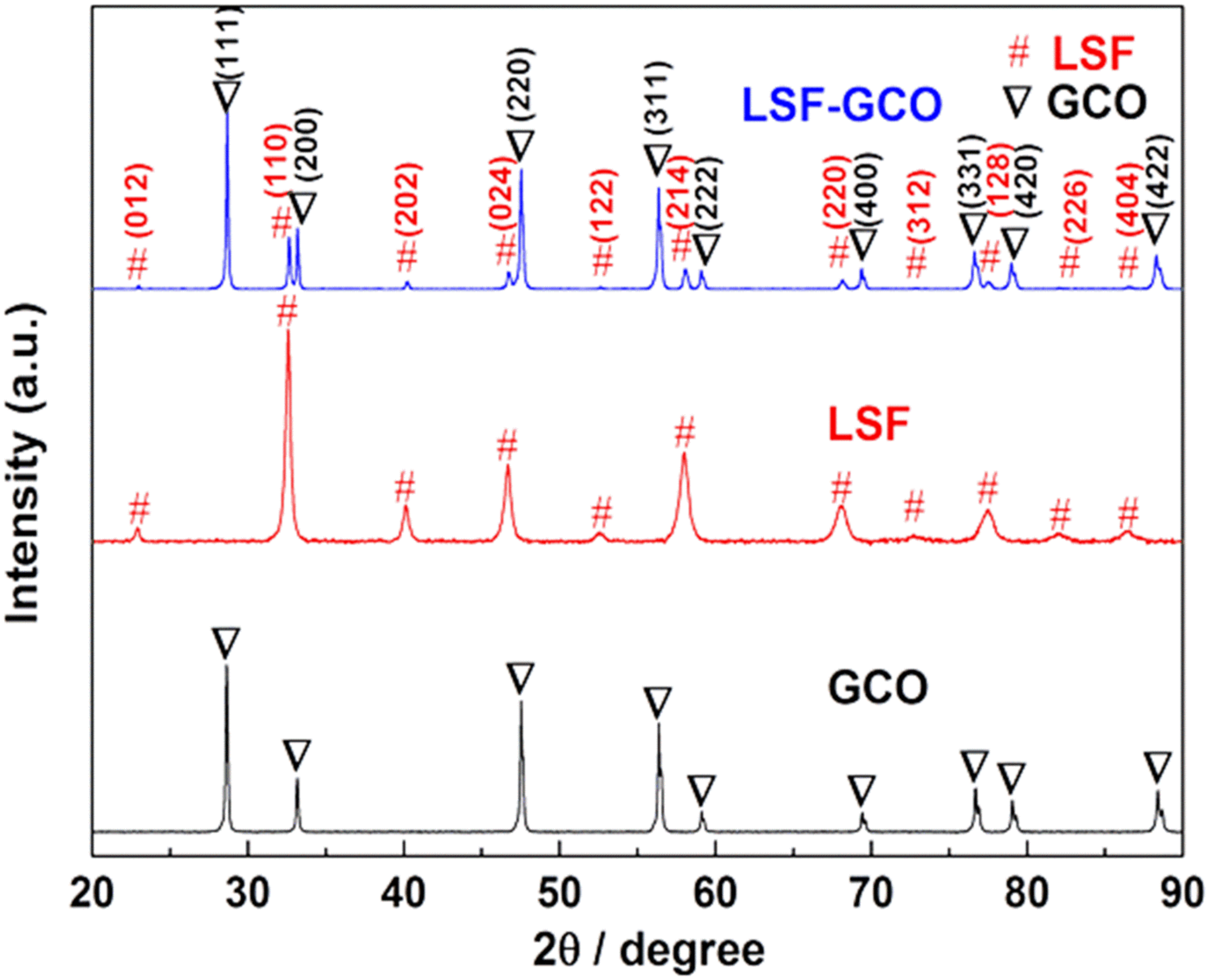

Figure 3. XRD patterns of powders of pure CGO and LSF and crushed sintered CGO-LSF membrane. Reported patterns for (▽) $Gd_{0.1}Ce_{0.9}O_{1.95-\delta}$ and (#) $La_{0.6}Sr_{0.4}FeO_{3-\delta}$ are indicated by symbols in the figure.

3.3. Electrical conductivity of the CGO-LSF composites

Figure 4 shows the total conductivity of LSF [33], CGO [44] and a CGO-LSF composite as a function of the oxygen partial pressure at 900 °C, in comparison with the calculated conductivity of CGO-LSF using the Bruggeman-Landauer (BL) effective medium model [45] for three different coordination numbers (the detailed calculation is given in Supporting Information, section 3). According to the BL model, the conductivity of CGO-LSF is expected to lie between the conductivities of the two phases. Consistent with this, the CGO-LSF shows increasing conductivity under high oxygen partial pressure, indicating that the CGO-LSF is dominated by the p-type electronic conductivity through a percolating LSF phase. The conductivity of the CGO-LSF composite also shows the expected pO_2 dependence under a low oxygen partial pressure; with decreasing pO_2 ($pO_2<1\times10^{-13}$ bar), the conductivity of the CGO-LSF increases, indicating a dominant n-type electronic conductivity. Compared to CGO, CGO-LSF possesses slightly lower n-type electronic conductivity at low pO_2. This is due to the partially blocked electrical conductivity of CGO by the neighboring low electrical conductivity LSF (at this pO_2).

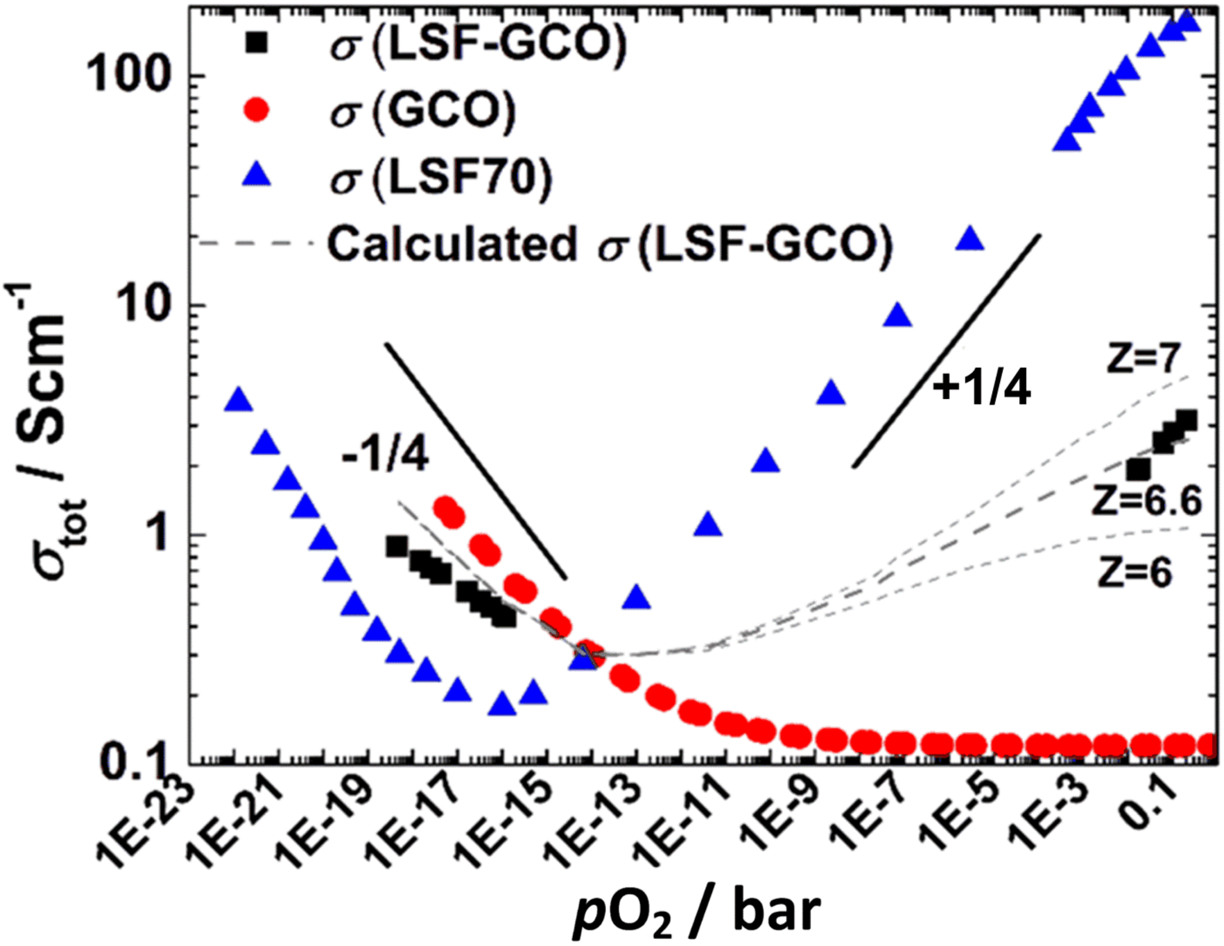

Figure 4. Total measured conductivity of the CGO-LSF composite (black) prepared in this study compared with reported values for LSF (blue) [33] and CGO (red) [44] as a function of the oxygen partial pressure at 900 °C. The dashed line represents the calculated total conductivity of CGO-LSF composite in terms of the symmetric Bruggeman-Landauer effective medium model.

It is evident that a small change in the value of Z (the number of nearest neighboring grains), leads to a significant variation in the calculated conductivity for a pO_2 above 1×10^{-9} bar. The best consistency between the calculated and measured conductivity is achieved with Z=6.6, which approaches the coordination number (Z=6) proposed by Wu and Liu [46]. The percolation threshold predicted from the model with this coordination number would be 30.3 vol.%, which is close to the used volume fraction in the composite (30 vol.%). Keeping the electronic conductor LSF volume fraction close to its minimum value will maximize the oxide ion conductivity because the low ionic conductivity of LSF in this work leads to a more tortuous path for oxide ions [47]. The amount of electronic conductor needed to ensure percolation in composites has been investigated in several studies. For instance, Seeharaj *et al.* reported that percolation could be achieved already at 20 vol.% of the $La_{0.6}Sr_{0.4}CoO_{3-\delta}$ for $Ce_{0.9}Gd_{0.1}O_{2-\delta}$ - $La_{0.6}Sr_{0.4}CoO_{3-\delta}$ (CGO-LSC) composites [48]. Joo *et al.* reported a threshold (20 vol.%) for a $Gd_{0.1}Ce_{0.9}O_{2-\delta}$ - $La_{0.6}Sr_{0.4}MnO_{3\pm\delta}$ (CGO-LSM) composite where the oxygen flux is also maximized [49]. Pippardt *et al.* [50] used a bond percolation model to interpret a surprisingly low percolation threshold of 10 vol.% in a $Gd_{0.2}Ce_{0.8}O_{1.9-\delta}$-$MnCo_{1.9}Fe_{0.1}O_4$ composite membrane.

In contrast with for instance studies on In contrast with for instance studies on $BaCe_{0.2}Zr_{0.7}Y_{0.1}O_{3-\delta}/Sr_{0.95}Ti_{0.9}Nb_{0.1}O_{3-\delta}$ (BCZY-STN) [51], the satisfactory consistency between the calculated and measured conductivity observed here for CGO-LSF suggests that there are no detrimental interfacial chemical reactions between the two phases nor any deterioration of the intrinsic properties of the two materials due to interdiffusion.

3.4. *Surface exchange coefficient (k_{ex}) and chemical diffusion coefficient (D_{chem}) of CGO-LSF*

Figure 5a-c shows the normalized ECR plots and fitted data as a function of time in an oxidizing and a reducing atmosphere in the temperature range from 750 °C to 950 °C occurring in a mixture of either

CO_2/O_2 or CO_2/CO, respectively. The general trend of the overall ECR results is that equilibrium is reached faster with increasing pO_2.

The solid red lines in Figure 5a-c represent the best least square fit with Eq. S1 in Supporting Information, where the surface exchange coefficient, k_{ex}, and D_{chem} have been used as fitting parameters. The surface exchange coefficients k_{ex} and chemical diffusion coefficients, D_{chem}, of CGO-LSF obtained by curve fitting at 900 °C are summarized and compared with relevant materials in Table 1. Søgaard *et al.* [33] reported that D_{chem} of LSF scales with the oxide ion conductivity $\sigma_{O^{2-}}$ and oxygen diffusion coefficient $D_{O^{2-}}$: ($D_{chem} = \gamma D_{O^{2-}}$, $\gamma = d\ln pO_2 / 2t_e d\ln C_O$, $D_{O^{2-}} = \sigma_{O^{2-}} Tk / 4e^2 C_O$, where C_O is the oxide ion concentration, t_e is the electronic transference number and k is the Boltzmann constant). We find that the effective D_{chem} of the CGO-LSF composites is significantly higher than that of LSF under the same experimental conditions, which is likely due to the higher oxide ion conductivity ($\sigma_{O^{2-}}$) contributed by CGO in the composite. More surprisingly, the k_{ex} of CGO-LSF is found to be higher that of pure LSF. Similar effects have been reported in recent studies of composites [52].

Figure 5d shows the Arrhenius plots of k_{ex} and D_{chem} of CGO-LSF under oxidizing and reducing conditions. The D_{chem} values under the two different atmospheres are very similar, as is the apparent activation energy. This is due to the invariable ionic conductivity of CGO over the investigated pO_2 range. (σ_{CGO} (0.01bar)=0.13 Scm^{-1} and σ_{CGO} (1×10^{-14} bar)=0.14 Scm^{-1}) [44, 53] Unlike D_{chem}, the effective k_{ex} values under the two atmospheres and the corresponding apparent activation energies show considerable difference. The k_{ex} value under reducing conditions is less temperature-dependent than under oxidizing conditions.

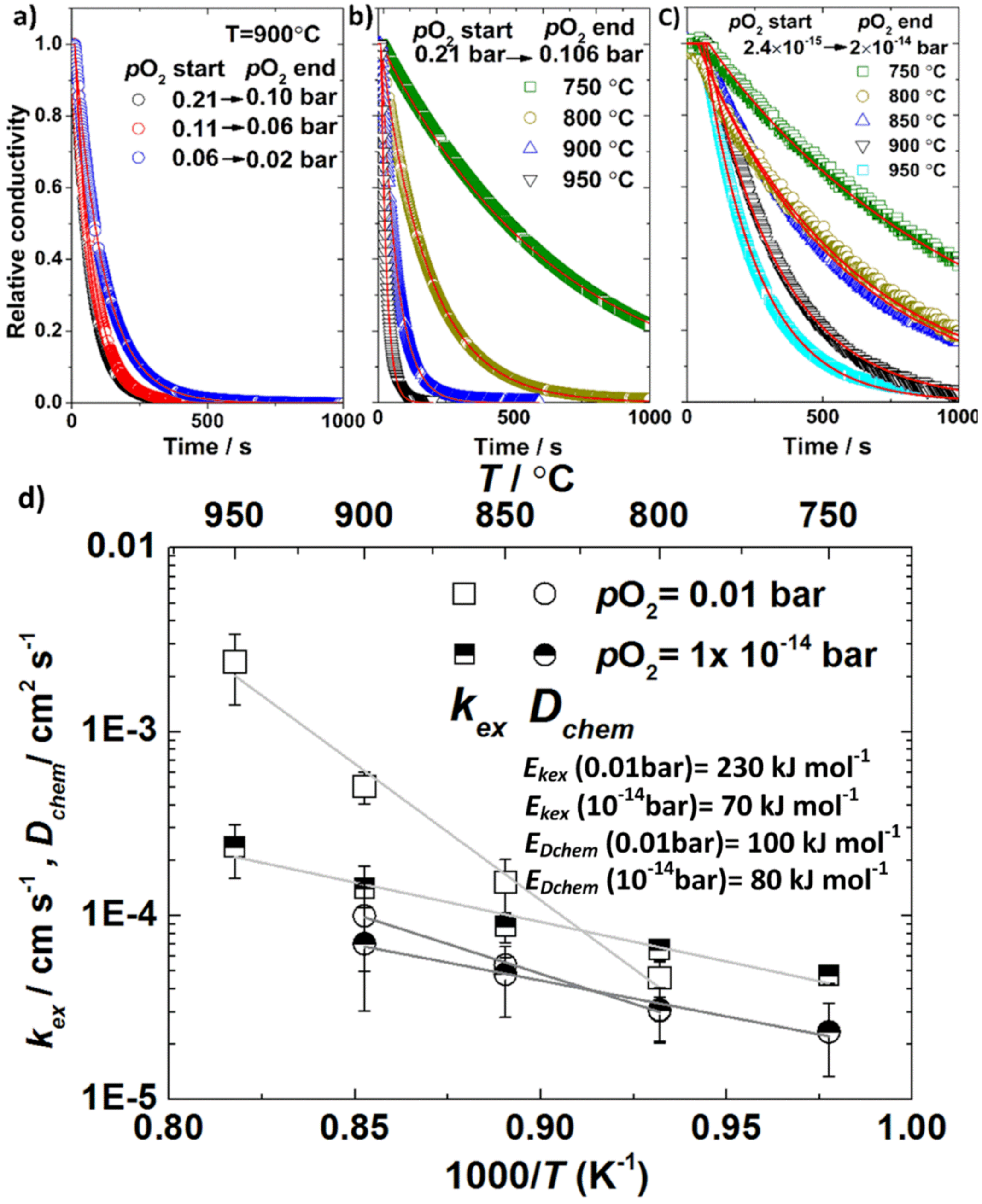

Figure 5. Normalized ECR plots for CGO-LSF in (a-b) O_2/CO_2 and (c) CO/CO_2 at (a) constant temperature of 900 ºC and pO_2 in the range of (b) 0.21 to 0.02 bar and (c) from 2.4×10^{-15} to 2.0×10^{-14} bar. The solid red lines represent the best least squares fit to Eq. S1 in Supporting Information, where k_{ex} and D_{chem} have been used as the fitting parameters. (d) k_{ex} and D_{chem} as a function of inverse temperature based on ECR curves.

The characteristic thickness (L_c) in Table 1 is calculated as $L_c \approx fD_{chem}/k_{ex}$ where f is the correlation factor which is fixed to be ~0.69 [54]. The estimated characteristic thickness of the CGO-LSF at a high pO_2 is much larger than that for most electrocatalytic single-phase perovskite materials, which typically have values in the range of 100 to 200 µm [55]. The large L_c value of CGO shows that oxygen permeation of a pure CGO membrane would tend to be limited by surface exchange. The L_c values of the composites are as expected found to lie between those characteristic thicknesses of CGO and LSF. The fairly large L_c values of the composite implies that the thin CGO-LSF membrane (100 µm) would tend to be more rate-limited by surface exchange compared with these single-phase perovskite materials. This will be discussed further in section 3.5.

Table 1. Oxygen diffusion coefficient (D_{chem}), surface exchange coefficient (k_{ex}) and estimated characteristic thickness (L_c) of the samples.

Material	**T (°C)**	D_{chem} **(cm² s⁻¹)**	k_{ex} **(cm s⁻¹)**	pO_2 **(bar)**	L_c **(cm)**
CGO-LSF	900	2.2×10^{-4}	9.6×10^{-4}	0.11	0.16
CGO-LSF	900	1.6×10^{-4}	5.0×10^{-4}	0.01	0.22
LSC[56]	900	3.2×10^{-5}	4.0×10^{-3}	0.03	0.005
LSF[57]	900	2.0×10^{-5}	3.0×10^{-4}	0.01	0.05
CGO[58]	900	n/a	n/a	0.94	~3.33
$La_{0.9}Sr_{0.1}FeO_{3-\delta}$ [59]	900	1.2×10^{-5}	3.1×10^{-4}	0.01	~0.03

3.5. Oxygen permeation fluxes (O_2, air/ N_2, He and CO_2-gradients)

The oxygen flux of the asymmetric circular CGO-LSF membrane (effective surface area=0.8 cm^2) with and without catalyst layers was measured as a function of temperature under a wide range of oxygen partial pressure gradients with the pO_2 on the permeate side ranging from 0.01 bar to 1×10^{-20} bar. In addition, planar 5×5 cm^2 CGO-LSF membranes with catalysts (feed side: infiltrated LSC, permeate side: porous CGO-LSF composite layers) with an active area of 4×4 cm^2 were also tested in air/N_2- and air/CO_2-gradients.

Figure 6 shows Arrhenius-type plots of the oxygen fluxes through the asymmetric CGO-LSF membranes with and without catalysts when the porous support (feed side) was exposed to air and the dense side (permeate side) to a 30 ml cm^{-1} flow of pure He. The fluxes of 5×5 cm^2 CGO-LSF membranes measured in air/N_2, CO_2-gradients are also plotted. Details of samples (catalyst, effective area and gas flows) are summarized in Table 2. The measured oxygen flux without the catalytic layers (0.06 ml cm^{-2} min^{-1} at 900 ^{o}C, Nr.1a) is much lower than the calculated flux for a 100 μm CGO-LSF membrane (Nr. 6, the detailed calculations are found in the Supporting Information) by more than one order of magnitude. The calculated oxygen flux (Nr. 6) is the ideally achievable flux solely determined by bulk ambipolar diffusion. Moreover, the apparent activation energy of the flux (171 kJ mol^{-1}, Nr. 1) lies closer to that of surface exchange coefficient (230±30 kJ mol^{-1}) rather than to that of bulk diffusion (64 $kJmol^{-1}$, Nr. 6), suggesting that the flux of the non-coated membrane is limited by the surface exchange. To describe in an approximate way the oxygen flux in the case of non-negligible losses at the surfaces, a modified Wagner's equation (Eq. 5) has been adopted, [35, 55]

$$J_{O_2} = \frac{1}{1+2L_c/L}\frac{RT\sigma_i}{16F^2L}\ln\left(p_{O_2}^{/}\Big/p_{O_2}^{//}\right) \qquad (5)$$

where R is the gas constant, F is the Faraday constant, L is the thickness of the membrane, σ_i is the ionic conductivity, $p_{O_2}^{/}$ is the oxygen partial pressure on the feed side and $p_{O_2}^{//}$ is the oxygen partial pressure on the permeate side. The factor $\left(1+2L_c/L\right)^{-1}$ (rather than 1 in Wagner's equation) can be thought of as a correction term to approximate the effects or finite surface exchange rate. Under a given apparent driving force ($\ln(pO_2'/pO_2'')$), L_c can be deduced from the measured flux and the max obtainable flux as

$$J_{O_2 measured} \big/ J_{O_2 bulk} = \left(1+2L_c/L\right)^{-1} \qquad (6)$$

where $J_{O_2 measured}$ is the measured flux, $J_{O_2 bulk}$ is the calculated flux in case of no surface limitation. The L_c-values of the CGO-LSF membranes deduced from the oxygen flux measurement and the ECR are compared in Figure 7. It is evident that the L_c deduced by ECR measurements and Eq. 6 are fairly close and more than 20 times the thickness of the dense membrane (100 µm), further confirming that the oxygen flux through the non-coated CGO-LSF is limited by surface exchange.

Compared to the asymmetric membrane without a catalyst, the membrane with a catalyst on both sides (LSC) displays a flux higher by one order of magnitude (1.41 ml cm^{-2} min^{-1} at 900 °C, Nr. 5). Furthermore the application of the surface catalysts leads to a reduction of the apparent activation energy (86.2 kJ mol^{-1}, Nr. 5). This suggests that the surface catalyst layers have effectively reduced the losses of chemical potential ($\Delta\mu_{O2}$) at the surfaces and that the flux is now in a regime of mixed control where losses at the surface and in the bulk are comparable. Nevertheless, the highest experimentally measured flux is still less than the calculated flux, further illustrating the mixed control. Applying a LSC layer on the dense permeate side of the membrane (Nr. 5) yields a ten-fold increase of the flux compared to a membrane solely infiltrated with LSC on the feed side (Nr. 2a), illustrating that surface losses are dominated by the permeate side. A similar observation was reported for a $Gd_{0.1}Ce_{0.9}O_{1.95-\delta}$-$La_{0.6}Sr_{0.4}Co_{0.2}Fe_{0.8}O_{3-\delta}$ asymmetric membrane prepared using the same method [38]. A surface catalyst is thus more important for the flux when applied on the low pO_2 side than on the high pO_2 side, which is consistent with the ECR measurements showing that k_{ex} decreases with decreasing pO_2, as shown in

Figure S3a of Supporting Information. Noticeably, the membrane coated with a CGO-LSF dual phase catalytic layer (Nr. 3a) shows a slightly lower flux compared to the membrane coated with LSC (Nr. 5). This is due to the larger surface exchange coefficient of LSC which serves as a better electrocatalyst in oxidizing condition.

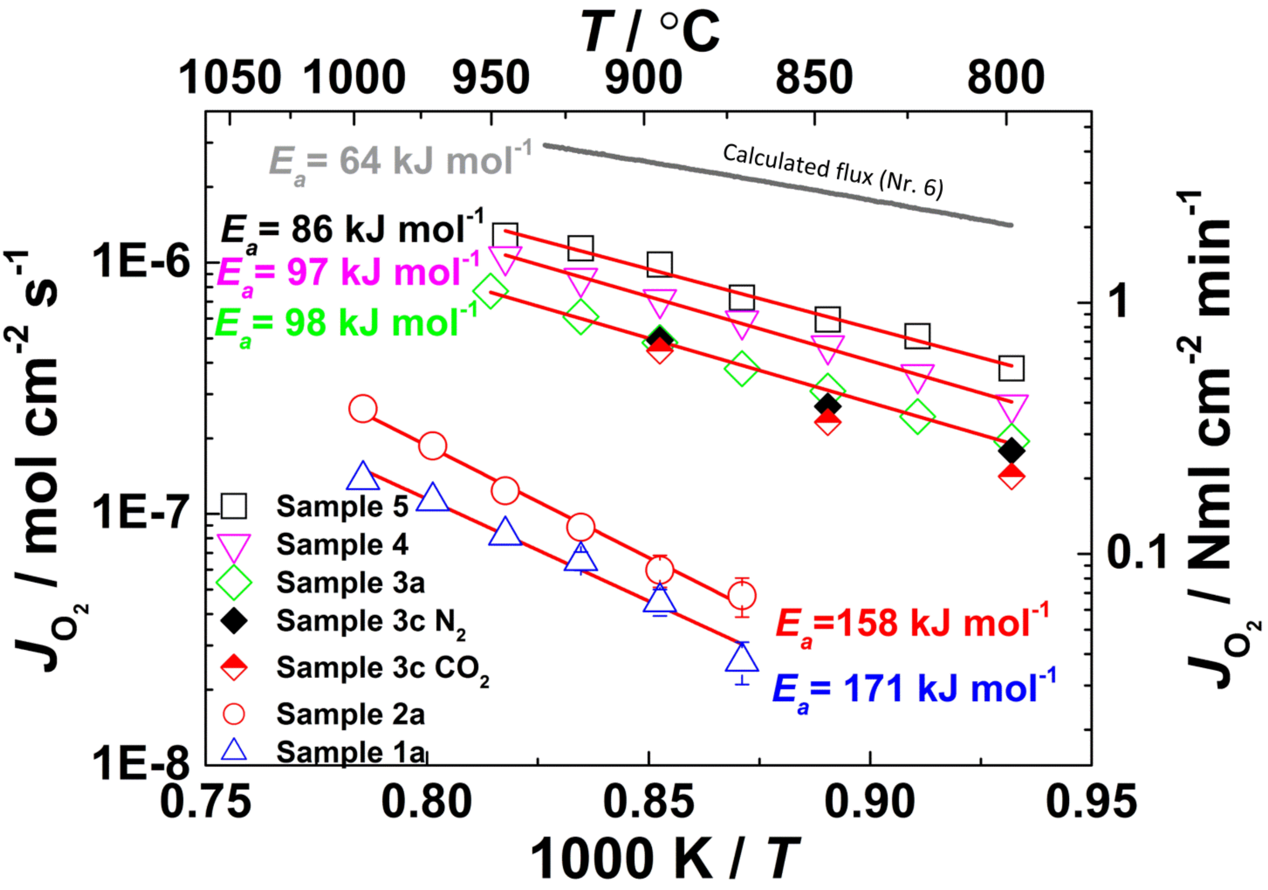

Figure 6. Arrhenius plots of the oxygen permeation flux of asymmetric CGO-LSF membranes measured under a gradient of Air/He, CO_2 as a function of inverse temperature. The calculated flux of a 100-µm thick CGO-LSF membrane (grey solid curve) is estimated based on Samson *et al.*[47] (see Supporting Information, Figure S1). The flux of Sample 3c are obtained under $\ln(pO_2'/pO_2'')\approx 3$

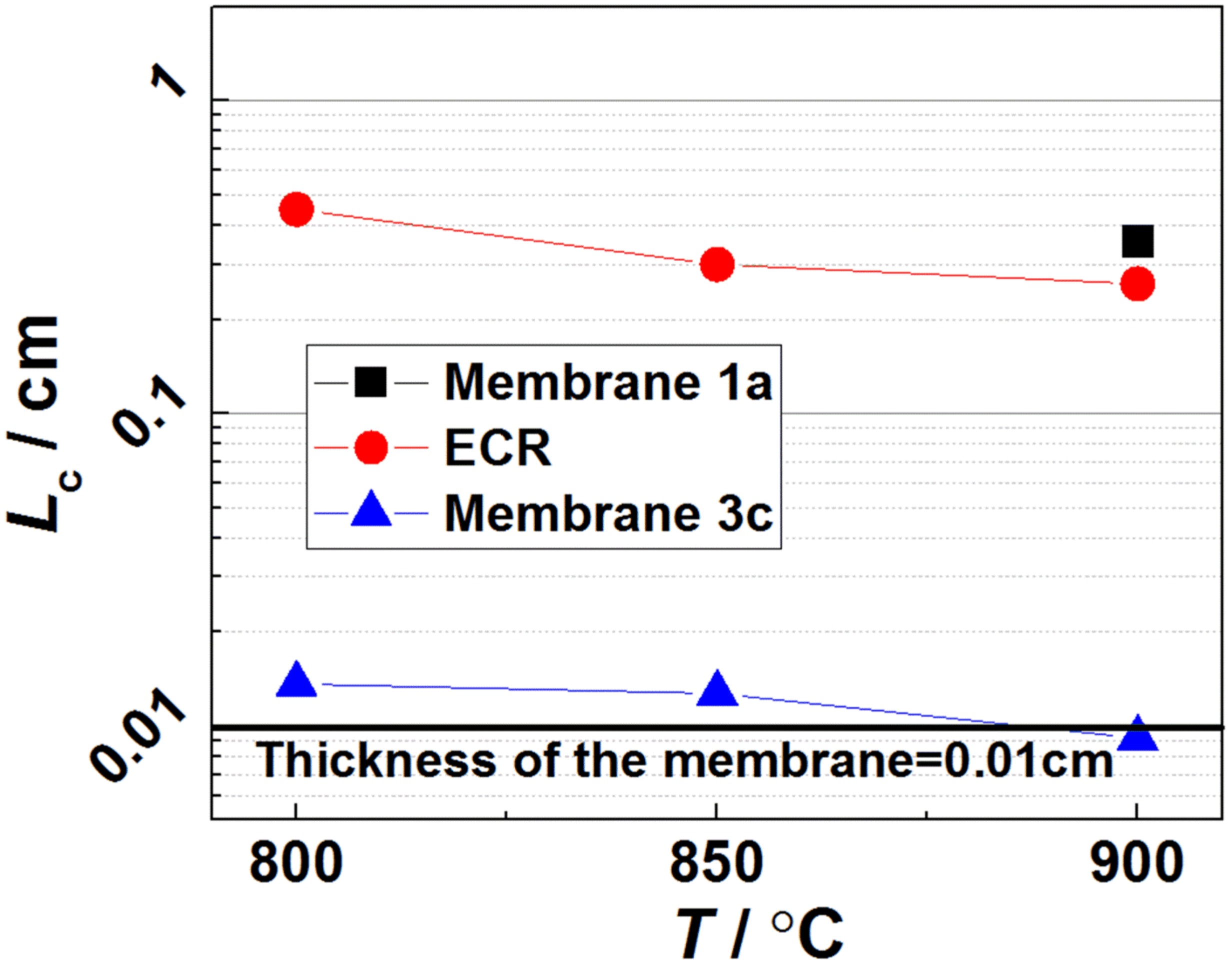

Figure 7. Characteristic thickness (L_c) of the membrane obtained by Eq. 6 and ECR as a function of temperature.

It is noteworthy that the oxygen flux through the 5×5 cm^2 membrane (Nr. 3c) is very close to that of the circular membrane from 800 °C to 900 °C, indicating a good reproducibility and the potential of the membrane for upscale. The L_c (Figure 7) of the membrane with CGO-LSF coating (Nr. 3c) is decreased by more than one order of magnitude compared to that of the non-coated membrane (Nr. 1a) and is comparable to the thickness of the membrane (100 µm). It can also be observed that the oxygen flux measured using CO_2 (Nr. 3c) as the sweep gas is slightly lower than that measured using N_2 or He. A similar phenomenon is reported in other studies of OTMs [6, 28, 60-62]. The phenomenon is proposed to be due to suppressed oxygen surface exchange rate due to the chemisorption of CO_2 on the surface of the activation layer (CGO-LSF) possibly due to occupation of oxygen vacancies by the oxide ions of CO_2 [61].

3.6. Oxygen permeation fluxes between air and CO/CO_2

Figure 8 shows Arrhenius-type plots of the oxygen permeation fluxes through the asymmetric CGO-LSF membranes with (Nr. 3b) and without catalysts (Nr. 1b) when the porous support (feed side) was exposed to air and the dense side (permeate side) to a 30 ml min^{-1} flow of pure CO. The flux measured under air/CO-gradient (Nr. 3b) is more than an order of magnitude higher than that measured under air/He-gradients (Nr. 3a). This is primarily attributed to the larger driving force across the membrane under air/CO-gradient (emf≈1.02 V at 900°C) than that under air/He-gradient (emf≈0.18 V at 900°C). It is noteworthy that the activation energy of the membrane flux without a catalyst is close to that of the oxygen surface exchange characterized under similar experimental conditions (75±20 vs.101.4 kJ mol^{-1} in Table 2), suggesting that the flux is rate-limited by the oxygen surface exchange on the permeate side in the CO/CO_2 mixture. Similar to the flux in air/He-gradients, the flux is not sensitive to the impregnation with LSC on the feed side (Nr. 2b vs. Nr. 1b) where only a slight enhancement of the flux is observed. When the permeate side is coated by a catalyst (CGO-LSF, Nr. 3b), the flux is profoundly enhanced at low temperatures. tenElshof *et al.* reported that the oxygen flux of a LSF membrane under air/CO-gradients is enhanced by the deposition of a Pt layer, which enhances the CO oxidation reaction rate [32]. Reddy *et al.* reported that doped ceria shows excellent catalytic activity for the oxidation of CO [63] and Sr-doped $LaFeO_3$ particles have further been reported to have considerable catalytic activity for methane-oxidation [34]. The composite layer applied here is found to work well as a catalyst for the CO oxidation.

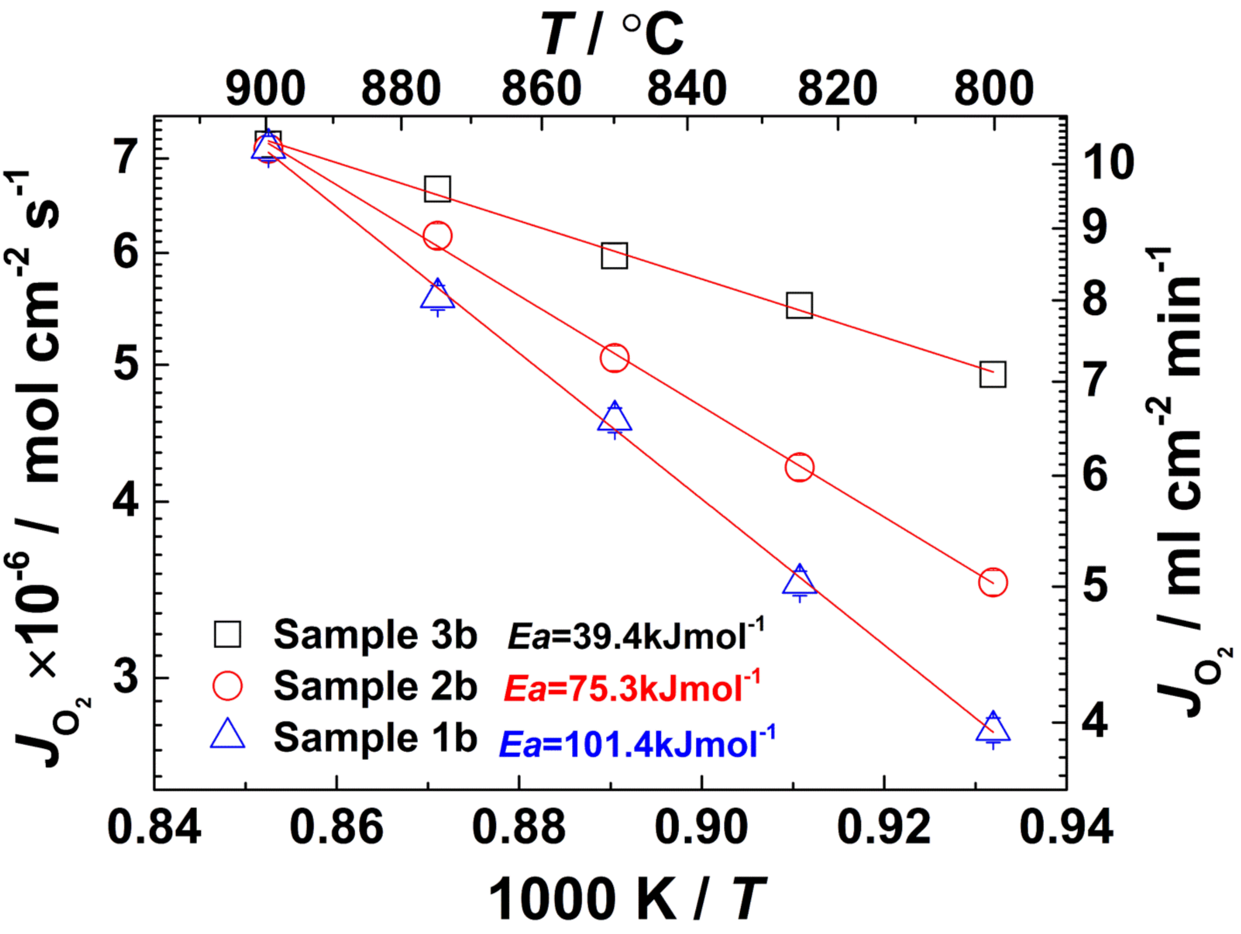

Figure 8. Arrhenius-type plot of oxygen permeation flux through the CGO-LSF composite membranes under an oxygen potential established between an air flow and a flow of CO. The existing pO_2 on the permeate side is around 1×10^{-19} bar at 900 °C. The red line is a best linear fit for the data.

3.7. Mass transfer polarization through the support

Figure 9 a-c show the oxygen permeation flux of a 5×5 cm^2 CGO-LSF based oxygen transport membrane (Nr. 3c in Table 2) as a function of $\ln(pO_2'/pO_2'')$ at 900 °C, 850 °C and 800 °C, respectively. At all three temperatures the flux is observed to be proportional to the driving force over the membrane.

Figure 10a shows the Arrhenius plots of oxygen flux under a fixed driving force $\ln(pO_2'/pO_2''=3)$ obtained from Figure. 9a-c. Using O_2 as the feed gas gives a higher flux than using air as the feed gas. When O_2 is used as the feed gas, mass transfer polarization can be disregarded. The enhancement of the flux ~1×10^{-7} mol cm^{-2} s^{-1} is significant compared with the experimental uncertainty ~1×10^{-8} mol cm^{-2} s^{-1} arising from the leak. Mass transfer polarization is more weakly dependent of temperature compared to surface exchange and bulk diffusion [64]. Hence if the flux improvement (at fixed pO_2) was due to reduced mass transfer polarization the effect should not increase with decreasing temperature. The decreased apparent activation energy found when using O_2 as the feed gas indicates that the slightly enhanced oxygen flux is due to the higher surface exchange coefficient at higher pO_2, as shown in Figure S3a of Supporting Information.

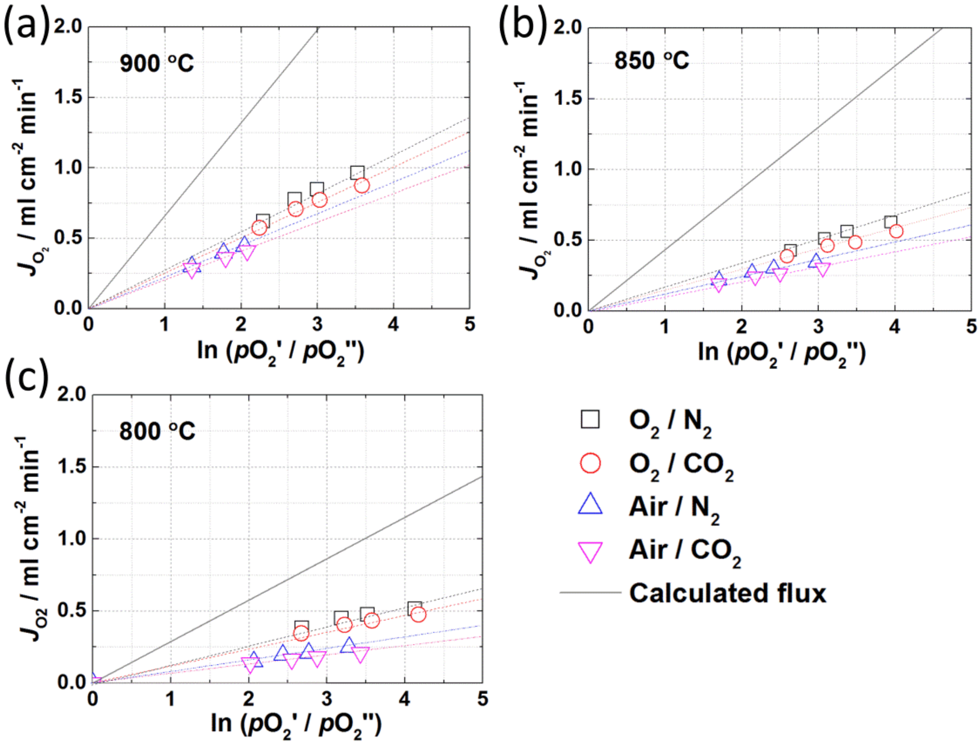

Figure 9. Oxygen permeation flux of a 5×5 cm^2 planar CGO-LSF membrane versus apparent driving force ln (pO_2’/pO_2’’) at (a) 900 °C, (b) 850 °C and (c) 800 °C, respectively. For simplicity the exit pO_2 has been used when calculating the abscissa value, approximating the experimental conditions also for these large area membranes as continuous flow stirred-tank reactor (CSTR)-like. (Treating instead the flow to be plug-flow-like shifts all points right. It maintains the observed proportionality between flux and driving force but reduces the slope of the curves, Figure S7 of Supporting Information). The solid lines represent the calculated oxygen fluxes based on deduced oxide ion conductivity (as illustrated in Figure S1 of Supporting Information) using Wagner’s equation.

The calculated resistance due to mass transfer polarization through the pore support is shown in Figure 10b. Details of the calculation are provided in section 4 of the Supporting Information. The explicit calculation reveals that the resistance due to mass transfer polarization across the porous support is less than 1% of the total resistance over a wide range of oxygen partial pressure gradients. With respect to the asymmetric membrane with an ordinary substrate prepared by pore formers, mass transfer polarization is usually quit significant [40, 65]. He *et al.* [40] found that the flux of an asymmetric membrane with similar finger-like pores shows a five-fold larger flux than a membrane prepared using an ordinary pore former. Huang *et al.* [41] reported that mass transfer polarization is negligible for a fuel cell with a finger-like anode support, in good agreement with this study. Baumann *et al.*[65] reported a six-fold lower oxygen flux of a BSCF-based asymmetric membrane when using air as the feed gas instead of pure O_2, which was ascribed to a significant mass transfer polarization through the porous support. In this study mass transfer polarization is negligible as gas transport is facilitated by the open finger-like pores formed in the phase-inversion tape casting.

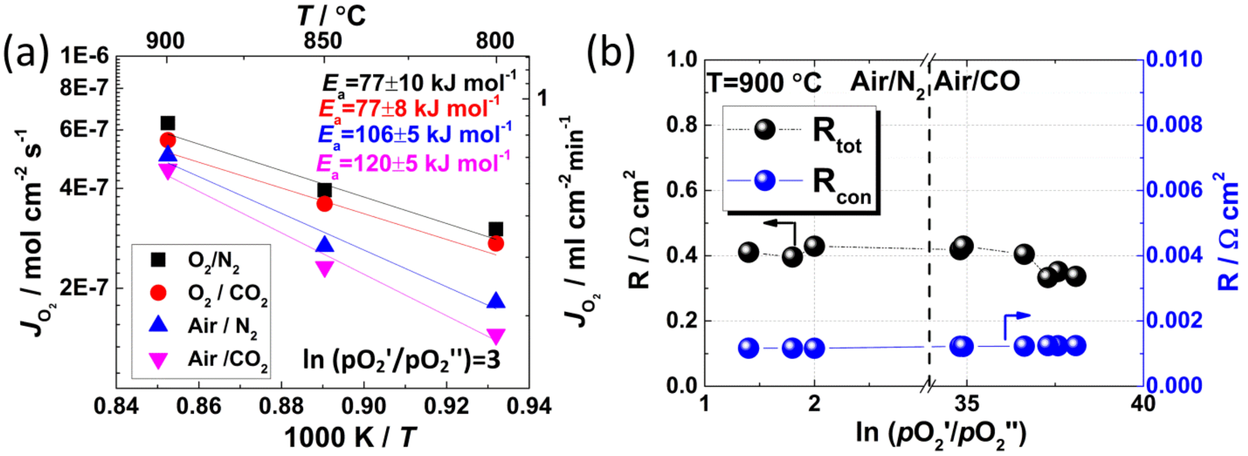

Figure 10. (a) Arrhenius plot of the oxygen flux measured under air,O_2/He,CO_2. The lines are best linear fit to the experimental data. The fluxes are obtained under ln(pO2'/pO2'')≈3 (b) Measured total resistance and calculated resistance of gas diffusion through finger-like substrate for air/N_2, CO at 900 °C.

Table 2. Oxygen permeation flux (J_{O2}) and activation energy (E_a) of the asymmetric CGO-LSF membranes, measured under gradients of Air/He,CO_2 and Air/CO (sample Nr. 6 is the calculated flux, as shown in Figure S1 of Supporting Information).

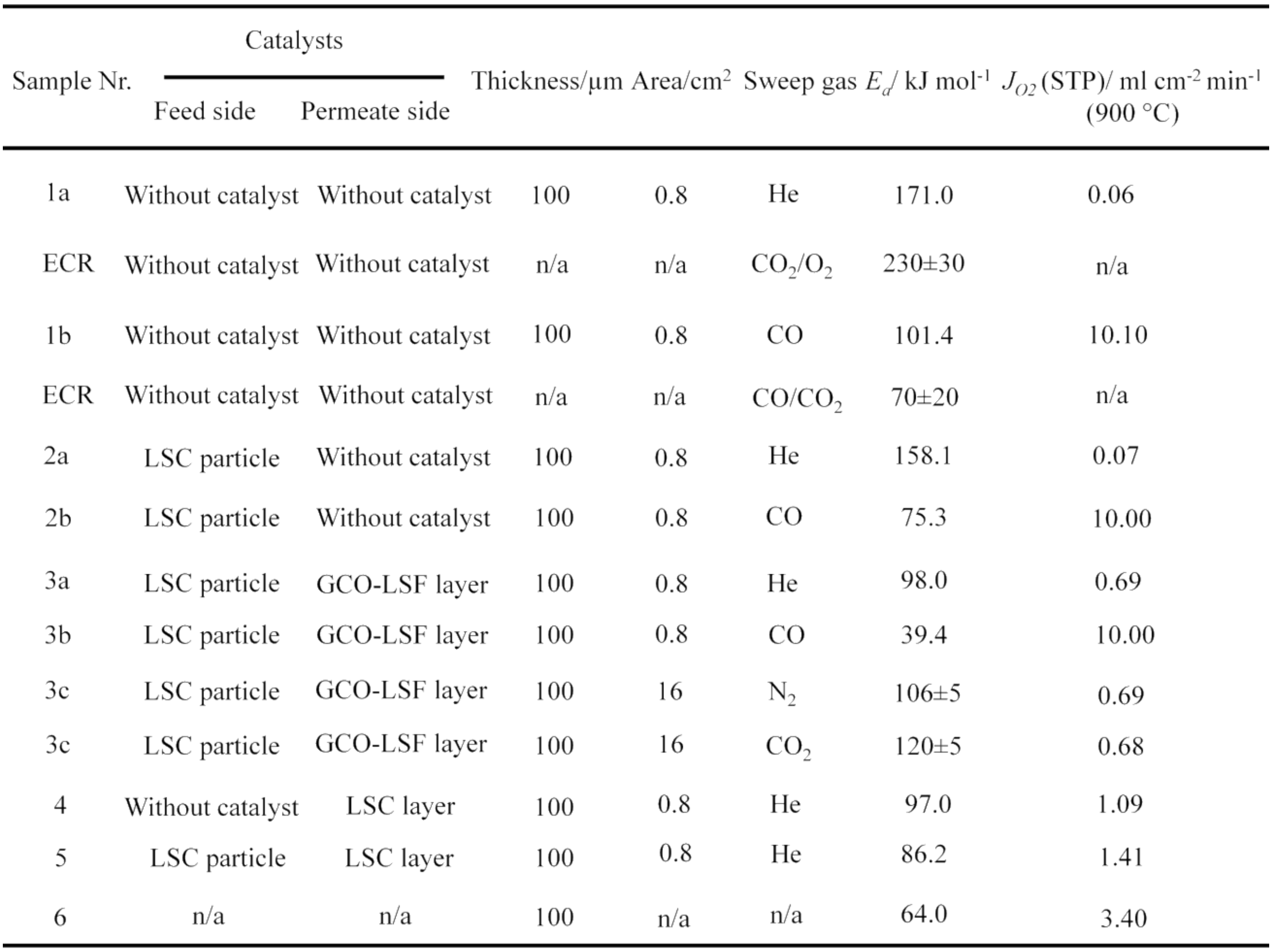

Sample Nr.	Catalysts		Thickness/µm	Area/cm²	Sweep gas	E_a/ kJ mol^{-1}	J_{O2} (STP)/ ml cm^{-2} min^{-1} (900 °C)
	Feed side	Permeate side					
1a	Without catalyst	Without catalyst	100	0.8	He	171.0	0.06
ECR	Without catalyst	Without catalyst	n/a	n/a	CO_2/O_2	230±30	n/a
1b	Without catalyst	Without catalyst	100	0.8	CO	101.4	10.10
ECR	Without catalyst	Without catalyst	n/a	n/a	CO/CO_2	70±20	n/a
2a	LSC particle	Without catalyst	100	0.8	He	158.1	0.07
2b	LSC particle	Without catalyst	100	0.8	CO	75.3	10.00
3a	LSC particle	GCO-LSF layer	100	0.8	He	98.0	0.69
3b	LSC particle	GCO-LSF layer	100	0.8	CO	39.4	10.00
3c	LSC particle	GCO-LSF layer	100	16	N_2	106±5	0.69
3c	LSC particle	GCO-LSF layer	100	16	CO_2	120±5	0.68
4	Without catalyst	LSC layer	100	0.8	He	97.0	1.09
5	LSC particle	LSC layer	100	0.8	He	86.2	1.41
6	n/a	n/a	100	n/a	n/a	64.0	3.40

3.8. Stability of CGO-LSF asymmetric membranes under a gradient of Air/CO

A stability test of the uncoated membrane (Nr. 1b in Table 2) was conducted by measuring the oxygen flux using ambient air on the porous membrane side and a flow of 30 Nml min^{-1} CO (1 bar) on the dense side. The measurements were carried out at 850 °C for 200 hours. The aging test was performed on a sample without surface catalysts. Results are shown in Figure 11a. After a slow transient over the first 50 hours, a stable flux of ca. 7 ml cm^{-2} min^{-1} (STP) was observed. Both sides before and after the measurement were also characterized by XRD. As shown in Figure 11b, the crystal structure on the feed side after the stability test is identical to the one before the test. However, additional peaks are observed on the dense membrane side, resulting from a reaction between the LSF in the membrane and the gas phase, resulting in formation of $SrCO_3$, La_2O_3 and Fe. The XRD results thus reveal that a partial decomposition of the LSF on the surface has occurred in the CO aging experiment. For comparison, SEM micrographs and elemental maps were recorded on the permeate side of the membrane before (Figure 11c) and after (Figure 11d) the stability test. The SEM-EDS maps before the stability test indicate that La, Sr and Fe reside at the same locations corresponding to the existence of a LSF phase. Ce is located in the rest of the area, which indicates the CGO phase is separated from the LSF.

After the stability test, a structural and compositional change is observed on the surface. Specifically, Sr is partly separated from La and Fe after test, whereas these elements were observed in the same areas before aging. Dark-field STEM elemental maps of grains that were scraped of the permeate side of the membrane after the stability are reproduced in Figure 12 below. The structure of an agglomerate of the grains is depicted in the dark-field STEM image in Figure 12a, while the distribution of elements from CGO and LSF are presented in Figure 12b and 12c, respectively. Figure 12c shows that the X-ray signal from Fe (blue) is accompanied by a weaker signal from La (red), while Sr (green) has clearly segregated from the LSF phase, in accordance with the XRD and SEM results. Figure 12b shows that grains with a dominating signal from Ce (red) are always accompanied by a weaker signal from Gd (green), consistent with the CGO phase. Some grains, however, with no signal from Ce (red), but with either strong signals from Fe (Figure 12c, blue) or Sr (Figure 12c, green) show a weak signal (ca. 3 at.%) from Gd (Figure 12b. green). The STEM-EDS analysis could thus also indicate a slight decomposition of CGO. From the XRD, SEM and STEM analysis it is concluded that, the LSF in the outermost surface partially decomposes during the stability test under interaction with CO/CO_2. Although a slight surface decomposition has been observed, it is noteworthy that no negative influence on the flux of the membrane was observed over the 200-hour aging test.

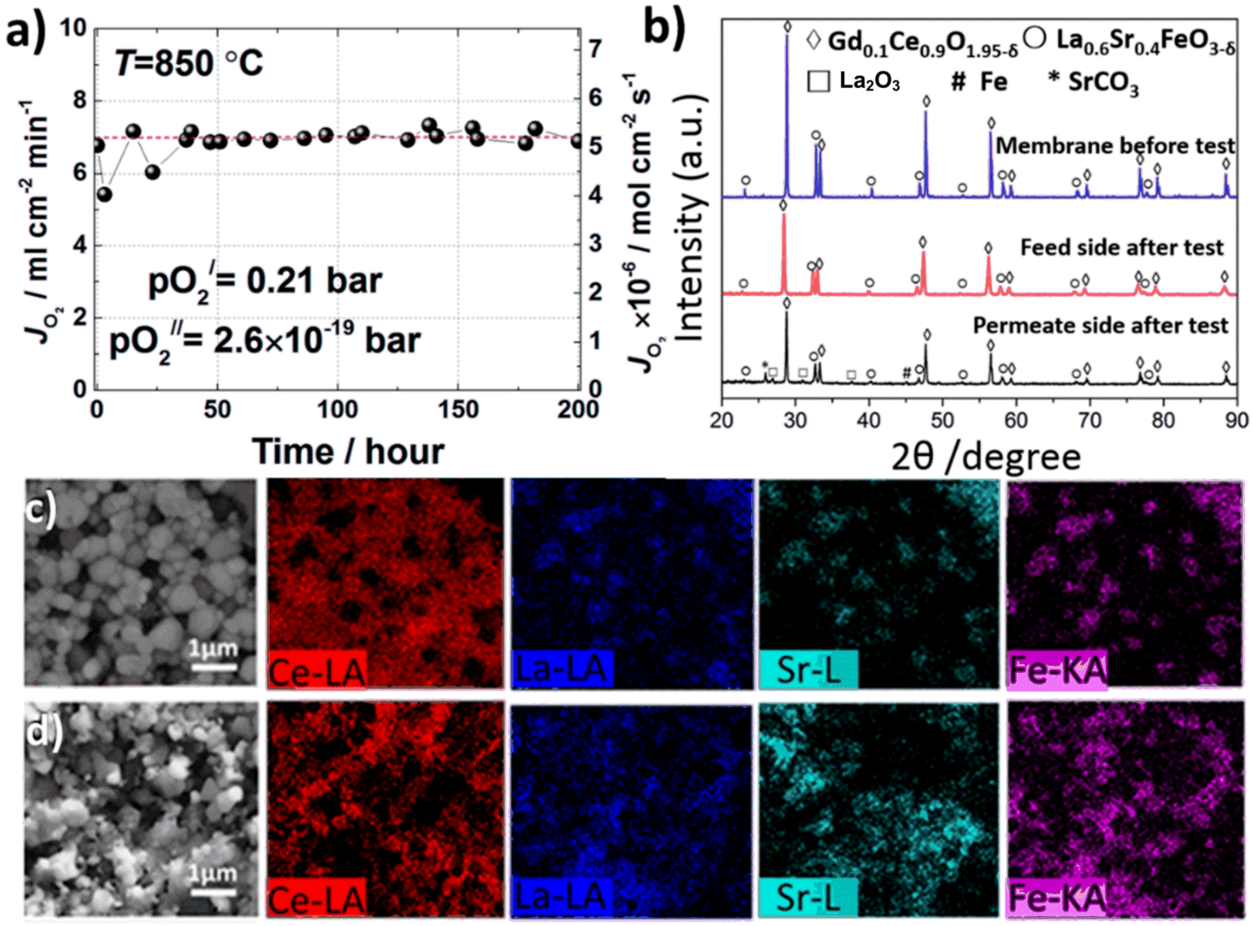

Figure 11. (a) Oxygen flux of a bare membrane under air/CO as a function of time at 850° C. (b) XRD patterns (left) of the CGO-LSF dual phase membrane before the test (blue) as well as the feed side (red) and permeate side (black) after testing under an oxygen gradient of air/CO. The diffraction patterns of the different phases are marked as follows: (◊) $Gd_{0.1}Ce_{0.9}O_{1.95-\delta}$ (○) $La_{0.6}Sr_{0.4}FeO_{3-\delta}$ (*) $SrCO_3$ (□) La_2O_3 (#) Fe. SEM micrograph and EDS mapping the permeate side of dense CGO-LSF membrane before (c) and after (d) flux measurement in air/CO.

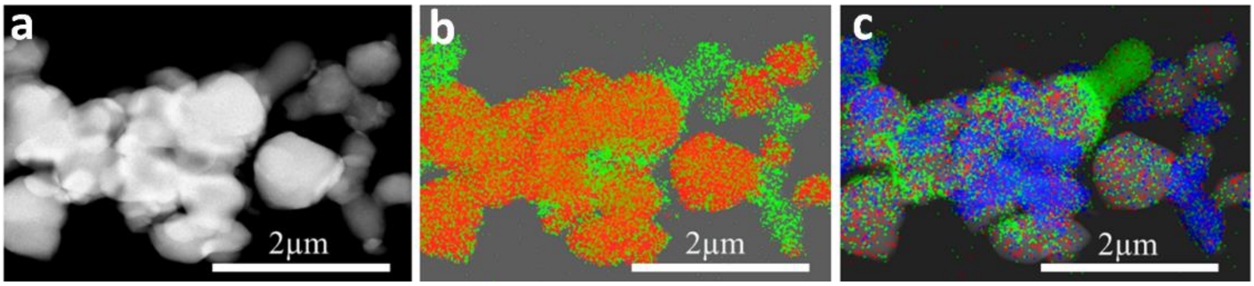

Figure 12. Microstructure features of the powder taken from the permeate side of dense CGO-LSF membrane (a). Dark-field STEM image (b) EDS elemental maps of the CGO phase, Ce L-alpha (red), Gd L-alpha (green); (c) EDS elemental maps of the LSF phase, La L-alpha (red) Sr L-alpha (green) Fe K-alpha (blue).

Thermodynamic calculations of the LSF stability under different pO_2 and pCO_2 conditions were also performed. The results of this analysis are summarized in Figure 13 showing the calculated decomposition pO_2 of LSF as a function of pCO_2. Above the solid curve LSF is stable, below partial decomposition occurs. CGO is considered to be stable under the present experimental conditions. According to the calculations, LSF starts to decompose to La_2O_3, Fe and SrO at $pO_2=1\times10^{-19.5}$ bar. When the pCO_2 is lower than 0.01 bar, the decomposition pO_2 is independent of pCO_2. When the pCO_2 is above 0.01 bar, LSF decomposes even under a higher pO_2 because of the simultaneous formation of $SrCO_3$. The decomposition pO_2 eventually increases up to 1×10^{-14} bar at a pCO_2 of 1 bar.

As illustrated in Figure 13, the experimental condition for the operation of the membrane (filled circle) in the aging test is located in the unstable region, which explains the observed partial surface decomposition. Formation of $SrCO_3$ was also observed in the sample after electrical conductivity test in a mixture of CO/CO_2, as shown in Figure S5 of Supporting Information. Even though the stable oxygen flux is observed, the slight surface decomposition may increase the risk of mechanical failure of the membrane for practical applications. To avoid this slight surface decomposition, operation should be restricted to conditions in the “stable region”. The situation is strongly alleviated by reducing the carbon activity by addition of steam as would be relevant under conditions of production of syngas from methane. However, as illustrated in Figure 13, from the calculation close to 50% of steam is required to stabilize the phase. Also noteworthy is that the problem will be alleviated by “kinetic stabilization” where the membrane is “kept” in the stability window by continuous oxidation from the high pO_2 side; the thermodynamic calculations represent a worst scenario [66].

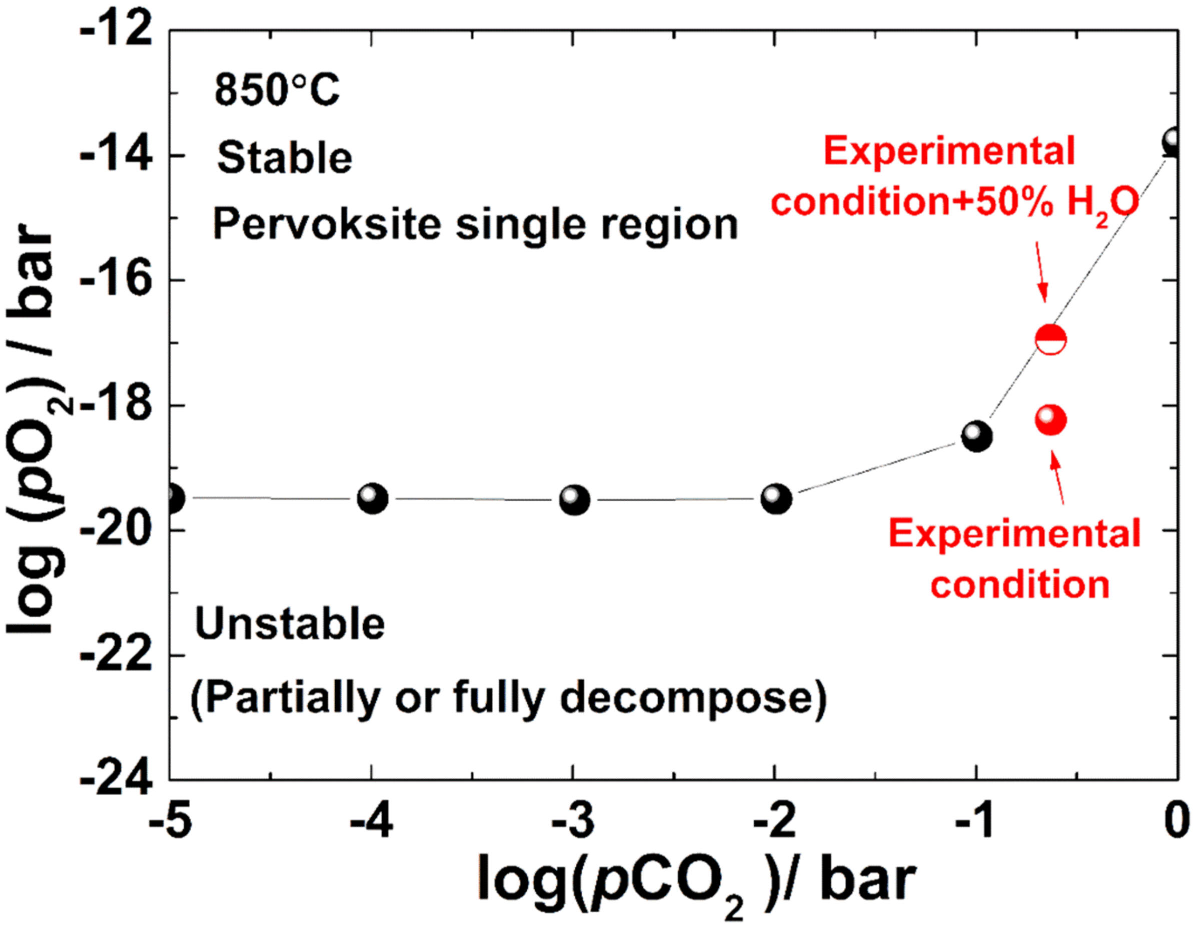

Figure 13. Thermodynamic calculation of chemical stability of LSF as a function of logpCO_2 and logpO_2 at 850°C.

4. Conclusions

Asymmetric 70 vol.% $Gd_{0.1}Ce_{0.9}O_{1.95-\delta}$-30 vol.% $La_{0.6}Sr_{0.4}FeO_{3-\delta}$ (CGO-LSF) dual phase composite membranes were fabricated by a phase-inversion tape casting technique. The membranes consisted of a 100-µm thick gas tight CGO-LSF separation layer and a ca. 1-mm thick porous substrate of the same material with finger-like pores orientated perpendicular to the surface. After fabrication, no intermixing of the two phases was detected within the resolution limit of XRD. For a membrane characterized under an oxygen gradient of air/He, oxygen permeation fluxes of 0.06 (STP) ml cm^{-2} min^{-1} and 1.49 (STP) ml cm^{-2} min^{-1} were obtained at 900 °C from a CGO-LSF asymmetric membrane with and without surface modification, respectively. The flux of the membrane tends to be limited by the oxygen surface exchange on the permeate side, which was further verified by electrical conductivity relaxation (ECR). High oxygen permeation flux values of ca. 10.00 (STP) ml cm^{-2} min^{-1} were achieved for membranes measured in Air/CO at 900 °C. Mass transfer polarization through the finger-like support was negligible under all experimental conditions. The bare asymmetric membrane shows a stable oxygen permeation flux under a large gradient (Air/CO) up to 200 hours without detectable degradation. However, post-test characterization (XRD, SEM and TEM) revealed partial decomposition of the LSF phase on the surface of the membrane. Thermodynamic calculations also predict the LSF to decompose under the applied conditions. The decomposition can be avoided by using a more humid sweep gas and increasing the pO_2. These results indicate that asymmetric CGO-LSF membranes prepared by phase-inversion tape casting have excellent oxygen transport characteristics and are potential candidates for oxygen permeation membrane applications.

Supporting Information

Figures S1-7 representing the calculated ionic conductivity of CGO-LSF, Rietveld refinement patterns of CGO-LSF, oxygen surface exchange and bulk diffusion coefficients as a function of pO_2, leak rate and SEM and EDX mapping images for CGO-LSF after electrical conductivity relaxation measurement, point dependence of pO_2 at permeate side of 5×5cm^2 membranes and comparison between CSTR and plug flow models, respectively. Table S1 shows the unit cell data. Video S1 showing the three dimensional tomography of the membrane. Table S2 shows the comparison between the driving forces obtained by CSTR and plug flow models.

Author Information

Corresponding Author

* Shiyang Cheng Tel: +47 91581243 E-mail: shiyanc@smn.uio.no

Present Addresses

‖Centre for Materials Science Nanotechnology, Department of Chemistry, FASE, Gaustadalleén 21, 0349 Oslo, Norway

Author Contributions

The manuscript was written through contributions of all authors. All authors have given approval to the final version of the manuscript.

Funding Sources

Project “ENEFOX“- Energy Efficient Oxygen Production for a Sustainable Energy System” (project no. 11-116387) supported by Danish council for Strategic Research.

Acknowledgments

The authors thank DSF (Danish council for Strategic Research) for the finical support on the project “ENEFOX“- Energy Efficient Oxygen Production for a Sustainable Energy System” (11-116387). The Imaging Industry Portal at the Technical University of Denmark is acknowledged for access to x-ray CT scanners. Mr. Henrik Henriksen’s assistance on 5×5 cm^2 membrane tests is greatly appreciated. Mr.

Yuqing Meng’s help on the experimental setup is greatly appreciated. Professor H.J.M.Bouwmeester is thanked for fruitful discussions.

References

1. Badwal, S. P.; Ciacchi, F. T., Ceramic Membrane Technologies for Oxygen Separation. *Adv. Mater.* **2001,** *13* (12‐13), 993-996.
2. Chen, C.-S.; Feng, S.-J.; Ran, S.; Zhu, D.-C.; Liu, W.; Bouwmeester, H. J. M., Conversion of Methane to Syngas by a Membrane-Based Oxidation–Reforming Process. *Angew. Chem. Int. Ed.* **2003,** *42* (42), 5196-5198.
3. Bredesen, R.; Jordal, K.; Bolland, O., High-Temperature Membranes in Power Generation with CO_2 Capture. *Chem. Eng. Process.* **2004,** *43* (9), 1129-1158.
4. Puig-Arnavat, M.; Soprani, S.; Sogaard, M.; Engelbrecht, K.; Ahrenfeldt, J.; Henriksen, U. B.; Hendriksen, P. V., Integration of Mixed Conducting Membranes in an Oxygen-Steam Biomass Gasification Process. *RSC Adv.* **2013,** *3* (43), 20843-20854.
5. Sunarso, J.; Baumann, S.; Serra, J. M.; Meulenberg, W. A.; Liu, S.; Lin, Y. S.; Diniz da Costa, J. C., Mixed Ionic–Electronic Conducting (MIEC) Ceramic-based Membranes for Oxygen Separation. *J. Membr. Sci.* **2008,** *320* (1–2), 13-41.
6. Esposito, V.; Søgaard, M.; Hendriksen, P. V., Chemical Stability of $La_{0.6}Sr_{0.4}CoO_{3-\delta}$ in Oxygen Permeation Applications under Exposure to N_2 and CO_2. *Solid State Ionics* **2012,** *227* (0), 46-56.
7. Chen, C.-S.; Zhang, Z.-P.; Jiang, G.-S.; Fan, C.-G.; Liu, W.; Bouwmeester, H. J., Oxygen Permeation through $La_{0.4}Sr_{0.6}Co_{0.2}Fe_{0.8}O_{3-\delta}$ Membrane. *Chem. Mater.* **2001,** *13* (9), 2797-2800.
8. Ten Elshof, J. E.; Bouwmeester, H. J. M.; Verweij, H., Oxygen Transport through $La_{1-x}Sr_xFeO_{3-\delta}$ Membranes. I. Permeation in air/He Gradients. *Solid State Ionics* **1995,** *81* (1–2), 97-109.
9. Wang, H.; Tablet, C.; Feldhoff, A.; Caro, J., A Cobalt-Free Oxygen-Permeable Membrane Based on the Perovskite-Type Oxide $Ba_{0.5}Sr_{0.5}Zn_{0.2}Fe_{0.8}O_{3-\delta}$. *Adv. Mater.* **2005,** *17* (14), 1785-1788.
10. Partovi, K.; Liang, F.; Ravkina, O.; Caro, J., High-Flux Oxygen-Transporting Membrane $Pr_{0.6}Sr_{0.4}Co_{0.5}Fe_{0.5}O_{3-\delta}$: CO_2 Stability and Microstructure. *ACS Appl. Mater. Interfaces* **2014,** *6* (13), 10274-10282.
11. Shao, Z.; Haile, S. M., A High-Performance Cathode for the Next Generation of Solid-Oxide Fuel Cells. *Nature* **2004,** *431* (7005), 170-173.
12. Shao, Z.; Yang, W.; Cong, Y.; Dong, H.; Tong, J.; Xiong, G., Investigation of the Permeation Behavior and Stability of a $Ba_{0.5}Sr_{0.5}Co_{0.8}Fe_{0.2}O_{3-\delta}$ Oxygen Membrane. *J. Membr. Sci.* **2000,** *172* (1), 177-188.
13. Engels, S.; Markus, T.; Modigell, M.; Singheiser, L., Oxygen Permeation and Stability Investigations on MIEC Membrane Materials under Operating Conditions for Power Plant Processes. *J. Membr. Sci.* **2011,** *370* (1–2), 58-69.
14. Petrov, A. N.; Cherepanov, V. A.; Zuev, A. Y., Thermodynamics, Defect Structure, and Charge Transfer in Doped Lanthanum Cobaltites: An Overview. *J. Solid State Electrochem.* **2006,** *10* (8), 517-537.
15. Yan, A.; Maragou, V.; Arico, A.; Cheng, M.; Tsiakaras, P., Investigation of a $Ba_{0.5}Sr_{0.5}Co_{0.8}Fe_{0.2}O_{3-\delta}$ Based Cathode SOFC: II. The Effect of CO_2 on the Chemical Stability. *Appl. Catal., B* **2007,** *76* (3–4), 320-327.
16. Van Doorn, R. H. E.; Bouwmeester, H. J. M.; Burggraaf, A. J., Kinetic Decomposition of $La_{0.3}Sr_{0.7}CoO_{3-\delta}$ Perovskite Membranes During Oxygen Permeation. *Solid State Ionics* **1998,** *111* (3–4), 263-272.
17. C. Chatzichristodoulou, M. S., J. Glasscock, A. Kaiser, S. P. V. Foghmoes, and P. V. Hendriksen, Oxygen Permeation in Thin, Dense $Ce_{0.9}Gd_{0.1}O_{1.95-d}$ Membranes II. Experimental Determination. *J Electrochem Soc* **2011,** *158* (5), F73.
18. Chatzichristodoulou, C.; Blennow, T. P.; Søgaard, M.; Hendriksen, P. V.; Mogensen, M. B., Ceria and Its Use in Solid Oxide Cells and Oxygen Membranes. In *Catalysis by Ceria and Related Materials,* World Scientific Publising Co.: **2013**, pp 623-782.

19. Chatzichristodoulou, C.; Søgaard, M.; Glasscock, J.; Kaiser, A.; Foghmoes, S. P. V.; Hendriksen, P. V., Oxygen Permeation in Thin, Dense $Ce_{0.9}Gd_{0.1}O_{1.95-\delta}$ Membranes II. Experimental Determination. *J. Electrochem. Soc.* **2011,** *158* (5), F73-F83.

20. Lobera, M. P.; Serra, J. M.; Foghmoes, S. P.; Søgaard, M.; Kaiser, A., On the Use of Supported ceria Membranes for Oxyfuel Process/Syngas Production. *J. Membr. Sci.* **2011,** *385–386* (0), 154-161.

21. Chatzichristodoulou, C.; Hendriksen, P. V., Electronic Conductivity of $Ce_{0.9}Gd_{0.1}O_{1.95-\delta}$ and $Ce_{0.8}Pr_{0.2}O_{2-\delta}$: Hebb-Wagner Polarisation in the Case of Redox Active Dopants and Interference. *Phys. Chem. Chem. Phys.* **2011,** *13* (48), 21558-21572.

22. Liu, T.; He, W.; Huang, H.; Wang, S.; Bouwmeester, H. J. M.; Chen, C., $Ce_{0.8}Sm_{0.2}O_{1.9}$–$La_{0.8}Sr_{0.2}Cr_{0.5}Fe_{0.5}O_{3-\delta}$ Dual-Phase Hollow Fiber Membranes Operated under Different Gradients. *Ind. Eng. Chem. Res.* **2014,** *53* (14), 6131-6136.

23. Luo, H.; Jiang, H.; Klande, T.; Cao, Z.; Liang, F.; Wang, H.; Caro, J., Novel Cobalt-Free, Noble Metal-Free Oxygen-Permeable $40Pr_{0.6}Sr_{0.4}FeO_{3-\delta}$–$60Ce_{0.9}Pr_{0.1}O_{2-\delta}$ Dual-Phase Membrane. *Chem. Mater.* **2012,** *24* (11), 2148-2154.

24. Wang, Z.; Sun, W.; Zhu, Z.; Liu, T.; Liu, W., A Novel Cobalt-Free, CO_2-Stable, and Reduction-Tolerant Dual-Phase Oxygen-Permeable Membrane. *ACS Appl. Mater. Interfaces* **2013,** *5* (21), 11038-11043.

25. Fang, W.; Liang, F.; Cao, Z.; Steinbach, F.; Feldhoff, A., A Mixed Ionic and Electronic Conducting Dual‐Phase Membrane with High Oxygen Permeability. *Angew. Chem. Int. Ed.* **2015,** *54* (16), 4847-4850.

26. Luo, H.; Efimov, K.; Jiang, H.; Feldhoff, A.; Wang, H.; Caro, J., CO_2-Stable and Cobalt-Free Dual-Phase Membrane for Oxygen Separation. *Angew. Chem. Int. Ed.* **2011,** *50* (3), 759-763.

27. Balaguer, M.; García-Fayos, J.; Solís, C.; Serra, J. M., Fast Oxygen Separation Through SO_2- and CO_2-Stable Dual-Phase Membrane Based on $NiFe_2O_4$–$Ce_{0.8}Tb_{0.2}O_{2-\delta}$. *Chem. Mater.* **2013,** *25* (24), 4986-4993.

28. Cheng, S.; Sogaard, M.; Han, L.; Zhang, W.; Chen, M.; Kaiser, A.; Hendriksen, P. V., A Novel CO_2- and SO_2-Tolerant Dual Phase Composite Membrane for Oxygen Separation. *Chem. Commun.* **2015,** *51* (33), 7140-7143.

29. Gurauskis, J.; Ovtar, S.; Kaiser, A.; Søgaard, M.; Hendriksen, P. V., Ceria Based Composite Membranes for Oxygen Separation. *ECS Trans.* **2014,** *64* (2), 251-258.

30. Luo, H.; Klande, T.; Cao, Z.; Liang, F.; Wang, H.; Caro, J., A CO_2-Stable Reduction-Tolerant Nd-Containing Dual Phase Membrane for Oxyfuel CO_2 Capture. *J. Mater. Chem. A* **2014,** *2* (21), 7780-7787.

31. Katsura, T.; Sekine, T.; Kitayama, K.; Sugihara, T.; Kimizuka, N., Thermodynamic Properties of Fe-Lathanoid-O Compounds at High Temperatures. *J. Solid State Chem.* **1978,** *23* (1–2), 43-57.

32. Ten Elshof, J. E.; Bouwmeester, H. J. M.; Verweij, H., Oxygen Transport Through $La_{1-x}Sr_xFeO_{3-\delta}$ Membranes II. Permeation in Air/CO, CO_2 Gradients. *Solid State Ionics* **1996,** *89* (1–2), 81-92.

33. Søgaard, M.; Vang Hendriksen, P.; Mogensen, M., Oxygen Nonstoichiometry and Transport Properties of Strontium Substituted Lanthanum Ferrite. *J. Solid State Chem.* **2007,** *180* (4), 1489-1503.

34. Khine, M. S. S.; Chen, L.; Zhang, S.; Lin, J.; Jiang, S. P., Syngas Production by Catalytic Partial Oxidation of Methane over $(La_{0.7}A_{0.3})BO_3$ (A = Ba, Ca, Mg, Sr, and B = Cr or Fe) Perovskite Oxides for Portable Fuel Cell Applications. *Int. J. Hydrogen Energy* **2013,** *38* (30), 13300-13308.

35. Bouwmeester, H. J. M.; Kruidhof, H.; Burggraaf, A. J., Importance of the Surface Exchange Kinetics as Rate Limiting Step in Oxygen Permeation Through Mixed-Conducting Oxides. *Solid State Ionics* **1994,** *72, Part 2* (0), 185-194.

36. Ramachandran, D. K.; Søgaard, M.; Clemens, F.; Gurauskis, J.; Kaiser, A., Fabrication and Performance of a Tubular Ceria based Oxygen Transport Membrane on a Low Cost MgO Support. *Sep. Purif. Technol.* **2015,** *147*, 422-430.

37. Kaiser, A.; Foghmoes, S.; Chatzichristodoulou, C.; Søgaard, M.; Glasscock, J. A.; Frandsen, H. L.; Hendriksen, P. V., Evaluation of Thin Film Ceria Membranes for syngas Membrane Reactors—Preparation, Characterization and Testing. *J. Membr. Sci.* **2011,** *378* (1–2), 51-60.

38. Huang, H.; Cheng, S.; Gao, J.; Chen, C.; Yi, J., Phase-Inversion Tape-Casting Preparation and Significant Performance Enhancement of $Ce_{0.9}Gd_{0.1}O_{1.95}$–$La_{0.6}Sr_{0.4}Co_{0.2}Fe_{0.8}O_{3-\delta}$ Dual-Phase Asymmetric Membrane for Oxygen Separation. *Mater. Lett.* **2014,** *137* (0), 245-248.

39. Liu, T.; Wang, Y.; Zhang, Y.; Fang, S.; Lei, L.; Ren, C.; Chen, F., Steam Electrolysis in a Solid Oxide Electrolysis Cell Fabricated by the Phase-Inversion Tape Casting Method. *Electrochem Commun* **2015,** *61*, 106-109.

40. He, W.; Huang, H.; Gao, J.-f.; Winnubst, L.; Chen, C.-s., Phase-Inversion Tape Casting and Oxygen Permeation Properties of Supported Ceramic Membranes. *J. Membr. Sci.* **2014,** *452* (0), 294-299.

41. Huang, H.; Lin, J.; Wang, Y.; Wang, S.; Xia, C.; Chen, C., Facile One-Step Forming of NiO and Yttrium-Stabilized Zirconia Composite Anodes with Straight Open Pores for Planar Solid Oxide Fuel Cell using Phase-Inversion Tape Casting Method. *J. Power Sources* **2015,** *274* (0), 1114-1117.

42. Liu, T.; Ren, C.; Fang, S.; Wang, Y.; Chen, F., Microstructure Tailoring of the Nickel Oxide–Yttria-Stabilized Zirconia Hollow Fibers toward High-Performance Microtubular Solid Oxide Fuel Cells. *ACS Appl. Mater. Interfaces* **2014,** *6* (21), 18853-18860.

43. Joo, J. H.; Yun, K. S.; Lee, Y.; Jung, J.; Yoo, C.-Y.; Yu, J. H., Dramatically Enhanced Oxygen Fluxes in Fluorite-Rich Dual-Phase Membrane by Surface Modification. *Chem. Mater.* **2014,** *26* (15), 4387-4394.

44. Wang, S.; Kobayashi, T.; Dokiya, M.; Hashimoto, T., Electrical and Ionic Conductivity of Gd‐Doped Ceria. *J. Electrochem. Soc.* **2000,** *147* (10), 3606-3609.

45. Landauer, R., Electrical Conductivity in Inhomogeneous Media. *AIP Conf. Proc.* **1978,** *40* (1), 2-45.

46. Wu, Z.; Liu, M., Modelling of Ambipolar Transport Properties of Composite Mixed Ionic-Electronic Conductors. *Solid State Ionics* **1996,** *93* (1–2), 65-84.

47. Samson, A. J.; Søgaard, M.; Hendriksen, P. V., (Ce,Gd)$O_{2-\delta}$-Based Dual Phase Membranes for Oxygen Separation. *J. Membr. Sci.* **2014,** *470*, 178-188.

48. Seeharaj, P.; Berenov, A.; Raj, E.; Rudkin, R.; Atkinson, A., Mixed-Conducting LSC/CGO Composites for Passive Oxygen Separation Membranes. *Solid State Ionics* **2011,** *192* (1), 638-641.

49. Joo, J. H.; Yun, K. S.; Kim, J.-H.; Lee, Y.; Yoo, C.-Y.; Yu, J. H., Substantial Oxygen Flux in Dual-Phase Membrane of Ceria and Pure Electronic Conductor by Tailoring the Surface. *ACS Appl. Mater. Interfaces* **2015,** *7* (27), 14699-14707.

50. Pippardt, U.; Boeer, J.; Bollert, C.; Hoffmann, A.; Heidenreich, M.; Kriegel, R.; Schulz, M.; Simon, A., Performance and Stability of Mixed Conducting Composite Membranes Based on Substituted Ceria. *J Ceram Sci and Tech* **2014,** *5* (4), 309-316.

51. Fish, J. S.; Ricote, S.; O'Hayre, R.; Bonanos, N., Electrical Properties and Flux Performance of Composite Ceramic Hydrogen Separation Membranes. *J. Mater. Chem. A* **2015,** *3* (10), 5392-5401.

52. Wang, Y.; Hu, B.; Zhu, Z.; Bouwmeester, H. J. M.; Xia, C., Electrical Conductivity Relaxation of $Sr_2Fe_{1.5}Mo_{0.5}O_{6-\delta}$-$Sm_{0.2}Ce_{0.8}O_{1.9}$ Dual-Phase Composites. *J. Mater. Chem. A* **2014,** *2* (1), 136-143.

53. Chatzichristodoulou, C.; Søgaard, M.; Hendriksen, P. V., Oxygen Permeation in Thin, Dense $Ce_{0.9}Gd_{0.1}O_{1.95-\delta}$ Membranes I. Model Study. *J. Electrochem. Soc.* **2011,** *158* (5), F61-F72.

54. Ishigaki, T.; Yamauchi, S.; Kishio, K.; Mizusaki, J.; Fueki, K., Diffusion of oxide ion vacancies in perovskite-type oxides. *J. Solid State Chem.* **1988,** *73* (1), 179-187.

55. Gellings, P. J.; Bouwmeester, H., *Handbook of Solid State Electrochemistry*. CRC press: **1997**.

56. Søgaard, M.; Hendriksen, P. V.; Mogensen, M.; Poulsen, F. W.; Skou, E., Oxygen Nonstoichiometry and Transport Properties of Strontium Substituted Lanthanum Cobaltite. *Solid State Ionics* **2006,** *177* (37–38), 3285-3296.

57. Ovtar, S.; Søgaard, M.; Hendriksen, P. V.; Norrman, K., A Mixed Ionic and Electronic Conducting Dual‐Phase Membrane with High Oxygen Permeability. Manuscript to be submitted, **2015**.

58. Manning, P. S.; Sirman, J. D.; Kilner, J. A., Oxygen self-diffusion and surface exchange studies of oxide electrolytes having the fluorite structure. *Solid State Ionics* **1996,** *93* (1–2), 125-132.

59. Ten Elshof, J.; Lankhorst, M.; Bouwmeester, H., Oxygen Exchange and Diffusion Coefficients of Strontium‐Doped Lanthanum Ferrites by Electrical Conductivity Relaxation. *J. Electrochem. Soc.* **1997,** *144* (3), 1060-1067.

60. Li, W.; Tian, T.-F.; Shi, F.-Y.; Wang, Y.-S.; Chen, C.-S., $Ce_{0.8}Sm_{0.2}O_{2-\delta}$–$La_{0.8}Sr_{0.2}MnO_{3-\delta}$ Dual-Phase Composite Hollow Fiber Membrane for Oxygen Separation. *Ind Eng Chem Res.* **2009,** *48* (12), 5789-5793.

61. Tan, X.; Liu, N.; Meng, B.; Sunarso, J.; Zhang, K.; Liu, S., Oxygen Permeation Behavior of $La_{0.6}Sr_{0.4}Co_{0.8}Fe_{0.2}O_3$ Hollow Fibre Membranes with Highly Concentrated CO_2 Exposure. *J. Membr. Sci.* **2012,** *389* (0), 216-222.

62. Luo, H.; Jiang, H.; Efimov, K.; Liang, F.; Wang, H.; Caro, J., CO_2-Tolerant Oxygen-Permeable Fe_2O_3-$Ce_{0.9}Gd_{0.1}O_{2-\delta}$ Dual Phase Membranes. *Ind. Eng. Chem. Res.* **2011,** *50* (23), 13508-13517.

63. Reddy, B. M.; Katta, L.; Thrimurthulu, G., Novel Nanocrystalline $Ce_{1-x}La_xO_{2-\delta}$ (x = 0.2) Solid Solutions: Structural Characteristics and Catalytic Performance. *Chem. Mater.* **2009,** *22* (2), 467-475.
64. Jørgensen, M. J.; Mogensen, M., Impedance of Solid Oxide Fuel Cell LSM/YSZ Composite Cathodes. *J. Electrochem. Soc.* **2001,** *148* (5), A433-A442.
65. Baumann, S.; Serra, J. M.; Lobera, M. P.; Escolástico, S.; Schulze-Küppers, F.; Meulenberg, W. A., Ultrahigh Oxygen Permeation Flux through Supported $Ba_{0.5}Sr_{0.5}Co_{0.8}Fe_{0.2}O_{3-\delta}$ Membranes. *J. Membr. Sci.* **2011,** *377* (1–2), 198-205.
66. Hendriksen, P. V.; Larsen, P. H.; Mogensen, M.; Poulsen, F. W.; Wiik, K., Prospects And Problems of Dense Oxygen Permeable Membranes. *Catal. Today.* **2000,** *56* (1–3), 283-295.

Electronic Supplementary Information (ESI)

5. Theoretical considerations (ECR)

Electrical conductivity relaxation (ECR) is commonly utilized to measure the oxygen diffusion and surface exchange coefficients of single [1-2] and dual phase composite [3-4] mixed ionic and electronic conductors (MIECs). It is based on the measurement of the total conductivity change of a dense sample upon an instantaneous change of the surrounding oxygen partial pressure. Changing the oxygen partial pressure a change in the charge carrier concentration (electrons or electron holes) is measured, which is related to the change in oxygen non-stoichiometry (δ) *via* the electroneutrality principle. The following assumptions are commonly made when using ECR;

i) Local electroneutrality,

ii) conductivity is proportional to the charge carrier concentration,

iii) the surface exchange reaction is a first order reaction with respect to the oxygen vacancy concentration;

$$J_z = D_{chem}\,\partial C\left(\pm l_z, t\right)/\partial z = k_{ex}\left(C\left(\pm l_z, t\right) - C\left(\pm l_z, \infty\right)\right) \tag{S1}$$

where J_z is the flux of oxide ions from the surface to the bulk and k_{ex}, is the rate constant, $C(\pm l_x, t)$ at the surface at time t, and $C(\pm l_x, \infty)$ represents the concentration of oxygen ions at the surface at equilibrium $(t = \infty)$.

iv) The change of the oxygen partial pressure occurs much more rapidly than the conductivity change of the sample.

v) The chemical diffusion coefficient D_{chem} is assumed to be constant within the pO_2-step range,

vi) L_x must be significantly larger than L_y and L_z.

Based on Fick’s laws of diffusion with the appropriate boundary conditions, the normalized conductivity as a function of time can be written as [5]:

$$\frac{\sigma_\infty - \sigma(\mathrm{t})}{\sigma_\infty - \sigma(\mathrm{t}=0)} = \sum_{n=1}^{\infty} \frac{2L_x^2 \exp(\frac{-\beta_{n,x}^2 D_{chem} t}{l_x^2})}{\beta_{n,x}^2(\beta_{n,x}^2 + L_x^2 + \mathrm{L}_x)} \sum_{n=1}^{\infty} \frac{2L_y^2 \exp(\frac{-\beta_{n,\mathrm{y}}^2 D_{chem} t}{l_y^2})}{\beta_{n,\mathrm{y}}^2(\beta_{n,\mathrm{y}}^2 + L_y^2 + \mathrm{L}_y)} \qquad \text{(S2)}$$

where σ_∞ denotes the conductivity after the relaxation has reached the new equilibrium, $\sigma(t)$ is the conductivity at a certain time t, and σ(t=0) represents the initial conductivity before the gas change. The above equation assumes that the gas change takes place at time t=0. $\beta^2_{n,x,y}$ is the n’th positive root to the equation $\beta^2_{n,x,y} tan\beta^2_{n,x,y}=L_{x,y}$., where $L_{x,y}$ is the dimensionless number. $L_{x,y}=k_{ex}l_{x,y}/D_{chem}$. Eventually, the two variables k_{ex} and D_{chem} can be obtained by fitting an experimental curve (normalized conductivity vs. time) with Eq. S2. The characteristic thickness of the materials can be calculated as $L_c \approx fD_{chem}/k_{ex}$. (f≈0.69) The larger the L_c value, the more oxygen diffusion is inhibited by the surface exchange kinetics relative to the diffusion for a thin mixed ionic and electronic conductor based membrane ($L<<L_c$).

6. Calculation of oxide ion conductivity of 70 vol.% CGO-30. vol.% LSF

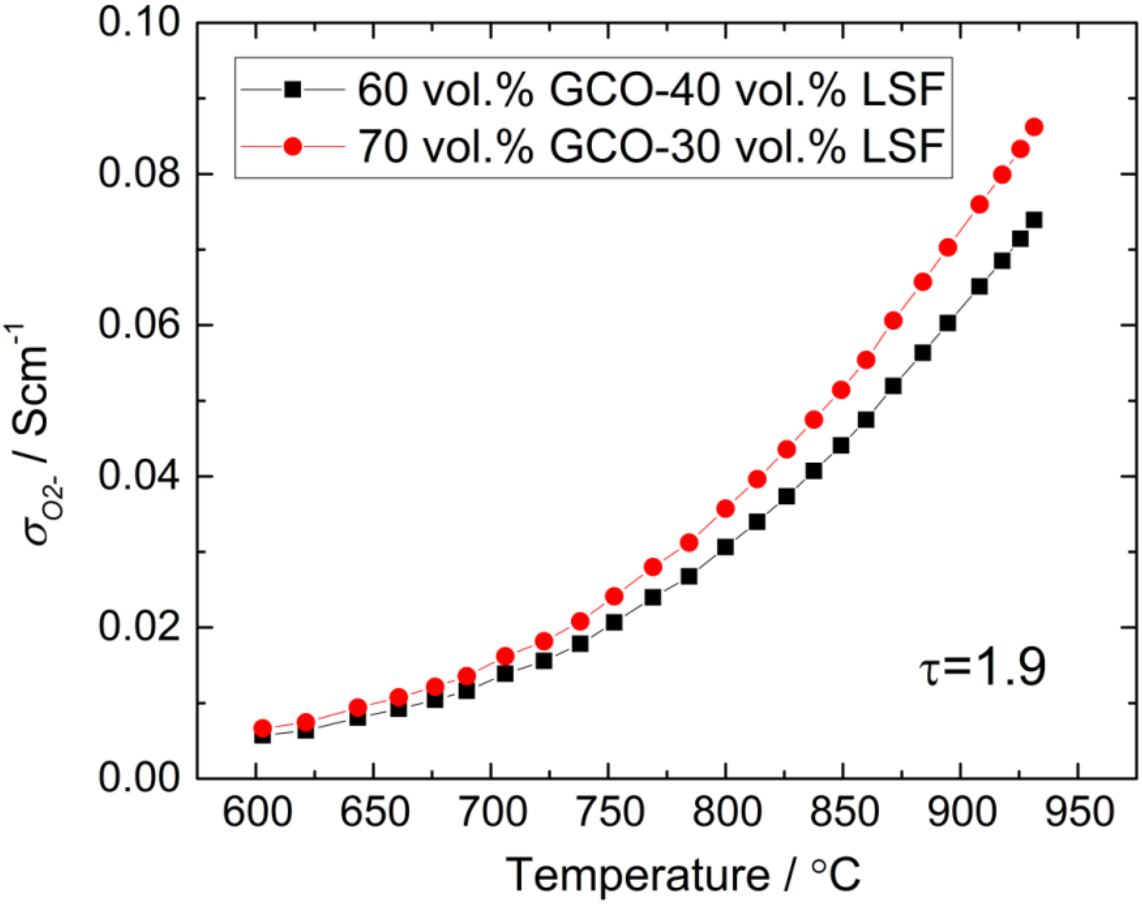

Figure. S1 The calculated oxide ion conductivity of a 60 vol.% CGO-40 vol.% LSF membrane and a 70 vol.% CGO-30 vol.% LSF membrane.

As shown in Fig S1, the oxide ion conductivity of the 60 vol.% CGO-40 vol.% LSF membrane is calculated in terms of the oxygen flux reported in Ref. [6]:

$$\sigma_{O^{2-}} = \frac{16F^2L}{RT}\frac{dJ_{O_2}}{d\ln pO_2^{"}} \qquad \text{(S3)}$$

According to Samson *et al.* [6], the flux of the CGO-based dual phase composite membrane can be calculated as

$$J_{O_2} = \frac{RT\sigma_{O^{2-}}\alpha}{16F^2L\tau}\ln\left(\frac{pO_2^{/}}{pO_2^{//}}\right) \qquad \text{(S4)}$$

where R is the gas constant, T is the temperature, F is Faraday constant, α is the volume percent of CGO, τ is the tortuosity, L is the thickness of the membrane, $pO_2^{/}$ is the oxygen partial pressure on the feed side and $pO_2^{//}$ is the oxygen partial pressure on the permeate side. Assuming the tortuosity factor in 70 vol.% CGO-30 vol.% LSF membrane is 1.9 [6], the oxide ion conductivity of a 1-mm thick 70 vol.% CGO-30 vol.% LSF membrane is simply 7/6 times that of the 1-mm thick 60 vol.% CGO-40 vol.% LSF membrane, as shown in Fig. S1. Since the total conductivity of CGO-LSF is dominated by the electronic conductivity of LSF (cf. Figure 4. of the main article), the theoretical flux of 100μm thick 70 vol.% CGO-30 vol.% LSF membrane at high pO_2 can be calculated by Wagner's equation in terms of the oxide ion conductivity in Figure. S1.

7. Calculation of electronic conductivity

The calculation of effective conductivity of dual phase is based on Bruggeman-Landauer (BL) effective medium model and the Wu and Liu (WL) model [7]. For a composite consisting of two randomly-distributed phases, the effective conductivity is described as

$$\sum_{k}^{2} \frac{\sigma_m - \sigma_k}{\left(\frac{1}{2}Z - 1\right)\sigma_m + \sigma_k} p_k = 0 \qquad \text{(S5)}$$

$$\sum_{k} p_k = 1 \qquad \text{(S6)}$$

Z is the coordination number (i.e. the number of nearest neighbouring grains), σ_k is the conductivity of each constituent phase, p_k is the volume fraction of each phase, σ_m is the effective conductivity of the composite.

The percolation p_c of the dual phase composite is, when $\sigma_1 << \sigma_2$. Z= 6 is the commonly used coordination number for three dimensional case. Percolation is in this model description achieved when

$$p_c = \frac{2}{Z} = \frac{1}{3} \qquad \text{(S7)}$$

In the analysis of the results carried out where Z is treated as a fitting parameter.

8. Calculation of gas diffusion resistance

The effect of Knudsen diffusion is negligible because the size of the pore far exceeds the size where Knudsen diffusion dominates. Hence, concentration driven mass transport is governed by ordinary binary diffusion through the finger-like microchannels. According to 3D tomography, the porosity of the finger like microchanneled substrate is 27±5%. The tortuosity of the substrate is in the range of 1.5-2 according to Wang's model [8] on the same structure.

First, the binary diffusion coefficient of N_2 and O_2 is calculated by the equation:

$$D_{AB} = \frac{3}{16}\frac{\left(4\pi kT/M_{AB}\right)^{1/2}}{n\pi\sigma_{AB}^{2}\Omega_{D}} f_{D} \qquad \text{(S8)}$$

The effective diffusivity is influenced by porosity (ρ) and tortuosity factor (τ)

$$D_{AB}^{eff} = \frac{\rho}{\tau} D_{AB} \qquad \text{(S9)}$$

The calculation of gas polarization resistance is based on Zhao *et al.* [9]. First, the limiting current density due to concentration polarization is calculated

$$i_{cs} = \left[\frac{4FD_{AB}^{eff}}{RTl}\right] p_{0} \left(\frac{p}{p-p_{0}}\right) \qquad \text{(S10)}$$

Second the concentration polarization through the porous substrate is deduced from

$$\eta_{con} = -\frac{RT}{4F}\ln\left(1-\frac{i}{i_{cs}}\right) \qquad \text{(S11)}$$

The current density is related to the measured oxygen flux.

$$i = 4FJ_{O_2} \qquad \text{(S12)}$$

The resistance arising from concentration polarization reads

$$R_{con} = \frac{\eta_{con}}{i} \qquad \text{(S13)}$$

The total resistance is calculated as

$$R_{tot} = \frac{V}{4FJ_{O_2}} \qquad \text{(S14)}$$

$$V = \frac{RT}{4F}\ln\frac{p_{O_2}^{/}}{p_{O_2}^{//}} \qquad \text{(S15)}$$

where V is the electromotive force (emf) of the membrane.

9. Rietveld refinement

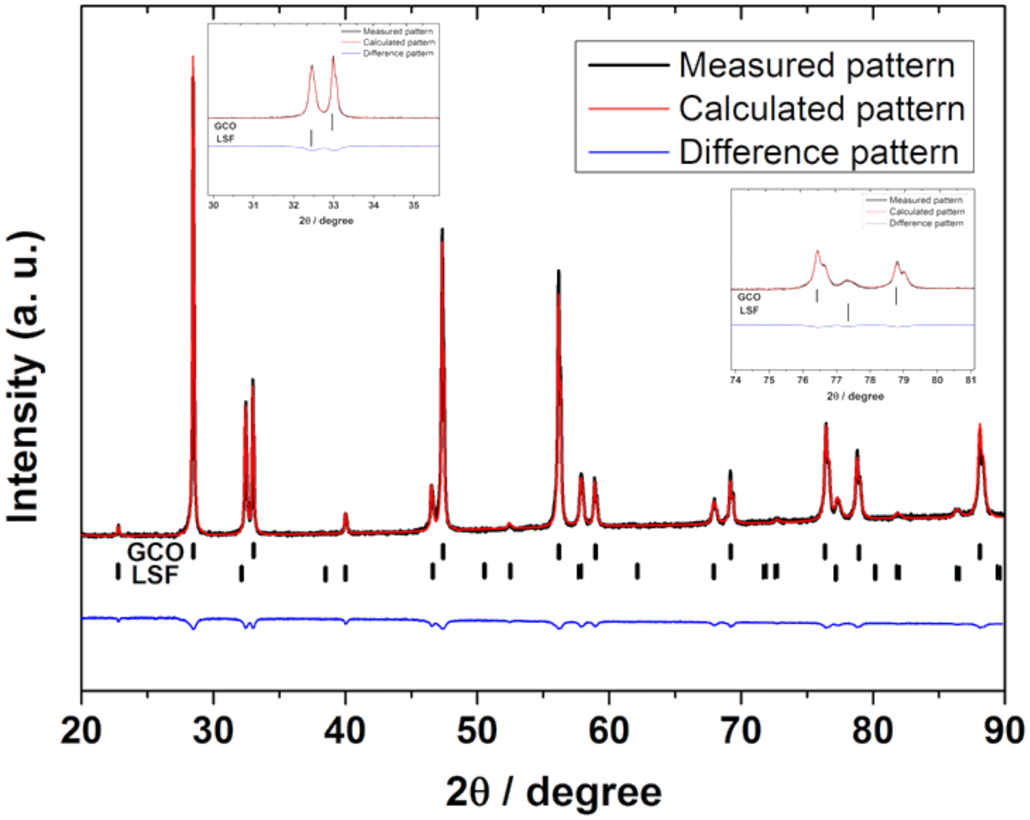

Figure. S2 Rietveld refinement patterns of the powder of the dual phase membrane sintered at 1300°C. The black curve is the measured pattern and the red curve is calculated pattern obtained from refinement.

The vertical bars are the Bragg position of each phase and the green curve means the differentiation of the fitted and experimental patterns. R_{wp}=5.42 R_p=3.99 χ^2=4.40, Zero shift=0.1871(6).

Table S1. Unit cell data determined from XRD for crushed sintered powder.

Phase	Crystal system	a (Å)	b (Å)	C (Å)	V (Å^3)	Volume %
CGO	Cubic	5.42710(7)	5.42710(7)	5.42710(7)	159.847(6)	67.25(48)
LSF	Rhombohedral	5.51759(10)	5.51759(10)	13.4985(25)	355.89(40)	32.75(48)

10. Surface exchange rate (k_{ex}) and chemical diffusion coefficient (D_{chem}) versus pO_2.

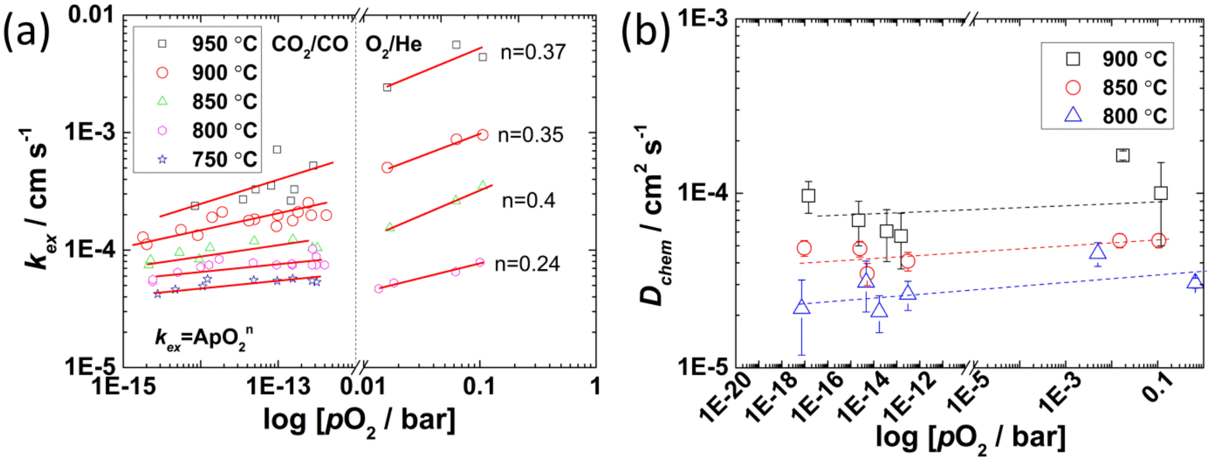

Figure. S3. (a) Oxygen surface exchange (k_{ex}) and (b) chemical diffusion coefficient (D_{chem}) of CGO-LSF as a function of oxygen partial pressure. (The lines are the best linear fit for the results)

11. Leak rate

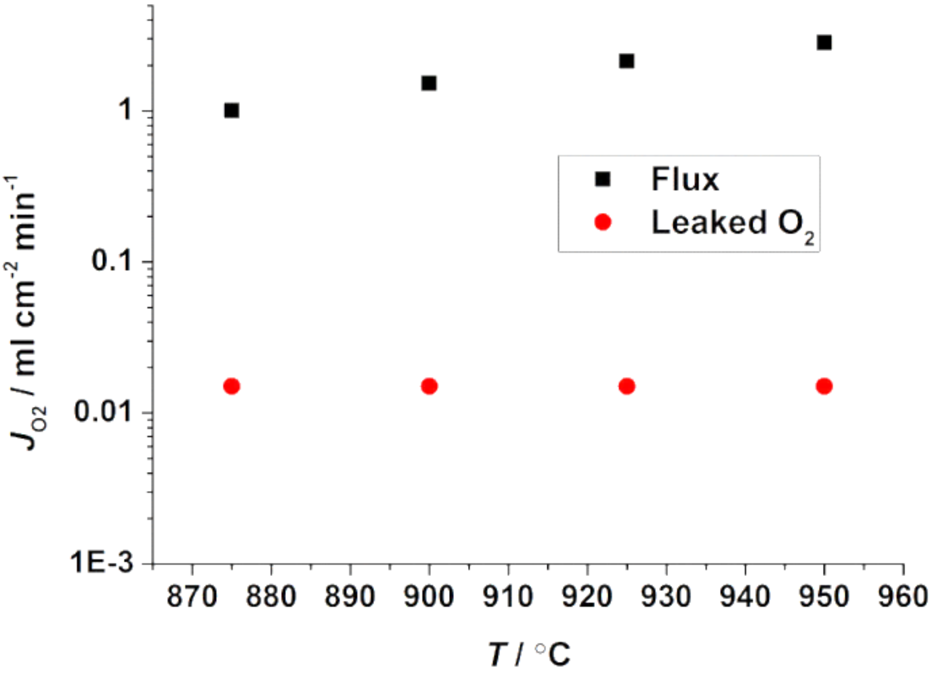

Figure. S4 A comparison between the permeated O_2 and leaked O_2.

Fig. S5 show the BSEM micrograph of a CGO-LSF sample after ECR measurement in a mixture of CO and CO_2. It can be clearly seen that particles with an average size of 2 μm appear on the surface. The EDS mapping confirms that the particle is rich in Sr.

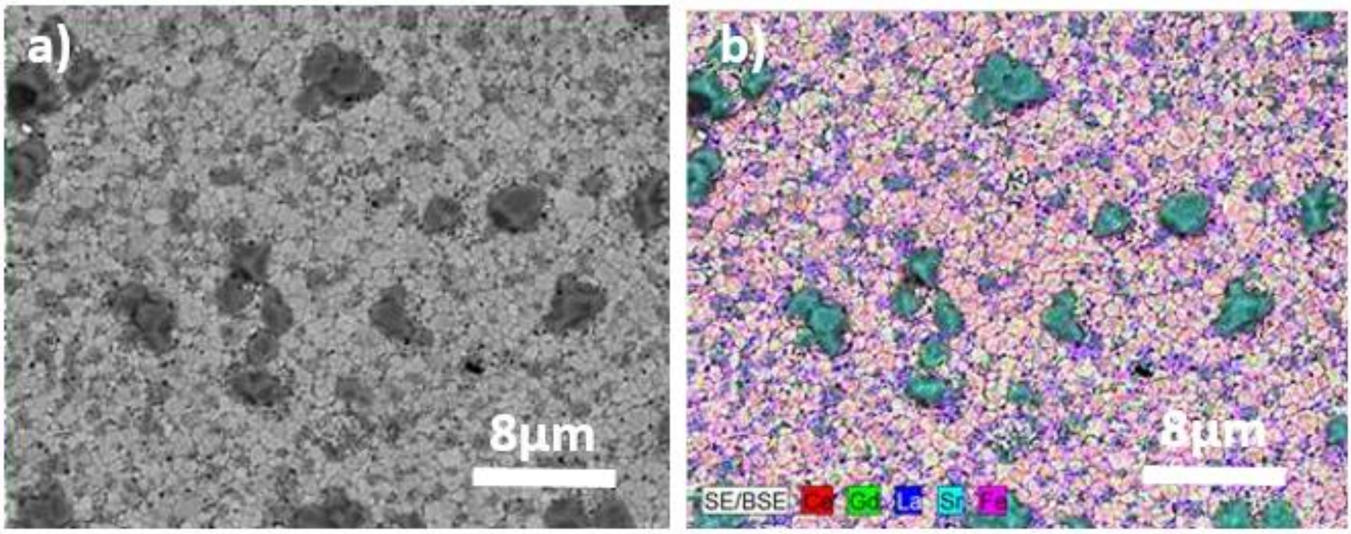

Figure. S5 (a) BSEM micrograph and (b) EDS elemental mapping of a CGO-LSF bar after ECR measurement in a mixture of CO and CO_2.

12. Derivation of average oxygen partial pressure in a Plug-Flow Setup and under CSTR conditions (Continuously Stirred Tank Reactor)

The oxygen permeation measurements of this work were carried out under conditions resembling either a Plug-Flow case or a Continuously Stirred Tank Reactor (CSTR) case. The flux measurement setup for test of the small circular membranes with a large open volume above is best treated as a CSTR case, where the average oxygen partial pressure on the permeate side of the membrane is equivalent to that of exit (or downstream) gas ($pO_{2out}=pO_2''$) since only negligible concentration gradients exist along the surface of the membrane. Hence, it is the pO_2 measured at the exit that is used when assessing the driving force for the oxygen flux. For simplicity, and to relate to directly measured quantities only, also the exit pO_2 was used when assessing the driving force over the membranes under various flows in Figure 9. However, for this setup where the extension of the cell (5 cm) is much larger than the height of the gas flow volume above it (~1 mm) the situation is much more plug-flow-like than CSTR like, i.e. there is a significant variation in pO_2 along the gas flow and thus over the active membrane area. The detailed situation will depend on the flow rate; For large gas flows it becomes plug flow like and for small flows eventually CSTR like. Therefore, the driving force for the flux decays from inlet towards to the outlet. To quantify the effects of the varying driving force, a simple model was setup to represent the plug flow case allowing calculation of the average driving force over the membrane (or characteristic pO_2). This was done segmenting the area in n segments and conducting an averaging. The oxygen concentration in the permeate gas in each segment is corrected for the dilution that occurs due to the permeated oxygen that is generated from the previous segments of the membrane.

$$\frac{\sum_{0}^{n} \frac{RT}{4F} \ln \frac{p_{O_2}^{/}}{p_{O_2(i)}}}{n} = \overline{V} \tag{S16}$$

$$\overline{V} = \frac{RT}{4F} \ln \frac{p_{O_2}^{/}}{p_{O_2 avg}} \tag{S17}$$

Where $\overline{V}$ is the average emf, n is the number of the segments used in the sectioning of the membrane, $p_{O_2(i)}$ is the oxygen partial pressure at segment i ($p_{O_2(0)}$ represents the pO_2 at the inlet; the impurity pO_2 level in the sweep gas is negligible). p_{O_2avg} is the average oxygen partial pressure on the permeate side (the characteristic pO_2 (pO_{2avg} which will give the correct average EMF over the membrane). The treatment here follows the one in Ref [10] but for the case of inert gases.

As illustrated in Figure S6 the larger the flow the more significant is the relative variation of the oxygen partial pressure (back mixing opposite to the flow direction *via* diffusion is neglected in the simplified treatment).

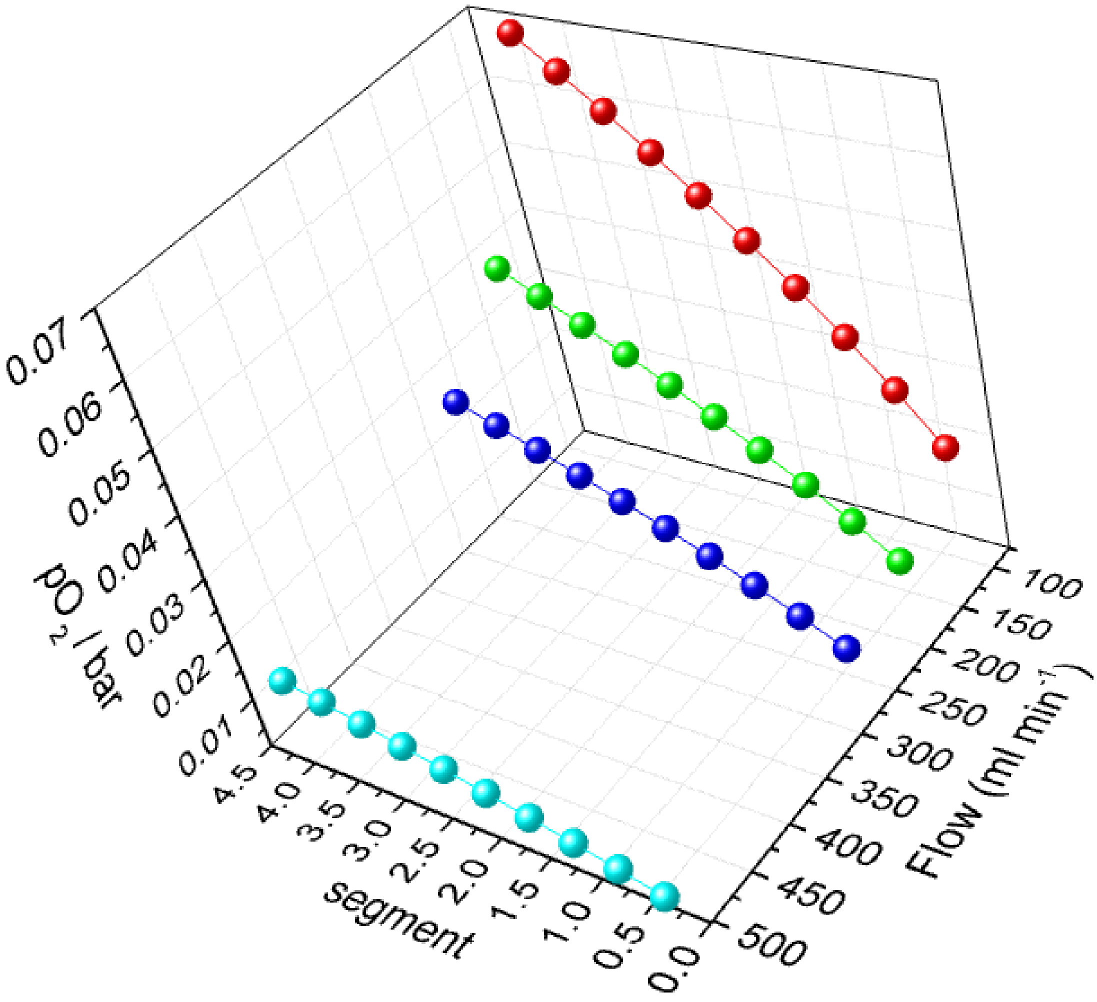

Figure S6 position dependence of pO_2 at the permeate side of the 5×5cm^2 membrane as function of flow of sweep gas at 900°C. Feed gas: O_2, sweep gas: N_2.

Table S2 Comparison between the apparent driving forces at 800°C obtained from the CSTR- and the Plug flow model.

Sweep rate / ml min^{-1}	$pO_{2\,in}$	pO_{2out}	$pO_{2\,avg}$	$Ln(pO_2'/pO_2'')$ *CSTR*	$Ln(pO_2'/pO_2'')$ *Plug flow*
89.46	1.04×10^{-4}	0.069	0.031	2.68	3.47
174.47	5.24×10^{-5}	0.041	0.019	3.18	3.96
258.08	3.53×10^{-5}	0.030	0.013	3.51	4.30
511.94	1.80×10^{-5}	0.016	0.007	4.12	4.89

Now having a characteristic pO_2 we can plot the flux data as a function of the average driving force rather than versus the driving force prevailing at outlet. This is a more correct representation of the situation. Results are illustrated below. The observed proportionality between flux and driving force is maintained from figure 9 but the slope of the curves decrease. The linearity of the trend curves becomes better when using the plug flow model than when using the driving force assessment based on exit conditions.

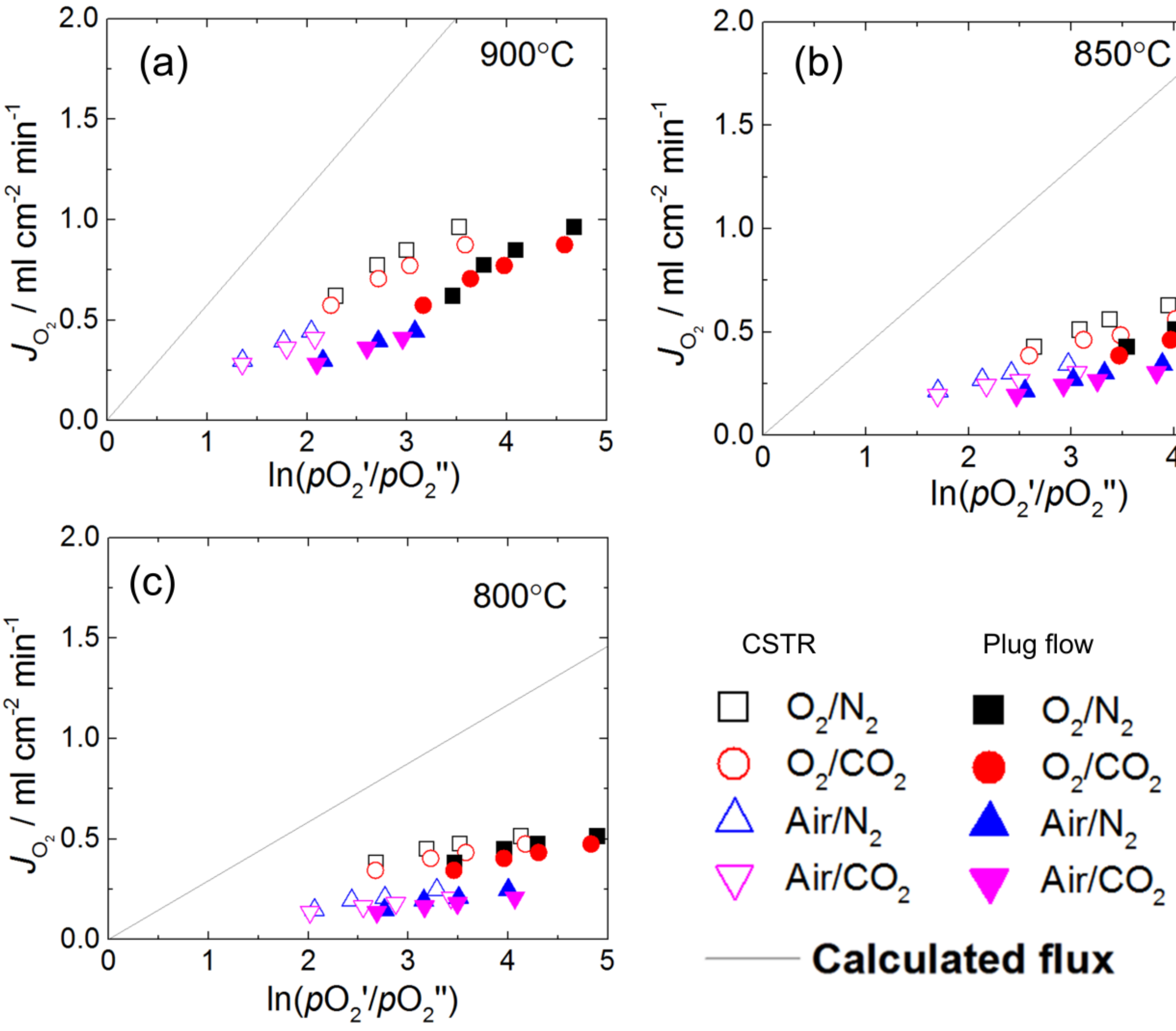

Figure S7 Comparison between the fluxes as a function of driving force obtained from CSTR model and plug flow model.

References

1. Søgaard, M.; Hendriksen, P. V.; Mogensen, M.; Poulsen, F. W.; Skou, E., Oxygen Nonstoichiometry and Transport Properties of Strontium Substituted Lanthanum Cobaltite. *Solid State Ionics* **2006,** *177* (37–38), 3285-3296.
2. Søgaard, M.; Vang Hendriksen, P.; Mogensen, M., Oxygen Nonstoichiometry and Transport Properties of Strontium Substituted Lanthanum Ferrite. *J. Solid State Chem.* **2007,** *180* (4), 1489-1503.
3. Wang, Y.; Hu, B.; Zhu, Z.; Bouwmeester, H. J. M.; Xia, C., Electrical Conductivity Relaxation of $Sr_2Fe_{1.5}Mo_{0.5}O_{6-\delta}$-$Sm_{0.2}Ce_{0.8}O_{1.9}$ Dual-Phase Composites. *J. Mater. Chem. A* **2014,** *2* (1), 136-143.
4. Zhang, Z.; Zhou, W.; Chen, Y.; Chen, D.; Chen, J.; Liu, S.; Jin, W.; Shao, Z., Novel Approach for Developing Dual-Phase Ceramic Membranes for Oxygen Separation through Beneficial Phase Reaction. *ACS Appl. Mater. Interfaces* **2015,** *7* (41), 22918-22926.

5. Carslaw, H. S.; Jaeger, J. C., Conduction of Heat in Solids. *Oxford: Clarendon Press, 1959, 2nd ed.* **1959,** *1*.
6. Samson, A. J.; Søgaard, M.; Hendriksen, P. V., (Ce,Gd)$O_{2-\delta}$-Based Dual Phase Membranes for Oxygen Separation. *J. Membr. Sci.* **2014,** *470*, 178-188.
7. Wu, Z.; Liu, M., Modelling of Ambipolar Transport Properties of Composite Mixed Ionic-Electronic Conductors. *Solid State Ionics* **1996,** *93* (1–2), 65-84.
8. Zhiwen, W. Master thesis, University of Science and Technology of China, **2014**.
9. Zhao, F.; Armstrong, T. J.; Virkar, A. V., Measurement of O_2-N_2 Effective Diffusivity in Porous Media at High Temperatures Using an Electrochemical Cell. *J. Electrochem. Soc.* **2003,** *150* (3), A249-A256.
10. Jensen, S. H.; Hauch, A.; Hendriksen, P. V.; Mogensen, M., Advanced test method of solid oxide cells in a plug-flow setup. *J. Electrochem. Soc.* **2009,** *156* (6), B757-B764.

Chpater 7: Enhanced mixed ionic and electronic conductivity of Pr-doped $Gd_{0.1}Ce_{0.9}O_{1.95-\delta}$

Shiyang Cheng, Christodoulos Chatzichristodoulou, Martin Søgaard, Andreas Kaiser and Peter Vang Hendriksen*

* Corresponding author: shic@dtu.dk

Department of Energy Conversion and Storage, Technical University of Denmark, Risø campus, Frederiksborgvej 399, DK-4000 Roskilde, Denmark

Abstract

The oxygen permeation flux of $Ce_{0.9}Gd_{0.1}O_{1.95-\delta}$ (CGO)-based oxygen separation membrane under oxidizing conditions is limited by the electronic conductivity of the material. This work aims to enhance the achievable bulk ambipolar conductivity of GCO by co-doping with the redox active element Pr. Gd/Pr co-doped ceria with the composition of $Pr_xGd_{0.1}Ce_{0.9-x}O_{2-\delta}$ (x=0, 0.02, 0.05, 0.08, 0.15, 0.25, 0.3 and 0.4) was prepared by solid state reaction. X-ray powder diffraction (XRD) indicates that Pr is completely dissolved in the cubic fluorite structure up to 40 cat.%. The thermal expansion coefficient (TEC) is observed to show nonlinear behaviour above 400 °C. The effect is related to the partial reduction of Pr at elevated temperature and increases with increasing Pr concentration. The electronic and total conductivities of the samples were measured as a function of temperature and oxygen partial pressure. Within the range from 10 cat.% to 15 cat.%, a drastic decrease of the activation energy of electron hole mobility is observed, which is proposed to result from the formation of continuous percolating Pr in the crystal structure. The ionic conductivity for the compositions undergoes a “hump” where the maximum ionic conductivity is observed for $Pr_{0.15}Gd_{0.1}Ce_{0.75}O_{1.95-\delta}$. The experimental oxygen flux of $Pr_{0.05}Gd_{0.1}Ce_{0.85}O_{1.95-\delta}$ is higher than that of GCO by one order of magnitude due to the enhanced electronic conductivity albeit still being limited by the electronic conductivity. The estimated maximum oxygen permeation flux of a 10 μm thick $Pr_{0.4}Gd_{0.1}Ce_{0.9}O_{1.95-\delta}$ -based membrane exceeds 10 Nml cm^{-2} min^{-1} at 900 °C under a small oxygen potential difference ($0.21/10^{-3}$ bar) which in terms of transport is promising for oxygen production and in oxy-fuel combustion.

Key words: Pr/Gd co-doped ceria; oxygen separation membrane; electronic conductivity; ionic conductivity

1. Introduction

Dense ceramic oxygen transport membranes (OTMs) have received considerable attention in recent years. They can be used to produce high purity oxygen for medical purposes, supply of oxygen in the steel industry, oxy-fuel combustion schemes, as well as in the cement and glass industries. OTMs can also be thermally integrated with a biomass gasifier that allows to produce syngas by partial oxidization of methane [1].

Acceptor doped-ceria has among other applications been intensively studied for several applications e.g. use in solid oxide fuel cells (SOFCs) [2], solid oxide electrolysis cells (SOECs) [3], electrocatalysis [4] and OTMs [5]. Gd-doped ceria (GCO) is be of particular interest for use in OTMs owing to the high oxide ion conductivity (0.12 Scm^{-1} for $Gd_{0.1}Ce_{0.9}O_{1.95-\delta}$ at 900 °C [6]), appreciable electrocatalytic activity and excellent chemical stability under harsh reducing and even corrosive gaseous conditions [2, 7]. Kaiser *et al.* [8] reported that the oxygen permeation flux of a 27-μm thick asymmetric 10 at.% Gd-doped ceria (GCO10)-based membrane exceeds 10 N ml cm^{-2} min^{-1} under a gradient of air/H_2 at 850 °C [9], which shows good perspectives for the OTM technology provided that long lifetime is achievable. However, the oxygen flux of ceria based membranes is relatively low when mildly reducing conditions are imposed on the permeate side (CO_2-sweep or a slight vacuum) because the low electronic conductivity of ceria ($<1\times10^{-3}$ Scm^{-1} at 900 °C in air [10]) limits bulk ambipolar diffusion. The low electronic conductivity also results in the slow oxygen surface exchange rate [11, 12], which may further limit the oxygen flux. To provide technologically relevant oxygen fluxes for high pO_2 applications, such as production of pure oxygen and in oxy-coal combustion conditions, the electronic conductivity of GCO needs to be enhanced preferably to a value close to that of the ionic conductivity (maximum ambipolar conductivity).

Doping redox active elements is a feasible strategy that can enhance the electronic conductivity of ceria [13-18]. Among the potential rare earth elements, Praseodymium (Pr) and Terbium (Tb) show significant redox activity under mildly reducing conditions (pO_2= 1×10^{-8}-1 bar). Upon the reduction of Pr and Tb, electron hole hops between the trivalent and tetravalent dopants so that the electronic conductivity of the host ceria may be boosted. For instance, the *p*-type electronic conductivity of 3 cat.% Pr-doped $Gd_{0.2}Ce_{0.8}O_{1.9-\delta}$ is enhanced (by ca. 10 times) in the temperature range from 600 °C to 750 °C [13]. The electronic conductivity of Tb and Pr dual-doped ceria can be modified by changing the ratio between the two dopants: higher relative amount of Pr gives rise to higher electronic conductivity, but also leads to larger chemical expansion [16]. Bishop et al. also found that doping Pr in ceria may induce large chemical expansion which affects the thermomechanical property. It is thus of importance to examine if an optimum amount of Pr doping exists that ensures satisfactory thermomechanical properties along with sufficient electronic conductivity.

When dissolved in the ceria lattice, Pr exists in mixed valence states (Pr^{3+} and Pr^{4+}) [16]. Upon increasing pO_2 and decreasing temperature, the concentration of Pr^{4+} increases accompanied by a reduction of oxygen vacancy concentration ($2\,\mathrm{Pr}_{Ce}^{/}+1/2\,O_2+V_O^{\bullet\bullet}=2\,\mathrm{Pr}_{Ce}^{\times}+O_O^{\times}$). In order to achieve simultaneously considerable oxygen vacancy and electron hole concentrations, different concentrations of Pr were doped in $Gd_{0.1}Ce_{0.9}O_{1.95-\delta}$ (partial Pr-substitution for Ce) in this work. This material is expected to have high oxygen vacancy concentration due to the doping with the valence stable trivalent Gd. The influence of dopant concentration on the total, electronic and ionic conductivity was investigated using ion-blocking Hebb-Wagner polarization in conjunction with electrochemical impedance spectroscopy. The influence of various degrees of Pr substitution in GCO on the oxygen permeation flux was addressed to assess the potential of these materials for oxygen separation applications.

2. Theoretical consideration

In $Pr_xGd_{0.1}Ce_{0.9-x}O_{1.95-\delta}$, negatively charged defects are formed by partial Gd (III)- and Pr (IV)- substitution for Ce (IV) in the cerium sublattice. Assuming ideal behaviour for Pr and Ce reduction in the lattice (invariable entropy and enthalpy), the defect reactions can be written:

$$Gd_2O_3 \xrightarrow{CeO_2} 2Gd_{Ce}^{/}+V_O^{\bullet\bullet}+3O_O^{x} \qquad (1)$$

$$2\,\mathrm{Pr}_{Ce}^{x}+O_O^{x}\rightarrow 2\,\mathrm{Pr}_{Ce}^{/}+V_O^{\bullet\bullet}+1/2\,O_2(g) \qquad (2)$$

$$K_{\mathrm{Pr}}=\exp\left(-\frac{\Delta H_{\mathrm{Pr}}^{0}-T\Delta S_{\mathrm{Pr}}^{0}}{RT}\right)=\frac{P_{O_2}^{1/2}\cdot\left[V_O^{\bullet\bullet}\right]\cdot\left[\mathrm{Pr}_{Ce}^{/}\right]^2}{\left[O_O^{x}\right]\cdot\left[\mathrm{Pr}_{Ce}^{x}\right]^2} \qquad (3)$$

$$2Ce_{Ce}^{x}+O_O^{x}\rightarrow 2Ce_{Ce}^{/}+V_O^{\bullet\bullet}+1/2\,O_2(g) \qquad (4)$$

$$K_{Ce} = \exp\left(-\frac{\Delta H_{Ce}^{0} - T\Delta S_{Ce}^{0}}{RT}\right) = \frac{P_{O_2}^{1/2} \cdot \left[V_O^{\bullet\bullet}\right] \cdot \left[Ce_{Ce}^{/}\right]^2}{\left[O_O^x\right] \cdot \left[Ce_{Ce}^x\right]^2} \tag{5}$$

The mass, site and electroneutrality conditions for co-doping Gd and Pr in ceria are:

$$\left[Ce_{Ce}^{/}\right] + \left[\mathrm{Pr}_{Ce}^{/}\right] + \left[Gd_{Ce}^{/}\right] = 2\left[V_O^{\bullet\bullet}\right] \tag{6}$$

$$\left[Ce_{Ce}^{/}\right] + \left[\mathrm{Pr}_{Ce}^{/}\right] + \left[Gd_{Ce}^{/}\right] + \left[Ce_{Ce}^{x}\right] + \left[\mathrm{Pr}_{Ce}^{x}\right] = 1 \tag{7}$$

$$\left[\mathrm{Pr}_{Ce}^{/}\right] + \left[\mathrm{Pr}_{Ce}^{x}\right] = x \tag{8}$$

$$\left[V_O^{\bullet\bullet}\right] + \left[O_O^x\right] = 2 \tag{9}$$

Based on the above defect reactions, a Brouwer diagram indicating the various regimes of dominating defects can be constructed. This is shown in Fig. 1. The electrical conductivity and oxygen nonstoichiometry were in this work investigated in the pO_2 range highlighted by the blue region in the diagram. Under oxidizing conditions, the redox reaction of Pr prevails, which contributes the p-type electronic conductivity [19, 20]. Assuming the reduction of cerium under oxidizing conditions is negligible, the variation in oxygen non-stoichiometry (δ) arising from redox of Pr is given by:

$$K_{\mathrm{Pr}} = \frac{p_{O_2}^{1/2}\delta(2\delta)^2}{(1.95-\delta)(x-2\delta)} \tag{10}$$

The equilibrium constant for the reduction reaction of Pr can be obtained by fitting Eq. 10 to oxygen nonstoichiometry vs. pO_2 -data.

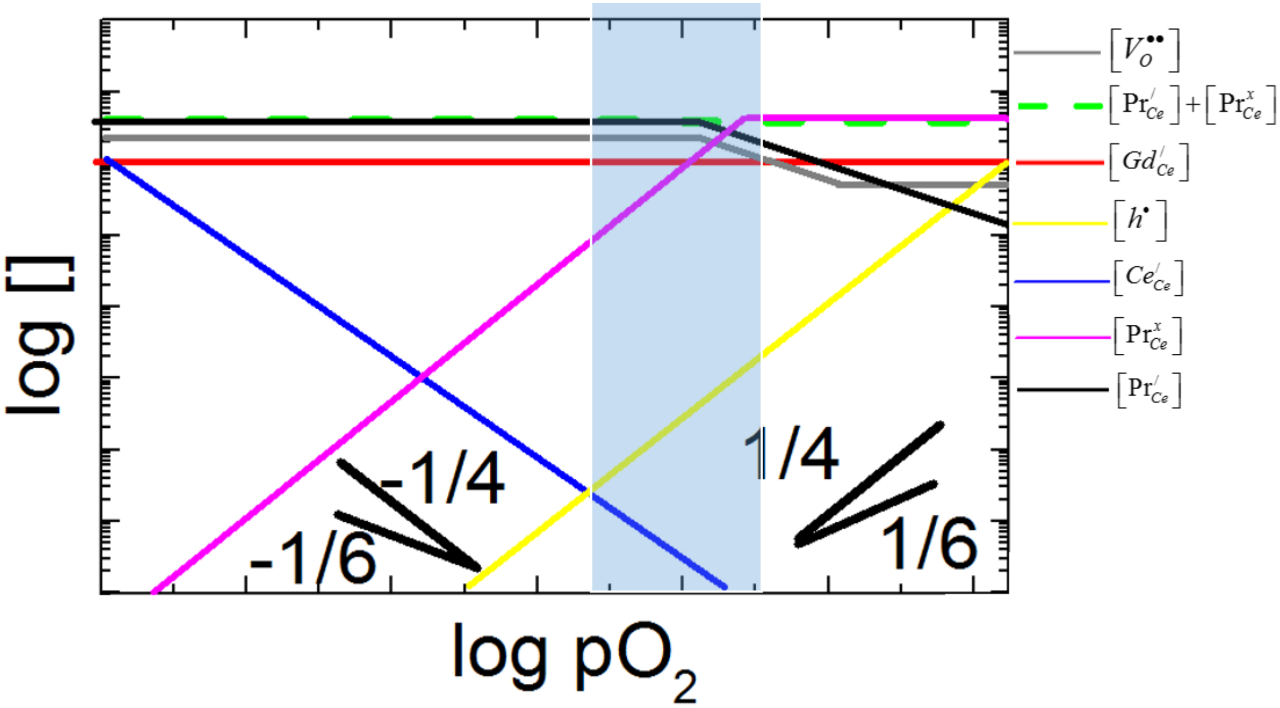

Fig. 1 Brouwer diagram for $Pr_{0.4}Gd_{0.1}Ce_{0.5}O_{1.95-\delta}$.. The blue regime corresponds to the defect range accessed experimentally in this work. (the electron hole refers to O2p band: $V_O^{\bullet\bullet}+1/2O_2(g)=2h^{\bullet}+O_O^x$)

3. Experimental

3.1. Sample preparation and phase identification

The specimens in this work were synthesized by solid state reaction. Stoichiometric amounts of starting powders of $Ce(NO_3)_3 \cdot 6H_2O$ (Sigma Aldrich 99.99%), Gd_2O_3 (Alfa Aesar 99.9%), Pr_6O_{11} (Alfa Aesar 99.9%) and Co_3O_4 (Alfa Aesar 99.9%, for cobalt containing samples) were mixed by ball milling in ethanol for 24 hours, and subsequently calcined at 1000 °C for 5 hours. The powders were then uniaxially cold pressed at 400 MPa followed by isostatic pressing at 600 MPa. Cobalt-containing and cobalt-free pellets were sintered at 1200 °C and 1600 °C for 10 hours, respectively.

The crystal structures of the crushed sintered specimens were characterized by X-ray powder diffraction (XRD). The XRD patterns were obtained with Cu Kα radiation using a Bruker Robot operating in Bragg-Brentano geometry in the 2θ range from 20° to 90°. The obtained XRD patterns were indexed with the ICCD (International Centre for Diffraction Data) database by means of the software DIFFRAC plus. The lattice parameter of each sample was calibrated with LaB_6 as internal reference, using the software WINPOW. Scanning electron microscopy (SEM) was carried out on a FE-SEM Zeiss Supera 35 electron microscope using an acceleration voltage of 15 kV.

3.2. *Thermogravimetry*

Thermogravimetric analysis (TGA) was performed using a Netzsch STA 409CD thermogravimeter and a Netzsch TG 439 thermal balance. The samples were prepared by uniaxially pressing the powder into pellets at a pressure of 400 MPa in a capillary die (ø = 0.5 cm). Porous samples were obtained by sintering the green sample at 1000 °C for 3 hours at heating and cooling rate of 2 °C min^{-1}. The data were corrected for buoyancy effects by measuring a same volume of Al_2O_3 powder under the same condition.

3.3. *Dilatometry*

Dilatometry measurements were performed using a differential contact dilatometer (DIL 402CD, NETZSCH GmbH, Germany). The samples are rectangular bars with a dimension of $1 \times 1 \times 10$ mm^3. An Al_2O_3 reference bar was measured simultaneously with the sample. The heating rate was 3 °C min^{-1} to a final temperature of 1000 °C. All the measurements were conducted in air with a total gas flow of 50 ml min^{-1} controlled by a mass flow controller.

3.4. *Impedance spectroscopy*

The total conductivity of each specimen was measured by Electrical Impedance Spectroscopy (EIS). Prior to the electrical measurements, symmetric $(La_{0.6}Sr_{0.4})_{0.99}CoO_{3-\delta}$ (LSC) electrodes were screen printed on the both sides of a 1-mm thick pellet (ø = 10 mm), followed by sintering at 1000 °C for 2 hours to obtain good adhesion between the specimen and the electrodes. The LSC electrodes were then covered with Pt layers (current collector) by hand painting in order to eliminate the contact resistance between the Pt current collector and the sample. EIS was carried out in the temperature range from 600 °C to 900 °C using a Solartron 1260 impedance spectrometers within the frequency range from 3 MHz down to 0.1 Hz under the amplitude of 20 mV. Impedance spectra were analysed and fitted by the software package “Z-view” and “Z-plot”. The specimens were placed in a closed alumina chamber in which the atmosphere was controlled by a mass flow controller. The oxygen partial pressure around the samples was monitored by a *in-situ* zirconia-based sensor.

3.5. *Microelectrode ion-blocking Hebb-Wagner polarization measurements*

The electronic conductivity of each sample was measured by means of a microelectrode ion-blocking Hebb-Wagner polarization method. Prior to the measurements, 1-mm thick dense circular samples (ø =10mm) were polished by SiC #300 sand papers, followed by further polishing using SiC #1000 and #1600 sand papers. The Hebb-Wagner measurement cell is schematically presented in Fig. 2. Similar setups have been used in a number of past works [13, 21-24]. A Pt microelectrode with a contact radius of 100-500 μm was placed on the sample under an external load. The periphery of the Pt microelectrode was sealed using a customized glass sealant (MgO/sodium aluminosilicate glass composites, 30/70 vol. %) to block the oxygen surface exchange. The Hebb-Wagner cell was mounted in between two Pt current collectors inside a furnace, allowing the atmosphere to be controlled. The oxygen partial pressure surrounding the reference/counter electrode was maintained at 0.21 atm by flowing 100 ml min^{-1} of air across the cell. The cell was initially heated up to 950 °C at the rate of 1 °C min^{-1} to soften the glass sealant, followed by cooling down to 750 °C at the same rate to achieve a gas tight solidified glass. The polarization measurement was then performed by stepwise varying voltage in 25 mV steps in the range from -800 mV to 200 mV. The steady state was achieved by dwelling for 12 minutes (more than 100 times the theoretical time to achieve equilibrium) in each step. The oxygen partial pressure in the vicinity of the microelectrode is calculated from

$$a_{O2,micro} = a_{O2,\mathrm{ref}} \exp(\frac{4FV}{RT}) \qquad (11)$$

where $a_{O2,\ micro}$ and $a_{O2,\ ref}$ is the oxygen activity near the microelectrode and reference electrode, respectively. V is the polarization voltage applied on the microelectrode relative to the reference/counter electrode. The sum of electron and electron hole conductivity in the vicinity of the ion-blocking microelectrode can, under a set of assumptions [13, 23, 25], be calculated in terms of the derivative of the steady state I-V curve:

$$\frac{\partial I}{\partial V} = 2\pi r_c (\sigma_e + \sigma_h) \qquad (12)$$

where r_c is the radius of the spherical microelectrode. If the microcontact is circular rather than spherical, the factor $2\pi r_c$ is replaced by $4r_c$ [23].

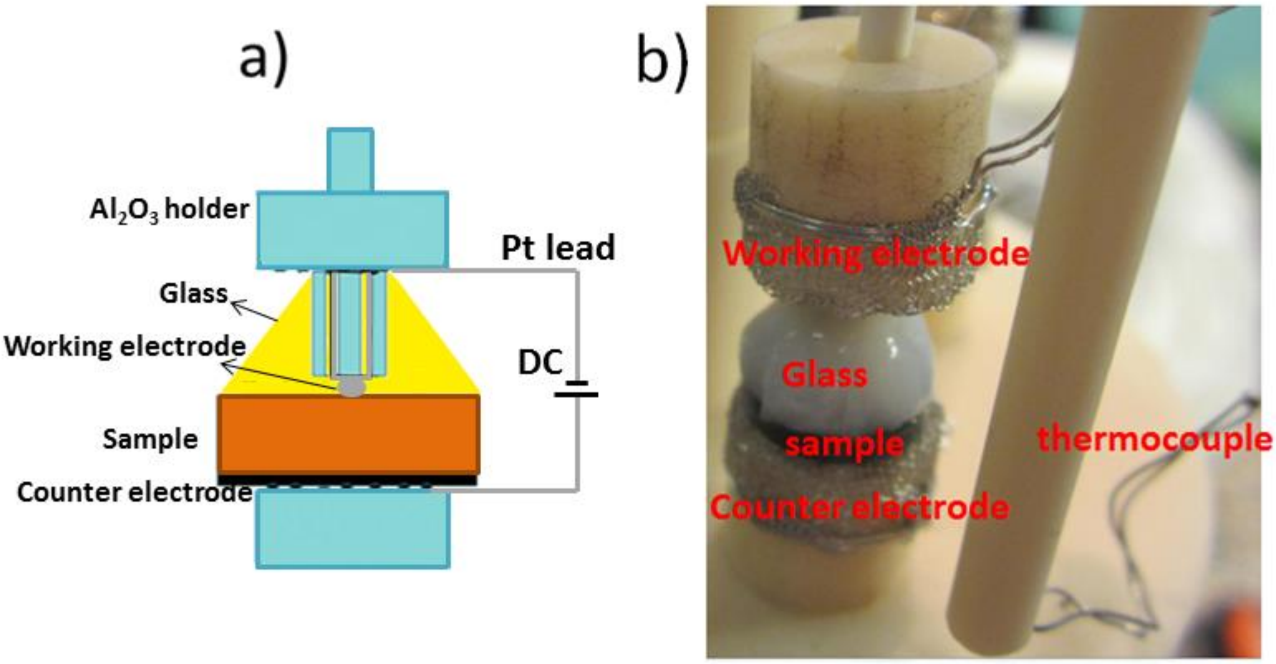

Fig. 2 (a) Schematic illustration and (b) image of the Hebb-Wagner polarization setup.

4. Results

4.1. *X-ray diffraction*

XRD powder diffraction patterns of $Pr_xGd_{0.1}Ce_{0.9-x}O_{1.95-\delta}$ (x=0.02, 0.05, 0.08, 0.15, 0.25, 0.3 and 0.4) and $Co_xPr_{0.05}Gd_{0.1}Ce_{0.85}O_{1.95-\delta}$ (x=0.02 and 0.05) are shown in Fig. 3. Zero shifts were calibrated using the pattern of the internal standard LaB_6. No significant shift of the (111) reflection was detected, indicating an insignificant influence of the dopant on the lattice parameter. No indication of secondary phases originating from side reactions or precipitation of insolvable dopants can be detected within the resolution limit of the XRD, which suggests that the solubility limit of Pr in CGO is more than 40 at.%. This is in accordance with the solubility limit of 70 at.% reported by Taksu *et al.* [26] for partial Pr-substitution for cerium in $Pr_xCe_{1-x}O_{1-0.5x}$ at 1400 °C.

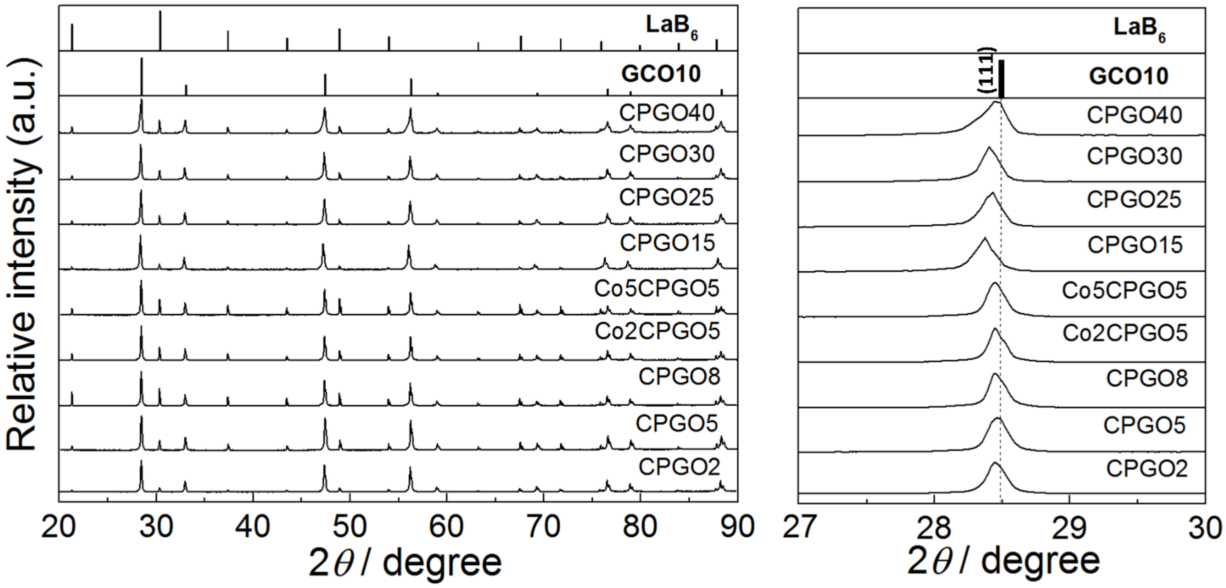

Fig. 3 Powder X-ray diffraction patterns of $Pr_xGd_{0.1}Ce_{0.9-x}O_{1.95-\delta}$ (x=0.02, 0.05, 0.08, 0.15, 0.25, 0.3 and 0.4) and $Co_xPr_{0.05}Gd_{0.1}Ce_{0.85}O_{1.95-\delta}$ (x=0.02 and 0.05). Inset: zoom corresponding to the (111) reflection in the 2theta range of 28-29 degrees.

4.2. *Lattice parameter and microstructure*

The lattice parameter from XRD is shown in Fig. 4 along with the values calculated using Kim's empirical formula [27]

$$a = 0.5413 + \sum_k \left(0.022\Delta r_k + 0.00015\Delta z_k\right) m_k \qquad (13)$$

where a is the unit cell parameter of the fluorite oxide solution at room temperature, ($\Delta r_k = r_k - r_h$) is the difference in ionic radius of the kth dopant (r_k) and the host cation (r_h) in eight-fold coordination from Shannon's compilation [28], ($\Delta z_k = z_k - z_h$) is the valence difference between dopant and host, and m_k is the mole percent of the kth dopant in the form of MO_x.

As displayed in Fig. 4, the experimentally observed lattice parameter approaches the calculated one assuming that all Pr is tetravalent (Pr^{4+}) and lies far from the calculated curve for Pr^{3+}. This suggests that the concentration of tetravalent Pr (Pr^{4+}) prevails in the Pr-doped CGO after slow cooling in air. Due to the close value between ionic radii of Pr^{4+} (CN=VIII 0.96 Å [28]) and Ce^{4+} (CN=VIII 0.97 Å [28]) the lattice parameter does not vary with Pr, in agreement with ref. [29]. The lattice parameter of the cobalt oxide containing samples does not vary with cobalt concentration, which indicates that the smaller sized cobalt (charge=2, CN=VIII 0.9 Å [28]) is not completely doped inside the crystal lattice of $Pr_{0.05}Gd_{0.1}Ce_{0.85}O_{1.95-\delta}$. Lewis *et al.* [30] also found that the lattice constant of CGO is not influenced by the addition of cobalt oxide because the cobalt is effectively insoluble to the CGO lattice, in agreement with this work.

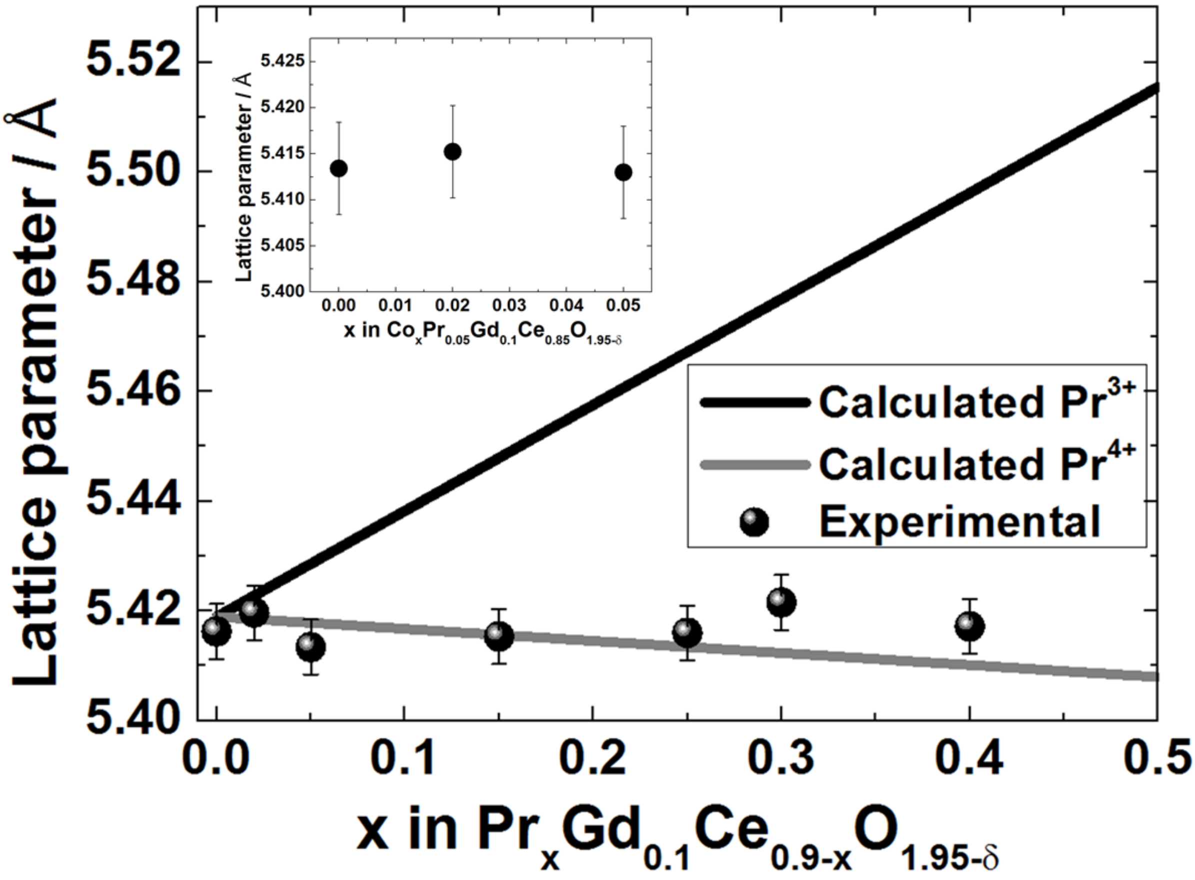

Fig. 4 Experimental and calculated lattice parameters vs. Pr concentration. Inset: lattice parameter vs. x in $Co_xPr_{0.05}Gd_{0.1}Ce_{0.9}O_{1.95-\delta}$.

Fig. 5 displays the microstructure of thermally etched samples. The average grain size of the cobalt oxide free samples sintered at 1600 °C lies in the range from 2 μm to 5 μm. The cobalt oxide containing samples sintered at 1200 °C are completely dense with relatively small average grain size (200-500 nm). This elucidates that cobalt oxide serves as a sintering aid with respect to the sintering of doped ceria, which is well in line with literature [31]. Table 2 summarizes the specific composition, sintering temperature (T_S), theoretical density, measured density, relative density and average grain size of the specimens in this work.

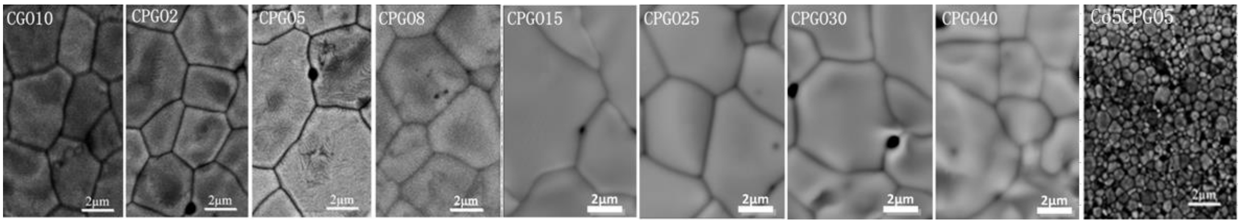

Fig. 5 Back-scattered SEM micrographs of polished and thermally etched surface of each sample.

Table 1. **Sintering temperature, density and grain size of pure and Pr-doped CGO.**

Abbreviated name	**Composition**	**T_s / °C**	**Theoretical density/ gcm^{-3}**	**Measured density / g cm^{-3}**	**Relative density %**	**d_g/μm**
CGO	$Gd_{0.1}Ce_{0.9}O_{1.95}$	1600	7.20	7.10	98.6	3.0±1.0
CPGO2	$Pr_{0.02}Gd_{0.1}Ce_{0.88}O_{1.95-\delta}$	1600	7.18	6.90	96.1	4.0±1.0
CPGO5	$Pr_{0.05}Gd_{0.1}Ce_{0.85}O_{1.95-\delta}$	1600	7.24	6.95	96.0	5.0±1.0
Co5CPGO5	$Co_{0.05}Pr_{0.05}Gd_{0.1}Ce_{0.85}O_{1.95-\delta}$	1200	7.25	7.05	97.2	0.2-0.5
CPGO8	$Pr_{0.08}Gd_{0.1}Ce_{0.82}O_{1.95-\delta}$	1600	7.22	7.10	98.3	4.0±1.0
CPGO15	$Pr_{0.15}Gd_{0.1}Ce_{0.75}O_{1.95-\delta}$	1600	7.31	6.60	90.3	4.0±1.0
CPGO25	$Pr_{0.25}Gd_{0.1}Ce_{0.65}O_{1.95-\delta}$	1600	7.03	6.50	92.5	5.0±1.0
CPGO30	$Pr_{0.3}Gd_{0.1}Ce_{0.6}O_{1.95-\delta}$	1600	6.92	6.20	89.6	6.0±1.0
CPGO40	$Pr_{0.4}Gd_{0.1}Ce_{0.5}O_{1.95-\delta}$	1600	6.70	6.30	94.0	6.0±1.0

4.3. Oxygen nonstoichiometry

Fig. 6 displays the oxygen nonstoichiometry data of the samples along with the best least square fit curves ($0.90<R^2<0.99$) using the ideal defect model (Eq. 10). In the investigated pO_2 regime (blue regime) the oxygen nonstoichiometry (δ) increases with decreasing oxygen partial pressure until it reaches a plateau (δ =x/2), where all the Pr is trivalent. The equilibrium constants (K_{Pr}) at each temperature were obtained from the fit of the defect model to the data. The standard enthalpy and entropy were obtained from the slope and intercept of the linear fit to the data of -ln(K_{Pr}) vs. 1/T according to the equation:

$$-\ln K_{\mathrm{Pr}} = \frac{\Delta H_{\mathrm{Pr}}}{RT} - \frac{\Delta S_{\mathrm{Pr}}}{R} \qquad (14)$$

The thermodynamic parameters of each composition are summarized in Table 2. It is noteworthy that the enthalpy of reduction of Pr decreases with increasing Pr concentration, indicating a more facile reduction of Pr and release of oxygen with increasing Pr concentration or oxygen nonstoichiometry. Chatzichristodoulou *et al.*[16] found the more facilitated expulsion of oxygen with increasing oxygen nonstoichiometry in Pr and Tb co-doped ceria. Stefanik *et al.* [32] also pointed out that the reduction enthalpy of Pr decreases with increasing Pr concentration, meaning higher Pr concentration gives rise to higher reducibility, in good agreement with this work.

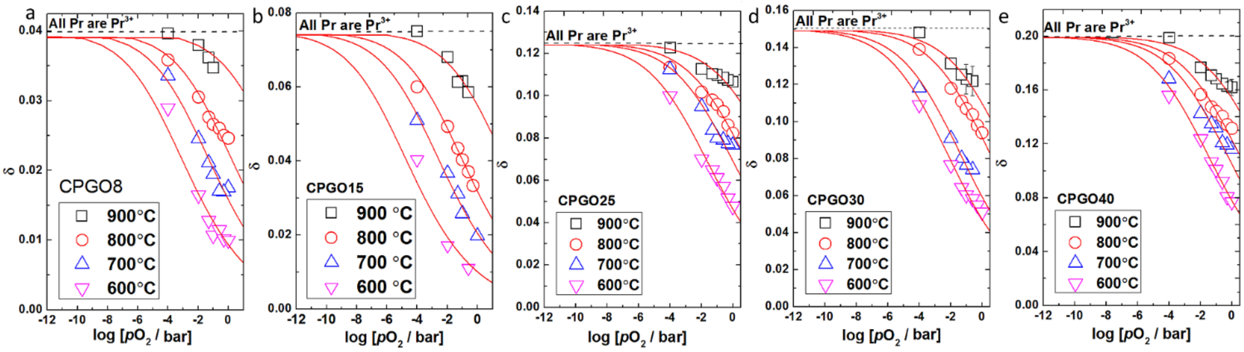

Fig. 6 Fit of the ideal defect model to the oxygen nonstoichiometry data of (a) CPGO8, (b) CPGO15, (c) CPGO25, (d) CPGO30 and (e) CPGO40 measured by TGA.

Table. 2 The thermodynamic parameters for the reduction of Pr in CPGO15, CPGO25, CPGO30 and CPGO40.

Sample	ΔH_{Pr} /kJ mol^{-1}	ΔS_{Pr} / J K^{-1} mol^{-1}	Ref.
CPGO8	200±34	158±34	This work
CPGO15	204±25	156±24	This work
CPGO25	132±15	108±14	This work
CPGO30	130±14	108±14	This work
CPGO40	112±10	93 ±12	This work
CPO10	137	n/a	[33]
CPO20	140	83	[19]

4.4. Thermal expansion

Thermal expansion curves of $Pr_xGd_{0.1}Ce_{0.9-x}O_{1.95-\delta}$ measured by cooling the samples from 900 °C to room temperature in air are shown in Fig. 7(a). Below 400 °C, all the samples show identical linear expansion. The thermal expansion curves display a non-linear behaviour with an inflection point in the range from 500 °C to 600 °C, particularly for the samples with 15 at.% Pr or more. It is evident that Pr-doped CGO follows a similar tendency as Pr doped ceria where the strain increases with increasing Pr concentration in the specimen. It has been reported that the increased and highly non-linear apparent TEC in Pr-doped ceria is primarily attributed to the thermally induced chemical strain originating from the combination of contraction of unit cell as the formation of oxygen vacancy and expansion of the unit cell due to the partial reuction of Pr. change of the oxygen stoichiometry and the associated change in cation radius [16, 34]. The total expansion (the measured quantity) is the sum of a thermal and a chemical expansion (stoichiometric expansion [35]), which can be written:

$$\varepsilon = \alpha \Delta T + \beta \Delta \delta \tag{15}$$

where α is the thermal expansion coefficient (TEC), and β is the stoichiometric expansion coefficient [35]. Assuming a constant thermal and stoichiometric expansion coefficient [35] upon a given oxygen partial pressure, the non-linear total expansion curve can be fitted by a linear thermal expansion curve and a nonlinear chemical expansion curve (Fig. 7b). Values of the thermal expansion and chemical expansion coefficients deduced from this type of fitting are listed in Table 3. Indeed, the chemical expansion coefficient decreases with increasing dopant concentration. For the samples doped with similar Pr concentration (**$Pr_{0.2}Ce_{0.8}O_{1.9-\delta}$ vs. CPGO25**), the chemical expansion coefficients are very close. (0.084 mol^{-1} for $Pr_{0.2}Ce_{0.8}O_{1.9}$ [16] and 0.086 mol^{-1} for CPGO25).

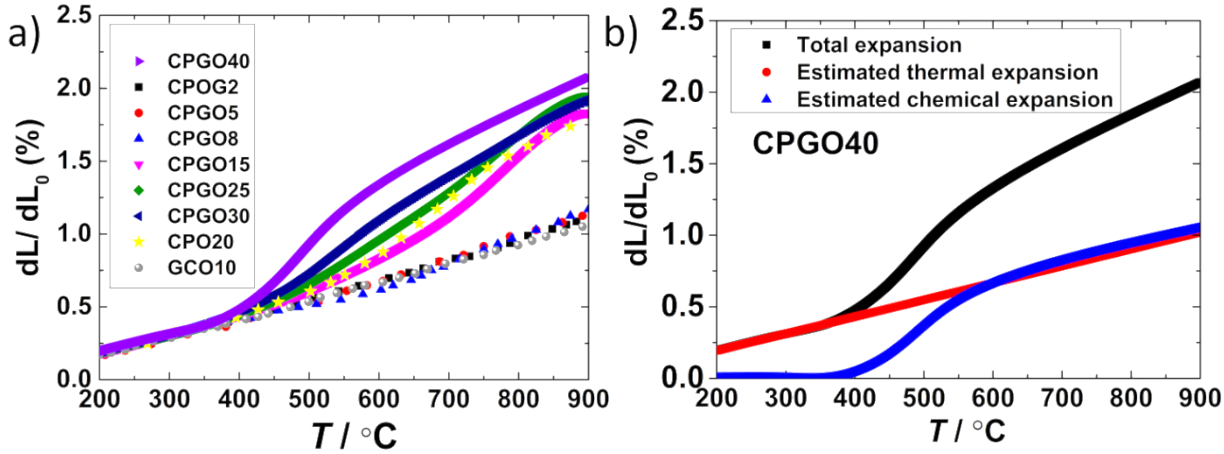

Fig. 7 (a) Thermal expansion curves for $Pr_xGd_{0.1}Ce_{0.9-x}O_{1.95-\delta}$ in air. The strain of CPO20 is the data taken from [16]. (b) Estimated thermal expansion and chemical expansion curve of CPGO40.

Table 3. Integrated thermal and expansion chemical expansion coefficients (200-900 °C)

Abbreviated name	α / K^{-1}	β / mol^{-1}
CGO	12.5×10^{-6}	n/a
CPGO2	13.8×10^{-6}	n/a
CPGO5	14.5×10^{-6}	n/a
CPGO8	11.5×10^{-6}	0.080
CPGO15	11.5×10^{-6}	0.082
CPGO25	11.4×10^{-6}	0.086
CPGO30	12.1×10^{-6}	0.073
CPGO40	12.5×10^{-6}	0.065
$Pr_{0.2}Ce_{0.8}O_{1.9-\delta}$ [16]	22.7×10^{-6}	0.084
$Tb_{0.2}Ce_{0.8}O_{1.9-\delta}$ [16]	18.2×10^{-6}	0.065

4.5. Total, bulk and grain boundary conductivity in air

Fig. 8 shows the impedance (Nyquist plots) of the eight samples obtained at 300 °C with fitting curves based on the equivalent circuit (RQ)(RQ). The high, intermediate and low frequency corresponds to the impedance contributed from the grain interior, grain boundary and electrode kinetics. The fit of the equivalent circuit to the impedance spectra is based on the assumption of a bricklayer model where the microcrystalline ceramic is treated as a block that consists of cubic grains separated by grain boundaries. The bulk (grain interior), grain boundary and electrode kinetics displays in the form of a series of distinguishable semicircles in the Nyquist plot. The semicircles were fitted with two parallel RQ elements in series, where R is the resistor, and Q is called constant phase element (CPE) with nomenclature $Z_{CPE}^{-1}=Y_{CPE}=Q_0(j\omega)^n=Q_0[\cos(n\pi/2)+j\sin(n\pi/2)]$ where $j=\sqrt{-1}$, ω is the frequency, Q_0 and n (in the range from 0 to 1) are frequency independent parameters which usually dependent on temperature [36]. We may obtain the two values Q_0 and n from the fit. The pseudo-capacitance for each parallel R and Q can be calculated from the equation $C=Q_0^{1/n}R^{1-1/n}$. The lowest capacitance in the range from 10^{-12} F to10^{-10} F is due to the grain interior whilst the much higher value in the range from 10^{-7} F to 10^{-9} F corresponds to the grain boundaries, e.g. 1.90×10^{-8} F for the sample with an average grain size of 1.6 μm [37]. The process with capacitance in the range from 10^{-4} F to 10^{-6} F stems from the electrode reaction. The parameters obtained by fitting the impedance spectra with the equivalent circuit (RQ)(RQ) are summarized in table. 4. The obtained pseudo-capacitances for grain interiors and grain boundaries derived in this work are within the range of typically observed in ceria based polycrystalline ceramics [37]. According to the resistances obtained by the fit, the grain interior and grain boundary conductivity are calculated by ohm's law.

$$\sigma_{tot} = \frac{d}{A\left(R_{gi}+R_{gb}\right)} \quad , \sigma_{gi} = \frac{d}{AR_{gi}} \quad , \sigma_{gb} = \frac{d}{AR_{gb}} \qquad (16)$$

where R_{gi} is the grain interior resistance, R_{gb} is the grain boundary resistance, A is the effective area of the electrode, d is the thickness of the sample.

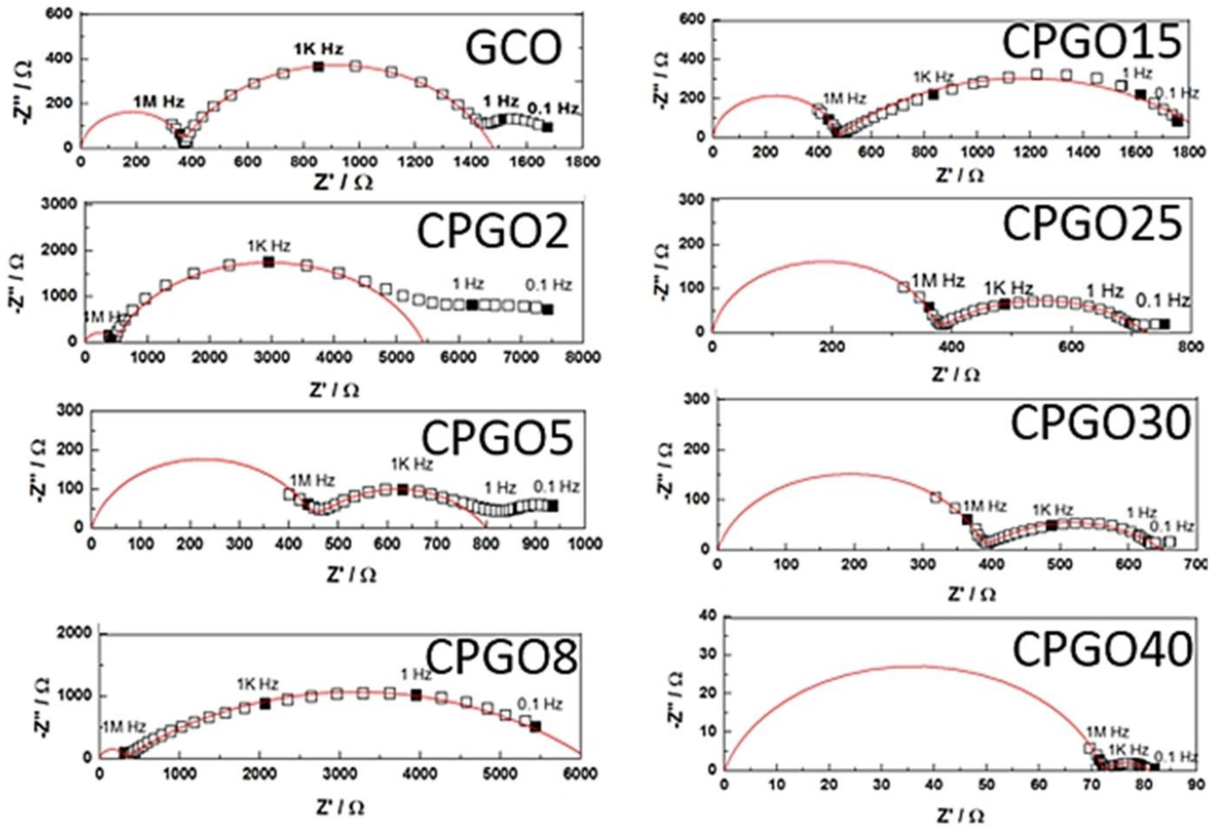

Fig. 8 Nyquist plot for the impedance of the sample at 300 °C in air: square empty points denote experimental data. The red solid curve corresponds to fit the data using the specific equivalent circuit (R1Q1)(R2Q2). The contact area was 0.9 cm^2 and the sample thickness was 0.1cm.

The oxygen partial pressure surrounding the specimen was controlled by changing the flow of air and nitrogen *via* the mass flow controllers. Impedance spectra were recorded two hours after the change of the flow to ensure that the steady state was reached. Fig. 9 shows the impedance spectra of CPGO40 recorded under various oxygen partial pressures. It can be clearly seen that the Nyquist plot shift towards higher resistance values with decreasing oxygen partial pressure, indicating a decreased electrical conductivity with decreasing pO_2. This is will be discussed in detail later in 4.7.

Table 4. Resulting parameters obtained by fitting the impedance values of the eight sample compositions in Fig. 8.

Composition	R1/Ω	Q1/($AV^{-1}s^{n1}$)	n1	C1/ (F)	R2	Q2/($AV^{-1}s^{n1}$)	n2	C2 / (F)
CGO	360	6.59e-10	0.93	2.03e-10	1157	1.91E-6	0.71	1.56e-7
CPGO2	460	1.00e-11	0.93	2.36e-12	4535	5.54E-7	0.83	1.61e-7
CPGO5	445	1.00e-9	0.85	7.57e-11	310	2.96E-6	0.72	1.95e-7
CPGO8	300	8.00e-11	0.97	4.65e-11	5500	4.03E-5	0.44	5.50e-6
CPGO15	465	1.00e-10	0.95	4.11e-11	1461	1.30E-4	0.50	2.47e-5
CPGO25	370	3.80e-10	0.91	7.98e-11	362	7.82E-5	0.48	1.60e-6
CPGO30	385	9.00e-10	0.85	6.52e-11	250	9.83E-5	0.50	2.40e-6
CPGO40	72	2.00e-9	0.82	1.24e-10	8.2	5.90E-3	0.48	2.20e-4

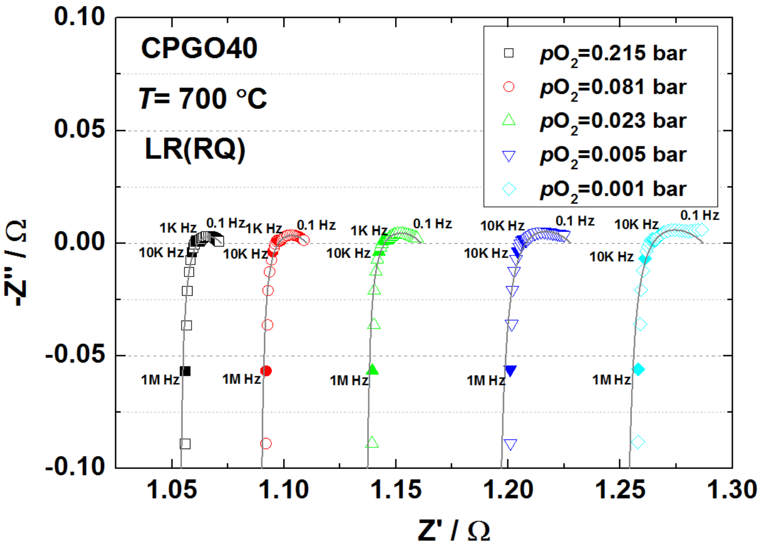

Fig. 9 Nyquist plot of CPGO40 recorded under different oxygen partial pressures.

Fig. 10 shows the Arrenhius plot of total (a), bulk (b) and grain boundary (c) conductivity of each sample. The apparent activation energies (*Ea*) for bulk and grain boundary obtained by fitting experimental data with the equation $\sigma T = \sigma_0 e^{\frac{-E_a}{kT}}$ are summarized in Table 5. The overall conductivities are influenced by the concentration of dopant to various degrees. The total conductivity of all the samples is governed by bulk conductivity above 700 ^{o}C. Below 700 ^{o}C, it is governed by both bulk and grain boundary conductivities particularly for the sample doped with low Pr concentration (CGO, CPGO2 and CPGO5). The total conductivity shows an increasing tendency with increasing Pr concentration, in agreement with Takasu *et al.* [26].

In addition, the bulk conductivity is enhanced when the concentration of Pr is higher than 15 at.%. In particular, the bulk conductivity of CPGO40 is larger than that of CGO by almost one order of magnitude at 400 ^{o}C. Furthermore, the bulk conductivity of all the samples shows a depressed slope above 500 ^{o}C, which corresponds to the decreased activation energies in the range from 500 ^{o}C to 900 ^{o}C (Table 5). A similar feature is reported in other relevant studies of doped-ceria [38, 39] and explained by the insignificant association between oxygen vacancies and acceptor dopants at high temperature [39]. Another reason is the changing concentration of charge carriers (oxygen vacancy) with increasing temperature.

As shown in Fig. 10(c), the grain boundary conductivity is more significantly influenced by the dopants as compared to bulk conductivity. The grain boundary conductivity of GPGO5 is higher than that of CGO by one order of magnitude. For samples doped with Pr concentration in excess of 5 at.%, the grain boundary resistance is too small to be detected from the impedance spectra. Lübke *et al*. [13] reported that the grain boundary conductivity of 3 at.% Pr-doped CGO20 is about 10 times higher than that of CGO at 500 ^{o}C. Bowman *et al.* [38] found that nano-scaled CGO20 doped with 4 at.% Pr possesses approximately 100 times higher grain boundary conductivity than that of CGO20. Our result is in good agreement with the previous literature [39]. The larger grain boundary conductivity in Pr-doped CGO may be associated with the increased electronic defect concentration in the vicinity of the grain boundaries, which are generally found to be Pr rich [13, 38].

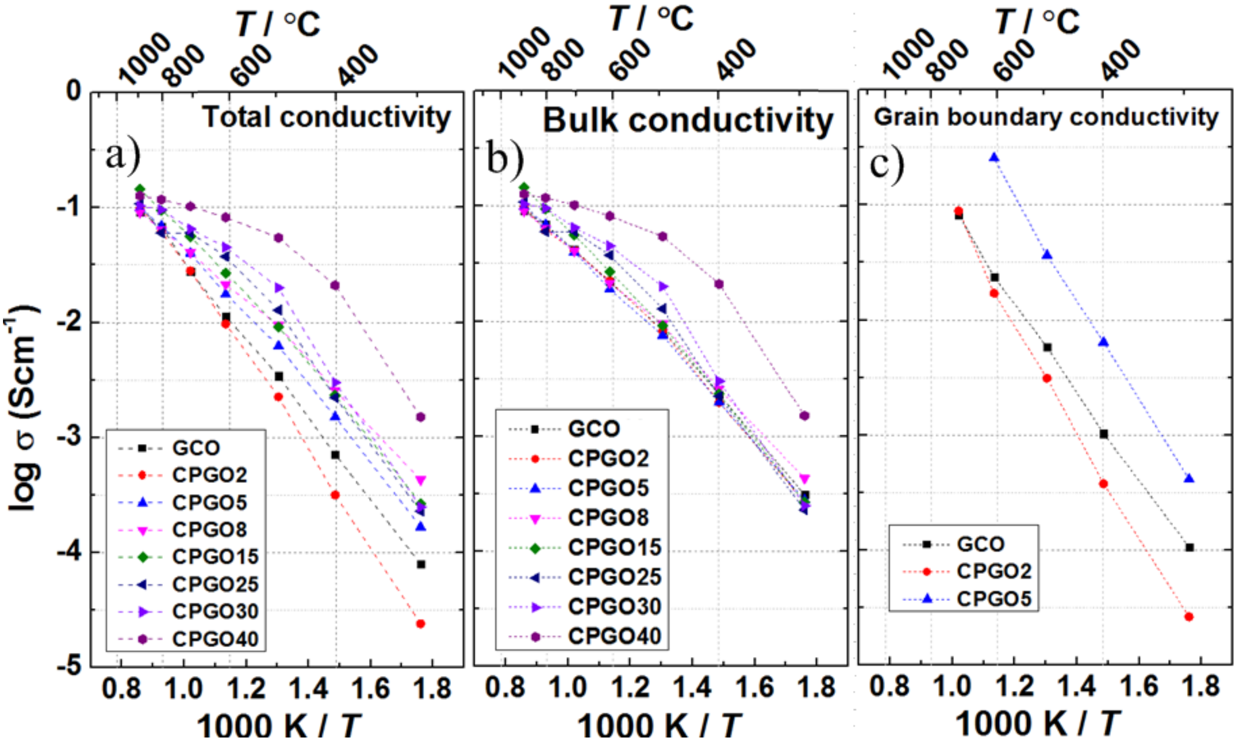

Fig. 10 (a) Total, (b) bulk, and (c) grain boundary conductivity in air as a function of temperature measured by electrochemical impedance spectroscopy in the temperature range from 300 °C to 900 °C.

Table 5. Apparent activation energies of bulk and grain boundary conductivity.

Sample composition	**Bulk, Ea T>500°C ($kJ\ mol^{-1}$)**	**Bulk, Ea T<500°C ($kJ\ mol^{-1}$)**	**Grain boundary Ea ($kJ\ mol^{-1}$)**
CGO	50	57	80
CPGO2	50	62	90
CPGO5	56	62	89
CPGO8	50	62	n/a
CPGO15	56	68	n/a
CPGO25	35	72	n/a
CPGO30	39	73	n/a
CPGO40	24	61	n/a

4.6. Electronic conductivity

The contact area of the Pt microcontact was determined by Newman's formula [40]

$$r_c = \frac{1}{4R_s\sigma} \qquad (17)$$

where r_c is the radius of the microcontact, R_s is the serial resistance found from the intercept with the real axis at the high frequency of the impedance spectra and σ is the specific conductivity of the sample. The contact radius is typically between 100 μm and 500 μm, in good agreement with ref. [23] where similar conditions were applied. We also found that the contact radius evaluated by impedance spectroscopy is not sensitive to the temperature or oxygen partial pressure. The S-shaped I-V curves of CPGO8 at 700, 800 and 900 °C are displayed in Fig. 11. Excellent coincidence of the braches recorded in the negative and positive polarization direction indicate that the hysteresis arising from creep of the Pt microcontact or sluggish equilibrium between the redox of Pr^{3+} and Pr^{4+} is negligible in this work, and accordingly confirms that the I-V curves are obtained in the steady state.

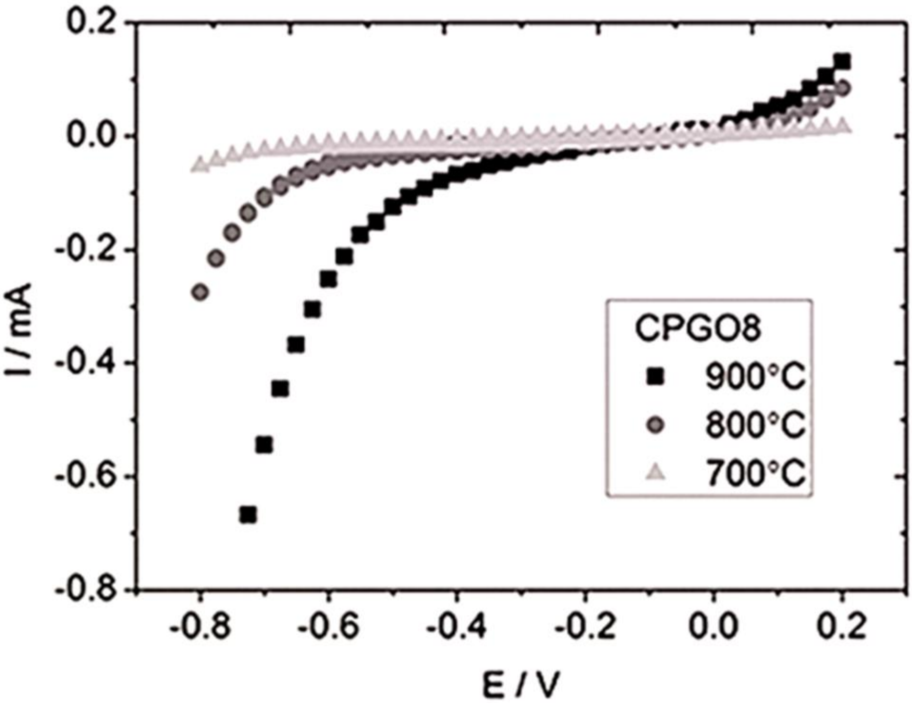

Fig. 11 Steady state current voltage polarization curve at 700 °C, 800 °C and 900 °C using air at the reference Pt electrode.

4.7. Electronic conductivity versus pO_2

The oxygen activity dependence of the partial electronic and total conductivity of each sample are presented in Fig. 12 at 700 °C, 800 °C and 900 °C. Electronic conductivity of CGO measured in this work agrees well with the electronic conductivity of CGO reported by Chatzichristodoulou *et al*. [23]. The electronic conductivity of CPGO is dominated by n-type and p-type under low and high oxygen partial pressures, respectively. The minium point in the middle corresponds to the transition from n-type to p-type conductivity. It is noteworthy that the minium point shifts towards lower oxygen partial pressure with increasing Pr concentration.

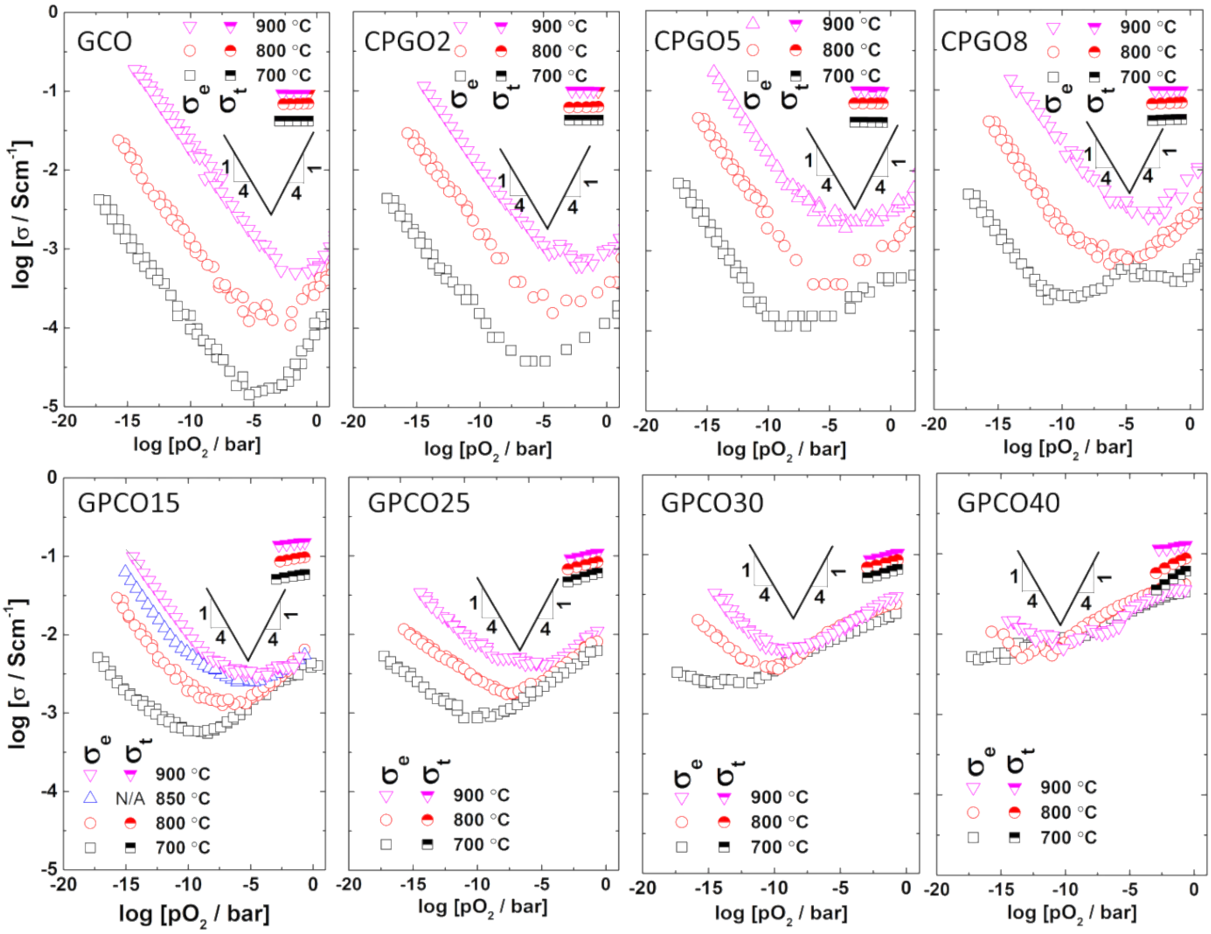

Fig. 12 Logrithim of electronic (empty) and total conductivity (half filled) of CPGOx (x=0, 2, 5, 8, 15, 25, 30 and 40) versus log pO_2 at 900 °C, 800 °C and 700 °C.

In contrast to the electronic conductivity of GCO which follows a typical relationship of $\sigma_t = \sigma_n^0 pO_2^{-\frac{1}{4}} + \sigma_p^0 pO_2^{\frac{1}{4}}$, the electronic conductivity of CPGOx possesses a more varied pO_2 dependency. The slope of the n-type electronic conductivity of slightly doped samples at low pO_2 approaches -¼, whereas the heavily doped samples (CPGO30 and CPGO40) the slope is depressed especially at low temperature. This is probably associated with the shift of the minimum point towards low pO_2 and the associated increased p-type contribution under reducing conditions masking the n-type contribution to the electronic conductivity.

Under oxidizing conditions, the slopes are within the range from $1/4 \text{ to } 1/8$, in agreement with ref. [13]. Evidently, the p-type electronic conductivity steadily increases with increasing Pr concentration. In particular for CPGO40, the p-type electronic conductivity is higher than that of CGO by two orders of magnitude at 700 °C. The observed enhancement of p-type conductivity is in line with previous literature [13, 16, 41, 42]. It is also seen that the electronic conductivity becomes insensitive to the temperature for these heavily doped samples (>15 at.%), which coincides with previous findings by Chatzichristoduolou *et al.* [23] and Schmale *et al.*[24]. This can be explained by the decreased concentration of Pr_{Ce}^{x} at elevated temperature (see Fig. 6) which compensates for the effect despite the increased mobility of electron holes [23].

The total conductivity is insensitive to the change of oxygen partial pressure in the range from 1×10^{-5} bar to 0.21 bar when the Pr concentration is lower than 8 at.%. The total conductivity is the sum of the oxide ion conductivity and electron hole conductivity. It is evident that the pO_2-dependent electronic conductivity is too low (ca. 100 times lower than the oxide ion conductivity) to introduce detectable changes on the total conductivity. The total conductivity shows detectable pO_2-dependence for samples doped with more than 15 at.% Pr. The pO_2-dependence becomes more pronounced with increasing Pr concentration because the electronic conductivity is sufficient to influence the total conductivity and the ionic conductivity becomes decrease with decreasing pO_2. This will be clearly visualized by the transport number of electron hole discussed later (Fig. 18).

In Fig. 13, the oxide ion conductivities of CPGO were obtained by subtracting the electronic conductivity from the total conductivity (see Fig. 12). It can be observed that the oxide ion conductivity steadily decreases with decreasing pO_2 for these heavily doped samples (>15 at. %). When the Pr concentration is lower than 15 at.%, the oxide ion conductivities are independent of pO_2. As pO_2 decreases, the concentration of acceptor dopants increases because of the increasing $\mathrm{Pr}_{Ce}^{/}$ concentration. Oxygen vacancy concentration accordingly increases to counterbalance the increased charge of acceptor dopant. Hence, the unaffected (GCO, CPGO2, CPGO5 and CPGO8) or decreased conductivity (CPGO15, CPGO25, CPGO30 and CPGO40) must be ascribed to a decreasing oxide ion mobility with increasing oxygen vacancy concentration and increasing concentration of Pr^{3+}. One does, in terms of ionic conductivity not benefit from doping beyond the 10 at.% Gd which is well documented in literature, where σ_i does not increase with amount of dopant beyond 10 at.% [43].

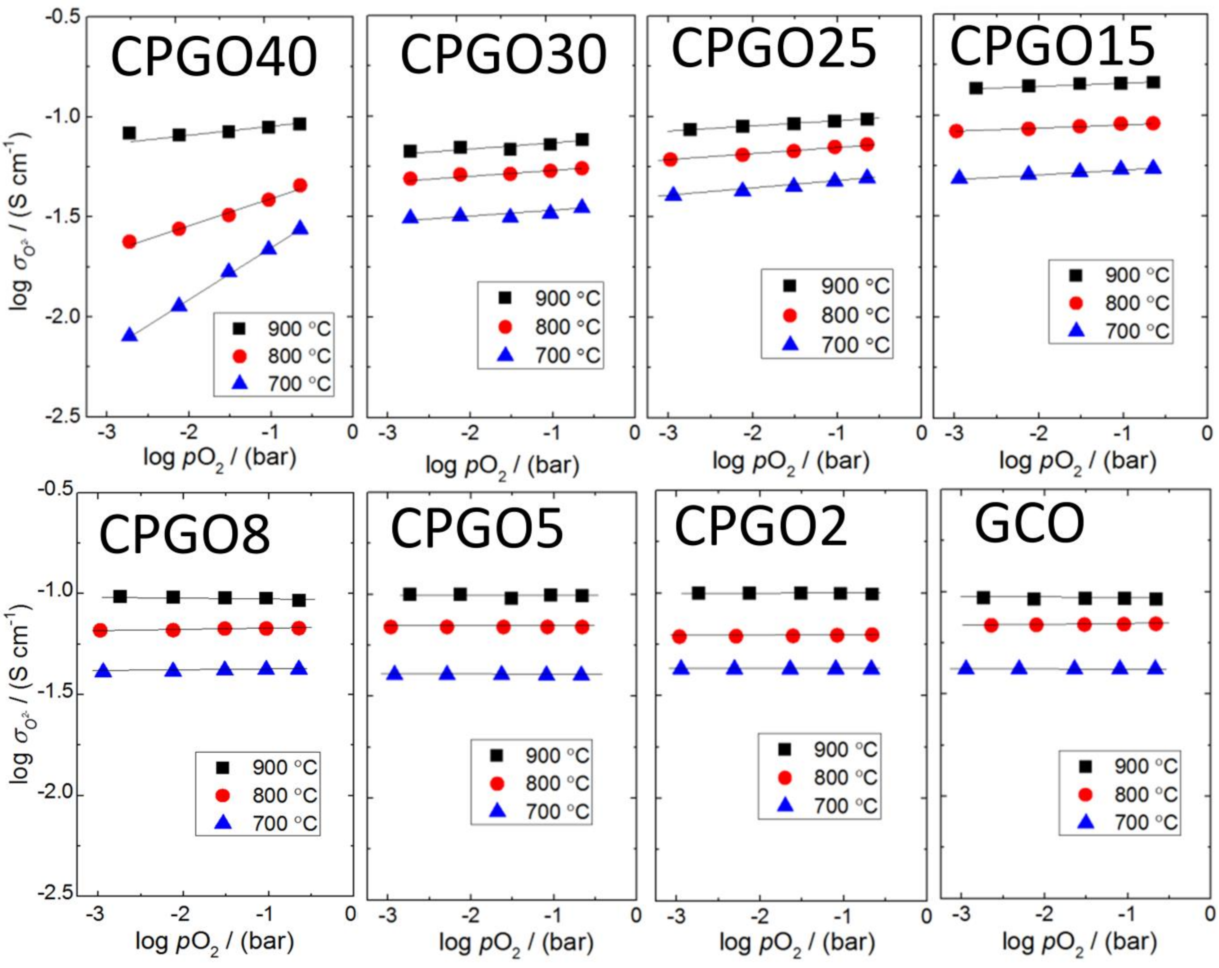

Fig. 13 Logarithm of oxide ion conductivity versus log pO_2 for each composition. The lines were obtained by linear fitting to the data.

4.8. Calculated and meaured oxygen permeation flux

Fig. 14 displays the calculated and measured oxygen flux of CPGO5, Co5CPGO5 and CGO as a function of temperature under a fixed oxygen partial pressure difference

($\ln(pO_2'/pO_2'')=7$). The calculated fluxes were obtained from Wagner's equation in terms of the measured electronic and ionic conductivity (see Fig. 12). It is noteworthy that the calculated flux is consistent with the measured flux. This indicates that the measured oxygen flux is limited by bulk ambipolar diffusion in the 1-mm thick membrane sample investigated rather than surface exchange. Another noticeable feature is that the oxygen flux of CPGO5 is higher than that of CGO by at least half an order of magnitude. The enhanced oxygen flux is due to the enhanced electronic conductivity. The cobalt oxide-containing samples possess slightly lower oxygen flux at low temperature as compared to the cobalt oxide free sample. It has previously been reported that cobalt oxide containing ceria based membranes show enhanced oxygen flux compared to the corresponding cobalt oxide free membrane because percolating cobalt oxide forms along the grain boundary enhancing electronic conductivity without influencing the ionic conductivity [17, 44, 45]. The observed decreased oxygen flux in cobalt oxide containing samples in this work may be due to the formation of discrete cobalt oxide particles at the grain boundaries resulting from the high sintering temperature (1200 °C) as opposed to a continuous percolating network found in other studies [17, 44, 45].

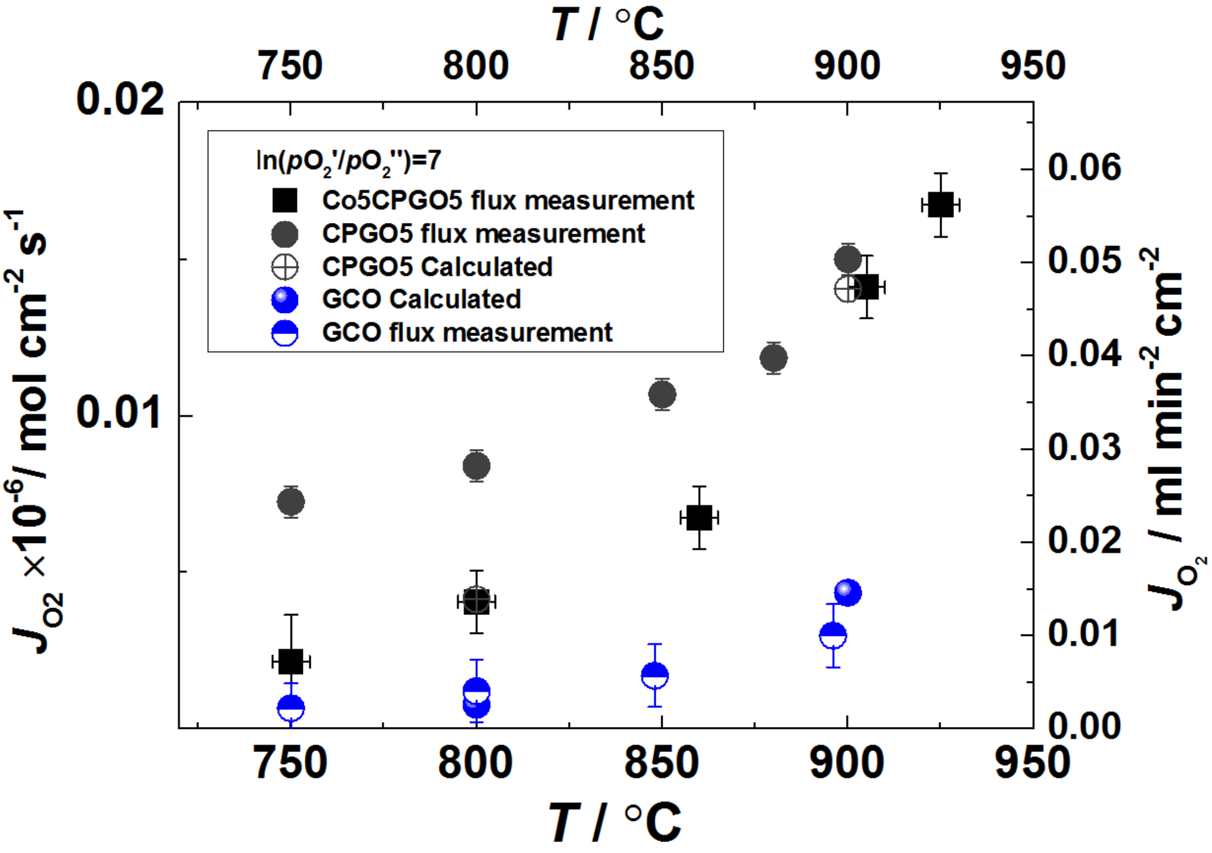

Fig. 14 Calculated and measured oxygen permeation flux for CGO, CPGO5 and Co5CPGO5.

5. Discussions

5.1. Electronic conductivity under oxidizing conditions

Praseodymium oxides (PrO_x) exist in variable compositions (x in the range from 1.5 to 2) at elevated temperatures where Pr take a varible valence, such as Pr^{3+}/Pr^{4+}. As the reduction of Pr occurs, the electrical conductivity of PrO_x significantly increase with increasing temperature, up to a value of 1.4 Scm^{-1} at 850 °C [46]. The electrical conductivity of PrO_x at high tempeature is assigned to electronic conductivity, which originate from the electron hopping between mixed-valence Pr^{3+}/Pr^{4+} cation present in the lattice. However, Gd-doped ceria is a oxide ion conductor with negligiable electronic conductivity under oxidizing condition. As observed in this work, combination of PrO_x and Gd-doped ceria by making a Pr/Gd co-doped ceria solid solution gives rise to mixed ionic-electronic conductivity.

The mechanism for the electronic conductivity of Pr in ceria has been explained by band theory. Stefanik *et al.* proposed that Pr-substitution for cerium forms discrete acceptor levels (Pr 4f) for the lightly doped ceria (below 10 at.%) [32, 33]. The discrete band is not capable to give rise to considerable electronic conductivity. As the dopant concentration increases, the discrete Pr states start to be continuous, resulting in a significant electronic conductivity. Lübke *et al.*[13] proposed that the Pr 4f states lie much closer to the O2p valence state edge than Ce 4f conduction band. At sufficiently high temperature, electron in the O2p state will be thermally excited and subsequenty localized in the Pr 4f impurity level, resulting in formation of holes in the valence state. According to the band theory, the electron may transport beween Pr^{4+} and Pr^{3+} dopants by way of oxygen ions.

The electron hopping is due to the interaction between the electronic defects with surrounding Pr and O ions. Due to the strong interaction and small size of the polaron, the electronic hopping should follow the small polaron mechanism, which is akin to the transport of ionic charge carriers. The electronic conductivity obeying small polaron mechanism can be evaluated by the equation as follows [32]:

$$\mu_{polaron} = \frac{(1-\left[\mathrm{Pr}_{\mathrm{Pr}}^{/}\right])ea^2 v_0}{kT} \exp\left(-\frac{E_H}{kT}\right) \tag{19}$$

$$\sigma_{polaron} = N\left[\mathrm{Pr}_{\mathrm{Pr}}^{/}\right]\mu_{polaron} e \tag{20}$$

$$\sigma_{polaron} = N\left[\mathrm{Pr}_{\mathrm{Pr}}^{/}\right](1-\left[\mathrm{Pr}_{\mathrm{Pr}}^{/}\right])\frac{e^2a^2v_0}{kT}\exp\left(-\frac{E_H}{kT}\right) \qquad (20)$$

$$\left[\mathrm{Pr}_{\mathrm{Pr}}^{/}\right] = \frac{\left[\mathrm{Pr}^{3+}\right]}{\left[\mathrm{Pr}^{3+}\right]+\left[\mathrm{Pr}^{4+}\right]} \qquad (22)$$

where $\mu_{polaron}$ is the mobility of the small polaron, $\left[\mathrm{Pr}_{Ce}^{/}\right]$ is the fractional occupancy of hole trapped on Pr ions. $\left[\mathrm{Pr}^{3+}\right]$ is the concentration of trivalent Pr, N is the volumetric density of Pr atoms in the material (mol cm^{-3}). v_0 is the phonon jump frequency, E_H is the activation energy for hopping of the electron hole (electron hole migration), a is the hopping distance. To obtain an Arrhenius type relation, Eq. (20) is rewritten as

$$\ln\left(\sigma_{polaron}T\right) = -\frac{E_H}{k}\frac{1}{T} + \ln C \qquad (23)$$

Where C is the pre-exponential factor (c= $Ne^2\left[\mathrm{Pr}_{\mathrm{Pr}}^{/}\right](1-\left[\mathrm{Pr}_{\mathrm{Pr}}^{/}\right])k^{-1}a^2v_0$). It needs to be noted that the quantity and type of electronic conductivity are both influenced by the concentration of Pr^{3+} and Pr^{4+}. When the concentration of Pr^{3+} prevails, the thermal energy allows the electron hole localized on Pr^{4+} to hop to the surrounding Pr^{3+}. In this case, the material should be a p-type conductor. When the concentration of Pr^{4+} prevails, the electron localized on Pr^{3+} may hop to the surrounding Pr^{4+}, yielding a n-type conductor. In this work, we investigate the p-type electronic conductivity by fixing the ratio between Pr^{3+} and Pr^{4+} to be 2.7 in terms of the TGA and electronic conductivity data.

As shown in Fig. 15A, the Arrhenius plots of electronic conductivity at a fixed Pr^{3+}/Pr^{4+} ratio (invariant Pr^{3+}/Pr^{4+} pair in Eq. 21) coupled with linear fitting were illustrated. The apparent activation energy and pre-exponential constant of electronic conductivity obtained by linear fitting in Fig. 15A were shown in Fig. 15C and 15D, respectively. As indicated by Eq. 22, the apparent activation energy in Fig 15C corresponds to the migration enthalpy of electron hole whilst the pre-exponential factor is associated with the phonon jump frequency v_0 and hopping distance a. The noticeable feature in Fig. 15A is that the p-type electronic conductivity is not linearly proportional to the dopant concentration especially at low temperatures where abrupt increase of conductivity occurs between x=0.08 and 0.15, associated with an abrupt decline of activation energy and pre-exponential factor in the same x range.

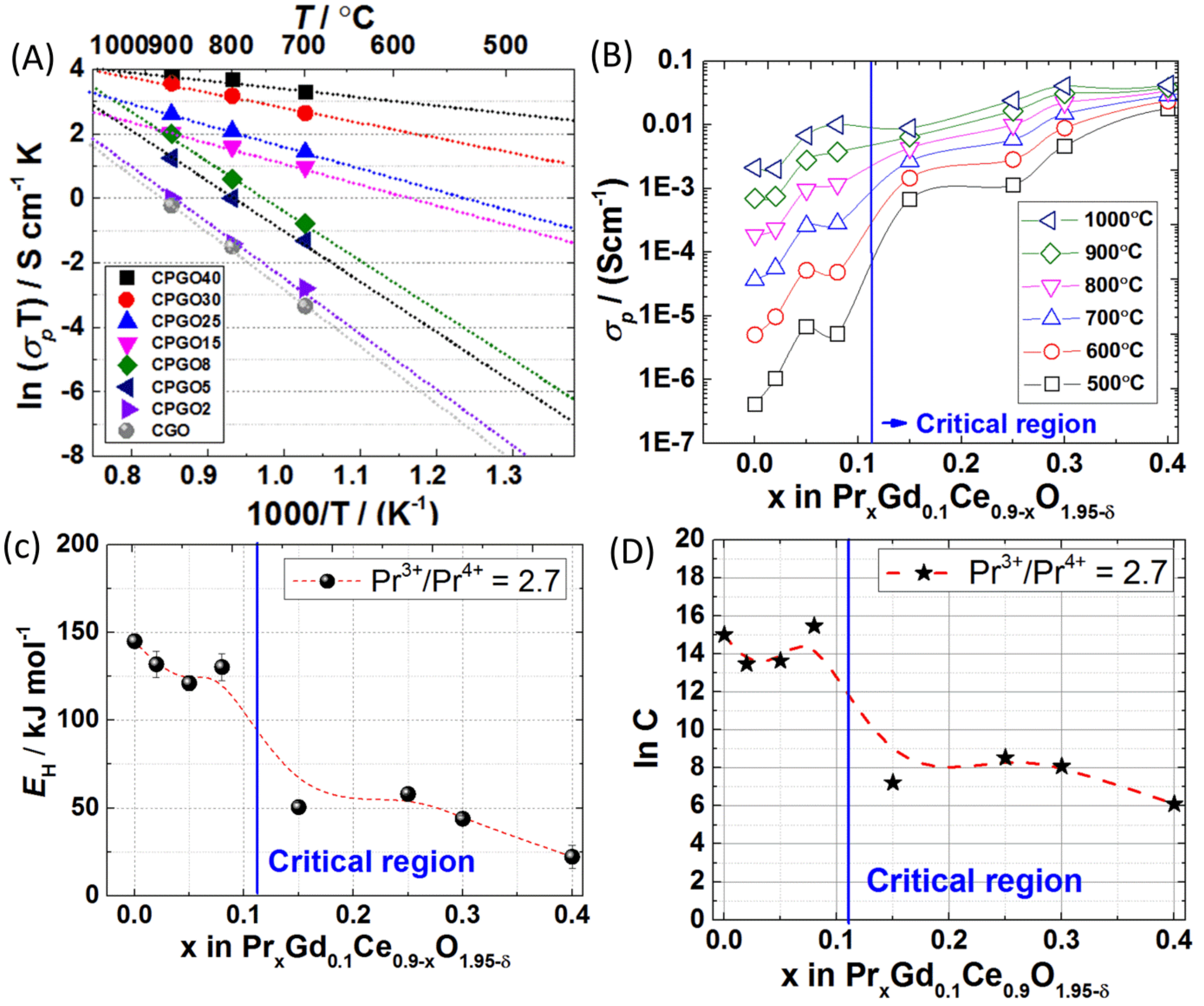

Fig.15 (A) Arrhenius plots of the electronic conductivity for CPGOx at a fixed Pr^{3+}/Pr^{4+}. (B) Electronic conductivity as a function of dopant concentration from 500 °C to 1000 °C. The electrical conductivity of PrO_x is taken from (C) Apparent activation energy and (D) pre-exponential factor of the electronic conductivity versus x obtained from linear fitting in (A). The dotted lines are plotted to guide the eye.

As a solid solution, Pr-doped GCO can somehow be treated as the PrO_x clusters homogenously embedded in the $Gd_{0.1}Ce_{0.9}O_{1.95-\delta}$ matrix. Electronic charge carriers (electron or hole) are localized in the PrO_x units and migrate via them upon thermal vibration. For the sample doped with low Pr concentration, the distance among the discrete PrO_x cluster are relatively long so that high energy is needed to allow electronic defects to jump across the CeO_2/Gd_2O_3-based clusters which are not electronic conducting. This could be visualized by the low electronic conductivity and high activation energy for x<0.1 in Fig. 15C. Furthermore, the high value of pre-exponential constant for the 0<x<0.1 indicates that the hopping distance (a in Eq. 20) between Pr sites is long for the sample doped with low Pr concentration.

As dopant concentration increases, a shorter distance between the Pr ions become is envisaged, resulting in decreased hopping distance and activation energy. The transient behaviour in the range 0.08<x<0.15 is akin to a percolation effect, which is generally recognized in the composite materials consisting of an electrical conductor and an insulator. That is, the abrupt increase of electrical conductivity occurs when the amount of the electrical conductor surpasses the percolation threshold above which the continuous electrical conducting pathways penetrate all the way through the composite material. In addition to composite materials, the similar phenomenon is observed also in the solid solutions. Swider and Worrell [47] employed percolation model to explain the n-type electronic conductivity of Ti-doped YSZ. A theoretical percolation threshold of 12.5% for Ti-YSZ was proposed based on bond percolation in the crystal structure. Kim *et al.* [48] recently developed a simple cubic percolation model to interpret the non-linear increment of electrical conductivity in perovskite based $BaZrO_3$-$BaFeO_3$ solutions. It is thus reasonable to apply percolation model in ceria.

Generally, the percolation threshold (Pc) for a close-packed crystal structure e.g. FCC is a function of the site coordination number Z, and can be evaluated as [49]

$$ZP_c = 1.5 \tag{24}$$

The shortest possible jump distance will be achieved provided that the electronic defect localized on a given Pr dopant located on a vertex of the cubic unit cell has at least one other Pr sites among the 12 nearest neighbour sites on the face centre. A possible percolating Pr-Pr pathway when the Pc is achieved is illustrated as shown in Fig. 16. The coordination number in the FCC type structure thus equals to 12 (Z=12 in Eq. 24). Therefore, the percolation threshold is ~12.5%, which means the electronic defect may infinitely hop among two neighbouring Pr cations when 12.5 at.% of the cations are occupied by Pr. As illustrated in Fig. 15, it is evident that the theoretical percolation threshold (12.5%) falls in the transient range (8 at.%-15 at.%) observed in Fig. 15C, which indicates a strong correlation between the structural connectivity of the dopants and the migration enthalpy for electron holes.

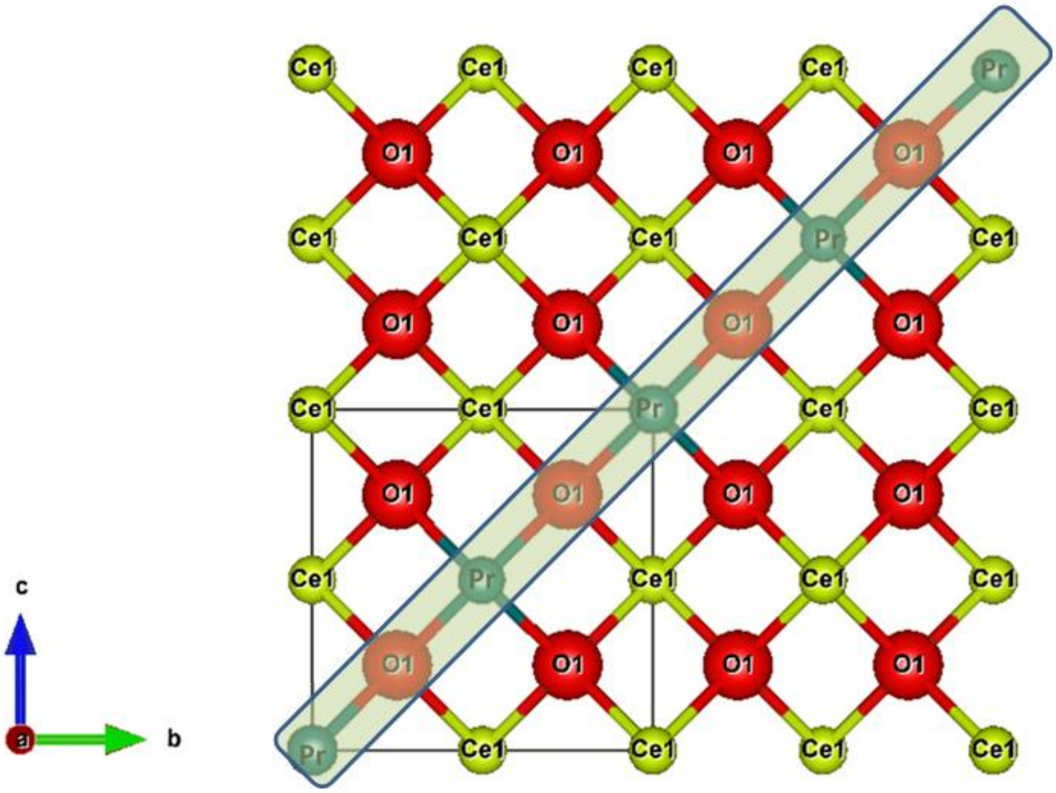

Fig.16 Schematic illustration of a (100) plane of a 2×2 matrix. A possible percolation path of Pr-Pr nearest neighbours is also shown in this figure.

In Fig. 17, the extrapolated electronic conductivity at 500 °C was fitted by a percolation model proposed by Kim *et al.* [48]. In this model, the percolation conductivity for x<Pc and x>Pc is phenomenologically described by two respect equations.

For x<P_c, the electrical conductivity is fitted with $\sigma(x) = \sigma_{GCO} x^{1/2} \left(P_c - x\right)^{-s}$

For x>P_c, the electrical conductivty is fitted with $\sigma(x) = \sigma_{\mathrm{Pr}O_x} \left(x - P_c\right)^{t}$

Where s and t are the universal size scaling exponents for non-percolation matrix and percolation phase. σ_{GCO} and $\sigma_{\mathrm{Pr}O_x}$ are the electronic conductivity of GCO and PrO_x at 500 °C, respectively. Pc is the fitting parameter. s and t are the two fitting parameters where t is in a theoretical limit range from 1.65 to 2 for the simple cubic percolation model. The best of the model to the Fig. 17 gives t=1.76, Pc=0.12 and s=-1.34, with the R^2, the coefficient of determination equal to 0.92. The model seems to satisfactorily fit the data in this work, which further elucidates that the electronic behavior would be well explained by the percolation concept.

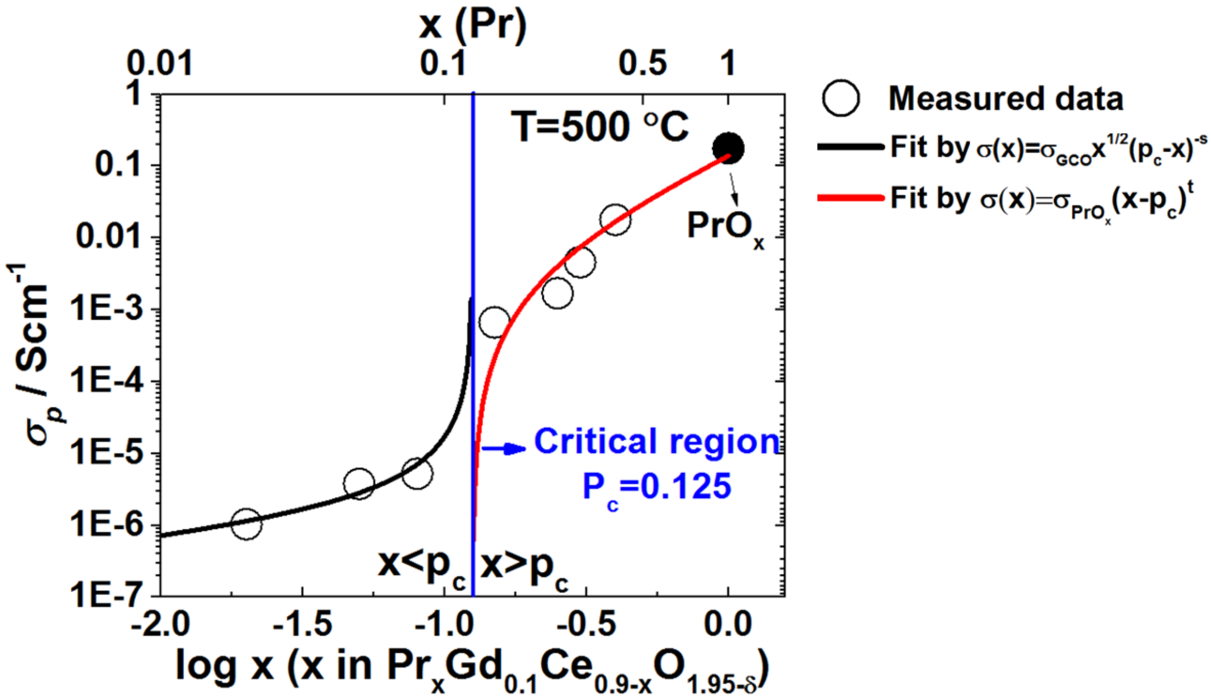

Fig. 17 Electronic conductivity at 500 °C (extrapolated data from Fig. 15A) as a function of x. The data is fitted with a simple cubic percolation with charge carrier donated by dopants. The data is fitted with by broken line. The percolation threhold (Pc) is estimated to be x=0.125 in the fitting. The fitting models for x<P_c and x>P_c are given in legend.

5.2. Electronic conductivity under reducing conditions

All the samples show n-type electronic conductivity under reducing conditions ($<1\times10^{-15}$ bar). For the sample doped with high Pr concentration, the n-type electronic conductivity becomes profoundly overshadowed by the considerable p-type electronic conductivity (Fig. 12). The n-type regime is associated with partial reduction of Ce^{4+} as described in Eq. 4. It is also noted that the apparent activation energy of n-type electronic conductivity decreases with increasing Pr concentration. Lübke *et al.* [13] found a slight decrease of the activation energy in CGO doped with 3 at.% Pr. Navarro *et al.* [50] also found that the 2 at.% Pr-doped GCO20 shows slightly decreased n-type conductivity relative to GCO20, in agreement with our results. In contrast to the trend observed in p-type electronic conductivity, the n-type electronic conductivity under reducing conditions steadily decreases with increasing Pr concentration. The decrease of n-type electronic conductivity is more pronounced at high temperature (900 ^{o}C). It is generally agreed that the n-type electronic conductivity in ceria is correlated with the electron hopping on the ceria sites (Ce^{3+}/Ce^{4+}) which is proportional to the total concentration of Ce ions [21]. Here, substitution of Pr for Ce decreases the total concentration of ceria site (Ce^{3+}/Ce^{4+}), accounting for the lower n-type electronic conductivity. Under strongly reducing conditions, Pr is completely reduced to Pr^{3+} and thus yeilds a relatively high oxygen vacancy concentration because of the higher total acceptor dopant concentration ($\left[Ce_{Ce}^{/}\right]$, $\left[\mathrm{Pr}_{Ce}^{/}\right]$ and $\left[Gd_{Ce}^{/}\right]$). The high oxygen vacancy concentration will likely also decrease the electron mobility [51, 52], due to the association between $Ce_{Ce}^{/}$ and $V_{O}^{\bullet\bullet}$ upon a large oxygen vacancy concentrations [53].

In addition, the activation energy of the n-type electronic conductivity was observed to decrease with increasing Pr concentration. The apparent activation energy is composed of two terms: $E = H_m + 1/4\,H_{Ce}$ where H_m is the enthalpy of electron migration and H_{Ce} is the standard reaction enthalpy. According to literature [53], the enthalpy of electron migration increases with increasing oxygen vacancy concentration in ceria. Although H_m of the materials in this work is not known, increasing H_m values are expected with increasing Pr concentraton. This indicates that Ce will be more readily reduced upon a higher Pr concentration. The simliar trend is also observed in Pr-doped ceria [33] and Gd-doped ceria [54]. It is also found that the reducibility of Ce^{4+} and Pr^{4+} in ceria tends to be facilitated by the increasing oxygen nonstoichiometry, leading to a non-ideal reduction behaviour [16]. We herein attribute the decreased activation energy of reduction of Ce to the high oxygen nonstoichiometry in heavily Pr-doped GCO.

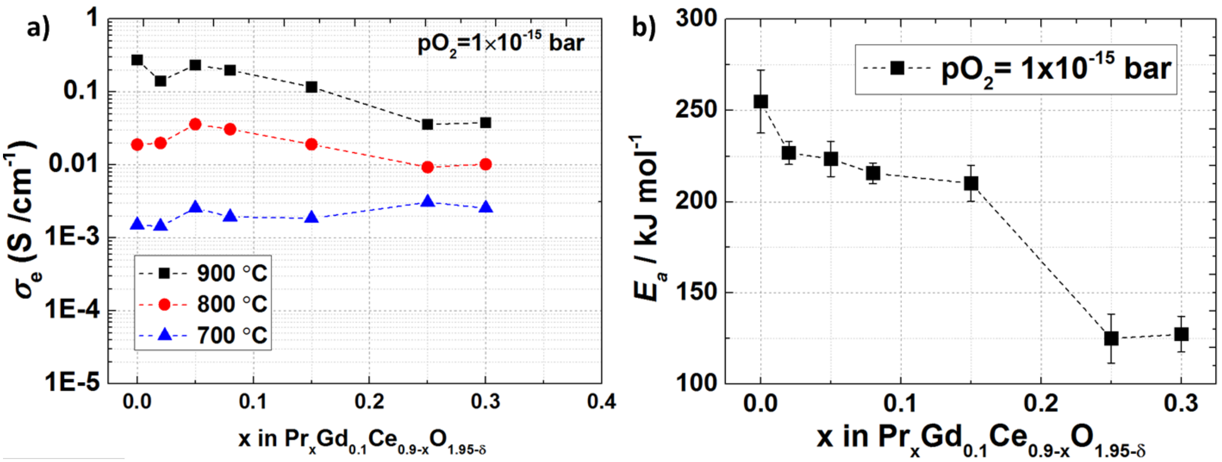

Fig. 18 (a) *n*-type electronic conductivity of CPGO under $pO_2=1\times10^{-15}$ bar as a function of x at 700, 800 and 900 °C. (b) Apparent activation energy of the electronic conductivity under $pO_2=1\times10^{-15}$ bar .

5.3. Ionic conductivity

For Pr and Gd co-doped ceria, more oxygen vacancies are expected to form to compensate the increased concentration of negatively charged aliovalent dopants ($\mathrm{Pr}_{Ce}^{/}$ and $Gd_{Ce}^{/}$). In analogy with purely Pr-doped or Gd-doped ceria [2], the ionic conductivity of Pr and Gd co-doped ceria does not monotonously increase with increasing oxygen vacancy concentration. Instead, the maximum ionic conductivity occurs around the acceptor dopant concentration of 25 at.% (15 cat% Pr^{3+} and 10 at.% Gd). According to Dholabhai's DFT calculations [55], 20 at. % dopant content in ceria shows the maximum ionic conductivity for 10 at.% Pr and 10 at.% Gd co-doped ceria, in good agreement with the experimental results in this work. Another noticeable feature is that the decrease of oxide ion conductivity above 25 at.% is associated with an increase of the apparent activation energy. The large activation energy of the electrical conductivity in heavily acceptor doped ceria is generally observed [2, 39], which is likely due to association between the extrinsic dopants and oxygen vacancies [39]. The possible association reactions can be written:

$2\mathrm{Pr}_{Ce}^{/}+V_O^{\bullet\bullet}\rightarrow \mathrm{Pr}_{Ce}^{/}\,V_O^{\bullet\bullet}\,\mathrm{Pr}_{Ce}^{/}$ or

$2Gd_{Ce}^{/}+V_O^{\bullet\bullet}\rightarrow Gd_{Ce}^{/}V_O^{\bullet\bullet}Gd_{Ce}^{/}$ or

$\mathrm{Pr}_{Ce}^{/}+V_O^{\bullet\bullet}\rightarrow\left[\mathrm{Pr}_{Ce}^{/}\,V_O^{\bullet\bullet}\right]^{/}$ or

$$\mathrm{Pr}_{Ce}^{/}+V_{O}^{\bullet\bullet}\rightarrow\left[\mathrm{Pr}_{Ce}^{/}V_{O}^{\bullet\bullet}\right]^{/},$$

whereby part of the mobile oxygen vacancies are trapped by the immobile dopants. As illustrated in Fig. 19, where the data for several different acceptor doped ceria compounds are compared, the defect association results in an increased apparent activation energy for oxide ion conductivity for the heavily doped samples.

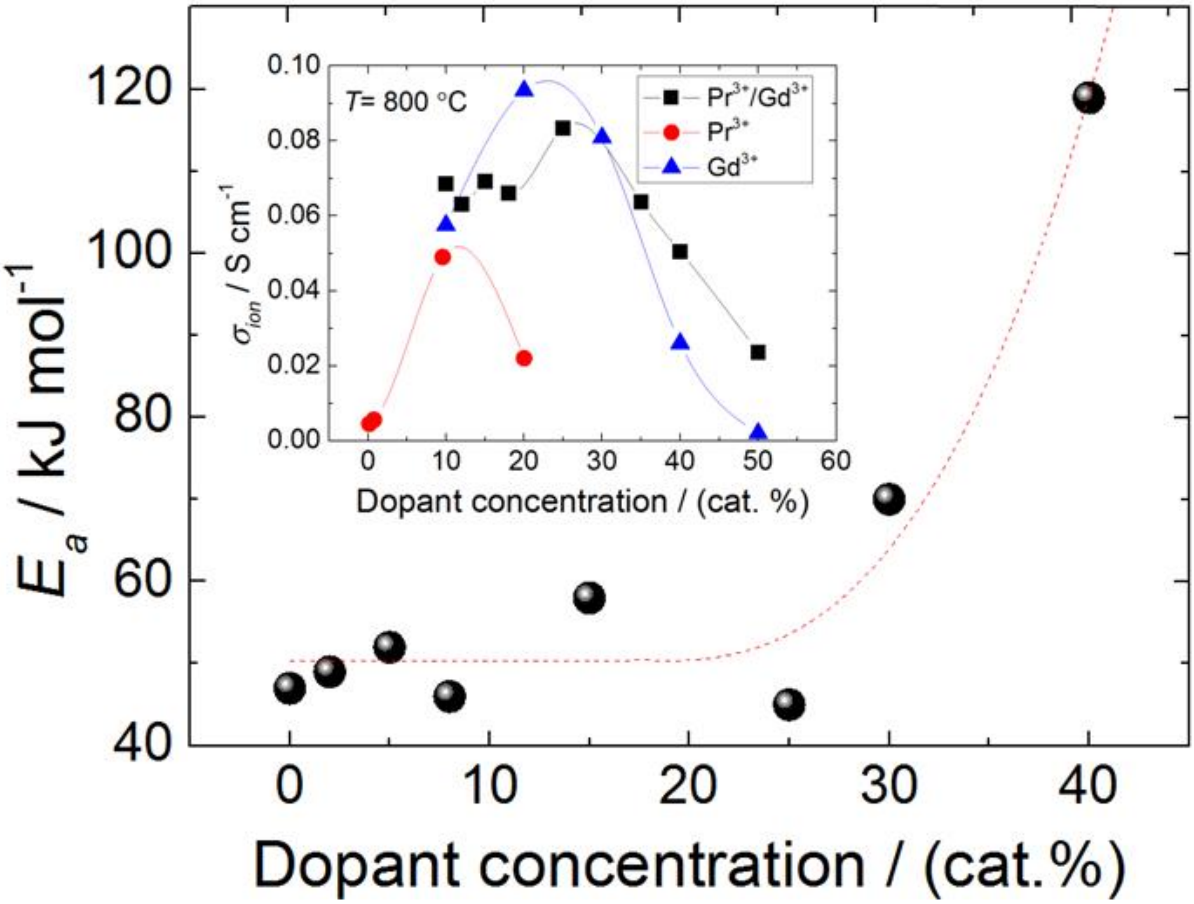

Fig. 19 Apparent activation energies of oxide ion conductivity in pure N_2 ($pO_2 \approx 0.001$ bar) as a function of Pr content. The lines were plotted to guide the eye. Inset:The oxide ion conductivity measured at 800 °C as a function of acceptor dopant concentration for different ceria solid solutions from [33, 56, 57]. The ratio of Pr^{3+}/Pr^{4+} at 800 ^{o}C in N_2 is in the range of 4-9.

5.4. Oxygen permeation flux

The maximum achievable oxygen flux occurs when the oxide ion and electronic conductivity in a MIEC are both high and equivalent (transport number=0.5). As shown in Fig 18a, the transport number of CPGO approaches to 0.5 when the Pr concentration is in the range from 30 at.% to 40 at.%. Shuk *et al.* [58] also found nearly equal electronic and ionic conductivity for $Pr_{0.3}Ce_{0.7}O_{1.85-\delta}$ at 700 °C, in good agreement with this work. The theoretical oxygen permeation flux can be calculated in terms of electronic and ionic conductivity using the Wagner's equation:

$$J_{O_2} = \frac{RT}{16F^2L}\int_{\ln pO_2^{//}}^{\ln pO_2^{/}} \frac{\sigma_e\sigma_i}{\sigma_e+\sigma_i}\ln pO_2 \qquad (25)$$

The calculated oxygen permeation flux follows the trend of t_e (Fig18 b), due to the fact that the oxygen permeation flux of $Pr_xGd_{0.1}Ce_{0.9}O_{1.95-\delta}$ is dominantly limited by the electronic conductivity until a Pr concentration of approximately 40 at.%, where the maximum oxygen permeation flux is achieved for the here considered composition range (0-40 at.%). Considering the bulk diffusion exclusively, the maximum oxygen flux for a 10-µm thick $Pr_{0.4}Gd_{0.1}Ce_{0.9}O_{1.95-\delta}$ based membrane may reach up to 10 Nml cm^{-2} min^{-1} at 800 °C under the driving force of 0.21 bar/0.001 bar approaching the required level for being commercially interesting [59]. However, the considerable chemical expansion of CPGO40 (Fig. 7) poses problems in terms of ensuring mechanical integrity and limits the applicability of the material [8]. To reduce risks of mechanical failure originating from chemical strain, very low thickness (1-10 µm) would be needed and the oxygen pressure gradient over the materials should be carefully controlled. A discussion of the consequence of chemical strain in supported membrane architectures can be found in ref. [60].

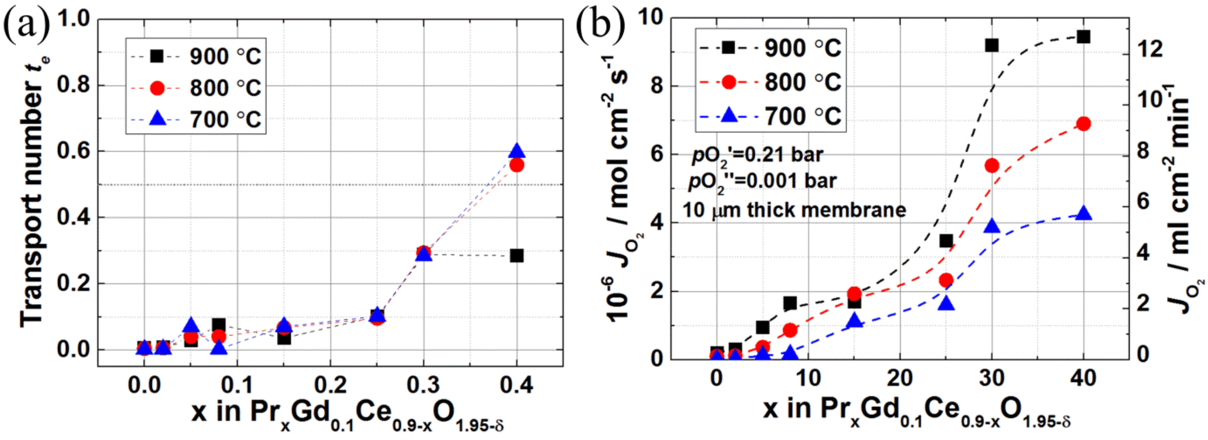

Fig. 20 (a) Calculated transport number and (b) oxygen permeation flux as a function of x in $Pr_xGd_{0.1}Ce_{0.9-x}O_{1.95-\delta}$ at 700, 800 and 900 °C.

6. Conclusions

The conducted investigation of the transport properties of Pr,Gd-doped ceria has led to the following conclusions;

1. Doping Pr in CGO ($Pr_xGd_{0.1}Ce_{0.9-x}O_{1.95-\delta}$) significantly enhances the electronic conductivity (0.04 Scm^{-1} for $Pr_{0.4}Gd_{0.1}Ce_{0.5}O_{1.95-\delta}$ vs. 5.6×10^{-4} Scm^{-1} for $Gd_{0.1}Ce_{0.9}O_{1.95-\delta}$ at 900 °C when pO_2=0.21 bar) under high oxygen partial pressures ($pO_2>10^{-8}$) and decreases slightly the n-type electronic conductivity (0.03 Scm^{-1} for $Pr_{0.4}Gd_{0.1}Ce_{0.5}O_{1.95-\delta}$ vs. 0.3 Scm^{-1} for $Gd_{0.1}Ce_{0.9}O_{1.95-\delta}$ at 900 °C when $pO_2=1\times10^{-15}$ bar) under low oxygen partial pressures ($pO_2<10^{-8}$).

2. Doping Pr in CGO leads to slight enhancement of the oxide ion conductivity of CGO when the total dopant concentration is lower than 30 at.% (0.083 Scm^{-1} for $Pr_{0.15}Gd_{0.1}Ce_{0.75}O_{1.95-\delta}$ vs. 0.67 Scm^{-1} for $Gd_{0.1}Ce_{0.9}O_{1.95-\delta}$ at 800 °C when $pO_2=1\times10^{-3}$ bar).

3. The thermal expansion increases with increasing Pr concentration, due to increased chemical expansion (14.5×10^{-6} K^{-1} for $Pr_{0.05}Gd_{0.1}Ce_{0.85}O_{1.95-\delta}$ vs. 12.5×10^{-6} K^{-1} for $Gd_{0.1}Ce_{0.9}O_{1.95-\delta}$ in the range from 200 °C to 900 °C).

4. The enthaply of the Pr^{4+} to Pr^{3+} reduction reaction enthalpy decreases with increasing Pr concentration (112±10 kJ mol^{-1} for $Pr_{0.4}Gd_{0.1}Ce_{0.5}O_{1.95-\delta}$ vs. 200±34 kJ mol^{-1} for $Pr_{0.08}Gd_{0.1}Ce_{0.82}O_{1.95-\delta}$), indicating a more facile reduciblitiy.

5. An abrupt decrease of the electron hole migration enthalpy is observed when the dopant concentration increased from 8 at.% to 15 at.%, which is likely associated with establishment of a percolation path between the Pr atoms as the chance of finding a Pr in the nearest neighbour shell to each Pr atom strongly increases at this substitution level. The percolation threhold can be intepreted by a simple cubic percolation model.

6. The acheviable oxyen permeation flux of CGO is enhanced by co-doping with Pr because of the enhanced electronic conductivity. CPGO40 is predicted to show the largest achievable flux as the electronic conductivity approaches the ionic one.

Acknowledgments

The authors thank DSF (Danish council for Strategic Research) for the finical support on the project “ENEFOX“- Energy Efficient Oxygen Production for a Sustainable Energy System” (11-116387).

References

[1] M. Puig-Arnavat, S. Soprani, M. Sogaard, K. Engelbrecht, J. Ahrenfeldt, U.B. Henriksen, P.V. Hendriksen, RSC Adv., 3 (2013) 20843-20854.
[2] M. Mogensen, N.M. Sammes, G.A. Tompsett, Solid State Ionics, 129 (2000) 63-94.
[3] S.D. Ebbesen, S.H. Jensen, A. Hauch, M.B. Mogensen, Chemical reviews, 114 (2014) 10697-10734.
[4] W.C. Chueh, Y. Hao, W. Jung, S.M. Haile, Nat Mater, 11 (2012) 155-161.
[5] M.P. Lobera, J.M. Serra, S.P. Foghmoes, M. Søgaard, A. Kaiser, Journal of Membrane Science, 385–386 (2011) 154-161.
[6] S. Wang, T. Kobayashi, M. Dokiya, T. Hashimoto, J. Electrochem. Soc., 147 (2000) 3606-3609.
[7] C. Chatzichristodoulou, P.V. Hendriksen, S.P.V. Foghmoes, S. Ricote, A. Kaiser, J. Classcock, S. Cheng.
[8] A. Kaiser, S. Foghmoes, C. Chatzichristodoulou, M. Søgaard, J.A. Glasscock, H.L. Frandsen, P.V. Hendriksen, Journal of Membrane Science, 378 (2011) 51-60.
[9] M.S. C. Chatzichristodoulou, J. Glasscock, A. Kaiser, S. P. V. Foghmoes, and P. V. Hendriksen, J Electrochem Soc, 158 (2011) F73.
[10] C. Chatzichristodoulou, M. Søgaard, P.V. Hendriksen, Journal of The Electrochemical Society, 158 (2011) F61-F72.
[11] P.S. Manning, J.D. Sirman, J.A. Kilner, Solid State Ionics, 93 (1996) 125-132.
[12] J.A. Lane, J.A. Kilner, Solid State Ionics, 136–137 (2000) 997-1001.
[13] S. Lübke, H.D. Wiemhöfer, Solid State Ionics, 117 (1999) 229-243.
[14] D. Fagg, V. Kharton, J. Frade, Journal of Electroceramics, 9 (2002) 199-207.
[15] D.P. Fagg, J.C.C. Abrantes, D. Perez-Coll, P. Nunez, V.V. Kharton, J.R. Frade, Electrochimica Acta, 48 (2003) 1023-1029.
[16] C. Chatzichristodoulou, P.V. Hendriksen, A. Hagen, Journal of The Electrochemical Society, 157 (2010) B299-B307.
[17] M. Balaguer, C. Solís, J.M. Serra, Chemistry of Materials, 23 (2011) 2333-2343.
[18] V.V. Kharton, A.P. Viskup, F.M. Figueiredo, E.N. Naumovich, A.L. Shaulo, F.M.B. Marques, Materials Letters, 53 (2002) 160-164.
[19] C. Chatzichristodoulou, P.V. Hendriksen, Journal of The Electrochemical Society, 157 (2010) B481-B489.
[20] S.R. Bishop, T.S. Stefanik, H.L. Tuller, Physical Chemistry Chemical Physics, 13 (2011) 10165-10173.
[21] S. Lübke, H.D. Wiemhöfer, Berichte der Bunsengesellschaft für physikalische Chemie, 102 (1998) 642-649.
[22] C. Chatzichristodoulou, S. Ricote, S.P.V. Foghmoes, J. Glasscock, A. Kaiser, P.V. Hendriksen, Solid State Ionics, 269 (2015) 51-56.
[23] C. Chatzichristodoulou, P.V. Hendriksen, Phys. Chem. Chem. Phys., 13 (2011) 21558-21572.
[24] K. Schmale, M. Grünebaum, M. Janssen, S. Baumann, F. Schulze-Küppers, H.-D. Wiemhöfer, physica status solidi (b), 248 (2011) 314-322.
[25] I. Riess, Solid State Ionics, 91 (1996) 221-232.
[26] Y. Takasu, T. Sugino, Y. Matsuda, Journal of applied electrochemistry, 14 (1984) 79-81.
[27] D.-J. Kim, Journal of the American Ceramic Society, 72 (1989) 1415-1421.
[28] R.t. Shannon, Acta Crystallographica Section A: Crystal Physics, Diffraction, Theoretical and General Crystallography, 32 (1976) 751-767.

[29] R. Torrens, N.M. Sammes, G. Tompsett, Journal of Electroceramics, 13 (2004) 683-689.
[30] G.S. Lewis, A. Atkinson, B.C.H. Steele, J. Drennan, Solid State Ionics, 152–153 (2002) 567-573.
[31] A. Kaiser, A.S. Prasad, S.P. Foghmoes, S. Ramousse, N. Bonanos, V. Esposito, Journal of the European Ceramic Society, 33 (2013) 549-556.
[32] T.S. Stefanik, M.I.T, 2004.
[33] S.R. Bishop, T.S. Stefanik, H.L. Tuller, Journal of Materials Research, 27 (2012) 2009-2016.
[34] H.L. Tuller, S.R. Bishop, D. Chen, Y. Kuru, J.J. Kim, T.S. Stefanik, Solid State Ionics, 225 (2012) 194-197.
[35] C. Chatzichristodoulou, P. Norby, P.V. Hendriksen, M.B. Mogensen, Journal of Electroceramics, 34 (2014) 100-107.
[36] J.R. Macdonald, E. Barsoukov, History, 1 (2005) 8.
[37] X. Guo, R. Waser, Progress in Materials Science, 51 (2006) 151-210.
[38] W.J. Bowman, J. Zhu, R. Sharma, P.A. Crozier, Solid State Ionics, 272 (2015) 9-17.
[39] H.J. Avila-Paredes, K. Choi, C.-T. Chen, S. Kim, Journal of Materials Chemistry, 19 (2009) 4837-4842.
[40] J. Newman, Journal of The Electrochemical Society, 113 (1966) 501-502.
[41] D.P. Fagg, I.P. Marozau, A.L. Shaula, V.V. Kharton, J.R. Frade, Journal of Solid State Chemistry, 179 (2006) 3347-3356.
[42] V.V. Kharton, A.P. Viskup, F.M. Figueiredo, E.N. Naumovich, A.A. Yaremchenko, F.M.B. Marques, Electrochimica Acta, 46 (2001) 2879-2889.
[43] C. Chatzichristodoulou, T.P. Blennow, M. Søgaard, P.V. Hendriksen, M.B. Mogensen, Ceria and Its Use in Solid Oxide Cells and Oxygen Membranes, Catalysis by Ceria and Related Materials, World Scientific Publising Co., 2013, pp. 623-782.
[44] D.P. Fagg, S. García-Martin, V.V. Kharton, J.R. Frade, Chemistry of Materials, 21 (2008) 381-391.
[45] V.V. Kharton, F.M. Figueiredo, L. Navarro, E.N. Naumovich, A.V. Kovalevsky, A.A. Yaremchenko, A.P. Viskup, A. Carneiro, F.M.B. Marques, J.R. Frade, Journal of Materials Science, 36 (2001) 1105-1117.
[46] V. Thangadurai, R. Huggins, W. Weppner, J Solid State Electrochem, 5 (2001) 531-537.
[47] K.E. Swider, W.L. Worrell, Journal of The Electrochemical Society, 143 (1996) 3706-3711.
[48] D. Kim, S. Miyoshi, T. Tsuchiya, S. Yamaguchi, Solid State Ionics, 262 (2014) 875-878.
[49] R. Zallen, The Percolation Model, The Physics of Amorphous Solids, Wiley-VCH Verlag GmbH, 2007, pp. 170.
[50] L. Navarro, F. Marques, J. Frade, Journal of The Electrochemical Society, 144 (1997) 267-273.
[51] M. Mogensen, T. Lindegaard, U.R. Hansen, G. Mogensen, Journal of The Electrochemical Society, 141 (1994) 2122-2128.
[52] H.L. Tuller, A.S. Nowick, Journal of The Electrochemical Society, 126 (1979) 209-217.
[53] B.C.H. Steele, Solid State Ionics, 129 (2000) 95-110.
[54] S. Wang, H. Inaba, H. Tagawa, M. Dokiya, T. Hashimoto, Solid State Ionics, 107 (1998) 73-79.
[55] P.P. Dholabhai, J.B. Adams, P.A. Crozier, R. Sharma, Journal of Materials Chemistry, 21 (2011) 18991-18997.
[56] H. Yamamura, H. Nishino, K. Kakinuma, K. Nomura, Journal of the Ceramic Society of Japan, 111 (2003) 902-906.
[57] T. Kudo, H. Obayashi, Journal of The Electrochemical Society, 123 (1976) 415-419.
[58] P. Shuk, M. Greenblatt, Solid State Ionics, 116 (1999) 217-223.
[59] R. Bredesen, K. Jordal, O. Bolland, Chem. Eng. Process. Process Intensif., 43 (2004) 1129-1158.
[60] P.V. Hendriksen, P.H. Larsen, M. Mogensen, F.W. Poulsen, K. Wiik, Catal. Today., 56 (2000) 283-295.

Supporting materials

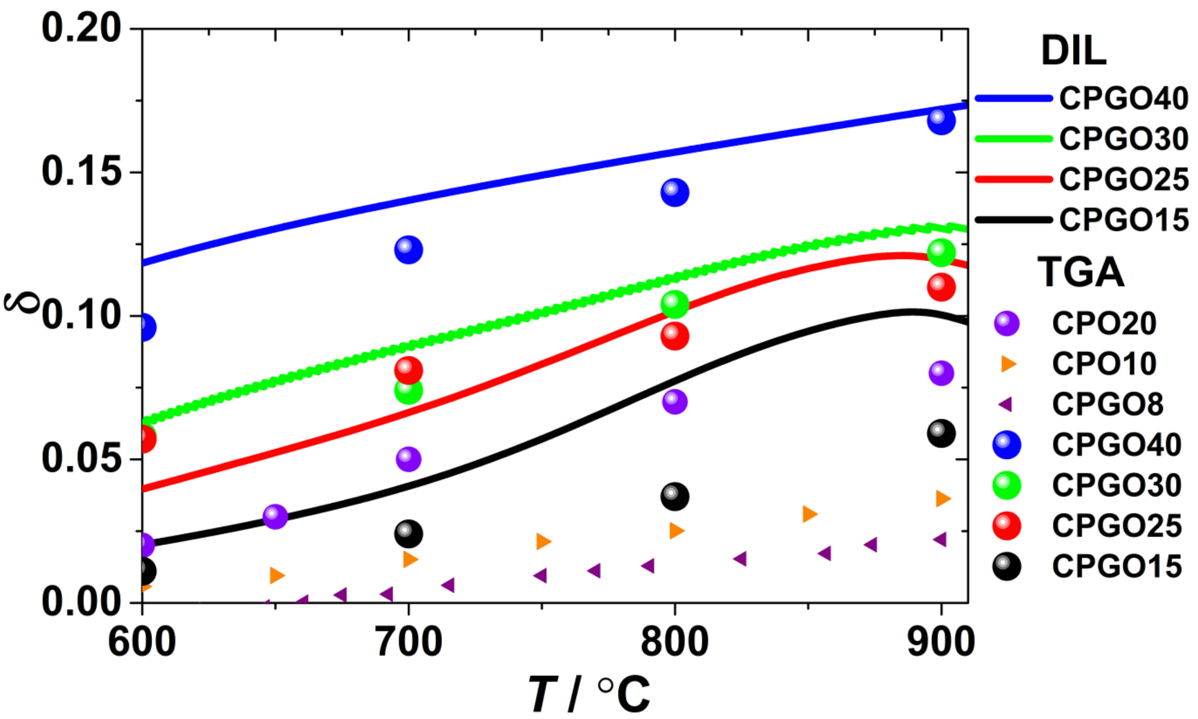

Fig. S1 Oxygen nonstoichiometry of CPGOx calculated by TGA (balls) and thermal expansion (solid lines) versus temperature.

1. Calculation of oxygen nonstoichiometry by TGA.

$$\delta = \frac{M}{m}\frac{\Delta m}{A_0} \tag{S1}$$

where m and M are the mass and weight of the sample, respectively. Δm is the observed change in mass and A_0 is the atomic mass of oxygen.

2. Calculation of oxygen nonstoichiometry by thermal expansion.

$$\varepsilon_{chem} = \frac{k a_{\mathrm{Pr}^{3+}} + (1-k) a_{\mathrm{Pr}^{4+}} - a_{\mathrm{Pr}^{4+}}}{a_{\mathrm{Pr}^{4+}}} \tag{S2}$$

$$\delta = \frac{1}{2}k \qquad \text{(S3)}$$

where ε_{chem} is the chemical expansion. k is the concentration of Pr^{3+}, $a_{Pr^{3+}}$ is the lattice parameter of the sample with Pr^{3+}, $a_{Pr^{4+}}$ is the lattice parameter of the sample with Pr^{4+} (see Fig. 4). The concentration of Pr^{3+} can be calculated by equation S2. The oxygen vacancy concentration equals to 0.5 k. As illustrated in Fig. S1, the concentration of oxygen vacancy deduced by the two techniques are very close for heavily doped samples (CPGO40, CPGO30 and CPGO25). The deviation observed in CPGO15 might be due to the overestimation of concentration of oxygen vacancy deduced by chemical expansion by assuming a temperature-independent thermal expansion coefficient (see Fig. 7b).

Table S1. Oxygen partial pressure for the fixed ratio between Pr^{3+} and Pr^{4+} (Pr^{3+}/Pr^{4+}=2.7) of CPGO at 700, 800 and 900°C.

Temperature / °C	**900**	**800**	**700**
CPGO40	1.70 bar	0.08 bar	9.0e-3 bar
CPGO30	0.76 bar	0.04 bar	5.6e-4 bar
CPGO25	0.20 bar	0.01 bar	5.0e-4 bar
CPGO15	0.10 bar	8.9e-4 bar	2.5e-5 bar

Chapter 8: Performance of $Ba_{0.5}Sr_{0.5}(Co_{0.8}Fe_{0.2})_{0.97}Zr_{0.03}O_{3-\delta}$ oxygen transport membrane fabricated by phase-inversion tape casting

Shiyang Cheng[1]*, Hua Huang[2], Søren B. Simonsen[1], Ming Chen[1], Martin Søgaard[3], Andreas Kaiser[1], Peter Vang Hendriksen[1], Chusheng Chen[2]

[1] Department of Energy Conversion and Storage, Technical University of Denmark, Risø campus, Frederiksborgvej 399, DK-4000 Roskilde, Denmark

[2] CAS Key Laboratory of Materials for Energy Conversion, Department of Materials Science and Engineering, University of Science and Technology of China, Hefei 230026, China

[3] Meneta Advanced Shims Technology A/S, Kirkegyden 52, DK-5270 Odense, Denmark

* To whom correspondence should be addressed. E-mail: shic@dtu.dk

To be submitted to Journal of membrane science

Abstract

Asymmetric $Ba_{0.5}Sr_{0.5}(Co_{0.8}Fe_{0.2})_{0.97}Zr_{0.03}O_{3-\delta}$ (BSCFZ)-based oxygen transport membranes were prepared by phase-inversion tape casting. The oxygen permeation flux of the asymmetric membrane was measured with and without additional catalysts as a function of temperature, apparent driving force, and feed side oxygen partial pressure. Particularly at lower temperatures (<800°C), the infiltration of the oxygen exchange catalyst $La_{0.6}Sr_{0.4}CoO_{3-\delta}$ (LSC) on the feed side and coating BSCFZ catalytic layer on the permeate side enhanced the oxygen permeation flux compared to the membrane without catalysts. The LSC catalyst on the feed side effectively improved the oxygen surface exchange but led to an increase in gas diffusion resistance as a side effect at very high fluxes because the pores on the feed side of the membrane were partially blocked by the infiltrated catalyst particles. The BSCFZ asymmetric membrane reached an oxygen flux of 55 ml cm^{-2} min^{-1} measured under a strong pO_2 gradient of O_2/H_2 at 950°C. This oxygen flux could not be sustained because of the fast degradation induced by thermodynamic decomposition. The asymmetric membrane without catalyst exhibited a stable flux of 11.2 ml cm^{-2} min^{-1} at 950°C for 150 hours and 7 Nml cm^{-2} min^{-1} at 850°C for 300 hours in O_2/N_2. Segregation of barium sulphate and cobalt oxide was found on the surface of the dense membrane, which is ascribed to the reaction between sulphur-containing binder (PESF) and elements from the membrane itself. Following the flux measurement

for the membrane without catalyst, significant loss of Co, Sr and Fe and enrichment of $BaSO_4$ was observed on the permeate side of the membrane, which is likely due to a kinetic demixing driven by the oxygen partial pressure gradient across the membrane.

Keywords: BSCFZ; phase-inversion; oxygen transport membranes; oxygen surface exchange; catalyst; kinetic demixing

1. Introduction

Oxygen transport membranes (OTMs) have been extensively investigated for numerous applications such as high-purity oxygen production, partial oxidation of methane, oxy-fuel combustion, biomass gasification and CO_2 capture [1]. Recently, most studies have focused on the development of perovskite-based OTMs because of their promising oxygen permeability. Among these perovskite-related oxides, $Ba_xSr_{1-x}Co_yFe_{1-y}O_{3-\delta}$ (BSCF) is a series of oxides exhibiting the greatest oxygen permeability [2]. However, BSCF is associated with multiple disadvantages including high thermal expansion [3], high creep rate [4], poor mechanical strength [5] and chemical instability under reducing conditions [6]. In particular, the phase transformation in the temperature range of 850-900°C [7] is problematic for long-term use. Efforts have been made to stabilize the cubic structure of BSCF. It has been reported that partial substitution of the B site (Co/Fe) with Zr effectively stabilizes the cubic phase of BSCF and in turn preserves a stable oxygen permeation flux [8, 9] as well as oxygen surface exchange rate [10]. Lu *et al.* [8] reported that the oxygen permeation flux of Zr-doped BSCF is slightly lower than that of BSCF, but the oxygen flux is more stable above 750°C. Ravkina *et al.* found that the maximum solubility of Zr in BSCF is less than 3 cat.%, above which the $(Ba,Sr)ZrO_3$ phase precipitates along the grain boundaries [11], which decreases the oxygen flux. Based on the literature, 3 cat.% Zr-doped BSCF is preferred to achieve a single-phase material with stable oxygen flux at high temperature. This is the composition studied in this work.

The fabrication of thin membranes is usually required for most oxygen membrane materials to achieve commercially relevant oxygen fluxes because the oxygen flux is inversely proportional to the thickness of the membrane (if the surface exchange reaction is not the main rate-limiting step [12]). To ensure sufficient mechanical strength, the thin film membrane layers have to be supported on a porous substrate. Such asymmetric membrane structures are often prepared by depositing the thin membrane layer on a planar or tubular porous substrate using techniques such as dip coating

[13], tape casting [14] or slip casting [15]. In light of the very large thermal expansion coefficient of BSCF (TEC ~20×10^{-6} K^{-1} [16]) compared to most structural ceramic materials, self-supported BSCF membranes are preferred to avoid high thermal expansion mismatch and high thermomechanical stress during thermocycling. Planar self-supported BSCF asymmetric membranes are normally processed by multilayer tape casting [17]. For the multilayer tape casting process it is however difficult to achieve the necessary gas permeability in the support when using conventional pore formers in the casting.

Phase-inversion tape casting is a novel technique that allows manufacture of asymmetric planar membranes in one step [18]. The as-prepared membrane consists of a dense membrane on top of a structure with finger-like pores. He *et al.* [19] reported that a $La_{0.8}Sr_{0.2}MnO_{3-\delta}$-$Zr_{0.84}Y_{0.16}O_{1.92}$ membrane on a finger-like support exhibited much higher flux than the same thickness of membrane on an ordinary porous support. Several studies concluded that solid oxide fuel cells and oxygen transport membranes prepared by phase-inversion tape casting effectively do not exhibit mass transfer polarization effects [18-21]. The unique finger-like pore structure thus facilitates gas transport by minimizing gas diffusion resistance in the support [19].

In the present work, we explore the oxygen permeation flux of a membrane produced by phase-inversion tape casting. The composition of the membrane is $Ba_{0.5}Sr_{0.5}(Co_{0.8}Fe_{0.2})_{0.97}Zr_{0.03}O_{3-\delta}$, and it was characterized with respect to oxygen permeability and chemical stability.

2. Experimental

2.1. Membrane Preparation

A polymer solution was prepared by mixing 0.75 wt.% polyethersulfone (PESF, Radel A-100, Solvay Advanced Polymers), 0.9 wt.% polyvinylpyrrolidone (PVP-K30, Sinopharm Chemical Reagent Co.) and 22.5 wt.% N-methyl-2-pyrrolidone (NMP, CP, Sinopharm Chemical Reagent Co.). A powder of 75.85 wt. % $Ba_{0.6}Sr_{0.4}(Co_{0.5}Fe_{0.5})_{0.97}Zr_{0.03}O_{3-\delta}$ (BSCFZ) from Treibacher Industrie AG was then dispersed in the polymer solution by planetary ball milling for 48 h. Prior to tape casting, the as-obtained suspension was vacuum degassed for 10 min to eliminate internal gas bubbles. The suspension was cast on a Mylar sheet with a doctor blade using a blade gap of 1.2 mm, followed by immersion in a water bath for ca. 12 hours for solidification and pore formation through phase inversion. The as-prepared wet green tapes were dried in an oven at 80 °C with an applied load (20 g cm^{-2}) to ensure flatness during drying. The dried tapes were then heated to 800 °C at a rate of 2 °C min^{-1} for debindering, followed by sintering at 1020 °C for 5 hours in air.

2.2.Application of catalytic layers

A highly porous BSCFZ catalytic layer was applied on the dense BSCFZ membrane layer by brush painting with a BSCFZ-based ink. The BSCFZ ink was prepared by mixing 50 wt.% BSCFZ powder from Treibacher Industrie AG with 50 wt.% Alpha-Terpineol (AR. Sinopharm Chemical Reagent, Co.). On the feed side, a precursor solution consisting of stoichiometric amounts of nitrate for a nominal composition of $La_{0.6}Sr_{0.4}CoO_{3-\delta}$ (LSC64) was infiltrated five times into the finger-like pores of the support structure as reported by Samson *et al.* [22]. The as-prepared catalytic layers were then calcined at 900°C for 1 hour to obtain good adhesion with the membrane/support surface.

2.3.Characterization of the membrane

The crystal structures of the crushed sintered specimens were characterized by X-ray powder diffraction (XRD). The XRD patterns were measured by a Bruker Robot Advance system operated with Bragg-Brentano geometry with Cu Kα 1 in a 2θ range of 20°-90°. The obtained XRD patterns were indexed and compared to the International Centre for Diffraction Data (ICCD) database with the software DIFFRAC Plus. The microstructure and chemical composition were examined by a Hitachi TM3000 and a FE-SEM Zeiss Supera 35 electron microscope using an acceleration voltage of 15 kV. Furthermore, the membrane surface was checked for defects and pinholes by light microscopy and an ethanol test.

Prior to the addition of the catalytic layers, an X-ray computed tomography (CT) scan was conducted on the BSCFZ membrane in a lab-based Xradia Versa XRM-410 instrument using a W reflection target at a power of 10 W. The scan was performed using a voltage of 140 kV, an HE02 filter (Xradia), 10x optical magnification, binning of 2, an exposure time of 12 s and a total of 3201 projections over a 360° rotation, resulting in a pixel resolution of 0.9 μm. The thickness of the scanned samples was 0.65 mm. The sample width was approximately 2 mm but varied with the sample height. The recorded data were reconstructed using Feldkamp-Davis-Kress reconstruction with smooth filter (0.5 kernel size) and beam hardening constant 0.3. After reconstruction, a non-local means filter (search window = 21, local neighbourhood = 5, similarity value = 0.6) was applied with the software Avizo Fire 8.0. Segmentation was performed to separate membrane solid and pores using global thresholds with the software Avizo Fire 8.0 (for total 3D pore volume) and ImageJ (for 2D pore diameters and pore density). Additional segmentations were performed to estimate errors in the quantitative analysis. Here, the segmented volumes were enlarged to make the volumes of the solid and pores as small or as large as possible without introducing gross errors. The additional segmentations therefore represent lower and upper limits in the quantitative X-ray CT analysis.

2.4.Measurement of oxygen permeation rate

The oxygen permeation measurements were performed in the customized test configuration displayed in Fig. 1. The sample, having a thickness of approximately 0.5 mm and a diameter of 10 mm, was initially sealed between two alumina tubes using a 30/70 vol.% mixture of a MgO/sodium aluminosilicate glass composite. The membrane was placed with the finger-like porous side facing the downwards in the middle zone of an adjustable-height tube furnace. The feed side tube below the membrane was supplied with gas from the feed side manifold, which featured a feed gas inlet and outlet. Similarly, the permeate side of the membrane was purged with gas from a “permeate side” manifold. The feed side was flushed with air or O_2 with a constant flow rate of 100 Nml min^{-1}, and the permeate side was flushed at various flow rates of N_2 or H_2 (between 30 Nml min^{-1} to 300 Nml min^{-1}). All gas flows were recorded by mass flow controllers. The net oxygen permeation flux can be deduced from the pO_2 difference between inlet and outlet gases. The pO_2 was monitored by two customized YSZ-based oxygen sensors. The total leak in the system was assessed by means of a mass flow meter on the permeate stream. When perfect sealing is achieved, the outlet gas flow rate is equivalent to the inlet flow added with the flow of the permeated oxygen. If there are leaks in the membrane or pinholes or cracks in the glass encapsulation, the flow rate of the outlet gas will be lower than that of the inlet gas. Typically, when a significant leak is observed during the permeation measurement, a thermally activated increase in oxygen flux is not observed. In the data reported here, the inlet and outlet flows were identical (within 1% uncertainty) and a thermally activated oxygen permeation flux was observed, indicating close to perfect sealing. The maximum leak originating from pinholes in the sealant and from other sources of oxygen in the permeate flow through the membrane is estimated to be lower than 5% at low temperature (600°C) based on the gas sensor. Below 600°C a large leak appeared as a result of sealant failure driven by thermal expansion mismatch between membrane and manifold tubes. The measurement was repeated to check the reproducibility of the results.

The oxygen permeation flux of the membrane using N_2 as the sweep gas can be written:

$$J_{O_2} = \frac{\dot{N}\left(pO_2^{out} - pO_2^{in}\right)}{A} \tag{1}$$

The oxygen flux measured using H_2 as the sweep gas can be written:

$$J_{O_2} = \frac{\dot{V}_{H_2O}^{out} - \dot{V}_{H_2O}^{in}}{2A} \tag{2}$$

where A is the net area of the permeate side of the membrane, pO_2^{in} and pO_2^{out} denote the oxygen partial pressure of the inlet and outlet, respectively, and $\dot{N}$ represents the mass flow rate of outlet gases. The ratio of the partial pressure of hydrogen to water is determined by $\frac{p_{H_2}}{p_{H_2O}} = K_{eq}(T) \Big/ p_{O_2}^{1/2}$ where $K_{eq}(T)$ is the thermodynamic equilibrium constant of the reaction $H_2O(g)=H_2(g)+0.5O_2(g)$. The inlet volume flow of water is expressed as $\dot{V}_{H_2O}^{out} = \dot{V}_{H_2}^{in}\, p_{H_2O}^{in} \big/ p_{H_2}^{in}$. The total volume flow over the membrane stays constant because each hydrogen molecule reacts with oxygen to form one water molecule ($\dot{V}_t = \dot{V}_{H_2O} + \dot{V}_{H_2}$). The volume flow of outlet water is estimated as $\dot{V}_{H_2O}^{out} = \dot{V}_t\left(1 + p_{H_2}^{out} \big/ p_{H_2O}^{out}\right)^{-1}$. The oxygen partial pressures are calculated *via* the Nernst equation from the emf values measured with the zirconia sensors.

$$E = \frac{RT}{4F} \ln \frac{pO_2}{pO_{2,ref}} \tag{3}$$

where E is the open circuit voltage of the oxygen sensor, R is the gas constant, $pO_{2,ref}$ is the oxygen partial pressure at the reference electrode (which is fixed at 0.21 bar), and T is the temperature of the oxygen sensor.

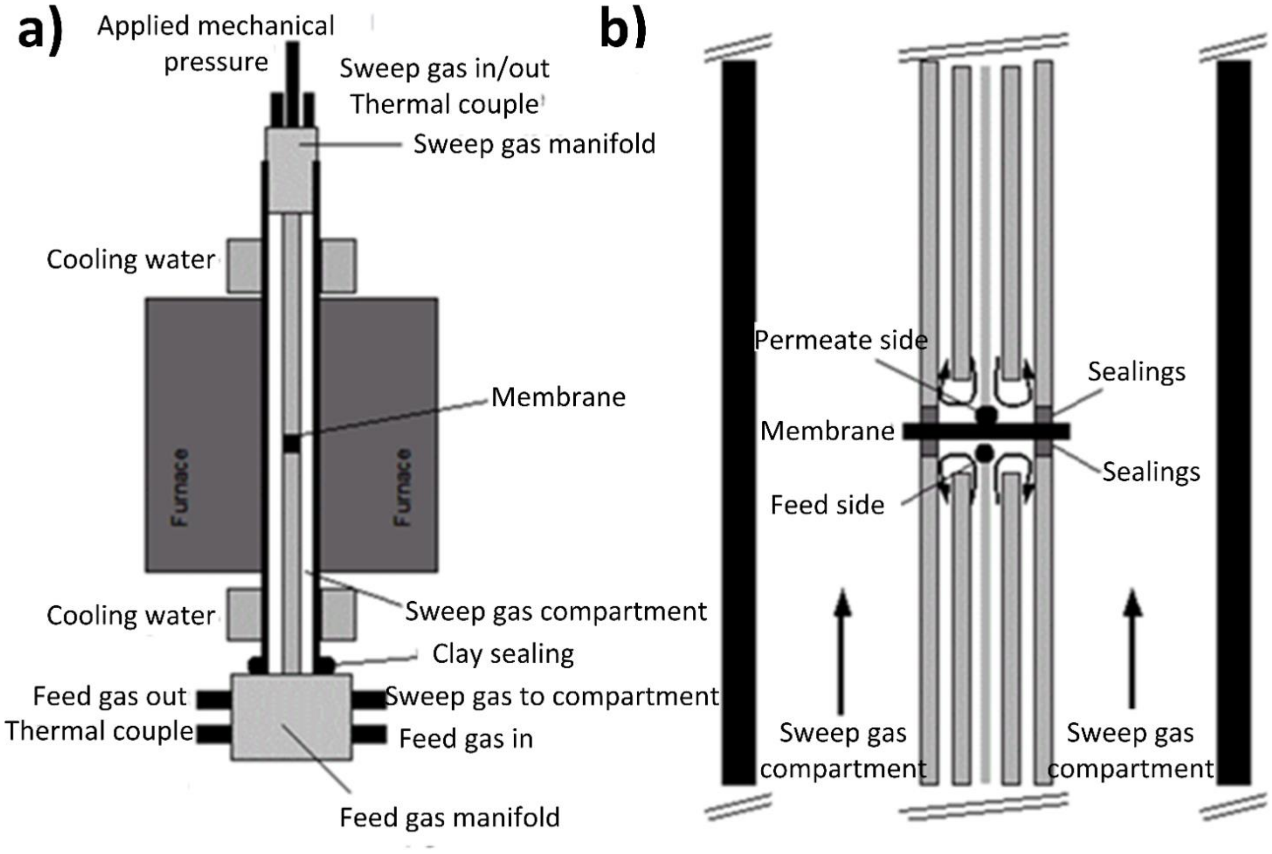

Figure. 1. (a) Schematic illustration of the membrane test rig. (b) Expanded view of the heated part of the membrane test rig.

3. Results and discussions

3.1.Characterization of the membrane assembly microstructure

Fig. 2a-b shows a polished cross section of an asymmetric membrane with catalysts introduced on both sides. According to Figure 2a, the hierarchical asymmetric membrane consists of a finger-like support (with a thickness of ca. 500 μm) and a dense layer (with a thickness of ca. 70-100 μm). With respect to the catalyst on the dense layer, a ca. 8 μm thick BSCFZ porous layer is observed (Fig. 2b). A LSC catalyst was impregnated in the porous support using solutions of Lanthanum-, strontium-, and cobalt- nitrates. Fig. 2c and d show views of the pores adjacent to the dense membrane before and after infiltration of the LSC catalyst, respectively. After infiltration, it can be clearly observed, that the pore bottom of the microchannel was homogenously covered by a fine layer of fluffy particles.

Fig. 3 presents (a) a volume rendering of and (b) a slice in the 3D reconstruction of the membrane based on an X-ray CT scan. A thin dense part (Fig. 3b, left side) and thicker porous part with elongated structures (Fig. 3b, right side) can be observed in agreement with Fig. 2. Fig. 3c presents a segmentation of the pores indicating that the individual pores are cylindrical with cross sections that are almost circular with varying diameter (Fig. 3c). Deviations from circular geometry are observed at locations where pores are in contact with each other. In Fig. 3c, the finger-like structure indicated by the SEM cross-sectional images (Fig. 2a) is more clearly observed. It can also be observed that the finger-like pores are relatively straight all the way through the support, yielding a low value of tortuosity factor. The pore volume as calculated from the segmentation (Fig. 3c) is 28 ± 3 %. From 2D slices in the 3D data, the mean pore diameter was measured as a function of distance from the dense surface (Fig. 3d, black). It can be observed that the mean pore diameter is ca. 80 µm in the centre of the membrane and that the mean pore diameter drops to ca. 40 µm at the porous surface. Similarly, measurements of 2D pore areas indicate that the pore area density is approximately constant (ca. 40 %) from the porous surface and ca. 300 µm into the membrane, after which it drops to zero when reaching the dense region. This finger-like structure is expected to be highly favourable to gas transport, which is quantified by the flux measurement to be discussed in section 3.2.

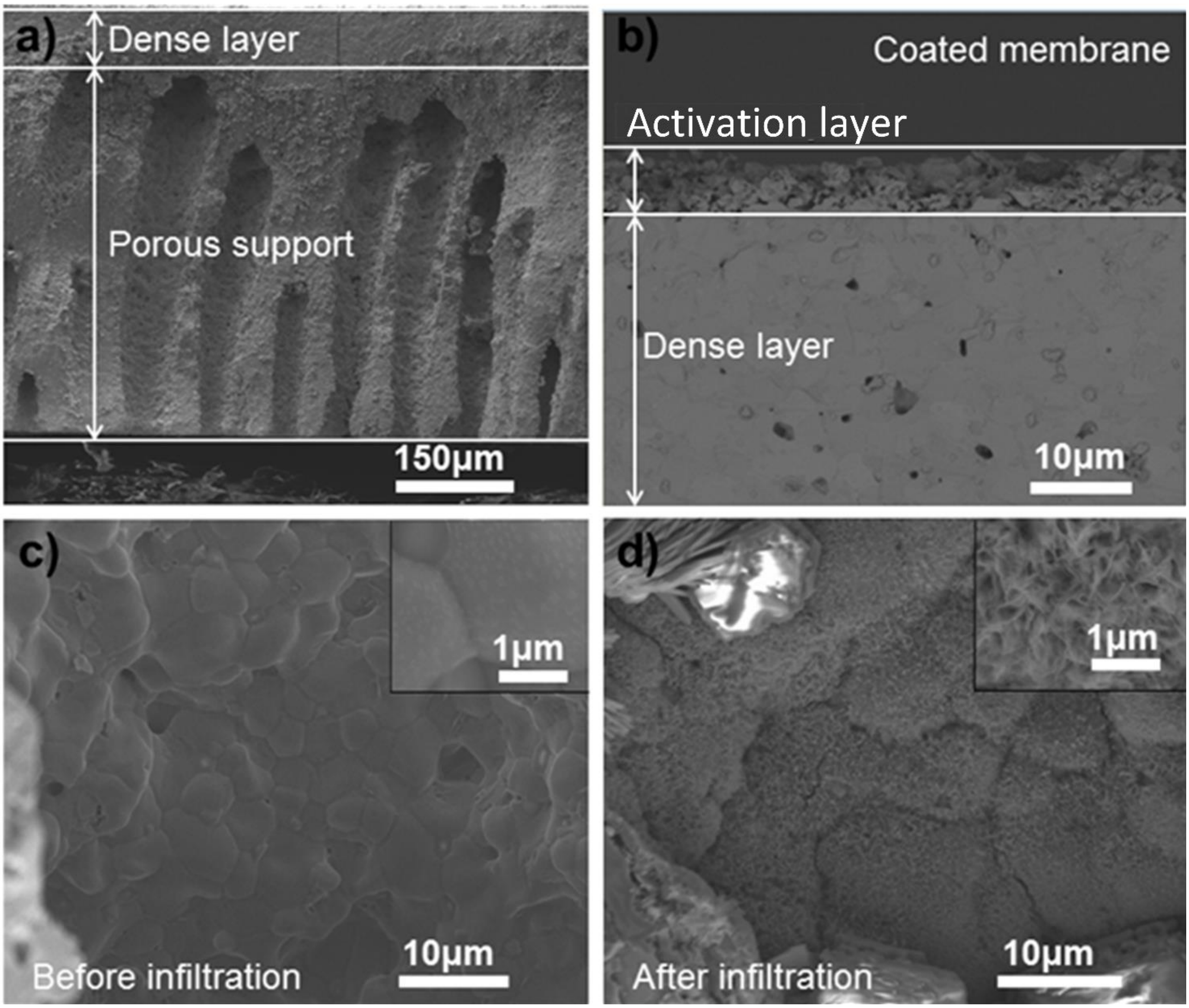

Figure. 2. SEM micrograph of (a) a cross section of an asymmetric BSCFZ membrane, (b) a cross section of an asymmetric BSCFZ membrane with BSCFZ catalyst layer on the permeate side, (c-d) a pore surface (c) before and (d) after catalyst infiltration. The inserts in (c-d) present enlarged views of the pore structure.

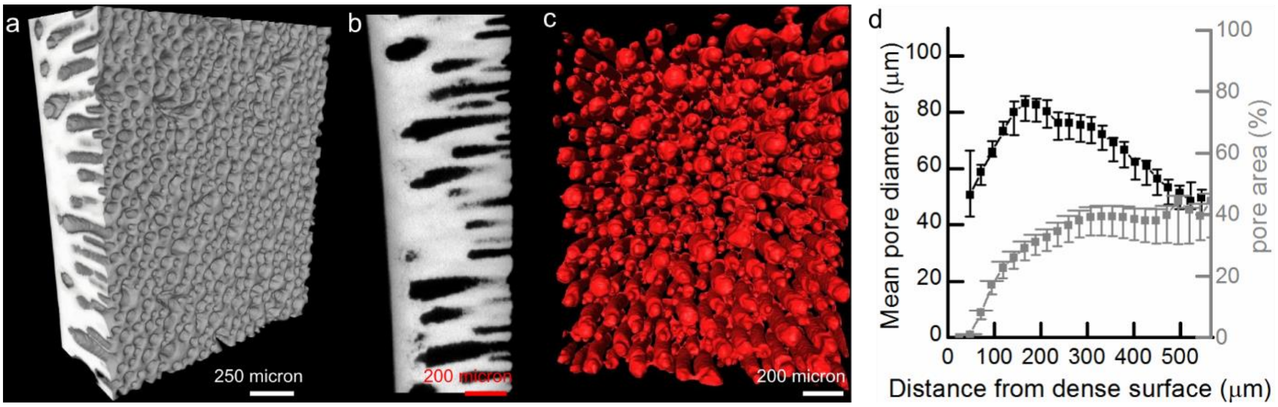

Figure. 3. (a) Volume rendering and (b) slices of the 3D reconstruction from an X-ray CT scan of the asymmetric BSCFZ membrane. (c) The segmented pore volume. (d) The mean pore diameter and the pore area for several 2D slices in the 3D dataset presented as a function of distance from the dense membrane surface. The error bars indicate the estimated error in the segmentation.

3.2.Oxygen permeation flux under small oxygen partial pressure gradients

Fig. 4 and Fig. 5 shows the oxygen fluxes of the sample measured in air/N_2 and O_2/N_2 as a function of apparent driving force ($\ln(pO_2'/pO_2'')$), respectively. In both cases, a clear linear relationship between J_{O2} and $\ln(pO_2'/pO_2'')$ was found for the 1mm thick pellets for all the temperature with a high correlation ($R^2>0.95$). The linear behaviour for the 1mm thick pellet indicates that the flux is mostly determined by the ionic transport in the bulk. For the 100 μm thick asymmetric membrane in both air/N_2 and O_2/N_2, the relationship somewhat follows the Wagner behaviour under small driving force ($\ln(pO_2'/pO_2''<2)$) whilst the curve starts to level off under the larger driving force where the more pronounced deviation from the expected Wagner behaviour was observed. The deviation is likely due to the surface exchange limitation, as reported in Schulz *et al.*[23], Kharton *et al.*[24] and Kim *et al.* [25].

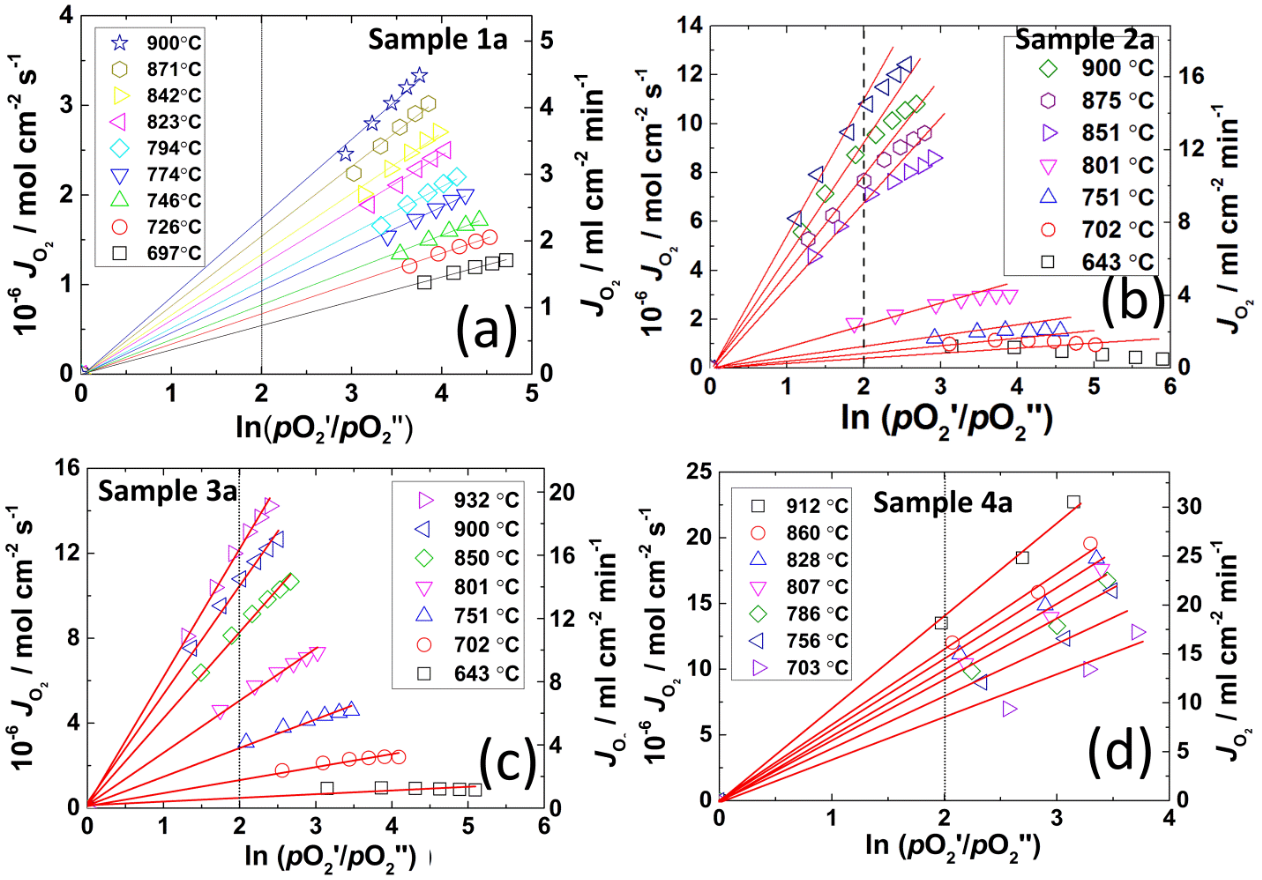

Figure. 4 Oxygen permeation flux versus apparent driving force ln(pO_2'/pO_2'') using pure O_2 as the feed gas and N_2 as the sweep gas, (a) 1mm thick symmetric disk (b) bare asymmetric membrane (c) asymmetric membrane with BSCFZ porous catalytic layer on permeate side (d) asymmetric membrane with LSC catalyst impregnated inside feed side and BSCFZ catalytic layer on the permeate side. The red solid lines are the linear fitting of the data with Wagner equation.

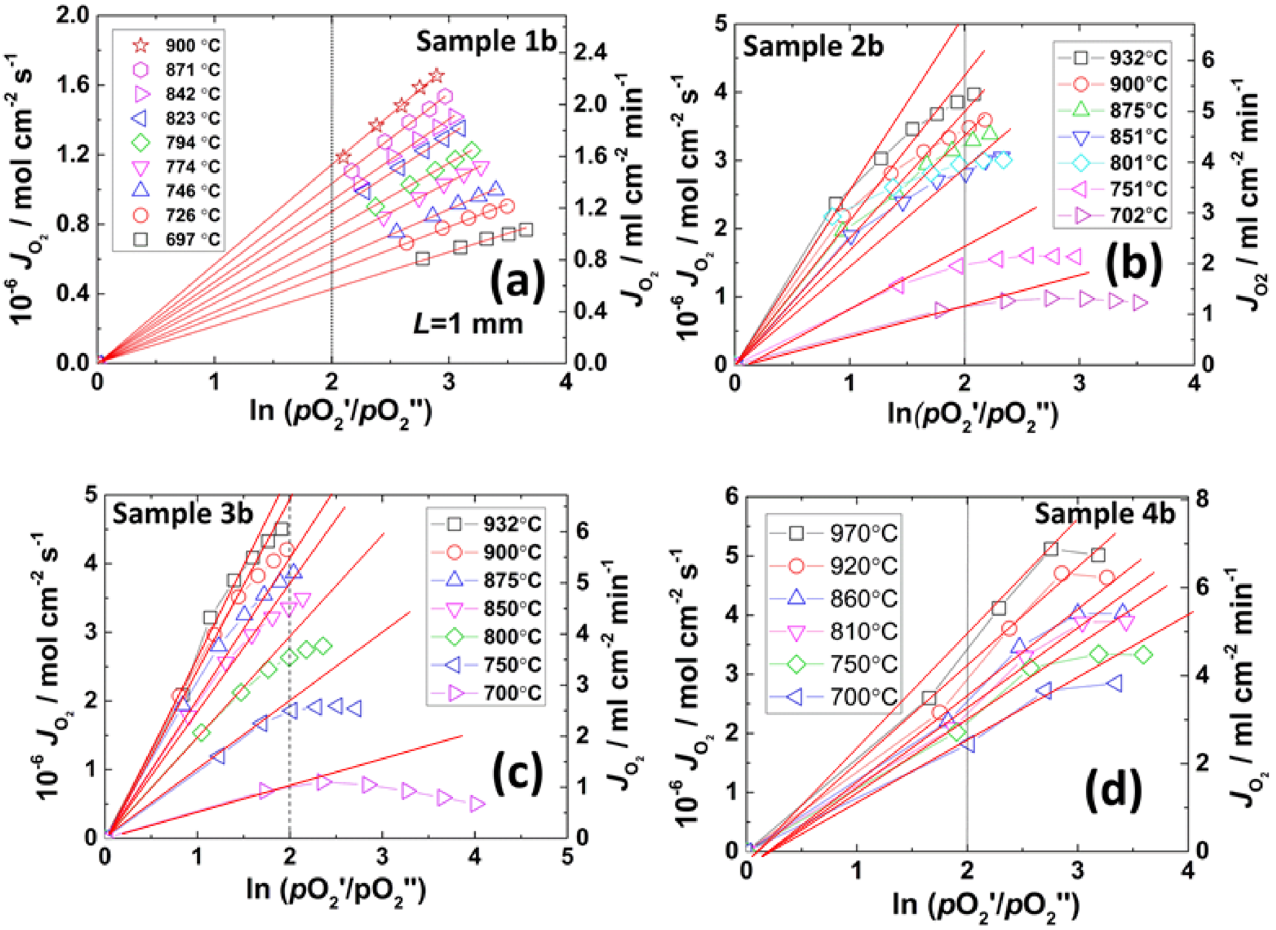

Figure. 5 Oxygen permeation flux versus apparent driving force ln(pO_2'/pO_2'') using air as the feed gas and N_2 as the sweep gas, (a) 1mm thick symmetric disk (b) bare asymmetric membrane (c) asymmetric membrane with BSCFZ porous catalytic layer on permeate side (d) asymmetric membrane with LSC catalyst impregnated inside feed side and BSCFZ catalytic layer on the permeate side. The red solid lines are the linear fitting of the data with Wagner equation.

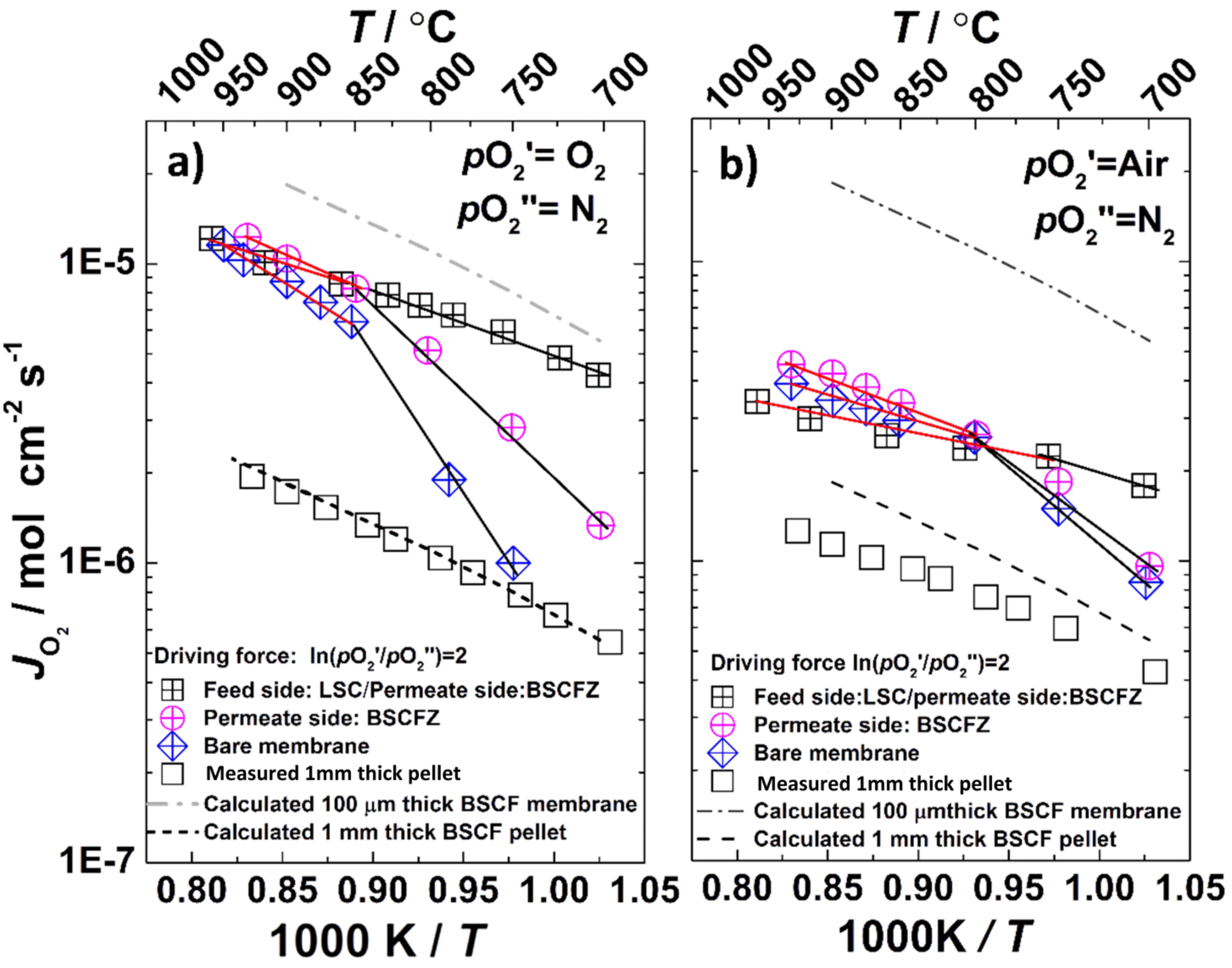

Figure. 6. Arrhenius plots of fluxes measured on the different membranes using different feed gases: (a) pure O_2, (b) air. The sweep gas is N_2. Calculated fluxes for 1mm thick BSCF pellet and 100µm thick BSCF membrane are also included.

Figure. 6 shows Arrhenius-type plots of the oxygen permeation fluxes of BSCFZ membranes with and without catalytic layers measured with (a) O_2 or (b) air as the feed gas and N_2 as the sweep gas upon an arbitrary oxygen partial pressure gradient ($\ln(pO_2'/pO_2'')=2$ in the temperature range; 700-950 °C obtained from Fig. 4. The theoretical fluxes for a 1 mm thick BSCF disc and a 100 µm BSCF membrane (calculated based on the ionic conductivity reported by Chen *et al.* [26]) are also plotted. The uncertainty of the measured flux is estimated to be less than 5% and originates primarily from the uncertainty in the area of the membrane being tested.

According to the generic model proposed by Baumann *et al.* [17], the oxygen flux of an asymmetric membrane is rate limited by a series of resistances, including mass transport polarization across the porous support, oxygen reduction on the feed side, bulk diffusion and oxide ion oxidation on the permeate side. For the measurement conducted with pure oxygen on the feed (Fig. 6a), the mass transfer polarization across the support can be disregarded [17]. It is found that the oxygen flux of the 1 mm thick BSCFZ disk coated with the BSCFZ catalytic layer on both sides is consistent with the theoretical flux calculated by Wagner's equation, indicating that the flux is rate determined by bulk ambipolar diffusion. This result also indicates that BSCF doped with 3 mol.% Zr exhibits a marginal flux reduction compared to that of pure BSCF, in good agreement with Ref.[11].

For all characterized membranes, the slope of the oxygen flux versus 1/T changes in the range from 800 °C to 850 °C. Similar features are also reported for BSCF membranes of various thicknesses [2, 11, 17, 27]. The change of slope in the Arrhenius plots corresponds to the change of apparent activation energy (E_a), which can be obtained by fitting the data to the equation

$$J_{O_2} = J_0 \exp\left(-\frac{E_a}{kT}\right) \quad (5)$$

The apparent activation energies for all the investigated membranes are summarized in Table 1. It can be observed that the activation energy in the high-temperature range (850-950 °C) is much smaller (<50 kJ mol^{-1}) than that in the low-temperature range (>60 kJ mol^{-1} at 750-800 °C). As the catalytic layers are introduced, the flux increases, especially in the low-temperature range (<800 °C). It has been reported that the activation energy for oxygen surface exchange is larger than that for oxygen ion diffusion in the bulk [17, 28, 29]. Because of the larger activation energy of the surface exchange process, the oxygen flux is more likely to be limited by bulk diffusion at high temperature and oxygen surface exchange at low temperature. The enhanced flux and decrease in activation energy for the membrane with the BSCFZ coating on the permeate side indicates that the fluxes are partially rate limited by the oxygen surface exchange on the permeate side. A further enhancement of oxygen flux at low temperature was obtained by infiltration of LSC on the feed side of the membrane, indicating the oxygen flux is also partially limited by the oxygen surface exchange on the feed side. The bottom of the finger-like pore is expected to serve as the "effective surface" accounting for the oxygen reduction. It is known that LSC is a high performance electrocatalyst for the oxygen reduction reaction [30]. The LSC nanoparticles deposited in the pores enlarge the net surface area of the feed side and further enhance the oxygen surface exchange rate. Nevertheless, the maximum flux is still lower than the theoretically achievable flux of a 100 µm thick BSCF membrane (upper dash dotted lines), indicating that the oxygen flux is still partially limited by the oxygen surface exchange

Table 1 Apparent activation energies of the permeation fluxes through membranes with and without catalyst under O_2/N_2, air/O_2 and 21 vol.% O_2+79 vol.% He/N_2, respectively.

*Membrane no.	Feed side	Permeate side	Thickness / mm	Driving force	*Ea*1 (850-950 °C) / kJ mol^{-1}	*Ea*2 (850-950 °C) / kJ mol^{-1}
1a	BSCFZ	BSCFZ	1.0	O_2/N_2	52	61
1b	BSCFZ	BSCFZ	1.0	Air/N_2	41	53
**1c	No catalyst	No catalyst	1.0	Air/He	35	64
2a	No catalyst	No catalyst	0.1	O_2/N_2	47	122
2b	No catalyst	No catalyst	0.1	Air/N_2	32	95
3a	No catalyst	BSCFZ	0.1	O_2/N_2	39	80
3b	No catalyst	BSCFZ	0.1	Air/N_2	53	85
4a	LSC	BSCFZ	0.1	O_2/N_2	39	80
4b	LSC	BSCFZ	0.1	Air/N_2	53	85
4c	LSC	BSCFZ	0.1	O_2+He/N_2	53	85

***The effective surface area of the membranes in this work is ~0.8 cm^2.**

****Data is taken from Ravkina *et al.*** [11].

It is observed that the oxygen flux measured in air/N_2 is lower than that measured in O_2/N_2. Berenov *et al.*[29] found that the oxygen surface exchange coefficient (k_{ex}) of BSCF exhibits a strong dependence on pO_2 following the relationship of $k \propto pO_2^n$ ($n \approx 1$). Using air as the feed gas thus leads to a lower oxygen surface exchange compared to that using O_2. For the 1 mm thick pellet without the effect of mass transfer polarization (i.e., without thick porous support), the oxygen flux measured in air/N_2 is somehow lower than the calculated flux. This provides a strong indication, that partial limitation by the surface exchange is the main reason for the lower flux observed in air/N_2.

To describe the oxygen flux limitation due to oxygen surface exchange, a modified Wagner's equation (Eq. 4) has been proposed to account in an approximate measure for the effects of the surface and for the relatively lower flux observed when $L<L_c$; [12].

$$J_{O_2} = \frac{1}{1+2L_c/L}\frac{RT\sigma_i}{16F^2L}\ln\frac{p^{/}_{O_2}}{p^{//}_{O_2}} \qquad (4)$$

The factor $(1+2L_c/L)^{-1}$ (rather than 1) can be thought of as a connection term to approximate the effects or finite surface exchange rate. Using the modified Wagner's equation, the characteristic thickness of the 1-mm thick BSCFZ pellet under an arbitrary apparent driving (ln (pO_2'/ pO_2''=2)) has been deduced and compared with that of BSCF pellets from publications, as illustrated in Figure 7. In all cases, the characteristic thickness (L_c) of BSCFZ or BSCF pellets decreases with decreasing temperature. The L_c of BSCFZ-coated BSCFZ pellet is slightly lower than that of LSC-coated BSCF, but much lower than that of uncoated-BSCF pellets at high temperature. This indicates that effect of surface exchange on the flux of BSCFZ pellets is more severe at high temperature.

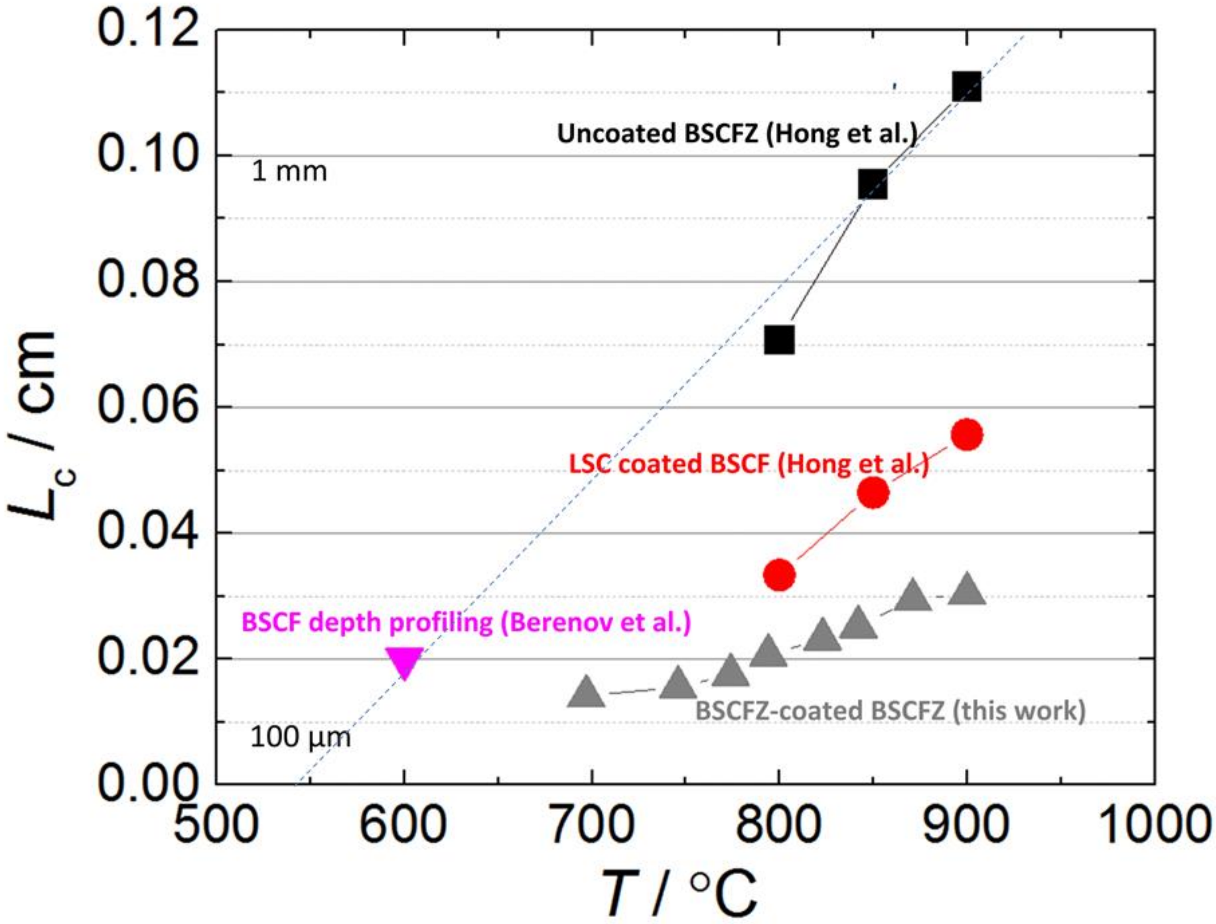

Figure. 7 The characteristic thickness of BSCFZ-coated 1mm thick pellet measured in air/N_2 as a function of temperature. The data of BSCF is taken from Hong *et al.*[27] and Berenov *et al.*[31]. The dashed blue line is the linear fitting.

Similar to the feature observed for the 1 mm thick disk, the lower fluxes observed for the asymmetric membrane using air as the feed gas represent a reduced exchange rate on the high pO_2 side. As illustrated in Figure 7, the thickness of the asymmetric BSCFZ membrane (100 µm) is far lower than the L_c of the uncoated BSCF, but slightly lower than that of coated BSCFZ. Based on this, the coated asymmetric membrane is thus expected to exhibit higher flux than uncoated asymmetric membrane especially at high temperature (>800°C). However, this cannot be observed in Fig. 6 where the flux of coated and uncoated membranes is very close (3.2×10^{-6} mol cm^{-2} s^{-1} vs. 3.0×10^{-6} mol cm^{-2} s^{-1} at 900 °C). Therefore, the surface exchange kinetics is not the only rate limiting step for the asymmetric membranes measured in air/N_2. Baumann *et al.* [17] found that the flux of an BSCF asymmetric membrane measured using air as the feed gas is six times lower than that measured using O_2 as the feed gas because mass transfer polarization prevails when the oxygen flux is sufficiently high. Here, the mass transfer polarization could explain the reduced fluxes observed here. To verify the effect of the mass transfer polarization, we here compare the fluxes measured using different species on the feed side as described in the next paragraph.

Fig. 8 displays Arrhenius plots of the flux for BSCFZ membranes with LSC (feed side) and BSCFZ (permeate side) catalytic layers measured using pure O_2 (black circles), 20% O_2/He (red triangles) and 20% O_2/N_2 (blue rectangular) at the feed side. According to the figure, the flux is influenced by the type of the feed gas and follows the following order: J_{O2} (pure O_2) > J_{O2} (20% O_2/He) > J_{O2} (air). This may seem surprising since the oxygen partial pressure for the two mixed gasses (air and 20% O_2/He) is identical (0.2 bar). A calculation based on the Lennard-Jones equation (Fig. S3), however, shows that the binary diffusion coefficient ca. 3 times higher for the O_2/He mixture than that for O_2/N_2 mixture. This in turn leads to a lower gas diffusion resistance R_{con}, defined as Eq. 6 and 7 [32]:

$$R_{con} = -\frac{RT}{4Fi}\ln\left(1-\frac{i}{i_{cs}}\right) \qquad (6)$$

$$i_{cs} = \left[\frac{4FD_{AB}^{eff}}{RTl}\right]p_0\left(\frac{p}{p-p_0}\right) \qquad (7)$$

$$i = 4FJ_{O_2} \tag{8}$$

$$D_{AB}^{eff} = \frac{\theta}{\tau} D_{AB}^{gas} \tag{9}$$

where R is the gas constant, T is the absolute temperature, F is the Faraday constant, i is the current density, i_{cs} is the limiting current density, l is the thickness of the support, D_{AB}^{eff} is the effective O_2-gas binary diffusion coefficient ($cm^2\ s^{-1}$), p_0 is the partial pressure of oxygen in the feed side, and P is the total pressure.

The calculated gas diffusion resistances (R_{con}) and measured total resistances (R_{tot}) are plotted in Fig. 8b. If porosity is low or the pore size is small compared to the mean free path the microstructure of the support will strongly affect the effective gas diffusion coefficient [33]. With the finger-like structure obtained *via* the phase inversion, it is evident that the tortuosity factor (τ) is relatively low ($\tau \sim 1$ in the calculation). The calculated gas diffusion resistances are ca. 0.4% of the total resistance i.e. diffusion is fast through the support. The tortuosity and relative density used in the calculation are based on an X-ray CT scan of a fresh sample (see Fig. 3). In the aged samples, the finger-like pores are blocked by relatively large particles that may result from the catalyst infiltration. The blocked pores will necessarily hamper the gas diffusion process and this may partly explain why the calculated resistance is lower that the measured resistance. Based on the observations in Fig. 8, the infiltration of the catalyst inside the pores effectively reduces the oxygen surface exchange resistance but increases gas diffusion resistance as a side effect [22]. This can also explain the observation that J_{O2} (with feed side catalyst)< J_{O2} (no feed side catalyst) for the membrane with infiltrated catalyst on the feed side at high temperature (>800°C, Fig. 6b).

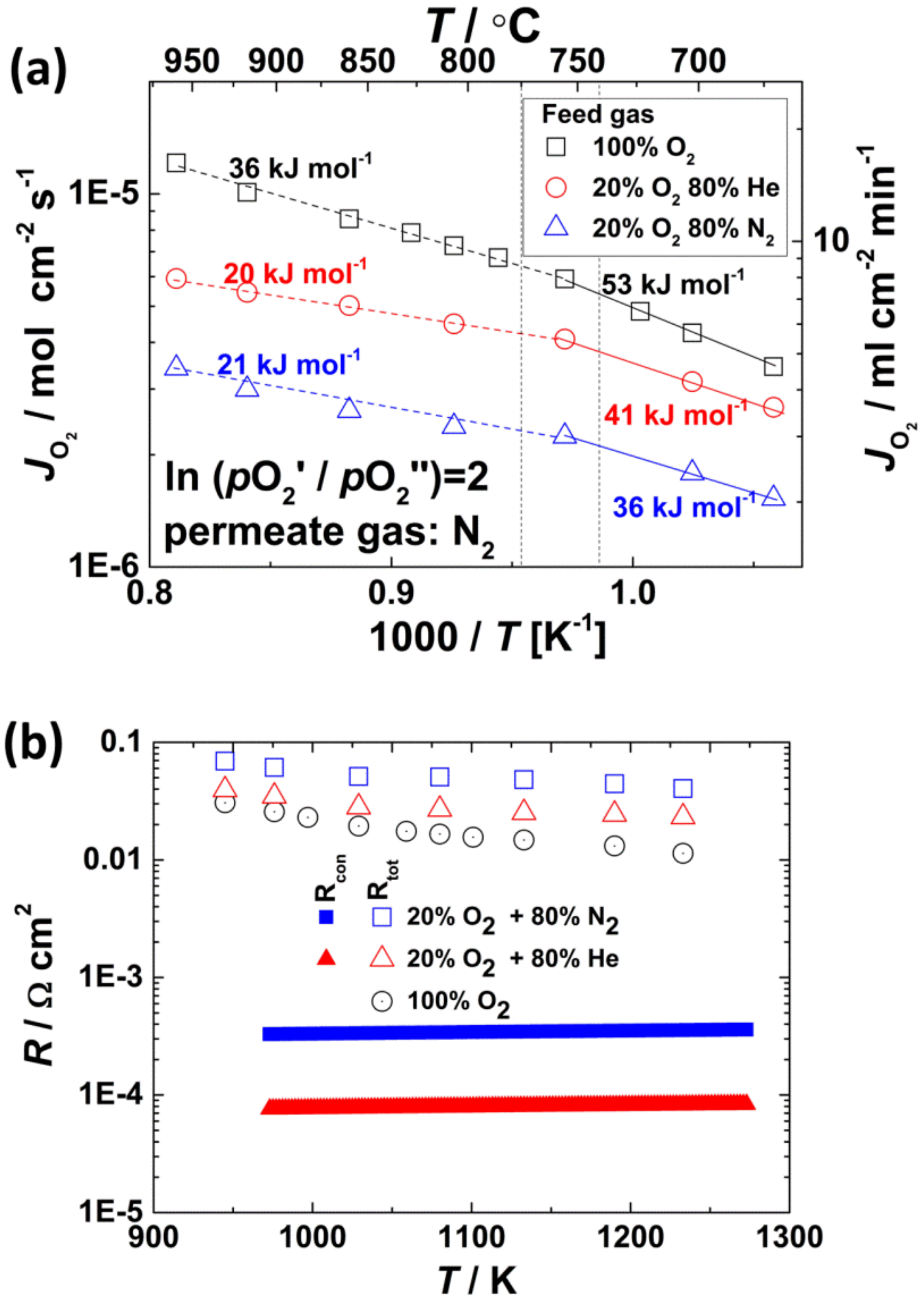

Figure. 8 a. Arrhenius plots of oxygen flux measured using pure O_2, 20% O_2+80% He and 20% O_2+80% N_2. b. the measured and calculated resistance for the membrane measured in O_2, 20% O_2+80% He and 20% O_2+80% N_2.

3.3.Oxygen permeation flux under large gradient (O_2/H_2)

The asymmetric membrane was tested under a large oxygen gradient using pure O_2 as the feed gas and pure H_2 as the sweep gas. As can be observed in Fig. 9, the BSCFZ asymmetric membrane exhibits a flux of 55 ml cm^{-2} min^{-1} at 900°C, approximately five times higher than the oxygen flux measured in O_2/N_2. The enhanced flux is due to the low pO_2 on the permeate side that results in a large apparent driving force across the membrane. The calculated flux (dashed line) is based on the ionic conductivity of BSCF [26] using the Wagner's equation. The calculated flux is in agreement with the measured flux at the lowest temperature (750 °C), but less than the measured flux at 900 °C in the first test (black squares). Note that the ionic conductivity used in the calculation is measured under oxidizing condition ($>1\times10^{-5}$ bar). The real ionic conductivity of BSCF under reducing condition, although not yet published, is expected to be higher than the value used in the calculation because the oxygen vacancy concentration is higher under the lower oxygen partial pressure.

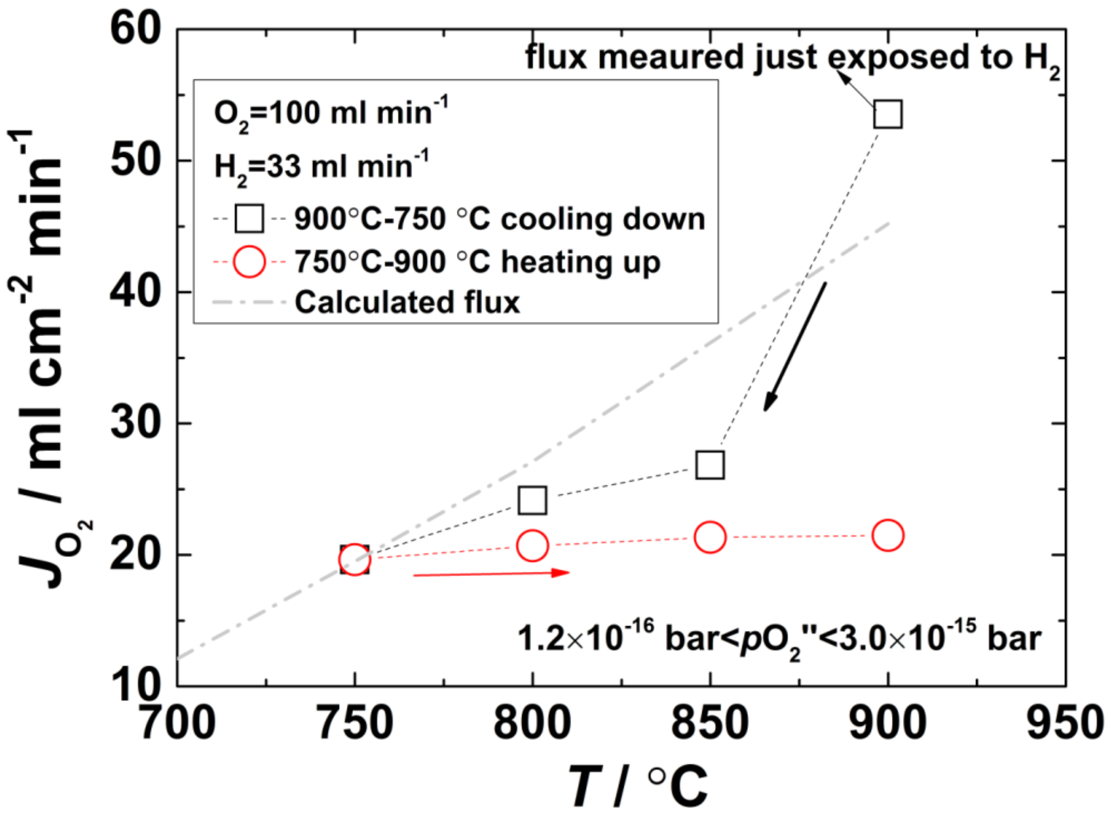

Figure. 9. Oxygen flux of BSCFZ measured using 100 ml min^{-1} O_2 on the feed side and 33 ml min^{-1} H_2.

The gas on the low pO_2 side was changed at 900 °C and temperature reduced. Afterwards the temperature was increased again (red curves marked is heating up). In the second test by heating from 750°C to 900°C the flux is much lower than that in the initial cooling run from 900°C to 750°C. Ovenstone *et al.* [6] reported that BSCF is not chemically stable in 4% H_2 at 300°C; above this temperature, BSCF decomposes into a complex series of oxides, even forming (Ba,Sr)O and Co-Fe alloy at a temperature of 750-900°C. The observed low flux is therefore likely a consequence of fast phase degradation arising from the decomposition of BSCF and formation of oxides or alloys that partially block oxide ion transport. We also found that the membrane suffers mechanical failure during the test. As the test proceeds, the decomposition of BSCFZ leads to a weakening of the sample. In addition to decomposition, the extraordinary strain induced by thermal and chemical expansion across the membrane under such a large chemical potential gradient (O_2/H_2) could also contribute to the mechanical failure [34].

3.4.Long term stability of the membrane

To evaluate the long term stability under the low potential gradient, the bare membrane was measured under a fixed driving force (O_2/N_2) at 950 °C and 850 °C (the working temperature of most OTMs) over an extended period (480 hours totally). As seen in Fig. 10a, a relatively stable flux of 11.2 ml cm^{-2} min^{-1} at 950 °C was observed over 150 hours. At 850 °C, the flux degrades from 8 ml cm^{-2} min^{-1} to 7 ml cm^{-2} min^{-1} in the first 100 hours. Over the following 200 hours a stable flux of 7 ml cm^{-2} min^{-1} is observed.

As seen in Fig. 10b, the pristine permeate side surface mainly consists of BSCFZ and CoO. Based on the SEM micrographs and EDS mapping (Fig. 10c), the dark dots are assigned to segregated CoO. A slight segregation of combined sulfur and barium can be detected (Fig. 10c), which is due to the formation of $BaSO_4$ (not observed in XRD). The slight concentration of $BaSO_4$ on the surface is likely due to the reaction between sulfur containing binder (PESF) and barium at high temperature. As $BaSO_4$ forms, cobalt oxide likely precipitates from the parent phase due to A/B site imbalance resulting from the loss of Ba from the A site. Leo *et al.* [35] also reported that for BSCF hollow fibers prepared with sulfur containing binder a small amount of cobalt oxide which was not incorporated into the B-site of the perovskite structure, as a compensation for the formation of (Ba,Sr)SO_4 [35].

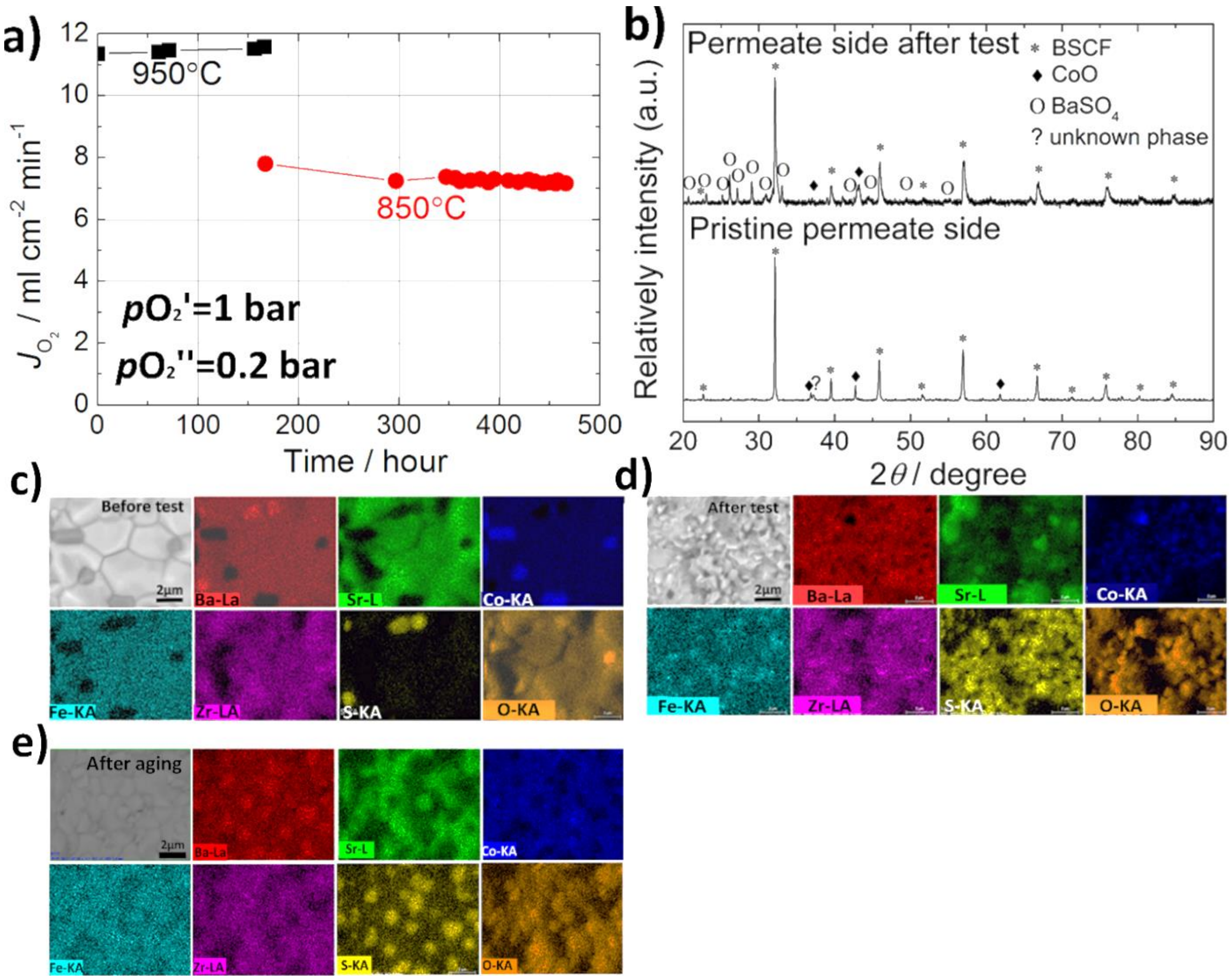

Fig. 10. (a) Oxygen permeation flux of a bare BSCFZ asymmetric membrane as a function of time at 950°C and 850°C. Feed gas: 100 ml min^{-1} O_2. Sweep gas: N_2 (total sweep gas flow: 150 Nml min^{-1}). (b) Normalized XRD patterns of the permeate side before and after test. Back scattered SEM micrograph and elemental mapping of the dense layer of the membrane: (c) before flux measurement (d) after 300-hour flux measurement (e) after aging test.

Table 2. Concentration (at.%) of the detectable elements from the SEM-EDS maps present in Figure 9c-e. The uncertainties are ±0.5 at.% in terms of repetitious measurements.

Atom.%	Ba	Sr	Co	Fe	S	O
Before tests	10	11	20	5	1	53
After permeation test	11	5	13	2	9	59
After single atmosphere aging test	10	9	16	4	4	57

To verify the influence of pO_2 gradient on elemental distribution, an identical membrane was subjected to an aging test carried out in an atmosphere with a fixed pO_2 (0.2 bar) at 850°C for 480 hours. The Back-scattered SEM micrographs and elemental mappings of the sample after flux measurement and the single atmosphere aging test are shown in Fig. 10d and e, respectively. Compared to the pristine (Fig. 10c) and the aged (Fig. 10e) surface, the permeate side surface becomes more porous after the flux measurement (Fig. 10d). As shown in Table 2, the concentration of Sr, Co and Fe after the oxygen flux measurement exhibits a considerable decrease (half of the concentration) compared to the pristine surface. Such considerable decrease in these elements is not observed in the air aged sample. In addition, the surface concentration of sulphur after the permeation test is dramatically increased relative to that of the pristine sample (9 times) and the sample after the air aging test (2 times). Based on this observation, the loss of cations (Sr, Co, Fe) and enrichment of sulphur on the permeate side of the membrane indicates a fairly strong correlation with the oxygen partial pressure gradient. Jung *et al.* [36] reported that the BSCF membrane exhibits kinetic demixing in which depletion of same of the cations is detected. The here observed loss of Sr, Co and Fe is likely to be a result of kinetic demixing. Liu *et al*. found that the permeate side of a BCZO membrane (with 20 ppm sulphur) was covered by a $BaSO_4$ layer after long-term testing, which was concluded to be driven by the existence of the oxygen potential gradient [37], also in consistency with observations reported here. Under a given oxygen potential gradient, oxide ions diffuse towards the permeate side, whereas the positively charged cations Ba, Sr, Co, and Fe diffuse in the opposite direction. Among the four mobile cations, the chemical diffusivity of Ba is the lowest because of its largest ionic size. This may account for the insignificant change in the concentration of Ba after testing. As driven by oxygen partial pressure gradient, sulphur is assumed to diffuse similarly as oxide ions in the form of sulphide or sulphate because the two possible species are negatively charged. In terms of thermodynamic calculations, sulphate is thermodynamically more favourable than sulphide within the pO_2 range across the membrane (in the pO_2 range from 0.21 bar to 1 bar in Fig. 11). Sulphur thus diffuses in the form of sulphate instead of sulphide, in agreement with Liu *et al.* [37]. As a result, $BaSO_4$ forms on the permeate side. Even so, it is evident that the surface is not fully covered by $BaSO_4$, possibly because the total concentration of sulphur in the membrane is insufficient to completely cover the surface. This may account for the slight long-term decrease of oxygen flux, as oxygen surface is not completely blocked.

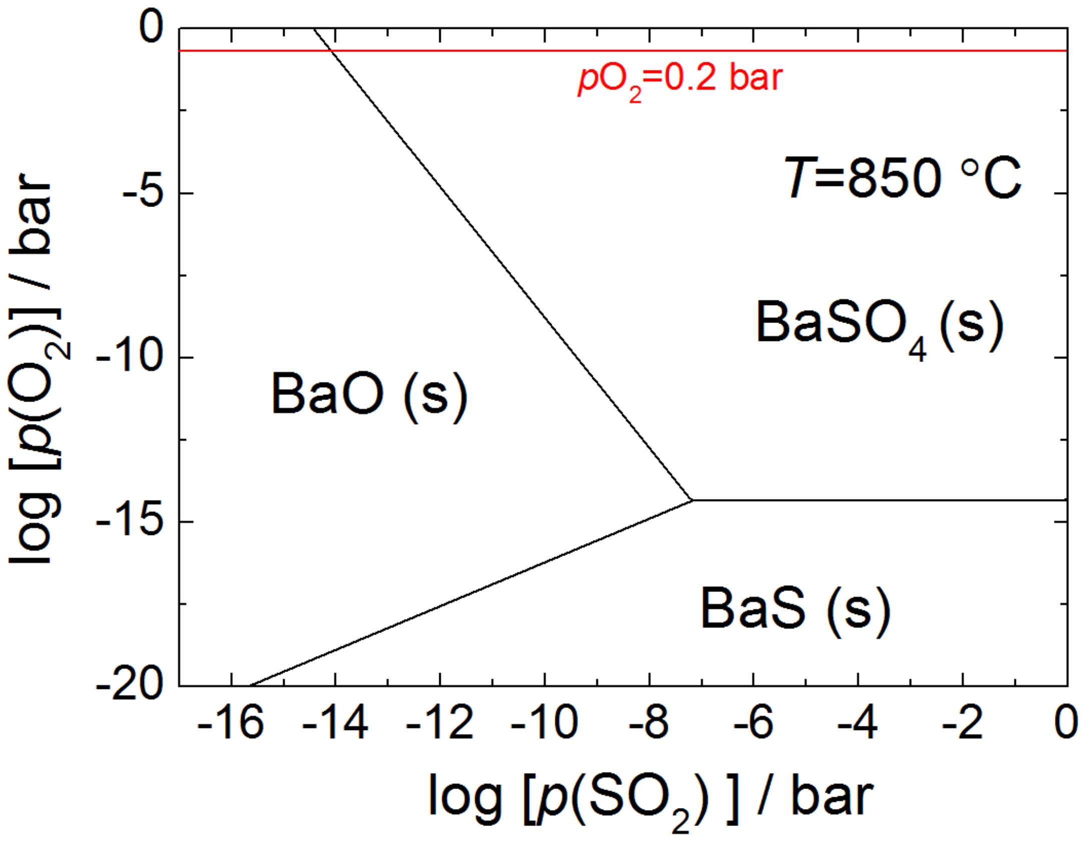

Fig. 11. Thermodynamic calculation of Ba-S-O as a function of pO_2 and pSO_2. The marked pO_2 corresponds to the pO_2 on the permeate side at 850°C as shown in Fig.7a.

4. Conclusions

A BSCFZ asymmetric membrane was fabricated by phase-inversion tape casting. The membrane consists of a “finger-like” highly porous support with a 100 µm dense layer. The structure of the membrane was thoroughly characterized by SEM and 3D-CT imaging. Membranes, with and without catalytic layers, were tested under a range of test conditions with varying gas flows on both sides. The main findings of the current study are:

1. The oxygen flux of the asymmetric membrane without surface catalysts is rate limited by bulk diffusion and oxygen surface exchange on both sides. The limitation by surface exchange is more pronounced at lower temperature.
2. The oxygen flux through the membrane at low temperature (<800°C) can be significantly enhanced by application of catalytic layers on both sides.
3. The impregnation of catalyst inside the pores in the support improves the surface exchange, but also introduces mass transfer polarization.
4. Under a large oxygen potential gradient (O_2/H_2), the membrane exhibits high flux but degrades fast as a result of thermodynamic decomposition.
5. The membrane exhibits a stable flux under O_2/N_2 at 950°C and 850°C for 480 hours.
6. A reaction between the sulphur containing binder and the Ba in the membranes was observed. The enrichment of barium sulphate on the low pO_2 side after the long-term test is the main degradation mechanism.

Acknowledgements

The authors thank DSF (Danish council for Strategic Research) for the finical support on the project “ENEFOX“- Energy Efficient Oxygen Production for a Sustainable Energy System” (11-116387).

References

[1] R. Bredesen, K. Jordal, O. Bolland, Chem. Eng. Process. Process Intensif., 43 (2004) 1129-1158.

[2] Z. Shao, W. Yang, Y. Cong, H. Dong, J. Tong, G. Xiong, Journal of Membrane Science, 172 (2000) 177-188.

[3] R. Kriegel, R. Kircheisen, J. Töpfer, Solid State Ionics, 181 (2010) 64-70.

[4] J.X. Yi, H.L. Lein, T. Grande, S. Yakovlev, H.J.M. Bouwmeester, Solid State Ionics, 180 (2009) 1564-1568.

[5] M. Lipinska-Chwalek, J. Malzbender, A. Chanda, S. Baumann, R.W. Steinbrech, Journal of the European Ceramic Society, 31 (2011) 2997-3002.

[6] J. Ovenstone, J.-I. Jung, J.S. White, D.D. Edwards, S.T. Misture, Journal of Solid State Chemistry, 181 (2008) 576-586.

[7] S. Švarcová, K. Wiik, J. Tolchard, H.J.M. Bouwmeester, T. Grande, Solid State Ionics, 178 (2008) 1787-1791.

[8] H. Lu, Z. Deng, J. Tong, W. Yang, Materials Letters, 59 (2005) 2285-2288.

[9] X. Meng, N. Yang, B. Meng, X. Tan, Z.-F. Ma, S. Liu, Ceramics International, 37 (2011) 2701-2709.

[10] S. Yakovlev, C.-Y. Yoo, S. Fang, H.J.M. Bouwmeester, Applied Physics Letters, 96 (2010) -.

[11] O. Ravkina, T. Klande, A. Feldhoff, Journal of Solid State Chemistry, 201 (2013) 101-106.

[12] H.J.M. Bouwmeester, H. Kruidhof, A.J. Burggraaf, Solid State Ionics, 72, Part 2 (1994) 185-194.

[13] J. Gurauskis, Ø.F. Lohne, K. Wiik, Solid State Ionics, 225 (2012) 703-706.

[14] A. Kaiser, S. Foghmoes, C. Chatzichristodoulou, M. Søgaard, J.A. Glasscock, H.L. Frandsen, P.V. Hendriksen, Journal of Membrane Science, 378 (2011) 51-60.

[15] M. Betz, F. Schulze-Küppers, S. Baumann, W.A. Meulenberg, D. Stöver, Advances in Science and Technology, Trans Tech Publ, 2011, pp. 93-98.

[16] S. McIntosh, J.F. Vente, W.G. Haije, D.H. Blank, H.J. Bouwmeester, Chemistry of Materials, 18 (2006) 2187-2193.

[17] S. Baumann, J.M. Serra, M.P. Lobera, S. Escolástico, F. Schulze-Küppers, W.A. Meulenberg, Journal of Membrane Science, 377 (2011) 198-205.

[18] H. Huang, J. Lin, Y. Wang, S. Wang, C. Xia, C. Chen, Journal of Power Sources, 274 (2015) 1114-1117.

[19] W. He, H. Huang, J.-f. Gao, L. Winnubst, C.-s. Chen, Journal of Membrane Science, 452 (2014) 294-299.

[20] X. Shao, D. Dong, G. Parkinson, C.-Z. Li, Journal of Materials Chemistry A, 1 (2013) 9641-9644.

[21] H. Huang, S. Cheng, J. Gao, C. Chen, J. Yi, Materials Letters, 137 (2014) 245-248.

[22] A. Samson, M. Søgaard, R. Knibbe, N. Bonanos, Journal of The Electrochemical Society, 158 (2011) B650-B659.

[23] M. Schulz, U. Pippardt, L. Kiesel, K. Ritter, R. Kriegel, AIChE Journal, 58 (2012) 3195-3202.

[24] V. Kharton, A. Kovalevsky, A. Yaremchenko, F. Figueiredo, E. Naumovich, A. Shaulo, F. Marques, Journal of membrane science, 195 (2002) 277-287.

[25] S. Kim, Y.L. Yang, A.J. Jacobson, B. Abeles, Solid State Ionics, 106 (1998) 189-195.

[26] Z. Chen, Z. Shao, R. Ran, W. Zhou, P. Zeng, S. Liu, Journal of Membrane Science, 300 (2007) 182-190.

[27] W.K. Hong, G.M. Choi, Journal of Membrane Science, 346 (2010) 353-360.

[28] Z. Shao, W. Yang, Y. Cong, H. Dong, J. Tong, G. Xiong, Journal of Membrane Science, 172 (2000) 177-188.

[29] J. Sunarso, S. Baumann, J.M. Serra, W.A. Meulenberg, S. Liu, Y.S. Lin, J.C. Diniz da Costa, Journal of Membrane Science, 320 (2008) 13-41.

[30] M. Søgaard, P.V. Hendriksen, M. Mogensen, F.W. Poulsen, E. Skou, Solid State Ionics, 177 (2006) 3285-3296.

[31] A. Berenov, A. Atkinson, J. Kilner, M. Ananyev, V. Eremin, N. Porotnikova, A. Farlenkov, E. Kurumchin, H. Bouwmeester, E. Bucher, Solid State Ionics, 268 (2014) 102-109.

[32] F. Zhao, T.J. Armstrong, A.V. Virkar, Journal of The Electrochemical Society, 150 (2003) A249-A256.

[33] R.C. Reid, J.M. Prausnitz, B.E. Poling, (1987).

[34] P.V. Hendriksen, P.H. Larsen, M. Mogensen, F.W. Poulsen, K. Wiik, Catal. Today., 56 (2000) 283-295.

[35] A. Leo, S. Smart, S. Liu, J.C. Diniz da Costa, Journal of Membrane Science, 368 (2011) 64-68.

[36] J.-I. Jung, D.D. Edwards, Journal of the European Ceramic Society, 32 (2012) 3733-3743.

[37] Y. Liu, X. Zhu, M. Li, H. Liu, Y. Cong, W. Yang, Angewandte Chemie International Edition, 52 (2013) 3232-3236.

Supporting materials

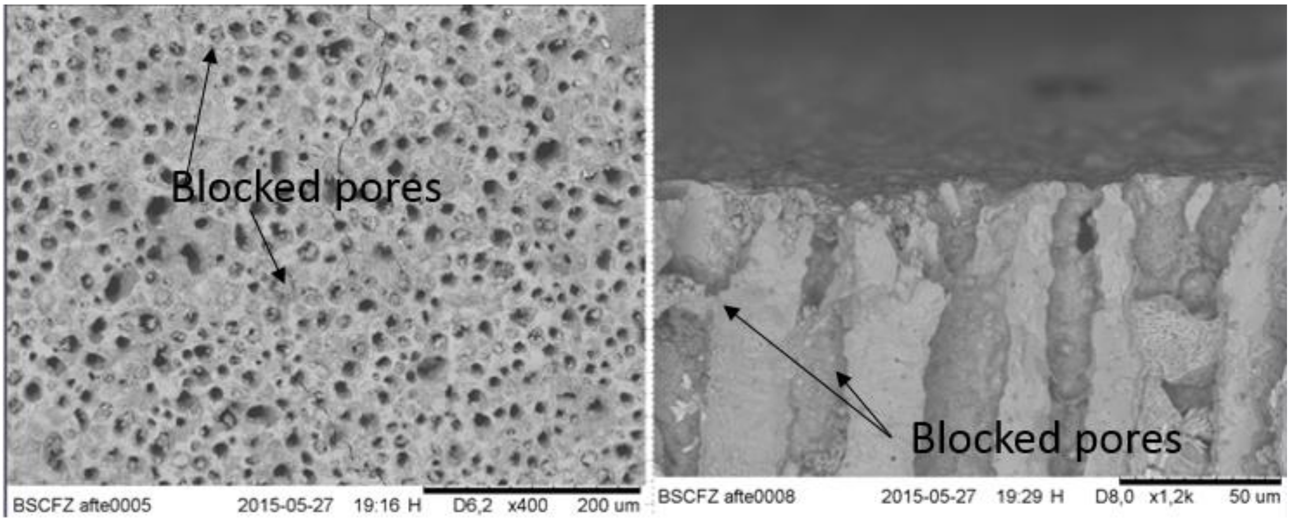

Fig. S1 a. view of feed side of the infiltrated membrane after test. b. cross section of finger pore on the top.

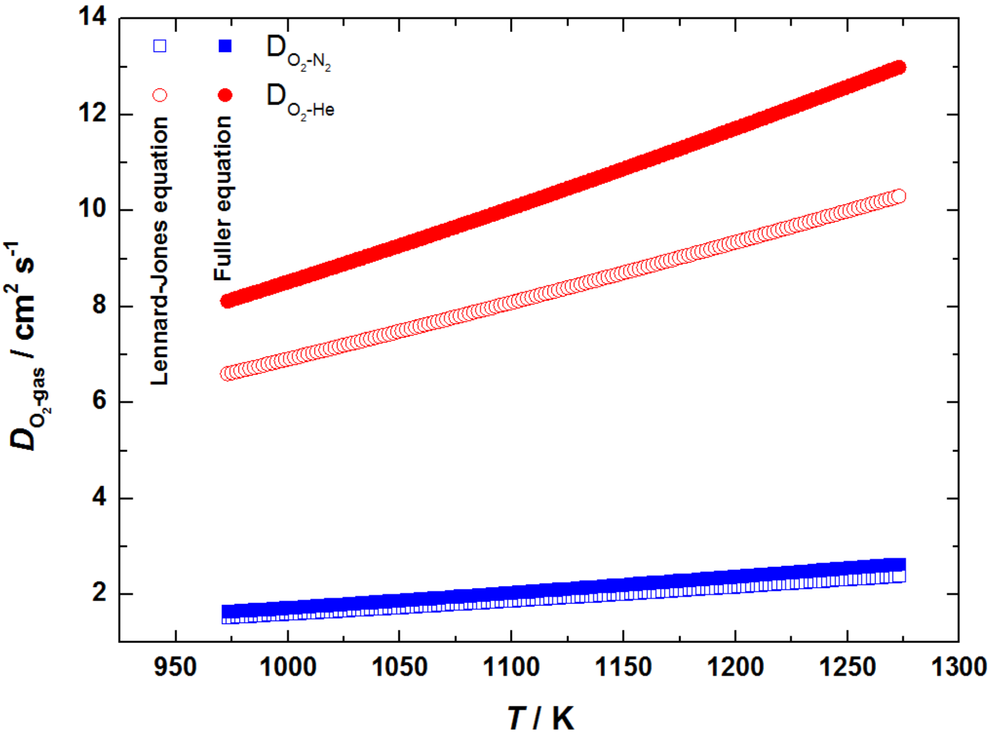

Fig. S2 Binary diffusivity of oxygen in N_2 and He as a function of temperature.

Chapter 9: Effects of adding ZnO dopant in $Gd_{0.1}Ce_{0.9}O_{1.95-\delta}$ on electrical conductivity

S. Cheng, M. Søgaard, A. Kaiser, P.V. Hendriksen*

Department of Energy Conversion and Storage, Technical University of Denmark, Risø campus, Frederiksborgvej 399, DK-4000 Roskilde, Denmark

Abstract

The influence on ionic and electronic conductivity of doping various concentrations of ZnO in $Gd_{0.1}Ce_{0.9}O_{1.95-\delta}$ (GCO) was investigated. The ZnO-containing GCO was sintered at a much lower temperature than that is customary for GCO. The lattice parameter increases with increasing ZnO concentration up to 3 at.%. XRD results confirmed that the solubility limit of ZnO in GCO is in the range of 2-3 at.%. The total conductivity was determined by means of impedance spectroscopy as a function of temperature in the temperature range from 600 °C to 900 °C. The electronic conductivity of $(ZnO)_xGd_{0.1}Ce_{0.9}O_{2-\delta}$, (x=0, 0.02, 0.05, 0.1) were measured as a function of oxygen activity in the range of $a_{O2}=10^2$ to 10^{-17} bar at 700, 800 and 900 °C using Hebb-Wagner polarization. As compared to that of GCO, the *p*-type electronic conductivity of ZnO-doped GCO under oxidizing condition was not influenced by the dopant, whilst the *n*-type electronic conductivity of ZnO-doped GCO under reducing condition was suppressed. The ionic conductivity was also slightly suppressed by doping ZnO. The results indicate that Zn^{2+} is dissolved in the lattice as an interstitial defect.

Key words: GCO; electronic conductivity; ionic conductivity; Hebb-Wagner polarization

Draft paper

1. Introduction

Gd-doped ceria ($Gd_xCe_{1-x}O_{2-0.5x}$, GCO) is a well-known fast oxide ion conductor. Due to the high ionic conductivity and low electronic conductivity at intermediate temperature, GCO has been investigated as a potential material for the electrolyte of intermediate temperature (<600°C) solid oxide fuel cell (IT-SOFC) [1]. However, the high *n*-type electronic conductivity at high temperature and under low oxygen partial pressure limits use of GCO in the electrolyte of SOFCs because the electron leak limits the efficiency [2]. However, mixed ionic and electronic conductivity is a major advantage in some applications and allows

GCO to be used as oxygen transport membranes (OTMs) with special applications in partial oxidization of methane [3, 4]. With respect to the relevant applications in OTMs under oxidizing condition, for instance high purity oxygen production, GCO is not favourable because of low electronic conductivity [5]. The electronic conductivity of GCO thus needs to be enhanced substantially to approach the value of ionic conductivity.

A number of studies reported that doping redox active elements or transition metals in GCO can effectively enhance the electronic conductivity under oxidizing condition [6-11]. Among available dopants, ZnO is particularly interesting because ZnO is environmentally friendly, abundant and inexpensive. Since the radii of Zn^{2+} (0.9A) and Ce^{4+} (0.97A) upon a coordination number of eight are very close, ZnO should be soluble in GCO at high temperature. Schmale *et al.* reported that ZnO is soluble in ceria up to 3.8 at.%. They also found that doping Zn in ceria is likely to yield a partial substitution of Ce^{4+} by Zn^{2+}, forming the positively charged oxygen vacancy to compensate the extrinsic aliovalent dopant. It was also previously been reported that Zn-doped ceria is a mixed ionic and *n*-type electronic conductor over a wide range of oxygen partial pressure [11]. However, the ionic conductivity of Zn-doped ceria is not sufficient to be used either in OTMs or in SOFCs because of the low solubility limit of Zn in ceria (ca. 3.8 at.%).

Besides, ZnO is an indirect semiconductor (band gap 3.8 eV) with fairly high *n*-type electronic conductivity [12, 13]. Cheng *et al.* reported that dual composite membrane composed of 50 vol.% GCO and 50 vol.% Al/Ga co-doped ZnO exhibited a high oxygen permeation flux in air/CO_2 because the percolating Al/Ga-doped ZnO phase serves as a good electronic conductor [14]. With respect to heavily ZnO-doped ceria the insoluble ZnO is likely to segregate along the grain boundary, leading to an enhanced *n*-type electronic conductivity [11]. Park *et al.* [15] reported that a composite consisting of YSZ and ZnO can be a potential cathode for SOFCs. Ge *et al.* [16] found that the grain boundary conductivity of GCO is enhanced by doping ZnO because ZnO acts as the scavenger to clean silica impurities along the grain boundary. In addition to these aforementioned positive effects on electrical properties, ZnO also plays a positive role on the sintering of ceria [17]. Compared to other commonly used sintering aids for instance Co_3O_4, NiO and CuO, ZnO has the special advantages in its low cost and nontoxicity. According to above summarized findings from literature, hypothesize that co-doping Zn and Gd in ceria could be a route to promote the mixed ionic and electronic conductivity in the ceria.

In this work, we analysed the ionic and electronic conductivity of Zn-doped GCO as a function of temperature and oxygen partial pressure to investigate the possible use of the compositions in OTMs or SOFCs.

2. Experimental

2.1.Sample preparation

The specimens in this work were synthesized *via* conventional solid state reaction. Stoichiometric amount of the starting materials, GCO (ultra-low surface area, Rhodia S.A.) and ZnO (Alfa Aesar 99.9%) were mixed by ball milling in ethanol for 24 hours, followed by calcination at 1000°C for 10 hours. The calcined samples were ball-milled in ethanol for another 24 hours to make fine powders. The powders were then uniaxially cold pressed at 400 MPa followed by isostatic pressing at 600 MPa. ZnO-containing and ZnO-free green pellets were sintered at 1300 °C and 1600 °C for 10 hours, respectively.

2.2.Total conductivity measurement

The total conductivity measurements were performed by Impedance Spectroscopy. Before the electrical measurements, symmetric Pt electrodes were screen printed on the samples, followed by sintering at 1000°C for 2 hours to obtain a good adherence between the specimen and the electrodes. Electrical impedance spectroscopy was carried out from 300°C to 1000°C using a Solartron 1260 impedance spectrometers within the frequency range from 3M to 0.5Hz, using constant voltage amplitude of 0.2 V. The oxygen partial pressure in this work was altered by changing the flow of oxygen and nitrogen around the sample and the oxygen partial pressure around the specimen was measured by a zirconia-based oxygen sensor.

2.3.Hebb-Wagner polarization measurement

The electronic conductivity was characterized by the Hebb-Wagner polarization method. Prior to measurement, 1-mm thick dense circular samples (ø =10mm) were polished by SiC #300 sand papers, followed by polishing using SiC #1000 and #1600 sand papers twice. The measurement setup is depicted in Fig. 1. The setup is similar to that used by Lübker et al. [18]. Pt microelectrodes, with a contact radius of 100-200μm was pressed on the pellet using an external load. The radius of the Pt contact was measured by SEM investigations and the impedance measurements. The Pt microelectrode and the sample surface were sealed by glass (MgO/sodium aluminosilicate glass composites, 30/70 vol.%) to block the surface exchange from oxygen to oxide ions. The Hebb-Wagner cell was mounted inside the measurement rig inside a closed furnace. The oxygen partial pressure at the reference electrode was kept at 0.21 bar by flowing 60ml min^{-1} air through the rig. The cell was heated up to 850°C at the rate of 1°C min^{-1} to ensure the microelectrode was well sealed by the glass. The polarization measurement was performed by increasing the voltage over the cell stepwise by 25 mV in the range from -800 mV to 200 mV. The current was assumed to have reached the steady state by waiting for 12 minutes in each step. The oxygen partial pressure near the microelectrode is calculated by:

$$a_{O2,micro} = a_{O2,\mathrm{ref}} \exp(\frac{4FV}{RT}) \qquad (1)$$

where $a_{O2,\ \mathrm{micro}}$ is the oxygen activity near the microelectrode, $a_{O2,\ \mathrm{ref}}$ is the oxygen activity near the reference electrode, V is the polarization voltage applied on microelectrode relative to the reference electrode, F is the Faraday constant, T is the absolute temperature, R is the gas constant. From Hebb-Wagner theory, the sum of electron and electron hole conductivity at the vicinity of the ion-blocking microelectrode can be calculated from the derivative of the steady state I-V curve as follow:

$$\frac{\partial I}{\partial V} = 2\pi r_c (\sigma_e + \sigma_h) \qquad (2)$$

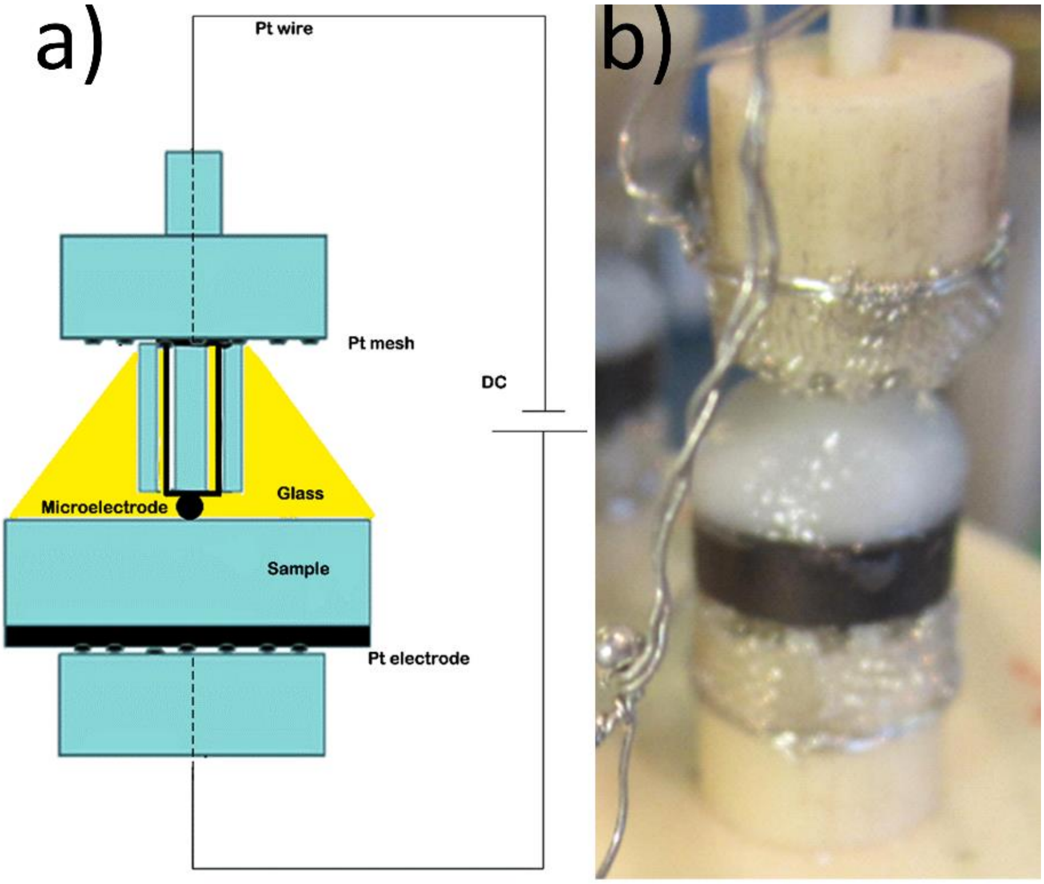

Fig. 1 (a) Schematic of the setup used for Hebb-Wagner polarization measurement (b) a photo of the cell.

3. Results and discussions

3.1. Phase identification

XRD powder diffraction patterns of GCO, CZ2, CZ5 and CZ10 are shown in Fig. 2a. The main phase of ZnO-doped GCO crystallizes in the cubic fluorite structure (Fig. 2a). The secondary phase originating from insoluble ZnO cannot be observed at CZ2, but is seen for CZ5 and CZ10 (the (101) peak of ZnO is clearly seen in the XRD patterns of CZ5 and CZ10 (Fig. 2b)). This strongly indicates that the solubility limit of ZnO in GCO is in the range of 2-5 at.%. As shown in Fig. 2d, the respective residual insoluble ZnO in CZ5 and CZ10 is approximately 2.3 at.% and 8.1 at.%, respectively. The concentration of soluble ZnO in CZ5 and CZ10 is thus in the range of 1.9 – 2.7 at.%, in accordance with that of CZ2. As seen in Fig 2c, the lattice parameter slightly increases with increasing concentration of ZnO below 5 at.%, followed by an invariable lattice parameter above 5 at.%. However, a decrease of the lattice parameter with increasing concentration of ZnO was also reported in ZnO-doped ceria and the formation of $Zn_{Ce}^{//}$

defects was proposed [11]. Here, we found an opposite trend in ZnO-doped GCO, which is tentatively ascribed to the formation of $Zn_i^{\bullet\bullet}$ interstitial defects. The assumed defect chemical reaction can be written:

$$ZnO + V_O^{\bullet\bullet} + V_i \longrightarrow Zn_i^{\bullet\bullet} + O_O^X \qquad (3)$$

In this reaction, an oxygen vacancy in GCO is annihilated by the oxide ion from ZnO, resulting in formation of interstitial Zn ion in the GCO lattice. As indicated by the reaction, the concentration of oxygen vacancies thus decreases, whilst the concentration of electronic defects is not influenced by the dopant. As shown in Table 1, ZnO-doped GCO sintered dense at a lower temperature (1300 °C) compared to pure GCO indicating that ZnO acts as a sintering aid, in agreement with Nicholas *et al.* [17].

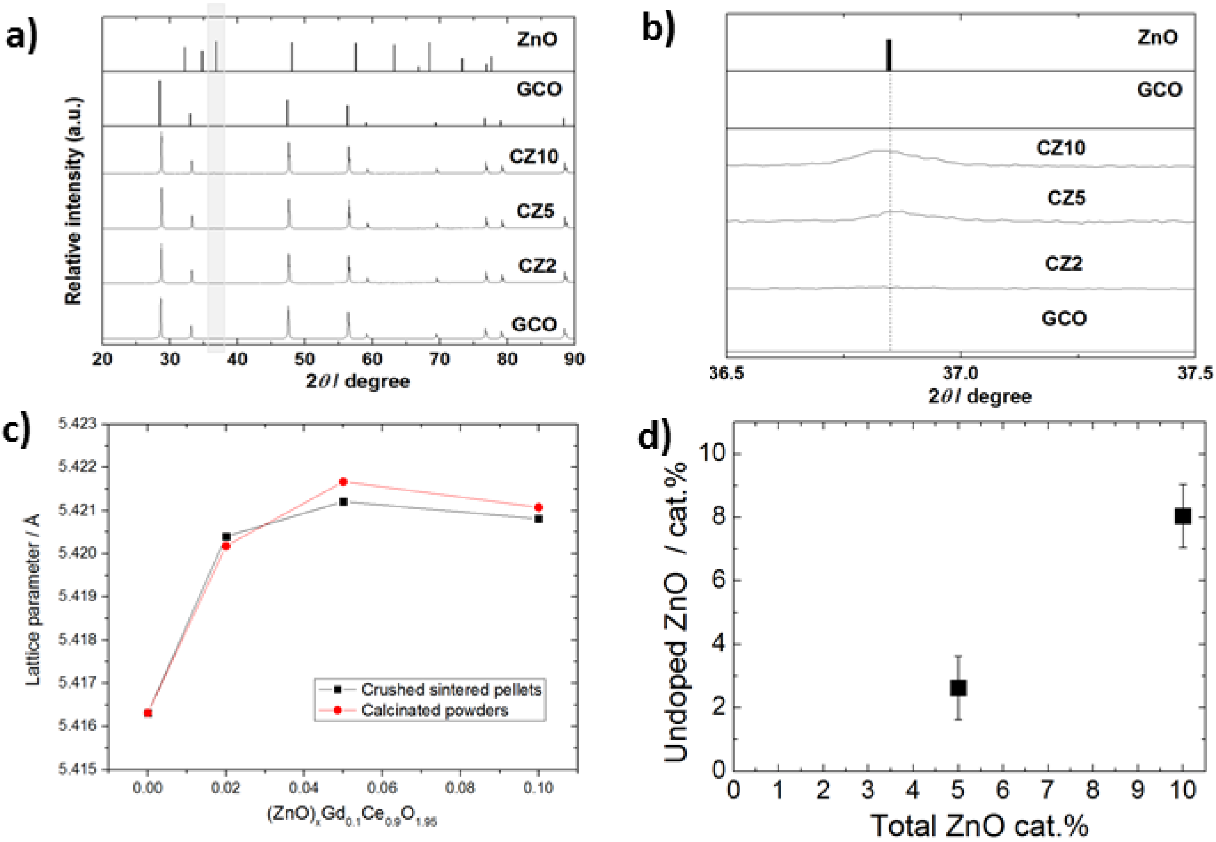

Fig. 2 (a) X-ray powder diffraction patterns of CGO, CZ2, CZ5 and CZ10 measured at room temperature b. zoom of the of (002) peak of ZnO phase (c) Lattice parameter of fluorite phase vs. x in $(ZnO)_xGd_{0.1}Ce_{0.9}O_{1.95}$. (d) Atomic percent of insoluble ZnO versus total atomic percent of ZnO.

Table 1. Composition, Sintering temperature and relative density of $(ZnO)_xGd_{0.1}Ce_{0.9}O_{1.95}$ (x=0, 0.02, 0.05 and 0.1).

Abbreviated name	Composition	Sintering temperature / ° C	Theoretical density / g cm^{-3}	Measured density / g cm^{-3}	Relative Density (%)
GCO	$Gd_{0.1}Ce_{0.9}O_{1.95}$	1600	7.20	7.10	99
CZ2	$(ZnO)_{0.02}Gd_{0.1}Ce_{0.9}O_{1.95}$	1300	7.30	7.10	97
CZ5	$(ZnO)_{0.05}Gd_{0.1}Ce_{0.9}O_{1.95}$	1300	7.40	7.00	95
CZ10	$(ZnO)_{0.1}Gd_{0.1}Ce_{0.9}O_{1.95}$	1300	7.25	7.00	97

3.2.Electronic conductivity

The contact area of the Pt microcontact was been determined by Newman's formula [19]

$$r_c = \frac{1}{4R_s\sigma} \qquad (4)$$

Where r_c is the radius of the microcontact, R_s is the serial resistance found from the intercept with the real axis at the high frequency limit of the impedance spectrum and σ is the conductivity of the sample. The contact radius is typically between 100-500 μm [5]. We also found that the contact radius evaluated by impedance spectroscopy is not sensitive to the temperature or oxygen partial pressure.

The I-V curves of CZ5 recorded at 600, 700, 800 and 900 °C are shown in Fig. 3. Excellent coincidence of the branches recorded in the negative and positive polarization direction indicates that no hysteresis arising from creep of the Pt microcontact, and confirms that the I-V curves were obtained in the steady state.

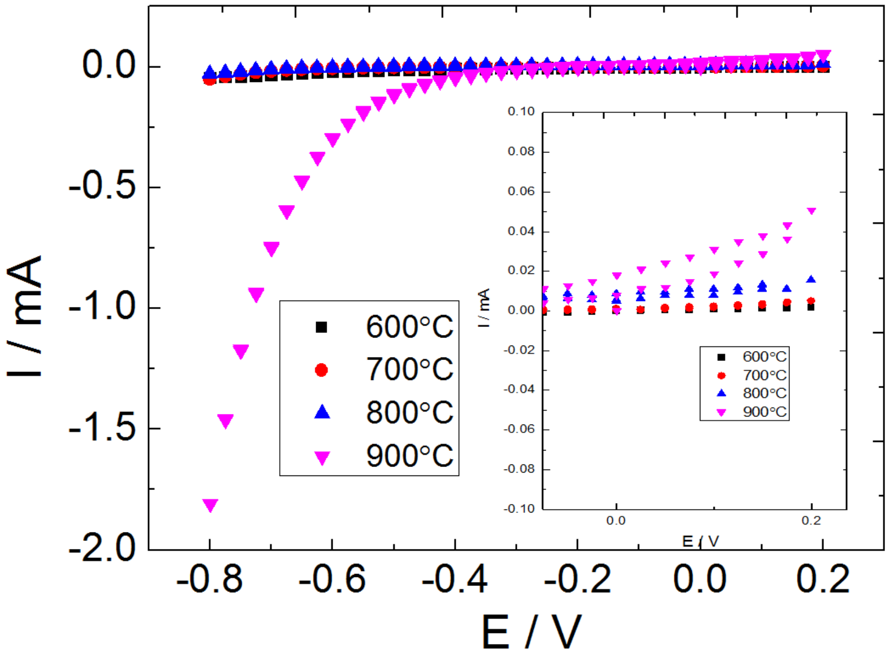

Fig. 3 Steady state current voltage polarization curve (CZ5) from 600°C to 900°C measured in air at the reference Pt electrode. The voltage is the voltage between the microelectrode and the reference electrode.

Fig. 4 shows the logarithm electronic conductivity of the sample as a function of logpO_2 at 700, 800 and 900 °C, respectively. The electronic conductivity of the samples consistently follows the typical relationship of $\sigma_t = \sigma_n^0 pO_2^{-\frac{1}{4}} + \sigma_p^0 pO_2^{\frac{1}{4}}$, which indicates that the samples exhibit *n*-type and *p*-type electronic conductivity under reducing and oxidizing condition, respectively. Under the oxidizing condition, doping ZnO in GCO leads to insignificant influence on the *p*-type conductivity. However, the *n*-type electronic conductivity of Zn-doped GCO under reducing condition is lower than that of GCO at each temperature. The results can be well explained by the aforementioned suggested defect chemical reaction (3), where the concentration of electronic defects is not influenced by the dopant.

It is generally agreed that the defect regime of *n*-type electronic conductivity of ceria is associated with the partial reduction of Ce^{4+} where the electron hops between Ce^{3+} and Ce^{4+} *via* a small polaron mechanism [20]. The defect chemical reaction expressing the partial reduction of cerium can be written:

$$2Ce_{Ce}^{x} + O_O^{X} \longrightarrow V_O^{\bullet\bullet} + 2Ce_{Ce}^{/} + 1/2\,O_2\left(g\right) \quad (5)$$

In GCO, the negatively charged electronic defect is compensated with the positively charged oxygen vacancy. Hence, the electroneutrality reads $\left[Ce_{Ce}^{/}\right]=2\left[V_{O}^{\bullet\bullet}\right]-\left[Gd_{Ce}^{/}\right]$. In ZnO-doped GCO, $Zn_{i}^{\bullet\bullet}$ is stable under oxidizing conditions. Under the reducing conditions, $Zn_{i}^{\bullet\bullet}$ will not be stable because of the fact that ZnO must be reduced to the metallic Zn which is volatile at high temperature [13]. The electronic defect annihilated by the interstitial Zn is likely to be associated with equation 6 since the metallic Zn may leave the system due to evaporation. This could also result in re-oxidation of $Ce_{Ce}^{/}$ to Ce_{Ce}^{x}, which accounts for the lower *n*-type electronic conductivity observed in Fig. 4.

$$2Ce_{Ce}^{/}+Zn_{i}^{\bullet\bullet}\longrightarrow 2Ce_{Ce}^{x}+V_{i}^{x}+Zn(g) \quad (6)$$

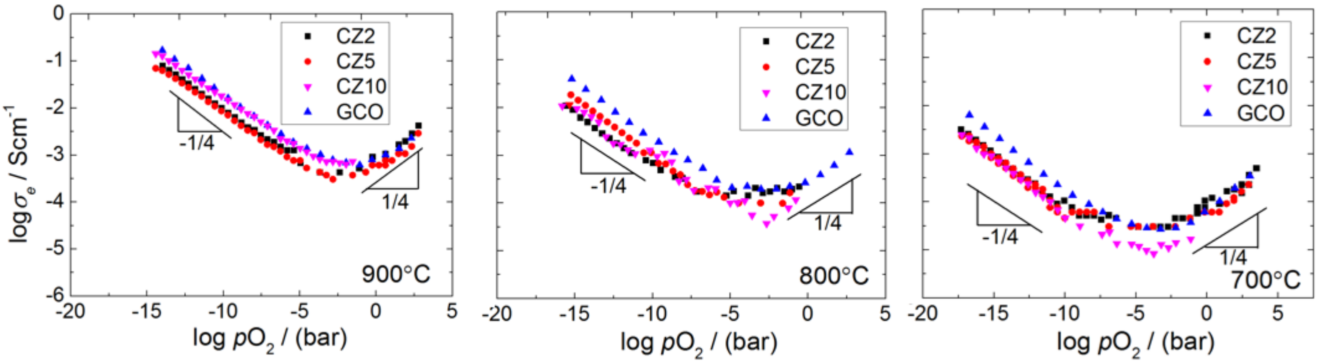

Fig 4. Electronic conductivity of CZ2, CZ5, CZ10 and GCO versus oxygen activity at the microelectrode in the steady state conditions (a) 900 °C (b) 800 °C (c) 700 °C.

3.3.Oxide ion conductivity

Fig. 5 shows the Arrhenius plot of the ionic conductivity of ZnO-doped GCO in air as measured by the ac. characterization. It is noted that the ionic conductivity of ZnO-doped GCO is slightly lower than that of GCO. With respect to CZ2 in which all ZnO is dissolved, the ionic conductivity is suppressed to the highest degree among the three samples (ca. 80% ionic conductivity of GCO). This result is in good agreement with the defect chemistry reaction (3). Schmale *et al.* reported that the substitution of Zn on the cerium site in ceria prevails rather than interstitial defects [11]. Unlike the case of pure ceria, the existence of high oxygen vacancy concentration in GCO is likely to facilitate the formation of the interstitial zinc defect instead of the oxygen vacancy. For the CZ5 and CZ10 where an undissolved second phase of ZnO is observed, the ionic conductivity is very close to that of CZ2. This suggests that the concentration of residual insoluble ZnO is not sufficient to form a percolating network that blocks the transport of oxide ion across the grain boundaries [11].

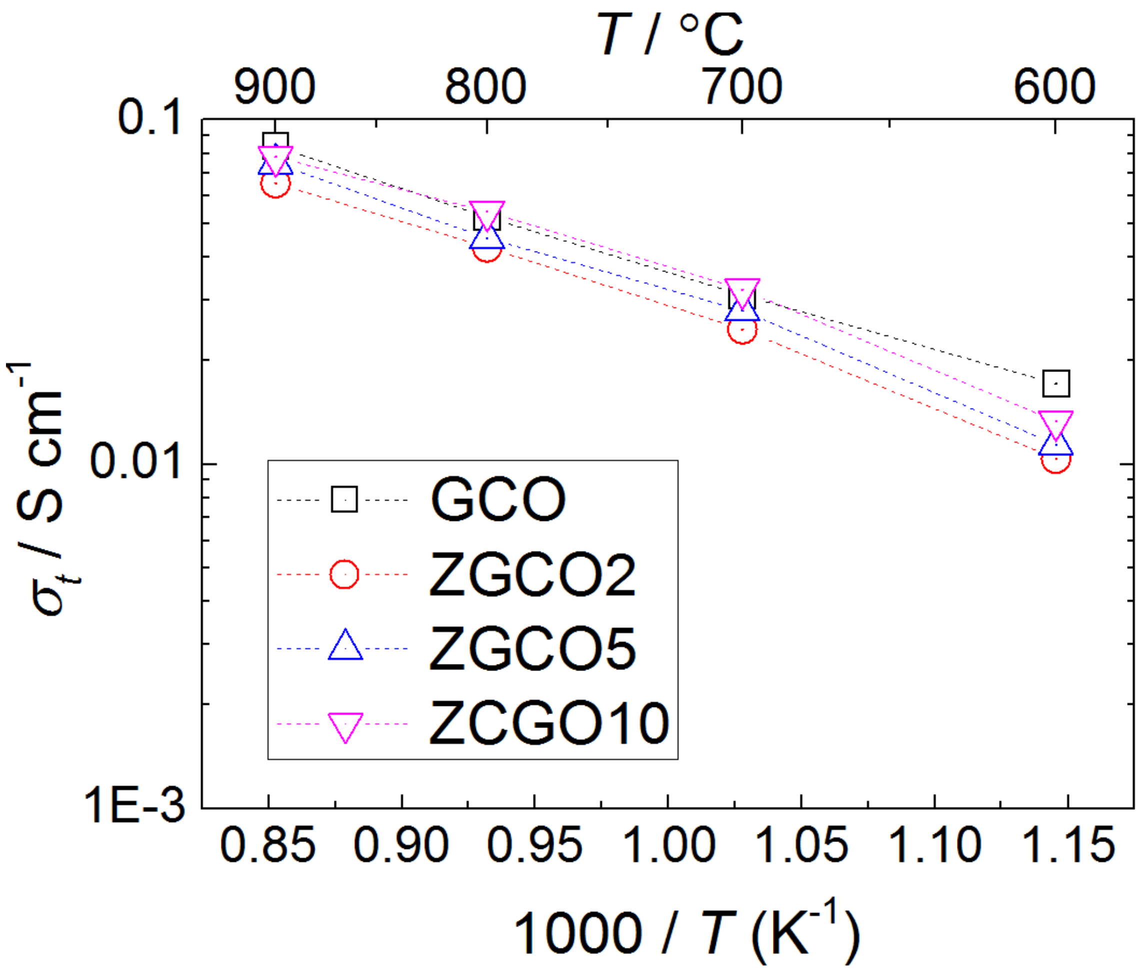

Fig. 5 Total conductivity as a function of temperature measured by Impedance Spectroscopy in the temperature range 600 -900 °C.

Conclusions

Following the variation of the lattice parameter vs. dopant concentration suggests that the solubility limit of ZnO in GCO is in the range 2-3 at.%. The ionic conductivity of GCO is slightly suppressed (ca. 70%) by doping ZnO, and so is the *n*-type electronic conductivity under reducing condition (ca. 20%). The investigation further showed that doping 2 at.% ZnO in GCO improves the sintering properties of GCO, but leads to decreased ionic and n-type electronic conductivity. From the effects on the conductivity it is suggested that Zn forms interstitial defects in GCO.

Acknowledgments

The authors thank DSF (Danish council for Strategic Research) for the finical support on the project “ENEFOX“- Energy Efficient Oxygen Production for a Sustainable Energy System” (11-116387).

References

[1] B.C.H. Steele, Solid State Ionics, 129 (2000) 95-110.

[2] B. Dalslet, P. Blennow, P. Hendriksen, N. Bonanos, D. Lybye, M. Mogensen, J Solid State Electrochem, 10 (2006) 547-561.

[3] C. Chatzichristodoulou, M. Søgaard, P.V. Hendriksen, Journal of The Electrochemical Society, 158 (2011) F61-F72.

[4] C. Chatzichristodoulou, M. Søgaard, J. Glasscock, A. Kaiser, S. P. V. Foghmoes, and P. V. Hendriksen, J Electrochem Soc, 158 (2011) F73.

[5] C. Chatzichristodoulou, P.V. Hendriksen, Physical Chemistry Chemical Physics, 13 (2011) 21558-21572.

[6] D.P. Fagg, I.P. Marozau, A.L. Shaula, V.V. Kharton, J.R. Frade, Journal of Solid State Chemistry, 179 (2006) 3347-3356.

[7] D.P. Fagg, J.C.C. Abrantes, D. Perez-Coll, P. Nunez, V.V. Kharton, J.R. Frade, Electrochimica Acta, 48 (2003) 1023-1029.

[8] Y. Ji, J.A. Kilner, M.F. Carolan, Journal of the European Ceramic Society, 24 (2004) 3613-3616.

[9] D. Fagg, V. Kharton, J. Frade, Journal of Electroceramics, 9 (2002) 199-207.

[10] K. Schmale, M. Grünebaum, M. Janssen, S. Baumann, F. Schulze-Küppers, H.-D. Wiemhöfer, physica status solidi (b), 248 (2011) 314-322.

[11] K. Schmale, M. Daniels, A. Buchheit, M. Grünebaum, L. Haase, S. Koops, H.-D. Wiemhöfer, J. Electrochem. Soc., 160 (2013) F1081-F1087.

[12] P.H. Miller, Physical Review, 60 (1941) 890-895.

[13] Ü. Özgür, Y.I. Alivov, C. Liu, A. Teke, M. Reshchikov, S. Doğan, V. Avrutin, S.-J. Cho, H. Morkoc, Journal of applied physics, 98 (2005) 041301.

[14] S. Cheng, M. Sogaard, L. Han, W. Zhang, M. Chen, A. Kaiser, P.V. Hendriksen, Chemical Communications, (2015).

[15] H.J. Park, S. Kim, Electrochemical and Solid-State Letters, 10 (2007) B187-B190.

[16] L. Ge, S. Li, Y. Zheng, M. Zhou, H. Chen, L. Guo, J. Power Sources, 196 (2011) 6131-6137.

[17] J.D. Nicholas, L.C. De Jonghe, Solid State Ionics, 178 (2007) 1187-1194.

[18] S. Lübke, H.D. Wiemhöfer, Solid State Ionics, 117 (1999) 229-243.

[19] J. Newman, Journal of The Electrochemical Society, 113 (1966) 501-502.

[20] H.L. Tuller, A.S. Nowick, Journal of The Electrochemical Society, 126 (1979) 209-217.

Chapter 10：Fabrication of ceria based tubular oxygen transport membrane

Abstract

In this chapter, the fabrication of ceria based single and dual phase tubular membranes will be introduced. For the dip coating of thin film membrane layers of a $Pr_{0.05}Gd_{0.1}Ce_{0.85}O_{1.95-\delta}$ (CPGO5) layer on MgO tubes, the influence of withdrawal speeds on the thickness of the thin membrane layer was investigated. The thickness of membrane increases with increasing withdrawal speed within the viscous drag regime whereas the opposite trend is observed in the capillary regime.

Full asymmetric oxygen transport membrane structures based on a $Gd_{0.1}Ce_{0.9}O_{1.95-\delta}$-$Al_{0.04}Zn_{0.96}O_{1.02}$ (GCO-AZO) membrane were also produced by dip coating a 3YSZ support with two porous GCO catalyst (support) layers and the active membrane layer (sandwiched between these catalyst layers). According to SEM and XRD, the GCO-AZO-based composite membrane was chemically compatible with the GCO catalyst layers and the YSZ support tube. The introduction of an additional buffer layer consisting of a mixture of GCO and YSZ between the YSZ support and the GCO catalyst layers could avoid problems with delamination between these layers that have been observed originally.

1. Experimental

1.1.Preparation of raw materials

Pr and Gd co-doped ceria (CPGO5) powder as membrane material was synthesized by solid state reaction. Stoichiometric amount of starting materials, $Ce(NO_3)_3 \cdot 6H_2O$, Gd_2O_3 and Pr_6O_{11} powders were mixed by ball milling in ethanol for 24 hours, followed by calcination at 1000 °C for 5 hours. Ultra-low surface area GCO ulsa powder ($Gd_{0.1}Ce_{0.9}O_{1.95-\delta}$ from Rhodia S.A., France) with specific surface area of S=35.5 m^2g^{-1} was used to produce the porous GCO catalyst backbone layer. Graphite powder was used as the pore former (particle size= ca. 4 µm, Graphite Kropfmuhl AS).

For the synthesis of AZO membrane powder ($Al_{0.04}Zn_{0.96}O_{1.02}$), γ-Al_2O_3 (99.5%, 40 nm to 80 nm APS powder; Alfa-Aesar) was mixed with ZnO (99.9%, 200 mesh powder; Alfa-Aesar) at a molar ratio of 4:96 (atomic ratio Al: Zn = 4:96) by roll milling in ethanol for 24 h in ethanol using zirconia balls. The resulting mixture was dried at room temperature for 24 hours followed by further drying at 130 °C for 3 h. The dried AZO powder was calcined in an alumina crucible at 900 °C in N_2 for 5 hours. After calcination, the AZO powder was sieved using a mesh (U.S. Mesh 325), corresponding to mean particle agglomerate-size of 48 µm. The as-prepared AZO powder was later mixed with GCO powder in a ratio of 50 vol.%

AZO and 50 vol.% GCO by ball milling in ethanol for 48 hours. The final GCO-AZO mixture was dried at 120 °C overnight, followed by sieving using a mesh (U.S. Mesh 100).

1.2.Preparation of dip coating slurries for membrane layers and GCO catalyst (support) layers

The composition of the 3 different slurries that were used in this work are summarized in Table 1. The powders for the dense membrane layers (GCO-AZO and CPGO5) were used as synthesized (as described above), whereas the GCO powder from Rhodia for the porous catalyst layer was pre-calcined at 1100°C for 2 hours. Low molecular weight polyvinylpyrrolidone (PVP K15, Sigma Aldrich) and high molecular weight Polyvinylpyrrolidone (PVP K30, Sigma Aldrich) was used as the surfactant and binder, respectively. Ethanol (Sigma Aldrich) was used as the solvent for the colloidal suspension. For membrane slurry preparation (GCO-AZO or CPGO5 slurries), first ethanol and surfactant were added to the powders and milled with zirconia balls in polyethylene bottles for 24 hours to achieve a fine particle size distribution. The binder was then added to these suspensions and ball milled for additional 48 hours. In the case of GCO slurries, the graphite powder was added to the suspensions after 24 hours of ball milling and further milled for another 30 min with the graphite.

Table 1. Composition of dense CPGO5, GCO-AZO and porous GCO ethanol based slurry.

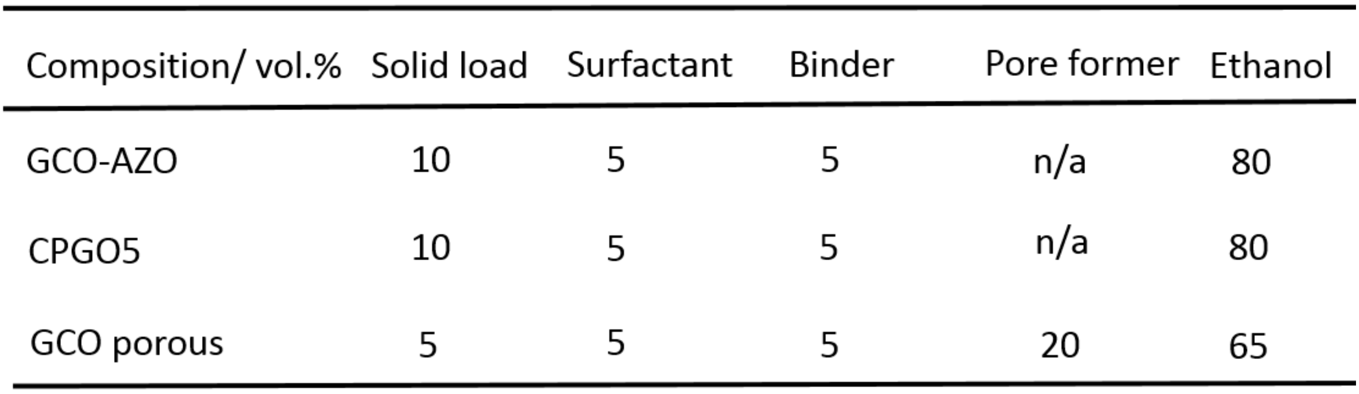

Composition/ vol.%	Solid load	Surfactant	Binder	Pore former	Ethanol
GCO-AZO	10	5	5	n/a	80
CPGO5	10	5	5	n/a	80
GCO porous	5	5	5	20	65

1.3.Deposition of suspension and sintering

The slurries were deposited as thin films on tubular MgO or 3YSZ supports by dip coating. The tubular supports were prepared by thermoplastic extrusion from MgO or YSZ powders and sacrificial pore former as described in more detail by Ramachandran *et al.* [1, 2]. The relationship between withdrawal speed and the membrane layer thickness after dip coating and sintering was investigated for thin film CPGO5 layers deposited on MgO supports. The different steps and the results are summarized as follows:

a) The MgO and YSZ tubes produced by thermoplastic extrusion contain ca. 60 vol.% of a fugitive pore former, thermoplast and other organic binders and plasticisers. To remove these pore formers and the binders from the tubes, a suitable debindering cycle and subsequent sintering step was developed (black curve in Fig. 1). Heating rates of 0.25 °C min^{-1} and 0.5 °C min^{-1} were used for debindering and sintering, respectively. A holding time of 2 hours at 300 °C, 450 °C and 600 °C during debindering was used to ensure a complete decomposition of the organic components. Afterwards, the temperature was increased to 1250 °C to achieve sintering (necking between the powder particles) resulting in sufficient mechanical strength for further handling and dip coating.

b) The pre-calcined tube was then dip-coated with the porous GCO catalyst layer and sintered at 1100 °C for 2 hours (see blue curve in Figure 1).

c) The application of the CPGO5 or an AZO-GCO membrane layers was achieved by dip coating the tubes twice, using a sintering cycle as shown in Fig. 1 (red solid and dashed curves).

d) Finally, the support tube (coated with 1st GCO catalyst layer and membrane layer) was coated with the 2nd porous GCO catalyst (support) layer (repetition of step 2, described above).

e) Both porous GCO layers (prepared in steps 2 and 4) were finally be subjected to the impregnation of catalysts for promotion of oxygen surface exchange. The details about infiltration may refer to Ramachandran *et al.* [2].

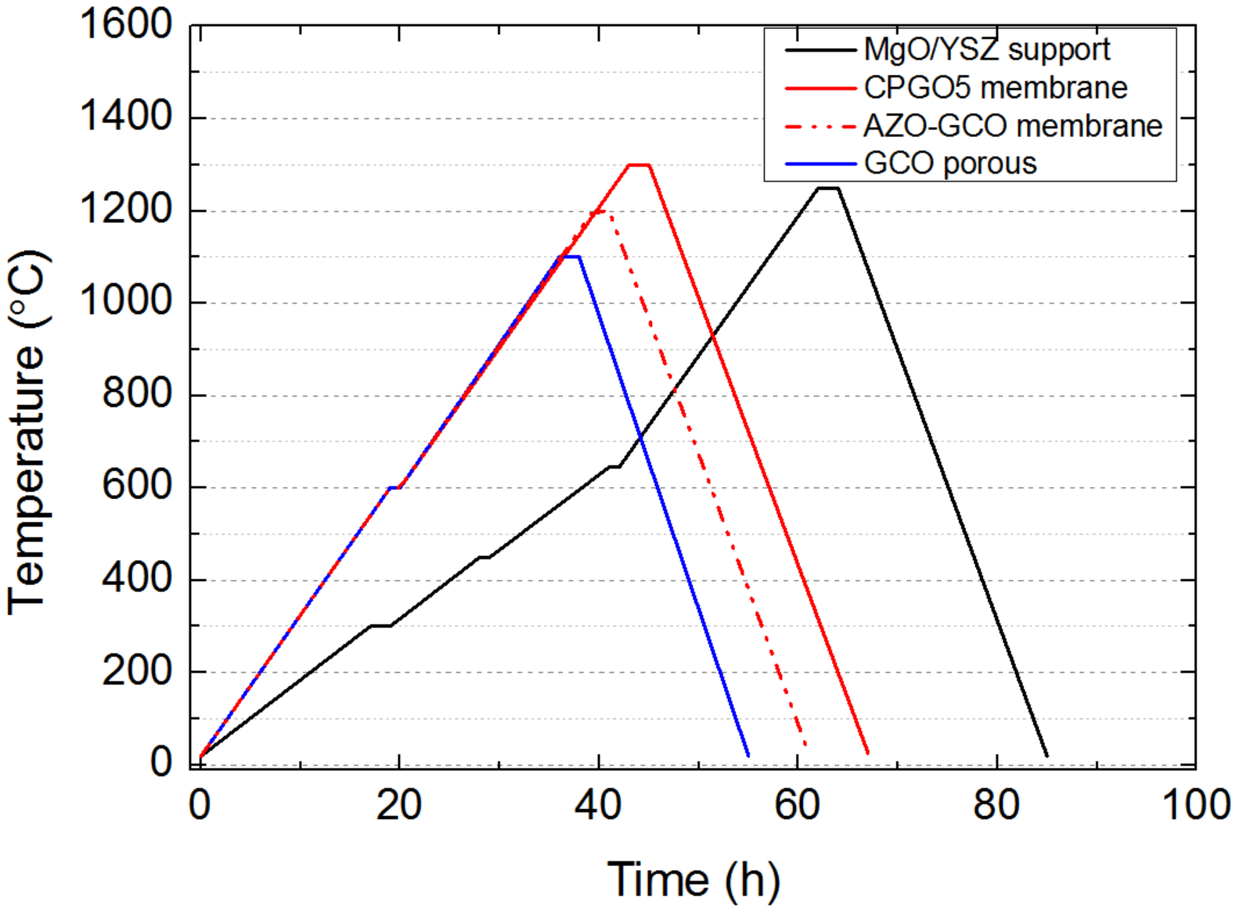

Fig. 1 Debindering and sintering cycles for membrane layers (CPGO5 and AZO-GCO) and porous GCO catalyst layers dip coated on MgO/YSZ support tubes for the preparation of asymmetric tubular oxygen transport membranes.

2. Results and discussion

2.1.Asymmetric MgO supported CPGO5 single phase membrane

Fig. 2 shows the BSEM micrographs of cross sections of thin film CPGO5 membrane layers directly deposited on MgO tubes at different withdrawal speeds. The membrane layers show perfect microstructure with no indication of defects, such as cracks, pinholes or delamination. (latter is not expected due to good match in TEC between MgO: 14×10^{-6} K^{-1}, 25-1000 °C [3] and CPGO5: 13.5×10^{-6} K^{-1}, 200-900 °C). The membrane layer thickness increases with the withdrawal speed. The relationship between the withdrawal speed and thickness of the green thin film and sintered thin film is plotted in Fig. 3. This behaviour follows the Landau-Levich model [4] (see equation 1) which has been described before in a number of dip coating studies of dip coating:

$$h = \frac{0.94\left(\eta U_0\right)^{\frac{2}{3}}}{\gamma_{LV}\left(\rho g\right)^{\frac{1}{2}}} \quad (1)$$

where η and ρ are the dynamic viscosity and density of the suspension, respectively. g is the acceleration due to gravity: 9.8 ms^{-1}, γ_{LV} is the liquid-vapour surface tension, U_0 is the withdrawal speed.

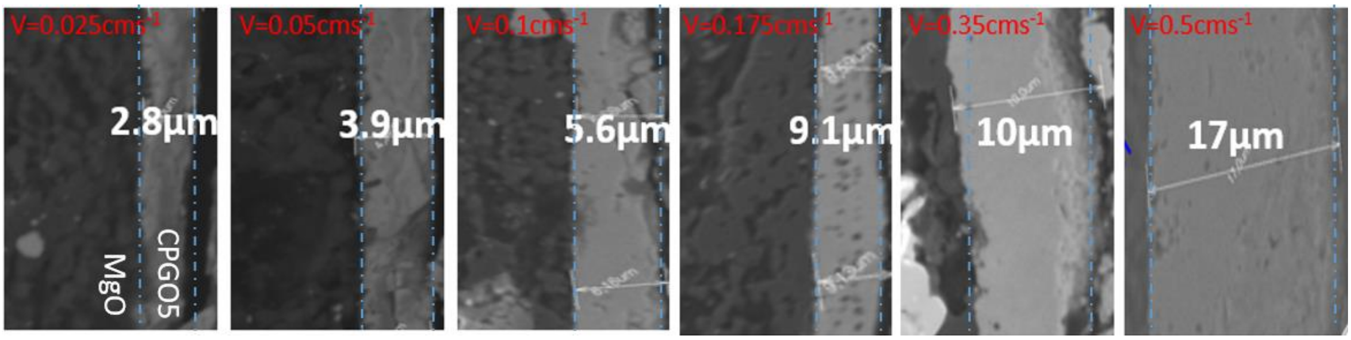

Fig. 2 SEM micrographs of dip coated GCO membrane on MgO porous support using elevated withdrawal speeds.

As illustrated in LL model, the subsequent thickness of the thin film scales with the withdrawal speed, in agreement with this result. This indicates that the thickness of the thin film relies on the gravity induced vicious drag opposing the adhesion of the suspension on the tube for a Newtonian and non-evaporating fluid [5, 6]. On the contrary, a reverse tendency was observed when the withdrawal speed is relatively low (<0.025cm s^{-1}). Grosso [6] reported that the deposition is not only governed by the viscous property of the suspension but also governed by a combination of convective capillarity and evaporation effects at speeds typically below 0.1 mm s^{-1}. Our results for very low speeds coincide with the behaviour proposed by Grosso. The traditional LL model is optimized by adding another term E / LU_o accounting for the capillary effect. The equation is written:

$$h = k_i\left(\frac{E}{LU_0} + DU_0^{\frac{2}{3}}\right) \quad (2)$$

where k_i is the solution composition constant, L is the substrate width, E is the evaporation rate, D is the constant in LL model. As shown in Fig. 3, the experimental data in this work can be satisfactorily fitted to the model. The transition speed between viscous drag and capillary regime is approximately 0.02 cm s^{-1}, which is in accordance with the range proposed by Grosso (<0.1 mm s^{-1}). After sintering, the thickness of the dense layer is approximately 0.2-0.3 of the green layer.

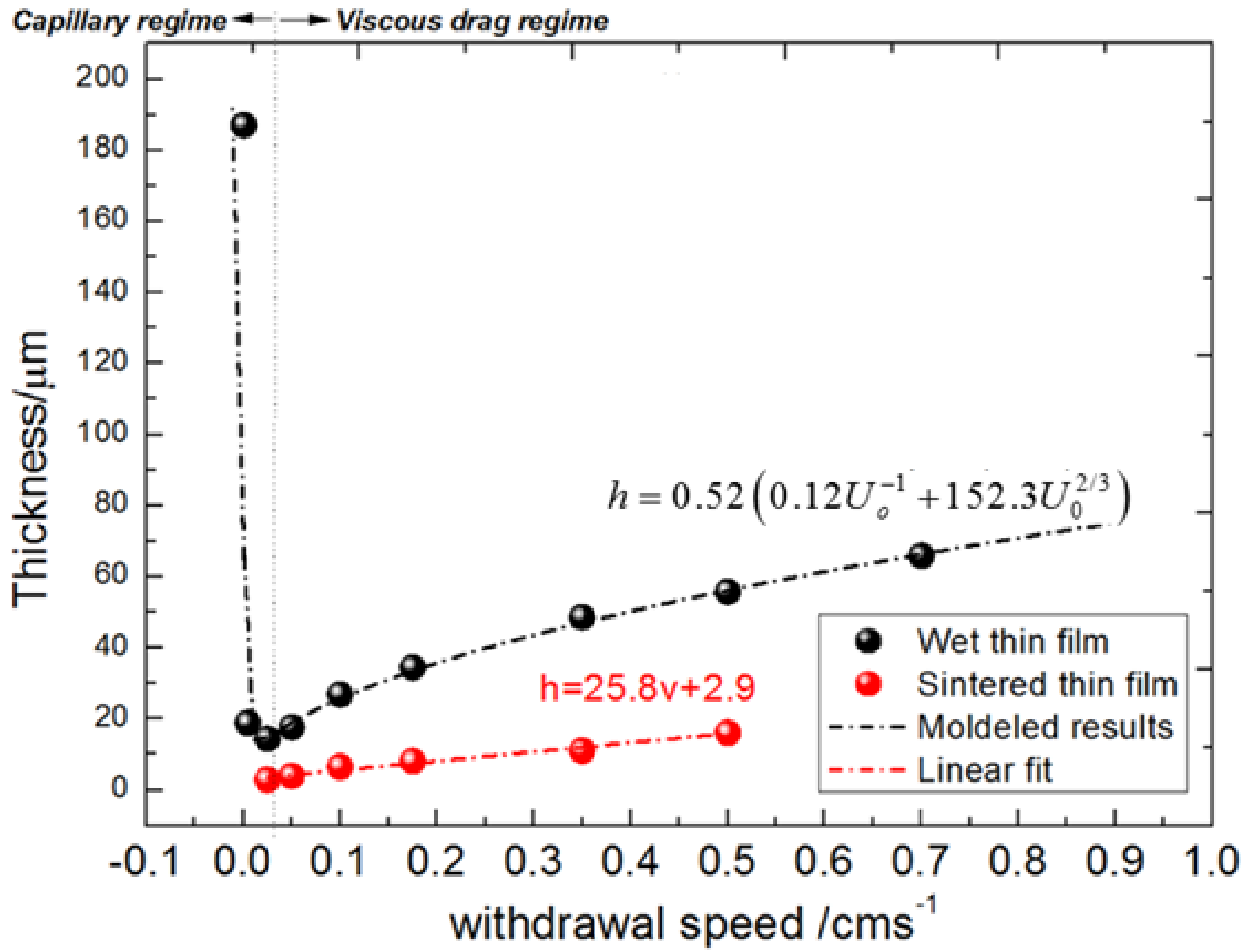

Fig. 3 Plots of thickness versus withdrawal speed showing the two regimes of depositions. The black filled points correspond to experimental thickness of the green thin film, the red filled points to the thickness of the same films after sintering. The half-filled points represent the thickness of the green thin film by twice dip coating. The black dashed curves are the fitted results in terms of equation (2) described by Grosso [6]. The inset is the ratio between the thickness of the sintered thin film and the green thin film.

Fig. 4a-d shows the photo of a membrane tube, a SEM surface micrograph and the cross sections of the CPGO5 based tubular membrane microstructure, respectively. As shown in Fig. 4b, the CPGO5 membrane layer is pinhole and defect free and consists of homogenous fine grain size. The porous GCO catalyst (support) layers in Fig 4 c are different in microstructure. The porous layer on the outside surface is very porous whereas the CGO layer between the MgO tube and the membrane layer is relatively dense. The stronger densification of the inside porous layer might be explained by a double sintering with a first co-sintering step on the shrinking MgO support tube whereas the second sintering is a constrained sintering together with the 2nd CGO layer on the outside of the membrane. Furthermore, the contact with the MgO tube might have an accelerating influence on the sintering of ceria [7].

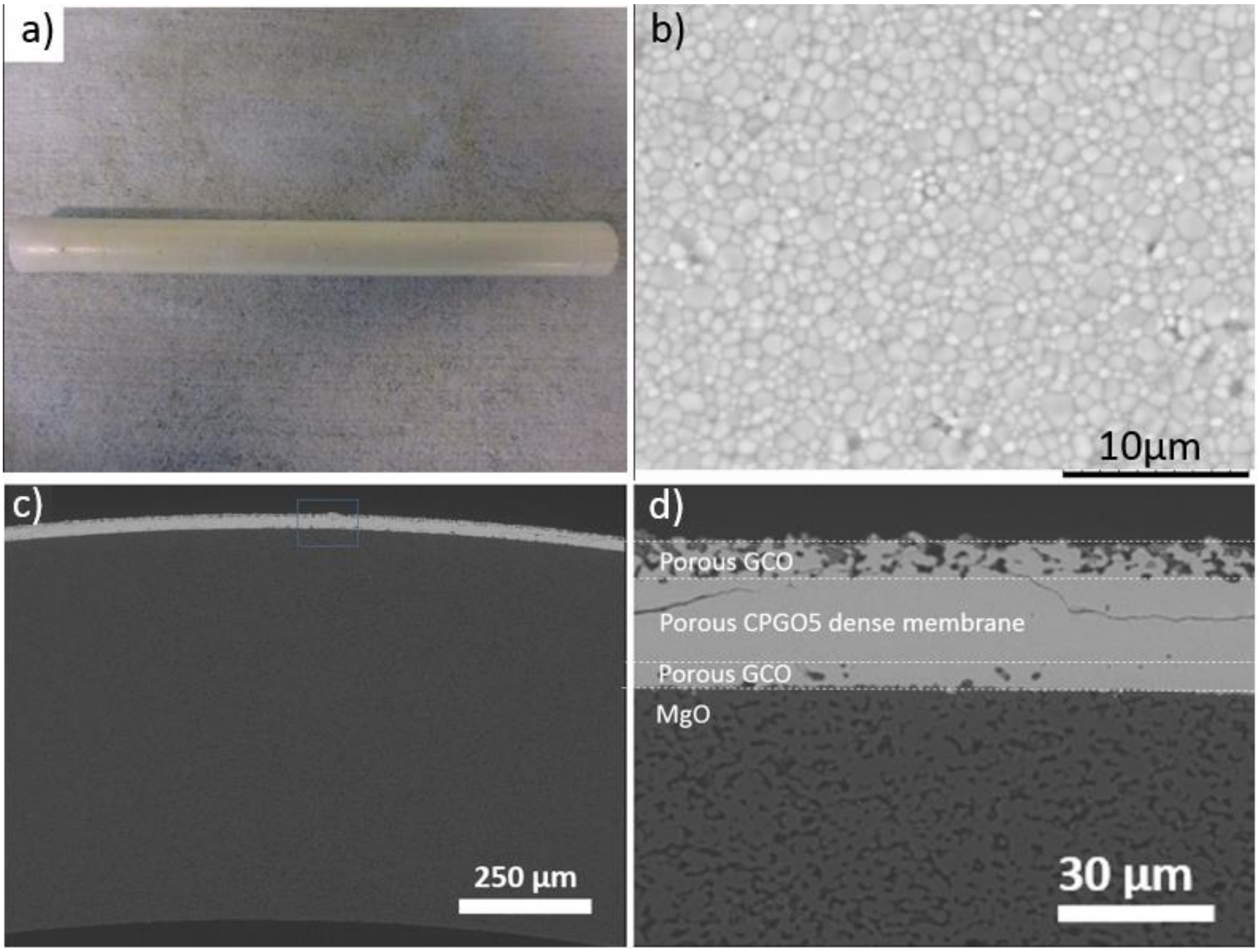

Fig.4 (a) A photo of a MgO tube coated with a CPGO5 membrane layer; (b) BSEM surface picture of the dense CPGO5 membrane after sintering; (c) and (d) SEM micrograph of a polished cross section of the CPGO5 membrane after sintering at different magnification. The blue rectangle in (c) shows the area that is enlarged in (d). All coatings were produced with a withdrawal speed of 0.5cms^{-1}.

2.2 *Asymmetric 3YSZ supported GCO-AZO dual phase membrane*

Fig. 5 displays the BSEM micrographs and EDS elemental mappings of a GCO-AZO based tubular membrane supported by a porous 3YSZ support. The combination of these materials was selected due to a reasonable match in thermal expansion coefficients of the GCO-AZO membrane material ($7\text{-}11.5\times10^{-6}$ K^{-1} in the temperature range 200-1000 °C, see Fig. S1 in supporting material, and the 3YSZ support material 10.5×10^{-6} K^{-1} [8] in the temperature range from 298K to 1273 K) because of the very high toughness of 3YSZ. Nevertheless, in practice a delamination between the GCO porous catalyst layer and the 3YSZ support can be observed. For this combination of materials, the thermal expansion match is not ideal and is considered as the main reason for the delamination. This problem was solved by applying two “buffer layers” consisting of mixtures of YSZ and GCO, thus creating a graded structure which has an additional layer with intermediate thermal expansion. Two buffer layers consisting of different volume percent of GCO and YSZ (70 vol.% GCO+30 vol.% YSZ (b) and 30vol.% GCO+70 vol.%YSZ (c)) were developed and successfully applied to effectively avoid delamination. Finally, an outside GCO porous layer was deposited on the membrane layer, resulting in no delamination or defect formation. The EDS mapping in Fig. 5 indicates an excellent chemical compatibility between each functional layer.

3. Conclusions

1. The thickness of membrane layers deposited by dip coating technique scales with the withdrawal speed of the support tubes in the viscous regime whereas the opposite trend is observed in the capillary regime.
2. CPGO5 is a membrane material that can well be matched with the TEC of inexpensive MgO supports.
3. The shrinkage of the MgO porous support (and the CPGO5 membrane) during co-sintering with the GCO layer and chemical reaction between MgO and GCO enhance the sintering of the 1st GCO catalyst layer.
4. Delamination could be observed between porous GCO catalyst layer and 3YSZ support tubes which is most likely due to TEC mismatch between GCO and 3YSZ. Delamination could be avoided by applying porous buffer layers consisting of mixtures of GCO and YSZ.
5. The GCO-AZO dense membrane show excellent chemical compatibility with the porous GCO catalyst layer.

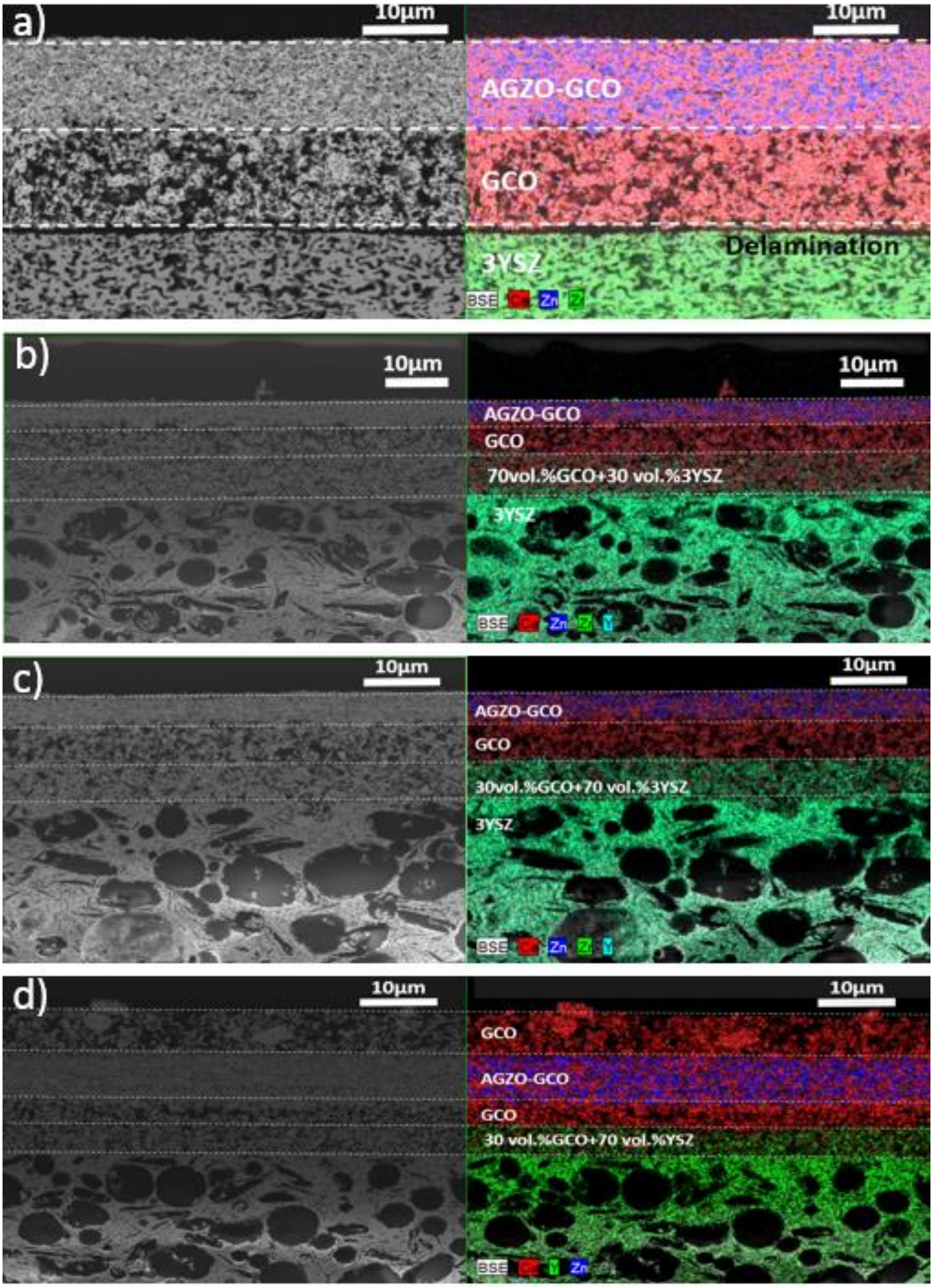

Fig. 5 SEM micrographs showing polished cross sections of AGZO-GCO membrane on the porous s 3YSZ support. a) AGZO-GCO/GCO/YSZ b) AGZO-GCO/GCO/70 vol.% GCO-30 vol.% YSZ c) AGZO-GCO/GCO/30 vol.%GCO-70 vol.%YSZ d) GCO/AGZO-GCO/GCO/30 vol.%GCO-70 vol.%YSZ.

References

[1] D. Kothanda Ramachandran, A. Kaiser, M. Søgaard, J. Glasscock, F. Clemens, EMPA Dübendorf, Laboratory for High Performance Ceramics (CH) EMPA Dübendorf, Laboratory for High Performance Ceramics (CH).

[2] D.K. Ramachandran, M. Søgaard, F. Clemens, J. Gurauskis, A. Kaiser, Separation and Purification Technology, 147 (2015) 422-430.

[3] Y. Shiratori, F. Tietz, H.P. Buchkremer, D. Stöver, Solid State Ionics, 164 (2003) 27-33.

[4] L.D.Landau, B.G. Levich, Acta Physiochim, 17 (1942).

[5] C.J. Brinker, G.C. Frye, A.J. Hurd, C.S. Ashley, Thin Solid Films, 201 (1991) 97-108.

[6] D. Grosso, Journal of Materials Chemistry, 21 (2011) 17033-17038.

[7] J.D. Nicholas, L.C. De Jonghe, Solid State Ionics, 178 (2007) 1187-1194.

[8] I. Yasuda, M. Hishinuma, Electrochemistry, 68 (2000) 526-530.

[9] S. Wang, H. Inaba, H. Tagawa, M. Dokiya, T. Hashimoto, Solid State Ionics, 107 (1998) 73-79.

Supporting materials

The lattice parameter of each phases in the composition were obtained by means of Rietveld refinement, as illustrated in Fig S1. A linear increase in the lattice parameters of the two phases can be observed. The increased lattice parameter of the two phases is a consequence of the thermal expansion. As for GCO10 that crystallizes in the cubic structure, the integrated average thermal expansion coefficient can be calculated

$$\alpha = \frac{(a_2 - a_1)}{a_1(T_2 - T_1)} \tag{S1}$$

where a_2 and a_1 are the cell parameters at temperatures T_2 and T_1, respectively. For ZnO crystallizing in the hexagonal structure, the thermal expansion coefficient of a and c direction of the unit cell is calculated by:

$$\alpha_a = \frac{(a_2 - a_1)}{a_1(T_2 - T_1)} \tag{S2}$$

$$\alpha_c = \frac{(c_2 - c_1)}{c_1(T_2 - T_1)} \tag{S3}$$

where a_1 and c_1 are the cell parameter at T_1 and a_2 and c_2 are the cell parameters at T_2. Based on the calculation, the linear thermal expansion coefficient of GCO is 11.8×10^{-6} K^{-1}, close to the value reported by Wang et al. [9] For AGZO, the linear thermal expansion coefficient in a and c directions of the unit cell are 9×10^{-6} K^{-1} and 7×10^{-6} K^{-1}, respectively. The close TEC between GCO and ZnO may be beneficial for the thermomechanical stability of the membrane. This can be verified by comparing the morphologies of the 1-mm thick GCO-AGZO membrane before and after the thermal cycling. (Fig. S2).

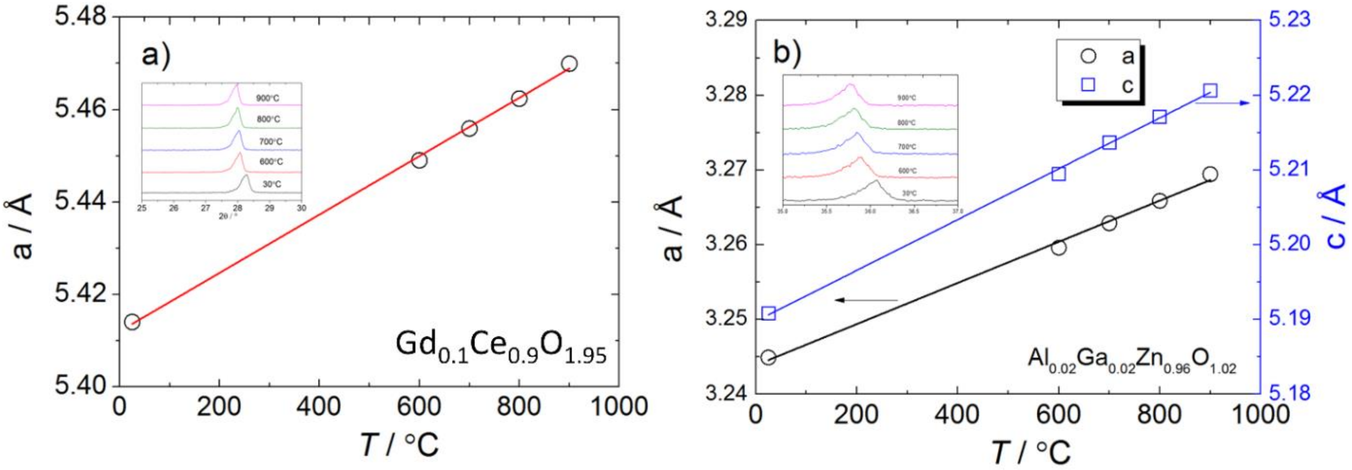

Fig. S1 (a) Lattice parameter of GCO in GCO-AZO composite as a function of temperature (b) Lattice parameters of AZO in GCO-AZO composite as a function of temperature

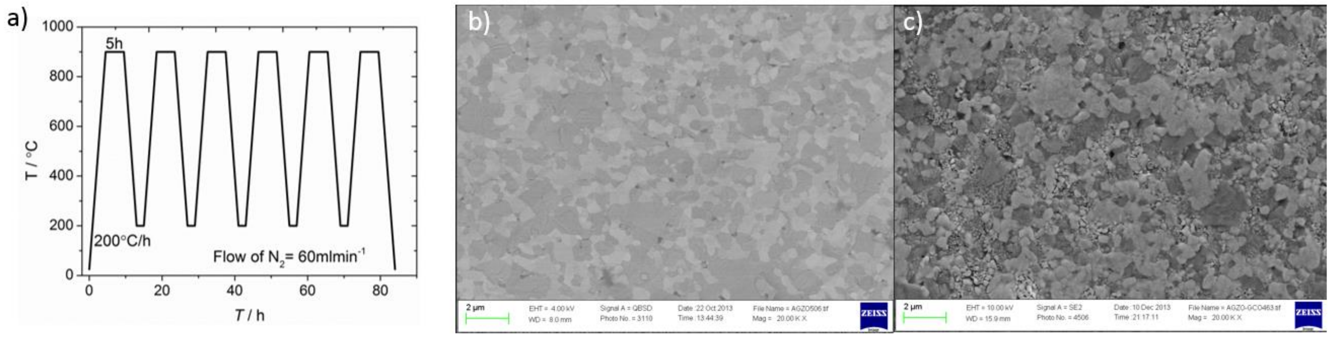

Fig. S2 (a) Thermal cycling for checking the TEC mismatch between AZO and GCO. BSEM micrograph of the membrane before (b) and after (c) the thermal cycling.

Chapter 11: Summary and conclusions

1. Pr/Gd/Co-doped ceria

Pr is soluable in fluorite-structured GCO (10 at.% Gd) up to 40 at.%. The Pr-doped GCO retains the cubic fluorite structure without showing significant effects on the lattice parameter. Doping Pr in CGO ($Pr_xGd_{0.1}Ce_{0.9}O_{1.95-\delta}$) significantly enhances the *p*-type electronic conductivity under high oxygen partial pressure ($pO_2 > 10^{-8}$) and slightly decreases the *n*-type electronic conductivity under low oxygen partial pressure. In the range of 10- 15 at.%, a drastic decrease of activation energy of electron hole migration was observed. This is likely due to significant increase of the electron hole mobility as continuous percolating Pr clusters forms in the crystal structure. Beside the benefit on the *p*-type electronic conductivity, doping 15-25 at.% Pr in CGO can slightly enhance the oxide ion conductivity of CGO. With the increasing Pr concentration, the acheviable oxygen permeation flux increases steadily because of the increasing electronic conductivity. The pitfall of doping Pr is the increased apparent TEC with increasing Pr concentration above 500 °C, which is induced by chemical expansion. Doping Pr in GCO thus simultanesouly introduces electronic conductivity and enhances chemical expansion. We thus conclude that one cannot develop a composition with sufficiently high electronic conductivity whilst retaining technologically reliable thermomechanical properties.

Co-doping cobalt oxide in Pr-doped GCO shows a positive effect on sinterability, but does not show positive effects on electrical conductivity and oxygen permeability.

2. Zn/Gd-doped ceria

Similar as cobalt oxide, addition of ZnO to GCO also shows a positive effect on sinterability. The solubility limit of ZnO in GCO is below 5 at.%. As shown in Fig. 11-1, the *p*-type electronic conductivity of GCO is not influenced by doping ZnO in GCO. Whereas, the *n*-type electronic conductivity of ZnO-doped GCO under reducing condition is partially supressed, in analogy with that of Pr-doped GCO. The mechanism for the decreased *n*-type electronic conductivity for ZnO-doped and Pr-doped GCO are different. With respect to Pr-doped GCO, the decreased *n*-type electronic conductivity is due to the decreased Ce concentration and increased oxygen vacancy concentration that impede the small polaron mirgation. Doping ZnO is hypothized to decrease the *n*-type electronic conductivity by means of annilation of negatively charged small polarons with exisiting positively charged zinc interstial defects.

3. $Al_{0.02}Ga_{0.02}Zn_{0.96}O_{1.02}$-$Gd_{0.1}Ce_{0.9}O_{1.95-\delta}$ -based dual phase composite membranes

Even thoguh the electronic conductivity of GCO cannot be enhanced by doping slight amounts of ZnO, the high effective ambipolar electronic conductivity can be achieved by making a dual phase material consisting of percolating GCO and $Al_{0.02}Ga_{0.02}Zn_{0.96}O_{1.02.}$ Dual phase composite membrane material, consisting of 50 vol.% $Al_{0.02}Ga_{0.02}Zn_{0.96}O_{1.02}$-50 vol.% $Gd_{0.1}Ce_{0.9}O_{1.95-\delta}$ (AGZO-GCO55) shows half the flux as ideally acheviable flux in GCO-based membrane. The total conductivity of the composite is higher than the ionic conductivity by two orders of magnitude, indicating the promising *n*-type electronic originating from percolating electronic conducting $Al_{0.02}Ga_{0.02}Zn_{0.96}O_{1.02}$. Fairly stable oxygen permeation in CO_2 could be proven in a 1.1-mm membrane for more than 500 hours at 860 °C and 940 °C. The 1.1-mm thick AGZO-GCO55 without LSC catalytic layer exhibits much lower flux as compared to that with LSC catalytic layer on both sides. Therefore, 1.1-mm thick AGZO-GCO55 membrane is rate limited by oxygen surface exchange. High performance catalytic layer is necessary to decrease the dominant surface exchange resistance. For the dual phase membrane with alkaline earth elements, for instance GCO-LSF, BSCF, the materials react with SO_2 at high temperature. The particular merit of AGZO-GCO55 is the chemical stability in SO_2-constaing gases. Unfortunately, ZnO is easily reduced to metallic zinc under strongly reducing condions. Metallic zinc easily evaporates at high temperature because of the relatively high saturated Zn vaporate pressure, resulting in a brittle porous GCO backbone. Use of the AGZO-GCO55 is thus confined in the low pO_2 relevant applications, for instance pure oxygen production and oxy-coal combustion.

4. $Gd_{0.1}Ce_{0.9}O_{1.95-\delta}$-$La_{0.6}Sr_{0.4}FeO_{3-\delta}$ -based asymmetric membranes

Using LSF as the electronic conducting phase allows the dual phase composite (GCO-LSF) to operate under a wide range of pO_2. Compared to AGZO, use of LSF as the electronic conductor is favorable in low pO_2. The flux of the GCO-LSF based asymmetric membrane prepared by phase-inversion tape casting is confirmed to be mostly limited by the oxygen surface exchange on the permeate side under both air/He and air/CO. Mass transfer polarization through the finger-like support is negligible over the wide range of apparent driving forces. The asymmetric membranes (without catalysts) show a stable oxygen permeation flux of 7 Nml cm^{-2} min^{-1} under the large oxygen partial pressure gradient (Air/CO) up to 200 hours without detectable degradation. Surface decomposition of LSF is due to the decomposition of LSF and the formation of $SrCO_3$. The stability of LSF is thus jointly influenced by pO_2 and pCO_2 and is hypotheized to be enhanced by using a humid CO.

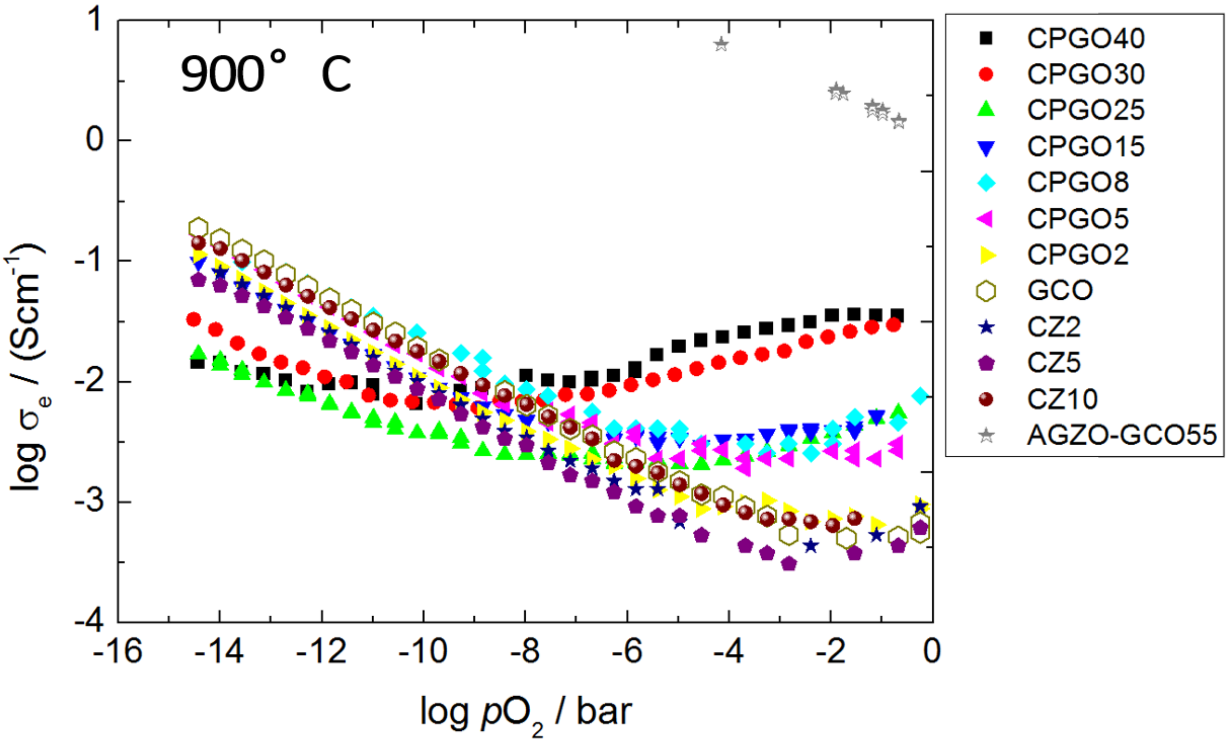

Fig. 11-1 Electronic conductivity of the Pr and Zn doped GCO as a function of logatrithm oxygen partial pressure at 900°C.

5. $Ba_{0.5}Sr_{0.5}(Co_{0.8}Fe_{0.2})_{0.97}Zr_{0.03}O_{3-\delta}$ -based asymmetric membranes

Doping 3 at.% Zr in BSCF (BSCFZ) may mitigate the phase transformation of BSCF from cubic to hexagonal around 850°C, and is not expected to depress the oxygen flux compared to Zr-free BSCF. In analogy with the observations on GCO-LSF, the oxygen flux of the asymmetric BSCFZ membranes (without catalysts) is rate limited by bulk diffusion and oxygen surface exchange on both sides. The limitation by surface exchange is more pronounced at lower temperature. The oxygen surface exchange at low temperature (<850 ºC) can be significantly promoted by application of catalytic layers on the active surfaces. The impregnation of catalyst inside the porous support improves the surface exchange on the feed side, but induces considerable mass transfer polarization because the pores are blocked by the infiltrated particles. Under a large oxygen potential gradient (O_2/H_2), the membrane shows high flux, but a fast degradation is observed due to thermodynamic decomposition of the material. Therefore, use of BSCFZ membranes is confined in low pO_2 applications. The flux through a bare membrane slightly degrades from 8 Nm cm^{-2} min^{-1} to 7 Nml cm^{-2} min^{-1} at 850 ºC over 480 hours. The slight decrease is associated with the enrichment of barium sulphate and the loss of cations in the permeate side. The chemical changes observed after the permeation measurements is due to the kinetic demixing and diffusion of sulphate ions driven by oxygen partial pressure gradient over the material. Asymmetric BSCFZ asymmetric membranes prepared by phase inversion tape casting exhibit stable oxygen flux at high temperature, which is suitable for pure oxygen production.

Based on the above conclusions and from some preliminary results, the following future work is recommended;

1. The dual phase composite membrane consisting of GCO-LSC shows stable oxygen flux under air/N_2 [1]. However, the huge TEC mismatch between the two phases leads to micro-cracks between the grains (Fig. 11-2b, Samson *et al.* [1]), which is problematic for the membrane after thermal cycling. Replacing GCO by CPGO5 in the composite membrane not only mitigate the formation of micro-cracks (11-2a), but also lead to slightly enhanced oxygen permeation flux (Fig. 11-2c). These benefits are due to the higher expansion and electronic conductivity induced by Pr-substitution. As shown in Fig. 11-2d, CPGO30 is suggested to be the optimal ionic conductor for LSC based composite membranes because it has a compatible TEC with LSC. It is interesting to measure the electronic conductivity of LSC-CPGO using ion-blocking Hebb-Wagner polarization to investigate the influence of the electronic conductivity of CPGO on the oxygen flux of GPCO-LSC.
2. We confirmed that AGZO-GCO55 can tolerate SO_2-containing atmosphere by aging the powder in SO_2. Further studies are suggested to focus on the oxygen flux of AGZO-GCO55 thin membranes under the SO_2-containing atmospheres.
3. The oxygen permeation flux of thin film AGZO-GCO55 with and without catalysts and the oxygen flux through AGZO-GCO55 as a function of thickness should be studied to elucidate the rate limiting process and the technological potential.
4. LSF-GCO membrane should be tested in humid CO/CO_2 to evaluate if the observed decomposition of LSF can be avoided.
5. A strong indication of kinetic demixing and sulphate segregation of BSCFZ membrane is observed after long term test. It would be interesting to use sulphate free binder to fabricate the membrane and compare the flux of the membrane with that of the sulphur-containing membrane.
6. The aligned orientated finger-like pores are favourable to gas diffusion. In the planar configuration, the aligned pores seem to exhibit a poor mechanical strength. It is important to investigate in future the mechanical strength of the planar asymmetric membrane prepared by phase-inversion tape casting.
7. The dense part of the asymmetric membrane prepared by phase-inversion tape casting is relatively thick (ca. 100 µm). A much thinner membrane is required to further boost oxygen flux. It is suggested

to dip coat a dense layer on top of the skin layer of the green tape after phase-inversion (Fig. 11-3). The sponge layer can be removed chemically or physically (c.f. Chapter 4). In this way, the thickness of the dense layer can be controlled by simply varying the withdrawal speeds in dip coating process (c.f. Chapter 10). Compared to planar configurations, tubular membrane is preferred because of the better mechanical properties. Here, we suggest preparation of an asymmetric tubular membrane using dip coating coupled with phase-inversion technique. The schematic of the processing is described in detail in Fig. 11-4. Using this method, an optimal asymmetric tubular structure could possibly be fabricated.

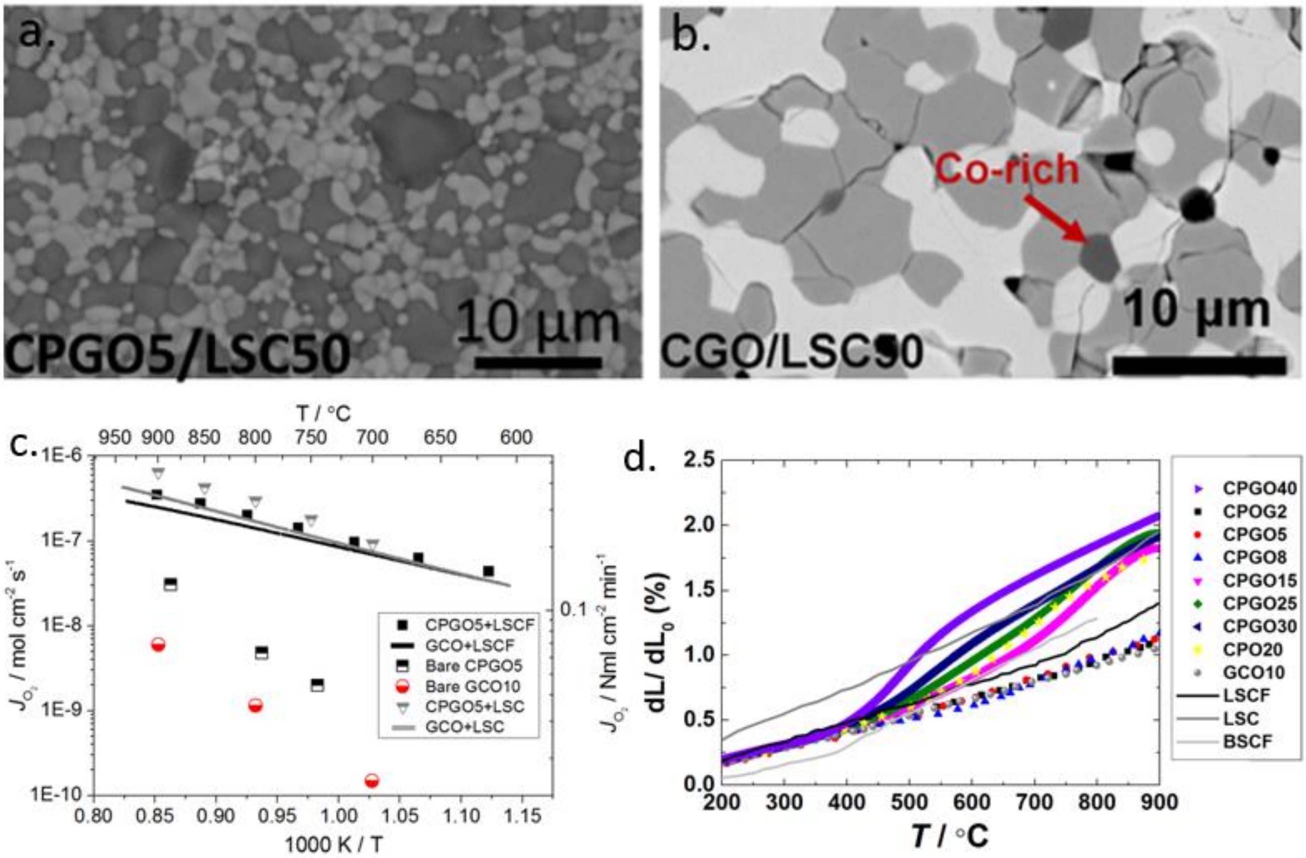

8.

9. **Fig.11-2 BSEM image of a polished (a)CPGO5-LSC and (b) GCO-LSC [1] dual phase composite (c) Arrhenius plot of the oxygen flux of GCO, CPGO5, CPGO5+LSC, CPGO5+LSCF, GCO, GCO+LSCF, GCO+LSC. (d)Thermal expansion curve of CPGOx, LSCF, LSC and BSCF [2]**

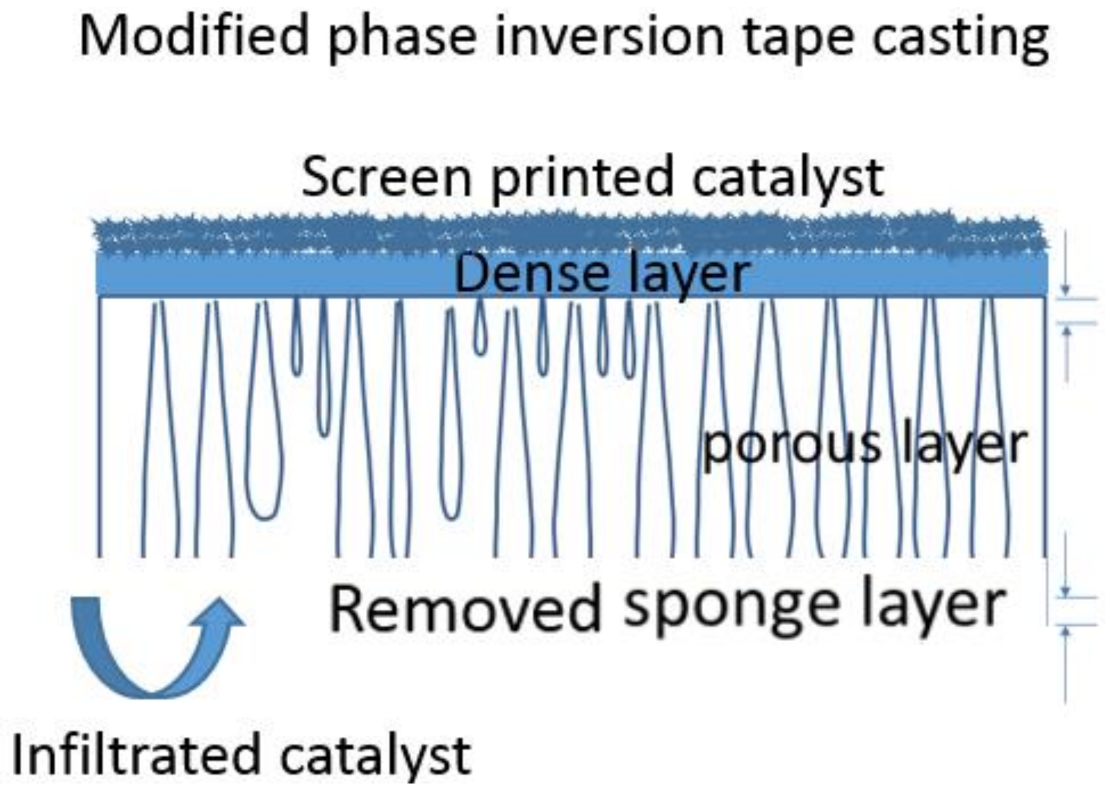

Fig. 11-3 Schematic illustration of the membrane prepared by modified phase inversion tape casting.

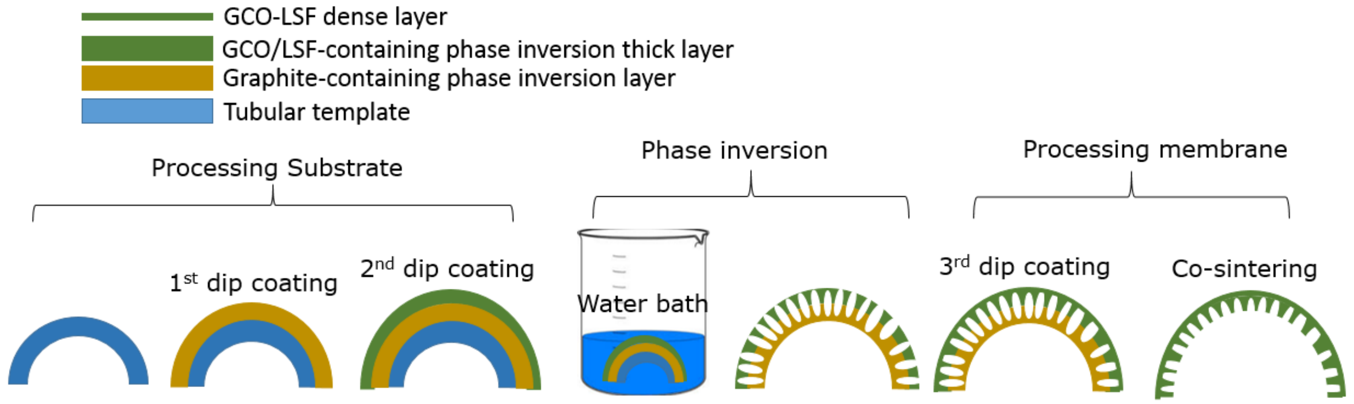

Fig. 10-4 Schematic illustration of preparation of tubular membrane by combined phase-inversion method and dip coating.

References

[1] A.J. Samson, M. Søgaard, P.V. Hendriksen, J. Membr. Sci., 470 (2014) 178-188.
[2] S. Li, Z. Lü, X. Huang, W. Su, Solid State Ionics, 178 (2008) 1853-1858.

Appendix

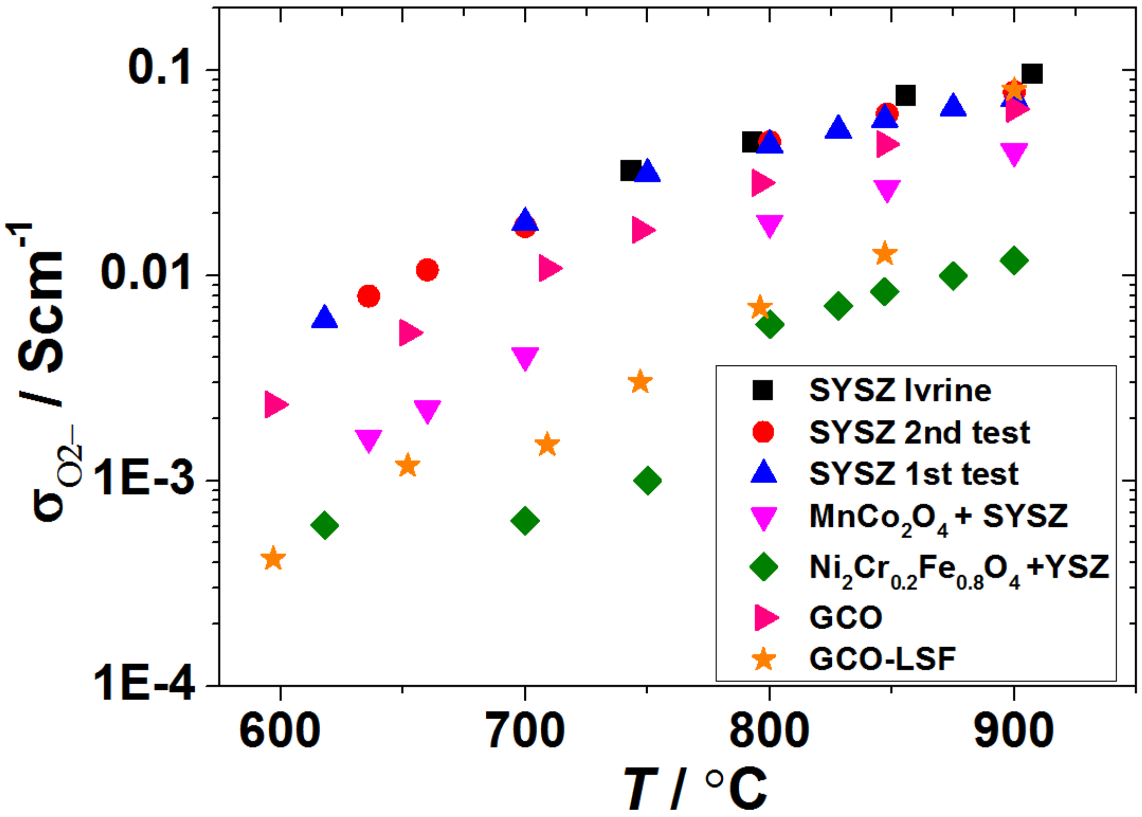

Fig. S1 Arrhenius plot of ionic conductivity of GCO and ScYSZ based composite materials measured using electron-blocking Hebb-Wagner polarization.

Materials Letters 137 (2014) 245–248

Contents lists available at ScienceDirect

Materials Letters

journal homepage: www.elsevier.com/locate/matlet

Phase-inversion tape-casting preparation and significant performance enhancement of $Ce_{0.9}Gd_{0.1}O_{1.95}$–$La_{0.6}Sr_{0.4}Co_{0.2}Fe_{0.8}O_{3-\delta}$ dual-phase asymmetric membrane for oxygen separation

Hua Huang [a], Shiyang Cheng [b], Jianfeng Gao [a], Chusheng Chen [a], Jianxin Yi [c,*]

[a] *CAS Key Laboratory of Materials for Energy Conversion, Department of Materials Science and Engineering, University of Science and Technology of China, Hefei 230026, China*
[b] *Department of Energy Conversion and Storage, Technical University of Denmark, Risø Campus, Frederiksborgvej 399, DK-4000 Roskilde, Denmark*
[c] *State Key Laboratory of Fire Science, University of Science and Technology of China, Hefei 230026, China*

ARTICLE INFO

Article history:
Received 16 August 2014
Accepted 4 September 2014
Available online 16 September 2014

Keywords:
Ceramic composites
Functional
Oxygen separation
Membrane
Phase inversion

ABSTRACT

The dual-phase $Ce_{0.9}Gd_{0.1}O_{1.95}$–$La_{0.6}Sr_{0.4}Co_{0.2}Fe_{0.8}O_{3-\delta}$ asymmetric membrane was prepared via a phase-inversion tape-casting method. The membrane consisted of a thicker porous support layer and a thinner dense layer. When the dense side of the membrane was coated with a $La_{0.6}Sr_{0.4}CoO_{3-\delta}$ catalytic activation layer, the oxygen permeation flux was markedly increased by a factor of 4.1–5.6, reaching 0.45 mL cm^{-2} min^{-1} at 900 °C. The flux increase can be attributed to enhanced surface oxygen exhange kinetics.

1. Introduction

Mixed ionic–electronic conducting materials can be made into dense ceramic membranes for cost-effective oxygen production, which have received much attention in recent years [1]. Two types of membrane configurations, namely the single-phase and the dual-phase configuration, have been explored. The single-phase membranes, typically made of perovskite-structured oxides, possess high oxygen permeation flux, but have insufficient structural stability [2–4]. In contrast, the dual-phase composite membranes, which usually consist of an oxide ion conductor and an electron conductor, exhibit much better chemical stability but unfortuantely significantly lower oxygen flux [5–7].

In order to increase the oxygen permeation flux of the membranes, one simple but effective way is to reduce the membrane thickness [8,9]. For very thin membranes it is necessary to prepare the dense oxygen separating layer on a porous support for enhancing not only the mechanical strength but also the surface oxygen exchange kinetics. Planar type and hollow fiber type asymmetric membranes have been successfully prepared by tape casting and phase inversion, respectively [10–12].

Recently, the phase-inversion tape-casting method, which combines both methods, was demonstrated to be simple and effective for preparing planar asymmetric membranes with enhanced oxygen permeability [12]. As the obtained membranes had catalytic activation layer (i.e. the support layer) on only one side, better oxygen permeation performance could be achieved by coating an extra catalytic layer to accelerate the surface exchange of oxygen on the other side of the membrane.

The present work obtained the $Ce_{0.9}Gd_{0.1}O_{1.95}$–$La_{0.6}Sr_{0.4}Co_{0.2}Fe_{0.8}O_{3-\delta}$ (CGO–LSCF) asymmetric membrane via phase-inversion tape-casting, and significantly improved its oxygen permeation performance by modifying the membrane surface with $La_{0.6}Sr_{0.4}CoO_{3-\delta}$ (LSC), an excellent catalyst for surface oxygen exchange reaction [13].

2. Experimental

CGO and LSCF powders were mixed in a weight ratio of 50:50, and subsequently dispersed in a *N*-methyl-2-pyrrolidone (NMP) polymer solution containing polyethersulfone (PES) and polyvinylpyrrolidone (PVP). The obtained slurry was cast on a Mylar sheet by a doctor blade, followed by solidification and drying. Sintering was performed at 1400 °C for 10 h in air to obtain the membranes. Some membranes were painted on the dense side with a slurry consisting of LSC powders and α-Terpineol. For comparison, the support side of the membrane was also modified by impregnation in a aqueous solution containing $La(NO_3)_3$, $Sr(NO_3)_2$, and $Co(NO_3)_2$. The modified membranes were then sintered again at 1000 °C for 30 min. More detailed experimental procedures can be found in the Supporting information.

---

[*] Corresponding author. Tel.: +86 551 63607817.
E-mail address: yjx@ustc.edu.cn (J. Yi).

http://dx.doi.org/10.1016/j.matlet.2014.09.016
0167-577X/© 2014 Elsevier B.V. All rights reserved.

Phase composition was verified by X-ray powder diffraction (XRD, X'PertPro, Philips). Microstructure and elemental analyses of the membranes were performed with SEM (FEI XL30) and EDS (Oxford Inca). The oxygen permeation through the membranes was investigated in a home-made setup described in [14]. Air was fed to the support (feed) side of the membrane, while helium was fed to the dense (permeate) side. By analyzing the composition of the effluent stream from the permeate side with an online gas chromatograph (GC9750, FuLi), the oxygen permeation flux was determined.

3. Results and discussion

Fig. 1 shows the XRD patterns of the prepared samples. Both LSCF and LSC powders exhibited the single-phase perovskite structure, and CGO powders exhibited a fluorite strucure. For the CGO–LSCF membrane fabricated by phase-inversion tape-casting, all the diffraction peaks can be assigned to either the CGO or the LSCF phase, indicating no significant formation of impurity phase.

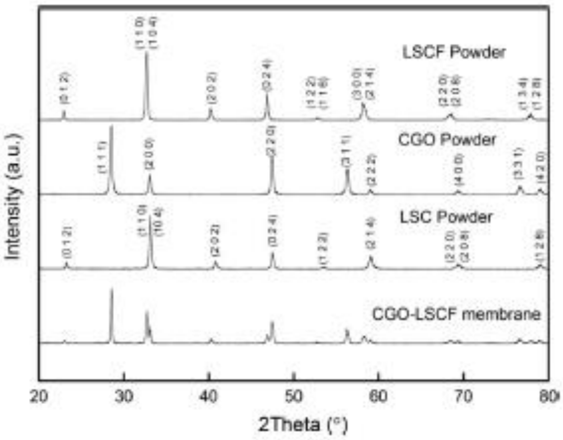

Fig. 1. XRD patterns of the CGO, LSCF, LSC powders, and the as-prepared membrane.

Fig. 2 shows the SEM micrographs for an as-prepared (unmodified) CGO–LSCF membrane after removal of its skin layer on the support side by polishing. The membrane consisted of a 900 µm-thick porous support layer and a 100 µm-thick dense layer (Fig. 2a). The support layer contained a significant amount of finger-like pores typically in the range of 20–100 µm (Fig. 2b). The overall porosity of the membrane was determined to be 31% by the Archimedes method in mercury, wherein the porosity associated with the finger-like pores was estimated to be 25% by image analysis [15]. Similar microstructure has been seen in other membranes prepared by phase-inversion tape-casting [12]. The CGO–LSCF membrane was composed of two kinds of grains that were sized several micrometers and evenly distributed (Fig. 2c). The brighter grains can be assigned to the CGO phase and the darker grains to the LSCF phase. Note, however, that repeated EDS analyses revealed signals of Gd, though in very weak intensity, in the spectra for the LSCF grains, which suggested diffusion of trace amount of Gd from CGO into LSCF during sintering of the composite membrane. The influence of Gd diffusion on the performance of the membrane requires further investigation in future.

Fig. 3 shows the SEM images for membranes modified with LSC. In the case of the permeate side, a 20 µm-thick LSC porous layer was coated onto the dense layer (Fig. 3a). With regard to the feed side, coating was unfavorable as the LSC slurry would enter the pores during preparation, leading to blocking of the gas transport in the support. As a result, the modification was carried out by impregnation instead. After this treatment, some extra puffy flakes composed of nano-sized particles were formed on the support side (Fig. 3b). These particles consisted of mainly La, Sr, Co, and O as revealed by EDS, and were hence assigned to LSC. This result indicated that the feed side surface of the membrane was decorated by the LSC fine particles.

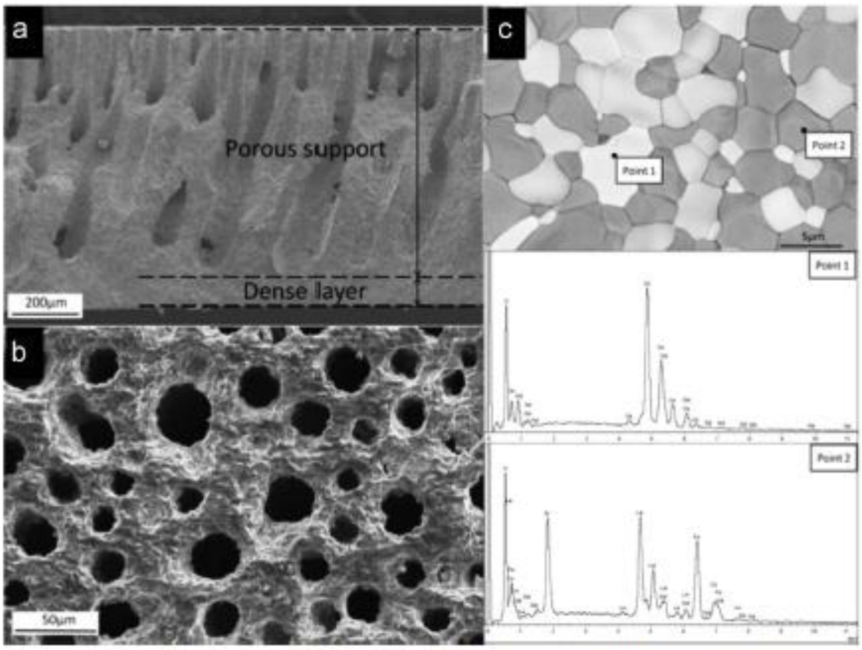

Fig. 2. Microscopy and EDS analyses of the as-prepared membrane. (a) cross section SEM image; (b) top view SEM image of the support layer; and (c) back-scattered electron image and EDS on the surface of the dense layer.

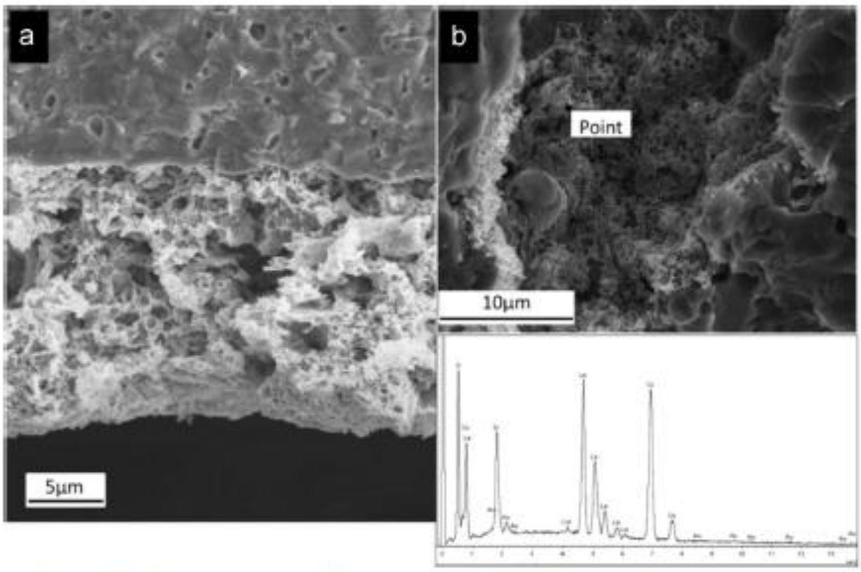

Fig. 3. SEM micrographs and EDS result of the membrane modified by LSC. (a) cross section of the permeate side and (b) inside a finger-like pore on the feed side.

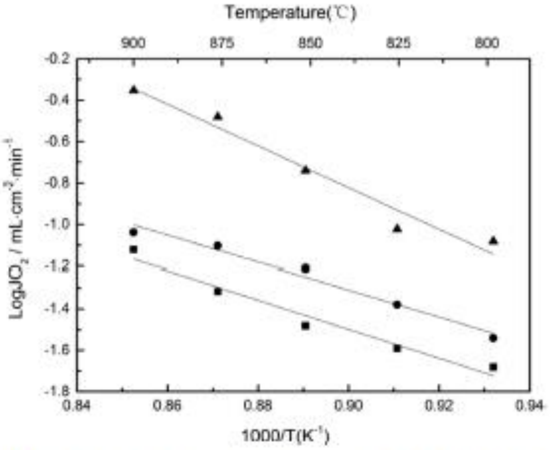

Fig. 4. Temperature dependence of oxygen permeation rate of CGO–LSCF membranes. (■) unmodified; (▲) modified with LSC on permeate side; and (●) modified with LSC on feed side. Solid lines are linear fits.

The oxygen permeation fluxes of the membranes were measured under an oxygen partial pressure gradient ranging from 0.21 bar/10^{-2} bar to 0.21 bar/10^{-4} bar at 800–900 °C. As shown in Fig. 4, the oxygen permeation rate at 900 °C was 0.08 mL cm^{-2} min^{-1} (STP) for the unmodified sample. This value is of medium range, but is lower than that of the $Zr_{0.84}Y_{0.16}O_{1.92}$ (YSZ)–$La_{0.8}Sr_{0.2}MnO_{3-\delta}$ (LSM) dual-phase membrane prepared by the same method [12]. Taking into account that the oxide ion conductivity is higher for LSCF and CGO than for LSM and YSZ, respectively, and that the present CGO–LSCF membrane had a thinner dense layer, a higher oxygen flux was expected for CGO–LSCF than for YSZ–LSM. One possible reason for the observed lower oxygen flux for the unmodified CGO–LSCF could be that the surface oxygen exchange kinetics was not fast enough. To verify this supposition, a LSC porous layer was coated onto the permeate surface of a CGO–LSCF membrane to accelerate the surface exchange. One can see that the oxygen permeation flux of CGO–LSCF was greatly increased by 4.1–5.6 times, reaching 0.45 mL cm^{-2} min^{-1} (STP) at 900 °C. Furthermore, the corresponding apparent activation energy (E_a) also increased from 133.9 ± 14.7 kJ/mol to 192.7 ± 21.8 kJ/mol, suggesting a change of the oxygen permeation mechanism. In great contrast, when the unmodified membrane was decorated on the feed side alone (by depositing nano-sized LSC particles onto the support layer), the oxygen flux increased only slightly and the E_a (123.8 ± 10.7 kJ/mol) remained almost unchanged within the experimental errors. These results demonstrated that the oxygen permeation of the (unmodified) CGO–LSCF membrane was primarily rate-limited by the surface exchange on the permeate side and could be significantly improved by coating a catalytic activation layer.

4. Conclusions

Dual-phase CGO–LSCF membranes were prepared via phase-inversion tape-casting. The asymmetric membrane consisted of a thicker porous support layer and a thinner dense layer for separation of oxygen. Significant increase of the oxygen permeation flux was achieved by surface modification with LSC catalyst on the dense side, but not on the support side. The results demonstrated that the oxygen permeation of the (unmodified) membrane was primarily rate-limited by the surface exchange on the dense side.

Acknowledgment

Financial support by the National Natural Science Foundation of China (21076205 and 50972138), the Fundamental Research Funds for the Central Universities (USTC: WK2320000021), the Scientific Research Foundation for the Returned Overseas Chinese Scholars, State Education Ministry (WF2320000005), Anhui Provincial Natural Science Foundation (1408085ME85), and the Opening Project of CAS Key Laboratory of Materials for Energy Conversion (KF2014003) is greatly acknowledged.

Appendix A. Supporting information

Supplementary data associated with this article can be found in the online version at http://dx.doi.org/10.1016/j.matlet.2014.09.016.